Plasma Physics Reports, Vol. 31, No. 11, 2005, pp. 893–898. From Fizika Plazmy, Vol. 31, No. 11, 2005, pp. 963–968.

TOKAMAKS

Analysis of Electron Thermal Diffusivity and Bootstrap Current in Ohmically Heated Discharges after Boronization in the HT-7 Tokamak*

X. M. Zhang[1, 2] and B. N. Wan[2]

[1] *Department of Physics, East China University of Science and Technology, Shanghai, 200237 China*
[2] *Institute of Plasma Physics, Chinese Academy of Sciences, P.O. Box 1126, Hefei, Anhui, 230031 China*
e-mail: zhangxm@ecust.edu.cn

Received October 6, 2004

Abstract—Significant improvements of plasma performance after ICRF boronization have been achieved in the full range of HT-7 operation parameters. Electron power balance is analyzed in the steady state ohmic discharges of the HT-7 tokamak. The ratio of the total radiation power to ohmic input power increases with increasing the central line-averaged electron density, but decreases with plasma current. It is obviously decreased after wall conditioning. Electron heat diffusivity χ_e deduced from the power balance analysis is reduced throughout the main plasma after boronization. χ_e decreases with increasing central line-averaged electron density in the parameter range of our study. After boronization, the plasma current profile is broadened and a higher current can be easily obtained on the HT-7 tokamak experiment. It is expected that the fact that the bootstrap current increases after boronization will explain these phenomena. After boronization, the plasma pressure gradient and the electron temperature near the boundary are larger than before, these factors influencing that the ratio of bootstrap current to total plasma current increases from several percent to above 10%. © *2005 Pleiades Publishing, Inc.*

1. INTRODUCTION

Heating the plasma to thermonuclear temperatures and confining it in such a way that a net positive energy balance can be achieved is the main task of present-day tokamaks. Much effort has been devoted to study of energy transport and confinement properties in small and large tokamaks worldwide. For better insight into plasma thermal transport processes, a detailed balance of energy losses should be performed on a series of typical reproducible ohmic discharges on the HT-7 tokamak, which, furthermore, can be helpful for understanding and improving energy confinement. In smaller and low- or medium-density plasma, ohmic power mainly heats electrons [1], but the electron power loses through thermal transporting to the boundary, radiating and transferring to the ions. Application of the low-Z wall coating has been taken out in many devices. Good plasma performances have been observed after coating a thin film on the wall [2, 3]. The introduction of low-Z materials as wall limiters or diverter plate materials leads to an extension of the operational range of tokamaks [4]. ICRF wall conditioning has been successfully developed for the first time on the HT-7 tokamak. Plasma performances before and after ICRF wall conditioning have been studied carefully [5, 6].

During the HT-7 experiment, the higher total current can be easily derived and the plasma current profile is broadened after boronization; these phenomena cannot be explained by the theory of neoclassical resistivity and ohmic law. Thus, the possibility of having an important fraction of the plasma current provided by the bootstrap current is projected during HT-7 discharges. Realization of steady-state operation with bootstrap current is an important subject for tokamak research. The existence of bootstrap current has been confirmed experimentally in tokamaks [7]. Especially in high-performance discharges with steeply peaked pressure profiles, a large fraction of bootstrap current has been achieved and is very important for steady-state operation in tokamaks [8]. In this paper, we will estimate the bootstrap current after boronization on the HT-7 tokamak.

The structure of this paper is as follows. The experimental diagnostics are briefly described in Section 2. Detailed analysis of the experiment results is given in Section 3, and conclusions and discussion are given in Section 4.

2. EXPERIMENTAL DIAGNOSTICS

HT-7 is a midsize tokamak device with a major radius of 1.22 m and a minor radius of 0.26–0.28 cm [9]. The electron density profile $n_e(r)$ is measured by a vertical five-channel far-infrared hydrogen-cyanide laser interferometer. The electron temperature profile $T_e(r)$ is derived from electron cyclotron emission. This

* This text was submitted by the authors in English.

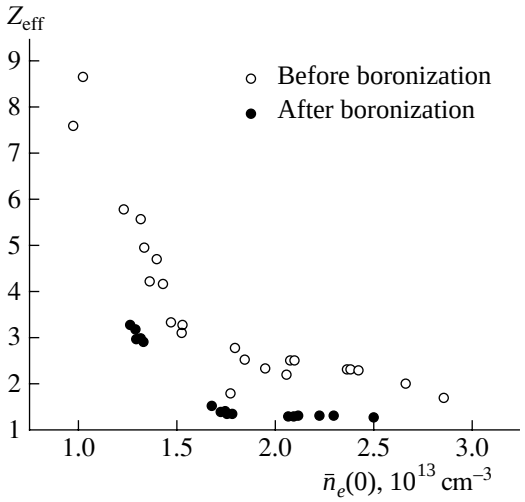

Fig. 1. Z_{eff} as a function of line-averaged density before and after boronization.

measurement was also confirmed by Thomson scattering and X-ray spectroscopy. The contribution of the power lost by radiation to the plasma power balance is determined from a 16-channel bolometer array. The ion temperature is measured by a ten-channel neutral particle analyzer. A four-channel visible bremsstrahlung emission is used to measure the effective plasma charge Z_{eff}.

An ion cyclotron range frequency (ICRF) wall-cleaning technique has been developed in the HT-7 Superconducting Tokamak using 3 g of nontoxic and nonexplosive solid carborane powder. During the HT-7 experimental runs, the technique improved the state of the first wall and decreased recycling, which is very beneficial for enhancement of plasma discharge.

3. EXPERIMENTAL DATA ANALYSIS

3.1. Power Balance Analysis after Boronization on the HT-7 Tokamak

After B-coating, plasma performance was immediately improved. The mental impurity lines disappeared. The visible lines of carbon and oxygen obviously reduced. The impurities and the radiation loss were reduced in the full range of operation parameters. Figure 1 shows the dependence of Z_{eff} on central line-averaged electron density in standard ohmic discharges for $I_p \approx 140$ kA, $B_t \approx 1.84$ T.

The ratio of radiation loss to ohmic power is considered to change with the central line-averaged electron density and plasma current. The ratio, $\alpha = P_{rad}/P_{OH}$, increases with central line-averaged electron density during steady-state normal discharges (see Fig. 2a), whereas it is decreased with increasing plasma current (see Fig. 2b).

Two typical shots are compared in Fig. 3. The longer waves represent the case after boronization. These two shots have nearly the same central line-averaged density, $\bar{n}_e(0) \approx 1 \times 10^{13}$ cm^{-3}, and plasma current, $I_p \approx 150$ kA. But the loop voltage, effective charge, and radiation loss drop significantly after boronization.

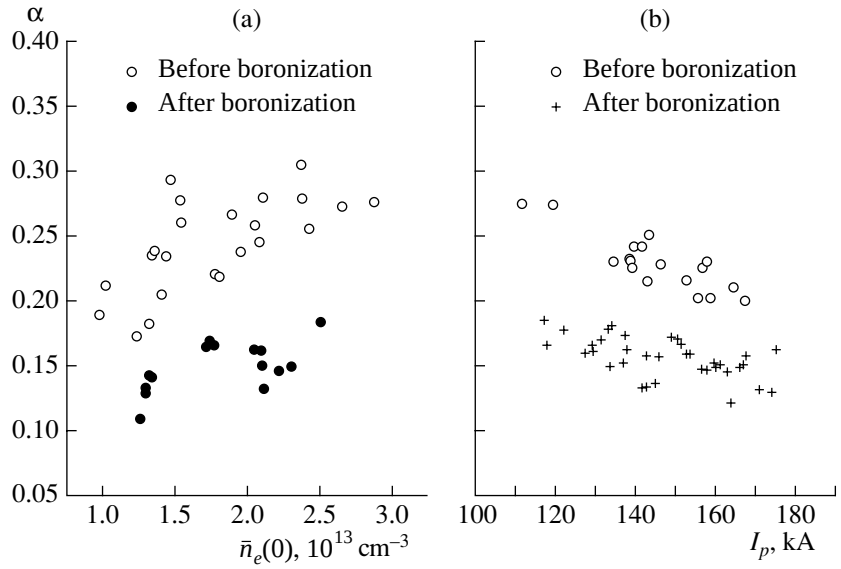

Fig. 2. Ratios of the radiated power (P_{rad}) to the ohmic input power (P_{OH}) in ohmically heated discharges: (a) as a function of the central line-averaged electron density, and (b) as a function of I_p ($\bar{n}_e(0) \approx 10^{13}$ cm^{-3}, $B_t \approx 1.84$ T).

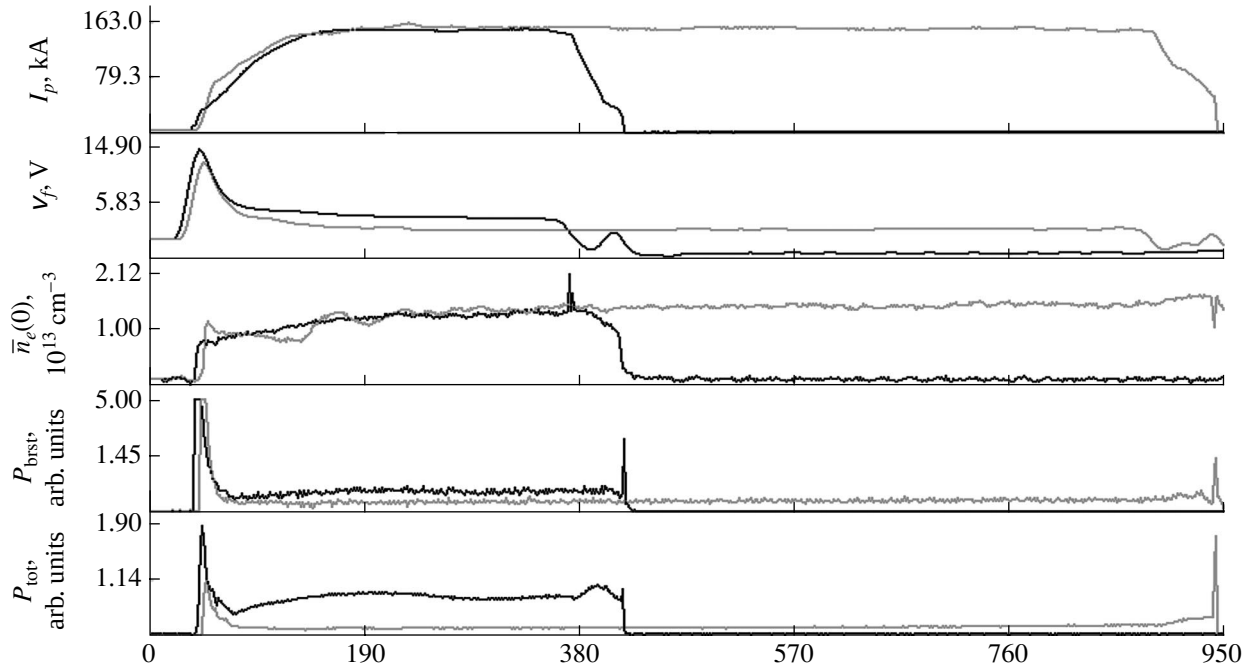

Fig. 3. Two typical pulses before (shot pulse) and after (longer) boronization with the similar parameters. (Central line-averaged electron density $\bar{n}_e(0) \approx 10^{13}$ cm^{-3}, and the plasma current $I_p \approx 150$ kA.) From top to bottom: plasma current I_p, loop voltage v_f, central line-averaged electron density, central-chord bremsstrahlung P_{brst}, and total radiation measurement P_{tot}.

After boronization, the electron density profile becomes broader, as shown in Fig. 4a. The electron temperature and profiles (Fig. 4b) measured by ECE were increased in the whole plasma region and had a larger gradient.

The electron diffusivities deduced from the power balance equations are shown in Fig. 5. After boronization, the electron diffusivity is reduced in the whole radial region under ICRF boronized condition. Hence, the energy confinement time is increased after boronization. The correlation between electron thermal diffusivity (at $r/a = 0.5$) and the central line-averaged electron density is shown in Fig. 6. It decreases with increasing the central line-averaged electron density.

3.2. Bootstrap Current Increment after Boronization

During the HT-7 experiment, the higher total current can easily be derived and the plasma current profile is broadened after boronization. These phenomena cannot be explained by the theory of neoclassical resistivity and ohmic law. Thus, the possibility of having an important fraction of the plasma current provided by the bootstrap current is projected during the HT-7 discharges.

In order to study the substantial bootstrap current expected after boronization, two typical shots before and after boronization are taken as a comparison. The electron density profiles and their temperature profiles are shown in Fig. 4. The plasma pressure profiles, which are shown in Fig. 7, are evaluated.

Different pressure profiles can give rise to different bootstrap current profiles. The total plasma current density j_{tot} is mainly divided into two parts, namely,

$$j_{tot} = \frac{E_{\|}}{\eta^{neo}} + j_{bs}.$$

where $E_{\|}$ is the toroidal electric field and η^{neo} is the neoclassical electric resistivity.

Then the bootstrap current can be evaluated by using the following formula [10]:

$$j_{bs} = -\frac{\varepsilon^{1/2} n}{B_\theta}\left[2.44(T_e + T_i)\frac{1}{n}\frac{dn}{dr} + 0.69\frac{dT_e}{dr} - 0.42\frac{dT_i}{dr}\right].$$

After boronization, the plasma pressure profile becomes broader, at which point the pressure gradient near the boundary is increased and the peak of the bootstrap current is nearer to the boundary (as seen in Fig. 8).

The value near the boundary contributes to the total integral current significantly, since the value of the radius near the boundary is larger. The nearer to the boundary of the peak of the bootstrap current density, the larger the value of the ratio of the bootstrap current to the total plasma current. The ratio of the bootstrap

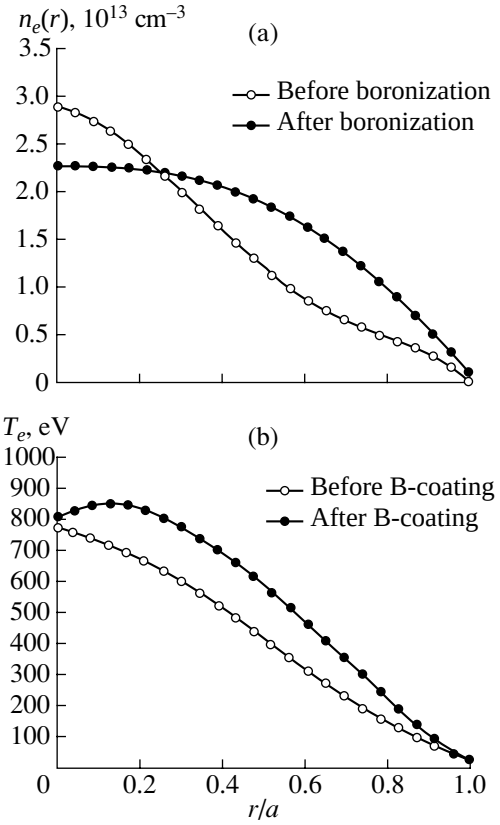

Fig. 4. Electron density and temperature profiles.

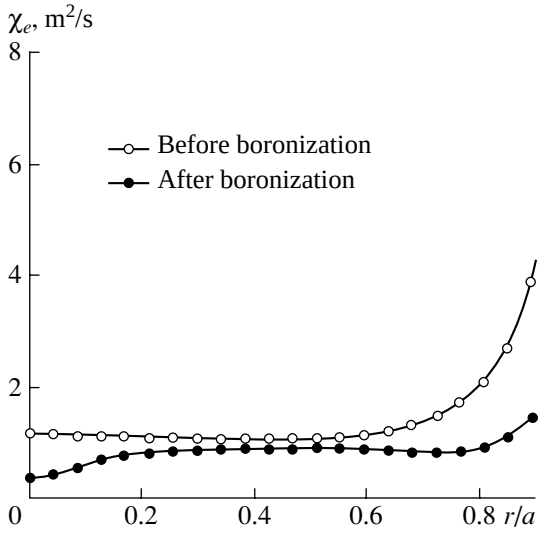

Fig. 5. Radial distributions of electron diffusivities before and after boronization.

current density to the total current density, j_{bs}/j_{tot}, can be obtained and is shown in the Fig. 9. The proportion of bootstrap current to total current is much higher near the boundary after boronization.

We take a few discharges for research. The table shows the fraction of the total bootstrap current to the total plasma current. The first three items are the data before boronization, and the rest are the data after boronization. Here I_p, I_{OH}, and I_{bs} are the total integral values of the plasma current, current evaluated by neoclassical electric resistivity, and bootstrap current. From the table, we can see that the fraction is increased from about several to tens of percent after boronization.

4. CONCLUSIONS AND DISCUSSION

Good plasma performance has been obtained with the B-coating wall on the HT-7 tokamak. Power balance is studied on the HT-7 tokamak. The ratio of the total radiation power to the ohmic input power increases with increasing the central line-averaged electron density, but decreases with the plasma current. It is obviously decreased after wall conditioning. The radiation loss may not be dominant on the HT-7 tokamak, since it seldom exceeds 40% during steady-state discharge. The electron heat diffusivity χ_e profile is estimated from the power balance equation. It is

The fraction of the bootstrap current to the total plasma current before and after boronization

Shot no.	Time, ms	Ne(0), 10^{13} cm^{-3}	I_p, kA	I_{OH}, kA	I_{bs}, kA	I_{bs}/I_p
*29518	317	0.93	117.9	113.2	4.7	2.6%
*29468	300	1.43	123.8	120.0	3.8	3.1%
*33997	350	1.51	104.7	102.9	1.7	1.7%
30448	595	1.47	154.5	136.9	17.6	11.3%
36724	350	1.06	127.2	113.7	13.5	10%
36744	480	1.14	151.8	133.2	18.4	12.1%
36777	300	1.08	166.5	144.7	21.8	13%
36791	280	0.97	173.5	147.7	25.8	14.8%

* The former three shots are the data before wall conditioning, and the rest are the data after boronization.

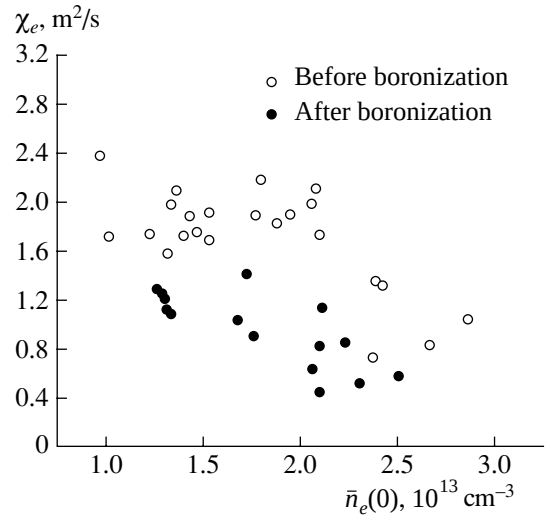

Fig. 6. Correlation between electron thermal diffusivity at r/a = 0.5 and the electron central line-averaged density ($I_p \approx 140$ kA, $B_t \approx 1.84$ T).

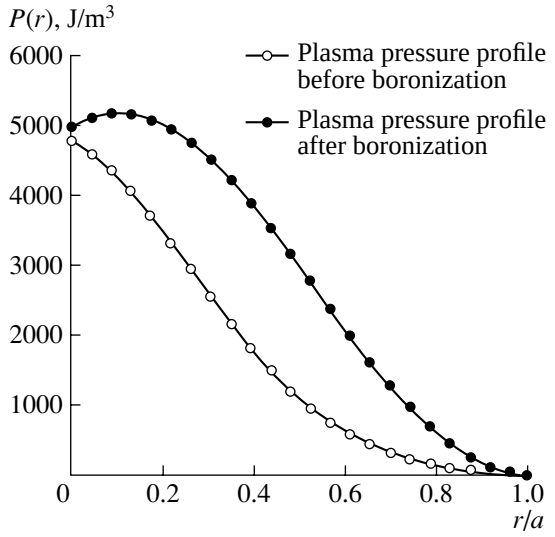

Fig. 7. Comparison of the plasma pressure profiles between before and after boronization.

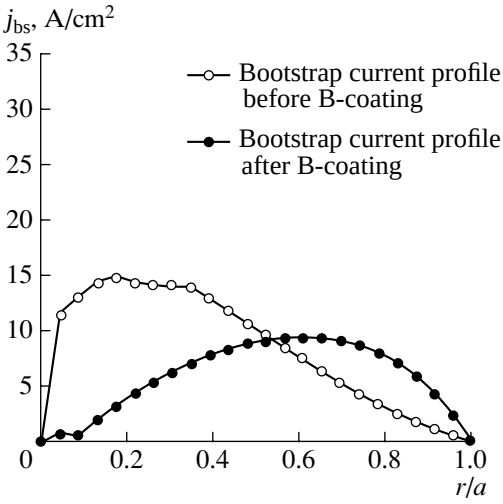

Fig. 8. Comparison of the bootstrap current density profiles between before and after boronization.

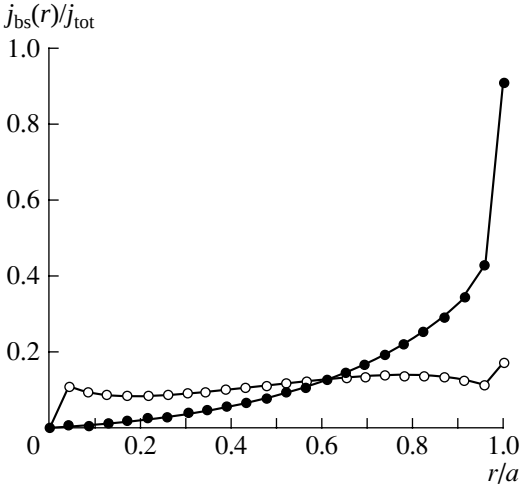

Fig. 9. Fraction of the bootstrap current density j_{bs} to the total plasma current density j_{tot} varying with the normalized radius. (○—data before boronization, ●—data after boronization.)

reduced throughout the main plasma after boronization, and the energy confinement is improved by from 8 to 15 ms. χ_e at half radius decreases with increasing central line-averaged electron density.

The results of the first estimation of bootstrap current on the HT-7 tokamak are exciting. Broadening plasma parameter profiles and increasing the pressure gradient in the plasma periphery after wall conditioning cause an increment of the bootstrap current profile near the boundary. The ratio of the total bootstrap current to the total current increases after wall conditioning, which is attributed to that from the boundary. It is less than 5% of the total plasma current before wall conditioning, but enhanced up to more than 10% for boronized wall conditions. The ratio is sensitive to the plasma pressure gradient near the boundary, namely, the greater the plasma pressure gradient in the plasma periphery, the greater the bootstrap current ratio. Furthermore, temperature increases in the plasma periphery and collision frequency decreases after wall conditioning; then, the banana particle orbit can be easily

completed, so these phenomena can also be proposed to enhance bootstrap current proportion on the HT-7 tokamak.

REFERENCES

1. J. Hugill, Nucl. Fusion **23**, 331 (1983).
2. J. Winter, Plasma Phys. Controlled Fusion **38**, 1053 (1996).
3. Y. P. Zhao, Chin. Phys. Lett. **14**, 916 (1997).
4. J. Li, Y. P. Zhao, X. M. Gu, *et al.*, Nucl. Fusion **39**, 973 (1999).
5. J. K. Xie, Y. P. Zhao, J. Li, *et al.*, J. Nucl. Mater. **290**, 1155 (2001).
6. B. N. Wan, Y. P. Zhao, and J. Li, Plasma Sci. Technol. **4**, 1375 (2002).
7. M. Isobe, N. Nakajima, K. Ida, *et al.*, Plasma Phys. Controlled Fusion **44**, A189 (2002).
8. V. S. Chan, C. M. Greenfield, L. L. Lao, *et al.*, Nucl. Fusion **40**, 1137 (2000).
9. X. M. Zhang, B. N. Wan, and X. J. Feng, Plasma Sci. Technol. **6**, 2194 (2004).
10. J. Wesson, *Tokamaks* (Clarendon, Oxford, 1997).

Plasma Physics Reports, Vol. 31, No. 11, 2005, pp. 899–907. Translated from Fizika Plazmy, Vol. 31, No. 11, 2005, pp. 969–977.

MAGNETIC CONFINEMENT SYSTEMS

Formation of a Narrow Radial Density Profile of Fast Ions in the GDT Device

V. V. Prikhodko[1, 2], A. V. Anikeev[1], P. A. Bagryansky[1], A. A. Lizunov[1], V. V. Maximov[1], S. V. Murakhtin[1], and Yu. A. Tsidulko[1]

[1] *Budker Institute of Nuclear Physics, Siberian Division, Russian Academy of Sciences, pr. Akademika Lavrent'eva 11, Novosibirsk, 630090 Russia*

[2] *Novosibirsk State University, ul. Pirogova 2, Novosibirsk, 630090 Russia*

Received December 1, 2004; in final form, February 10, 2005

Abstract—The radial density profile of fast ions with a mean energy of 10 keV is measured in experiments with a two-component high-β plasma in the GDT device. Fast ions are produced by injecting neutral beams into a warm plasma. The measured fast-ion density profile is found to be narrower than that calculated with allowance for the neutral beam trapping and Coulomb scattering. Special experiments with a movable limiter have indicated that the formation of a narrow fast-ion density profile in GDT cannot be attributed to the loss of fast ions. Possible mechanisms responsible for this effect are discussed. © *2005 Pleiades Publishing, Inc.*

1. INTRODUCTION

1.1. Experimental Setup

The gasdynamic trap (GDT) (Fig. 1) is a long, axisymmetric magnetic-mirror confinement system with a high ($R \approx 50$) mirror ratio. The confined plasma consists of two ion components with very different energies [1, 2]. One component (the "target" plasma) is a collisional hydrogen plasma with a temperature of $T_i \approx T_e \approx 100$ eV and density of $n_t \sim 10^{14}$ cm^{-3}. For these parameters, the ion mean free path with respect to scattering into the loss cone is shorter than the mirror-to-mirror length, thereby making it possible to operate in the gasdynamic mode of confinement. The target plasma is produced in the initial stage of a discharge by a plasma source placed in one of the two end tanks.

After the GDT is filled with the target plasma, a neutral beam injection (NBI) system is switched on. The system consists of six injectors [3] producing 20-keV neutral deuterium beams. The beam duration is 1.1 ms, and the total NBI power is 4.3 MW. The neutral beams, which are injected in the midplane at an angle of 45° to the axis, are trapped by the target plasma and produce the fast ion component. Fast ions are confined adiabatically and gradually relax in the target plasma. As a result, the electron temperature of the target plasma increases from $T_e \approx 5$ eV to $T_e \approx 100$ eV. Measurements show that the average energy of the fast-ion component is about 10 keV [4]. A specific feature of GDT experi-

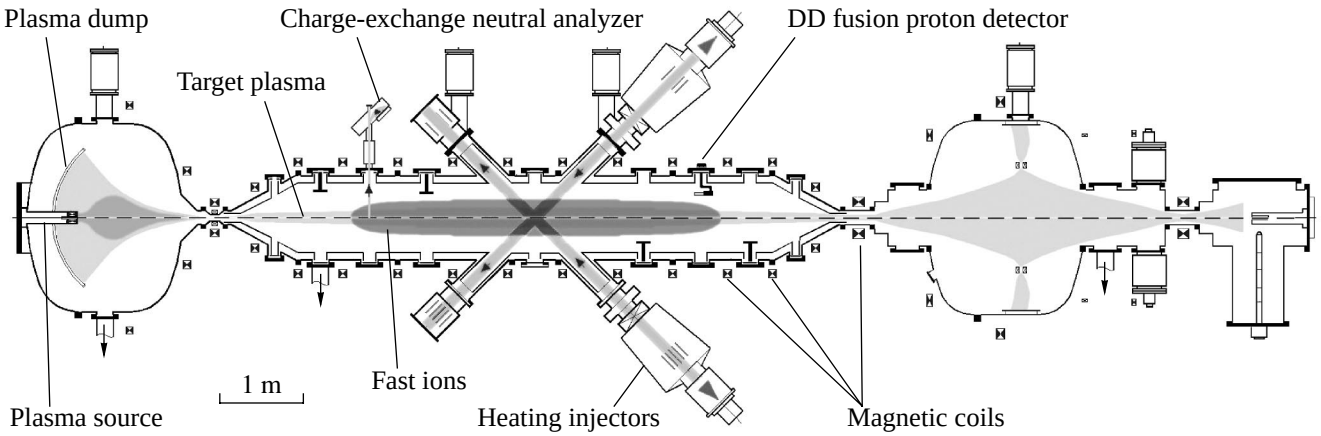

Fig. 1. The GDT layout.

1063-780X/05/3111-0899$26.00 © 2005 Pleiades Publishing, Inc.

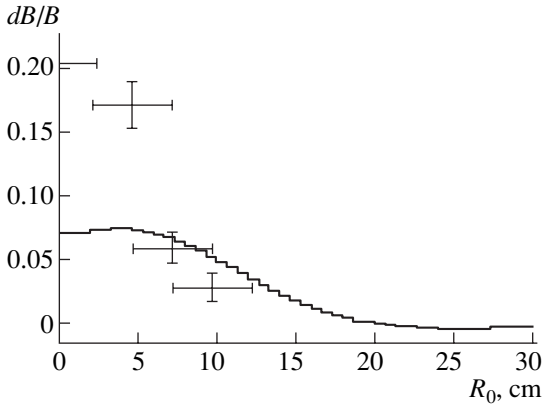

Fig. 2. Measured (symbols) and calculated (solid line) profiles of the magnetic field perturbation caused by the plasma diamagnetism.

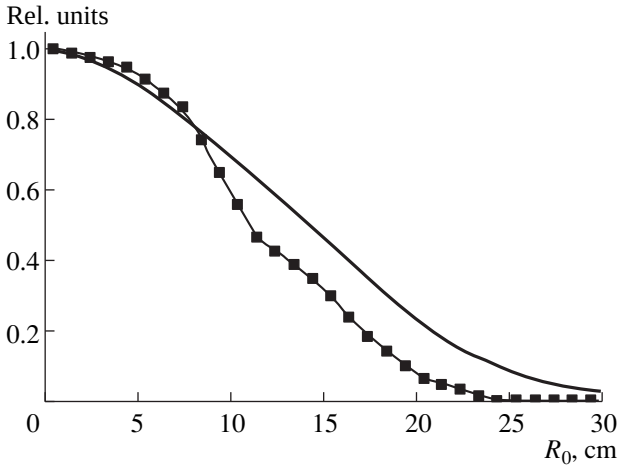

Fig. 3. Measured density profile of the target plasma (squares, the FWHM is a = 22 cm) and the calculated density profile of the trapped ions (solid line, the FWHM is a = 28 cm).

ments is a relatively low magnetic field in the midplane of the device, B_0 = 0.26 T. In this case, the Larmor radius of fast ions with energies close to the injection energy is comparable to the target plasma radius, which is about 12 cm.

1.2. Formulation of the Problem

The ratio between the energy of the injected deuterium neutrals and the electron temperature of the target plasma is high enough ($\frac{E_i}{T_e} \gg \left(\frac{9\pi}{16}\frac{M}{m}\right)^{1/3}$) for the fast ions to relax without substantial angular scattering. Since the initial angular spread of the heating beams is small and they are injected at an angle of 45° to the device axis, the turning points of the fast ions lie in the regions where the mirror ratio is R = 2. In these regions, the axial fast-ion density profile is highly peaked. This is a distinctive feature of the GDT-based neutron source proposed in [5]. It is proposed that the test zones of the neutron source will be arranged around the tuning points of the fast deuterium and tritium ions, where the flux density of the 14-MeV neutrons is expected to be maximum. In this context, it is of interest to study the fast-ion density profiles near the turning points, as well as the physical mechanisms governing their formation.

In the previous GDT experiments, the radial profile of the magnetic field was measured by means of active beam spectroscopy [6]. The splitting of the H_α line was measured using a 40-keV diagnostic hydrogen beam. From these measurements, the radial profile of the magnetic field perturbation caused by plasma diamagnetism, $\Delta B/B = (B_{vac} - B)/B_{vac}$, was determined (see Fig. 2; hereafter, the radial coordinate is mapped onto the GDT midplane along the magnetic field lines). The width of this radial profile is on the order of the Larmor radius of a deuteron with an energy close to the injection energy. For comparison, Fig. 2 also shows the calculated profile of the magnetic field perturbation caused by the diamagnetic effect of fast ions. The profile was calculated using the MCFIT code [4, 7], which is based on the theory of binary Coulomb collisions and allows one to simulate the interaction between fast ions and the target plasma. A brief description of the MCFIT code is given in the Appendix. The calculated reduction in the magnetic flux through a contour enclosing the plasma agrees well with the diamagnetic loop signal. At the same time, the measured profile of the magnetic field perturbation turns out to be considerably narrower than the calculated one. This indicates that the radial profile of the fast-ion density may also be narrower than the calculated one, because, under the GDT experimental conditions, the magnetic field perturbation produced by the target plasma near the turning points is small compared to that caused by the fast ions and, therefore, the profile of the magnetic field perturbation is related only to the profile of the fast-ion pressure.

The full width at half-maximum (WFHM) of the expected fast-ion density profile determined by the trapping of neutrals can be roughly estimated as $R_{fi} = \sqrt{R_{tp}^2 + \rho^2} \approx 13$ cm [8], where R_{tp} = 11 cm is the characteristic radius of the target plasma (the WFHM of the measured density profile) and ρ = 7 cm is the Larmor radius of deuterons with energies equal to the injection energy. To determine the width of the radial fast-ion density profile more accurately, we performed special calculations with allowance for the measured density profile of the target plasma, the current density profiles of the heating beams, and the known ionization cross sections. Figure 3 shows the radial density profile obtained in this way for fast ions with energies equal to the injection energy. The width of the calculated fast-ion density profile is 28 cm (hereafter, by the profile

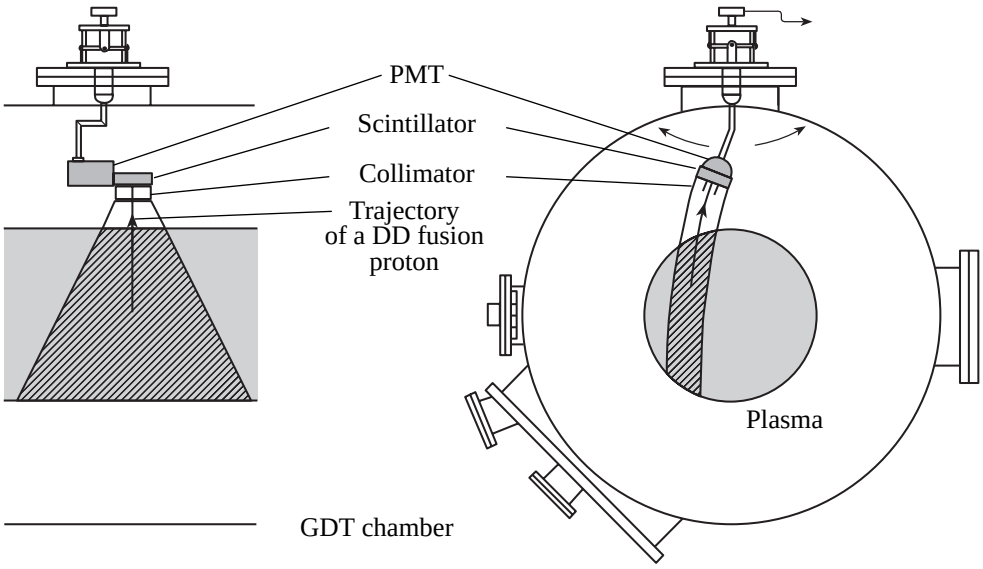

Fig. 4. Layout of the system for detecting DD fusion protons.

width, we mean the FWHM of the profile mapped onto the midplane of the device along the magnetic field lines). At the same time, the width of the profile of the magnetic field perturbation caused by the diamagnetic effect of the fast ions is less than 15 cm.

It is well known that, when collisions are ignored, there is no radial transport in an axisymmetric magnetic field. Taking into account classical collisions results in a small inward-directed radial drift. The displacement of the guiding center of a particle decelerated in a nonuniform plasma was estimated, e.g., in [8]. Under our experimental conditions, this displacement is $\Delta R \approx$ 2 cm; i.e., ion deceleration in a nonuniform plasma has little effect on the width of the fast-ion density profile. That the drift is small is also confirmed by the results of computer simulations with the MCFIT code. The magnetic field perturbation caused by the high plasma pressure (the high-β effect) enlarges the magnetic surfaces and, consequently, broadens the ion density profile. The narrowing of the fast-ion density profile cannot be explained by the ion loss from the edge plasma. This follows from studying the fast-ion energy balance and also from the results obtained in a special experiment described below. To study the formation of the fast-ion density profile under high-β conditions in more detail, we performed experiments with the use of specially designed diagnostics. The results of these experiments are presented here.

The paper is organized as follows. Section 2 describes experiments on the measurement of the radial profile of the flux of fusion-reaction products. Section 3 is devoted to measurements of the profile of the charge-exchange neutral flux. Section 4 describes the results of an analysis of the energy balance of fast ions and a special experiment with a movable limiter. In Section 5, the experimental results are discussed. Based on the results of theoretical studies [9], a physical mechanism for the rearrangement of the fast-ion density profile is proposed. In the Conclusions, the results obtained are summarized, and in the Appendix, the MCFIT code is briefly described.

2. MEASUREMENTS OF THE RADIAL PROFILE OF THE FUSION PROTON FLUX

The experiments were performed with a hydrogen target plasma. Hence, fusion reactions occurred only in binary collisions between fast deuterons,

$$\mathrm{D + D} \longrightarrow \begin{array}{l} (50\%) \longrightarrow \mathrm{T}(1.01\ \mathrm{MeV}) + p(3.02\ \mathrm{MeV}) \\ (50\%) \longrightarrow \mathrm{He}^3(0.82\ \mathrm{MeV}) + n(2.45\ \mathrm{MeV}). \end{array}$$

Measurements of the radial profile of the 2.45-MeV neutron flux require a rather complicated and massive collimator. For this reason, in our measurements, we used the proton branch of the DD reaction.

The layout of the detector of the DD fusion protons is shown in Fig. 4 [10, 11]. The detector consisted of a scintillator and a photomultiplier tube (PMT). The DD fusion protons and neutrons entering the scintillator

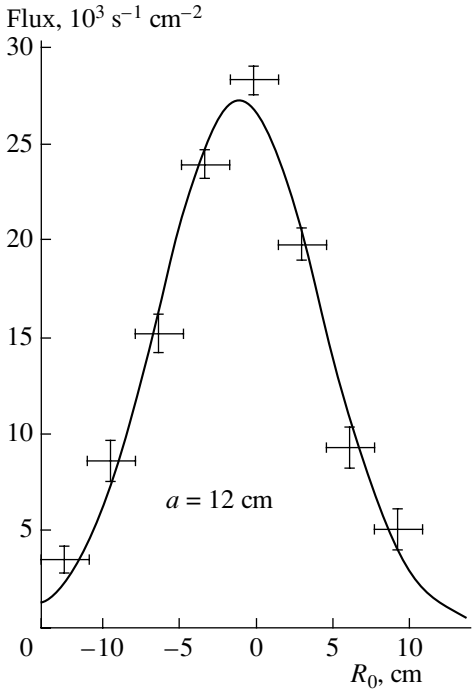

Fig. 5. Measured radial profile of the flux of the DD fusion products.

produced a light burst, which was detected by the PMT. The PMT signal was amplified and was then digitized by a fast analog-to-digital converter (ADC). The scintillator was covered with an aluminum foil, which protected the detector from plasma radiation but insignificantly affected the proton flux. A stainless-steel shade that was impenetrable for protons but was transparent for neutrons could be placed in front of the scintillator. The detector components had little effect on the flux of the DD fusion neutrons. The detector was installed inside the GDT vacuum chamber and could be displaced along the radius within 9 cm on both sides from the device axis. The distance from the plasma axis to the scintillator surface was about 30 cm. A blind collimator, which was placed in front of the scintillator, allowed us to measure the radial profile of the proton flux with a spatial resolution of about 3 cm (4 cm in the midplane coordinates).

The data were acquired during the entire injection pulse. The duration of the light pulse produced by a proton or a neutron was 35–40 ns, which corresponded to seven to eight ADC sampling periods. This enabled the detector to operate in a single-particle counting mode. A few hundred particles per shot were detected, so we could calculate the amplitude distributions of the pulses and discard small-amplitude pulses corresponding to the multiplier noise and to scattered low-energy neutrons. Double events were ignored because their probability was below 1%.

The profile of the DD proton flux was measured in several steps. First, we produced a series of background shots with a closed shade in order to determine the average number of the detected neutrons. Then, for each position of the detector, we produced a series of shots with an open shade. In each series, we determined the average number of the detected neutrons and protons. To separate the contributions from protons and neutrons, we subtracted the neutron flux from the total particle flux. Finally, we again produced a series of background shots with a closed shade in order to improve the neutron statistics and to check on whether the parameters of the experiment change.

Figure 5 shows the measured profile of the DD proton flux. Its width is $a_{\mathrm{DD}} = 12$ cm. The width of the profile of the DD proton flux can be roughly estimated assuming that the Larmor radius of fast ions is infinitely small and that their density profile is Gaussian: $n_{fi}(r) \sim \exp(-r^2/R_{fi}^2)$. The radial profile of the DD proton flux is then described by the function $n_{\mathrm{DD}}(r) \sim n_{fi}^2(r) \sim \exp\left(-\dfrac{r^2}{R_{fi}^2/2}\right)$, and its width is $a_{\mathrm{DD}}^{\mathrm{theor}} = 2R_{fi}/\sqrt{2} = 18$ cm.

A more accurate estimate of the width of the DD proton flux was obtained as follows. It was assumed that the spatial distribution of the fast-ion guiding centers was determined by the trapping of the neutral beams in the target plasma. The fast-ion energy distribution was taken to comply with a stationary solution to the kinetic equation describing the relaxation of fast ions in plasma under the assumption $T_e \ll E_f$, where T_e is the electron temperature and E_f is the mean fast-ion energy. [12]. This assumption seems to be reasonable because estimates show that, under our experimental conditions, the characteristic fast-ion relaxation time is comparable to the NBI duration. The calculated width of the profile of the DD proton flux was found to be $a_{\mathrm{DD}}^{\mathrm{theor}} = 20$ cm (Fig. 6), which substantially exceeded the measured value.

The profile shown in Fig. 5 was constructed using the experimental data acquired during the entire injection pulse (1.1 ms), while Fig. 7 shows a profile constructed using the results of measurements over the first 0.4 ms after the beginning of injection. The widths of these profiles coincide to within the experimental error. Hence, we can conclude that the narrow profile of the flux of the DD reaction products forms over a time shorter than 0.4 ms.

3. MEASUREMENTS OF THE RADIAL PROFILE OF THE CHARGE-EXCHANGE NEUTRAL FLUX

This diagnostics was designed to measure the density of fast ions with preset initial coordinates and velocity directions [4]. The main components of the diagnostic system were an active target, a stripping chamber, and a 45° electrostatic analyzer (Fig. 8). A microchannel plate (MCP) was used as a particle

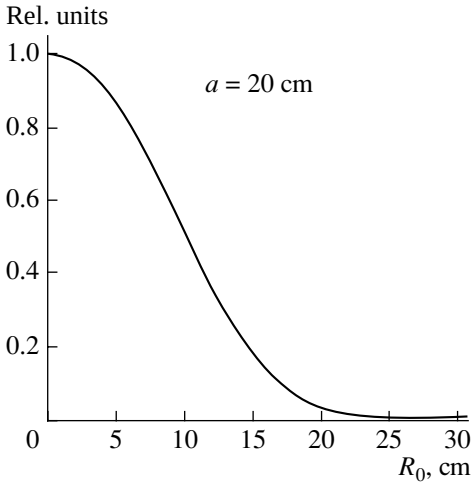

Fig. 6. Calculated radial profile of the flux of the DD fusion products.

coordinate detector. The active plasma target for the charge exchange of fast ions was produced by a diagnostic neutral-beam injector [13]. A hydrogen neutral beam with an energy of 40 keV was injected perpendicular to the device axis. The diameter of the beam was 4 cm, and the equivalent current was about 4 A. After passing through the plasma, the beam was attenuated by 20–30%. The beam diameter determined the spatial resolution along the Y axis (ΔY = 4 cm). The charge-exchange neutral flux was collimated using two apertures. The first aperture was placed in front of the stripping chamber. The size of this aperture along the device axis determined the size of the scanned region along the Z axis (ΔZ = 1.2 cm). The particles then entered the stripping chamber filled with helium. The second collimating aperture 1 mm in diameter was made in the plates of the electrostatic capacitor. The small diameter of this aperture allowed the particles to be spatially separated in the 45° analyzer. Therefore, the coordinates at which a particle fell on the MCP depended on the particle energy and its initial coordinate X (see Fig. 8). The MCP amplified the secondary electron current, which was then measured using collectors on the MCP back side. The positions and sizes of the collectors determined the initial coordinates of the detected particles and the energy resolution of the system ($\Delta E = 0.06\bar{E}$, where $\bar{E} = 2|e|U_{\text{analyser}}$, e is the electron charge, and U_{analyser} is the capacitor voltage), as well as its resolution over the X coordinate, ΔX = 3.1 cm ($X_i = i\Delta X$, with i = –5, …, +5).

In order to separate the flux of the particles produced at the active target from the total charge-exchange neutral flux, we carried out experiments with and without the target. At each point, we made, on average, five to seven shots with and without the target. Figure 9 shows typical signals from the charge-exchange neutral analyzer, and Fig. 10 shows the measured pro-

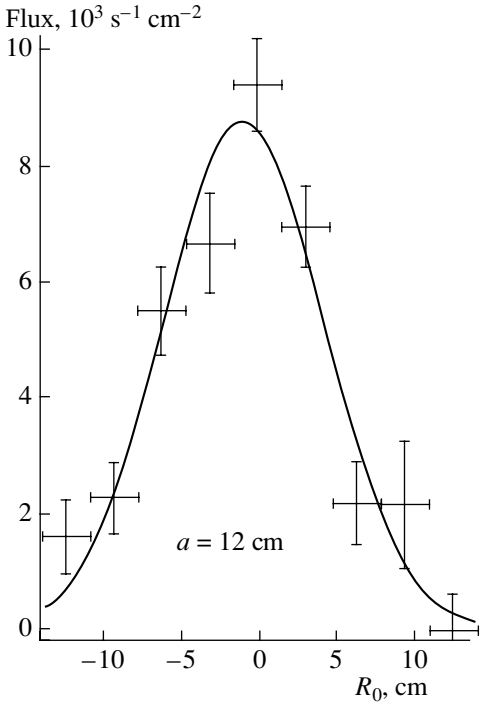

Fig. 7. Radial profile of the flux of the DD fusion products measured during the first 0.4 ms after the beginning of injection.

files of the charge-exchange neutral flux. For neutrals with energies close to the beam energy (E = 18–20 keV), the profile width is a_{CX} = 28–31 cm; for neutrals with an energy of E = 16 keV, the profile width is a_{CX} = 19 cm; and for neutrals with an energy of E = 13 keV, it is a_{CX} = 16 cm.

The signal from the MCP analyzer is proportional the number of the fast particles that have undergone

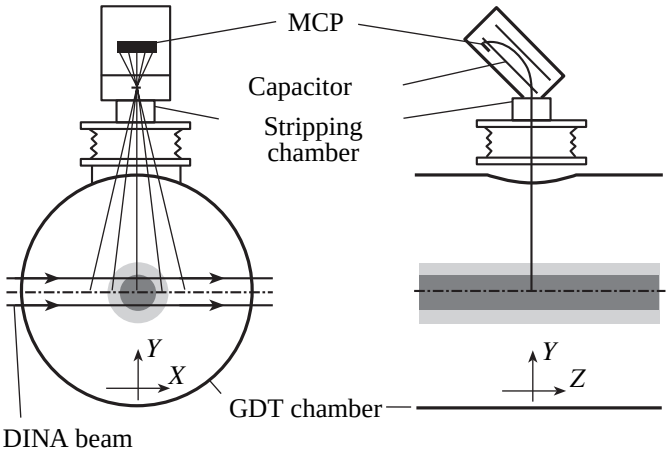

Fig. 8. Charge-exchange neutral analyzer with an active target.

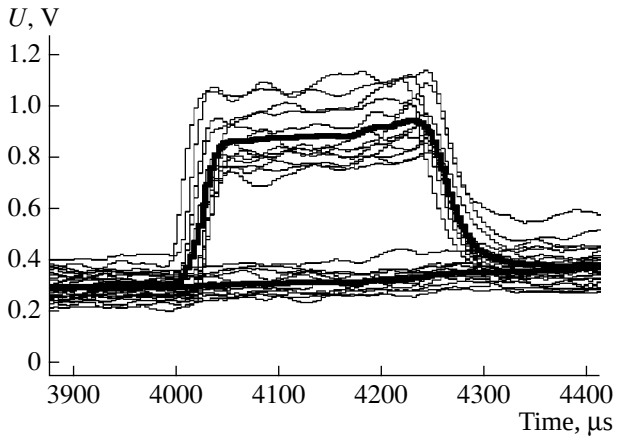

Fig. 9. Typical signals from the charge-exchange neutral analyzer in shots with and without an active target. Heavy lines show the average signals.

charge exchange in the plasma. Note that there is a systematic error in determining the signal from the active target, because the 40-keV protons that are produced due to the charge exchange of the active-target neutrals in the target plasma are lost with a high probability on the limiters, whereas the neutralized particles of the active target remain in the target plasma. These particles form a gas cloud, which introduces a systematic error in determining the density profile of the charge-exchange fast particles. The calculated density of this neutral gas is $n_n \sim 10^9$ cm^{-3}, which corresponds to an error of about 5–10% of the valid signal. The radial profile of this neutral gas is wider than the target plasma profile; therefore, this systematic error does not affect the profile widths.

4. EXPERIMENT WITH A MOVABLE LIMITER

Taking into account the measured profile of the charge-exchange neutral flux, we can conclude that the density profile of the fast ions with energies of E = 13 keV is nearly half as narrow as the initial fast-ion density profile determined by the trapping of the heating beam (E = 20 keV). There may be two reasons for the formation of such a narrow profile: the fast ions either drift toward the device axis or they are lost from the plasma periphery. To clear up how the loss of fast ions affects the formation of their radial density profile, we carried out a special experiment with a movable limiter.

The movable limiter (or the "knife"; see Fig. 11) was a metal plate that was insulated from the vacuum chamber and could be displaced in the radial direction. The fast ions moving in Larmor orbits were lost if their trajectories crossed the knife limiter. The target plasma was limited by annular limiters that were installed

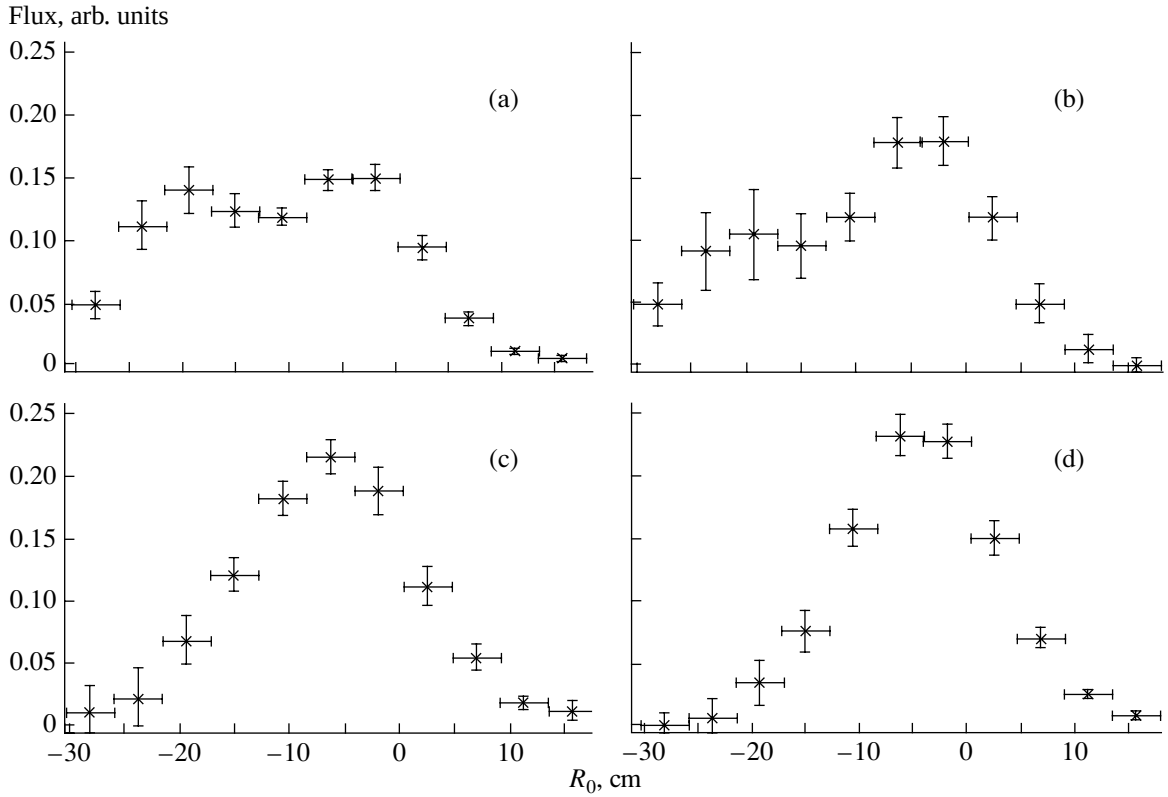

Fig. 10. Profiles of the charge-exchange neutral flux for E = (a) 20, (b) 18, (c) 16, and (d) 13 keV.

behind the turning points of the fast ions at a radius of R_0 = 15 cm in the midplane coordinates. Hence, the movable limiter, which was displaced within the interval R_0 = 15–30 cm, slightly influenced the target plasma.

Assuming that fast ions are lost from the plasma periphery, one could expect that the knife limiter inserted into the plasma to a radius larger than the half-width of the established fast-ion density profile would insignificantly affect the number of the accumulated fast ions. As a consequence, this would also insignificantly affect the plasma energy, the target-plasma temperature, etc. However, if the fast ions drift toward the device axis, then the knife limiter inserted to a radius on the order of the half-width of the trapping region would cause a substantial decrease in the number of fast ions and, consequently, in the plasma energy.

Figure 12 shows the results of the experiment with the movable limiter. As an illustration, Fig. 12 also shows the results of simulations by the MCFIT code. The energy of the fast-ion component begins to change when the knife limiter is inserted to a radius of 20–22 cm. When the distance from the limiter to the axis is 14–16 cm, the energy of the fast-ion component halves. The experimental data agree well with the calculated results (a discrepancy at radii of 14–16 cm can be explained by the effect of the limiter on the target plasma being ignored in calculations). This allows us to conclude that the loss of fast ions from the plasma periphery is insignificant. This conclusion is also confirmed by an analysis of the fast-ion energy balance [14].

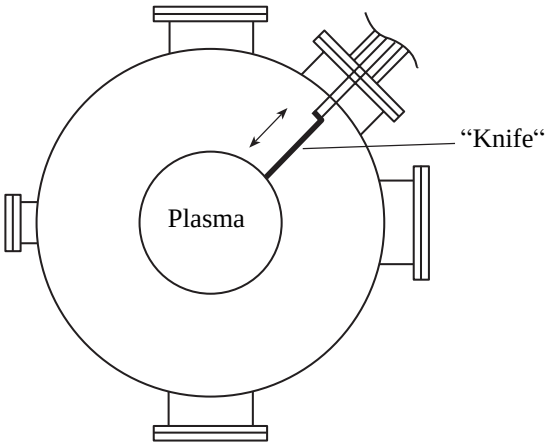

Fig. 11. Position of a movable knife limiter.

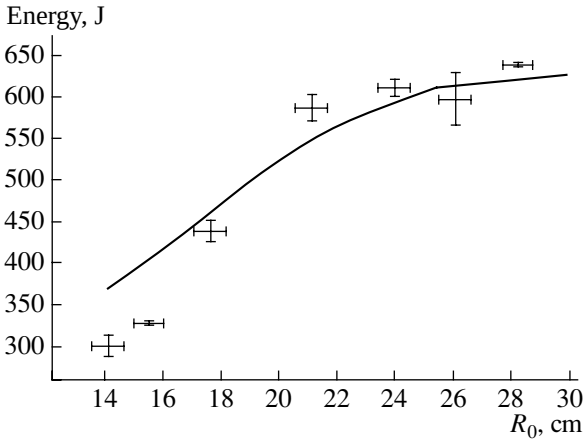

Fig. 12. Total fast ion energy content as a function of the radius of the movable limiter. Symbols show the experimental data, and the solid line shows the results of numerical simulations.

5. DISCUSSION

The results of our experiments allow us to conclude that the density profile of the fast ions with energies that are 20–50% lower than the injection energy is nearly twice as narrow as the initial profile. Classical collisions in axially symmetric magnetic fields result in a small radial drift toward the axis. The displacement of the guiding center of a charged particle in a nonuniform plasma was estimated, e.g., in [8]. Under our experimental conditions, this displacement is as small as $\Delta R \approx 2$ cm and, therefore, slightly influences the width of the fast-ion density profile. Anomalous scattering of fast ions cannot lead to the observed effect because it would result in a diffusive broadening of the density profile. The formation of a narrow fast-ion density profile cannot also be explained by transverse losses.

A discrepancy between the widths of the trapped-ion density profile and the profile of the magnetic field perturbation allows us to suggest that there is anomalous radial transport of fast ions toward the axis. In [9], a two-dimensional collisionless problem was considered and it was shown that the most compact distribution of the guiding centers possesses the minimal sum of the magnetic field energy and the energy of the fast ions whose magnetic moment μ is conserved. Therefore, an axisymmetric distribution of the guiding centers with a monotonically decreasing density profile is stable, and, vice versa, the presence of a dip at the center results in the onset of instability driven by nonuniform gradient drift. In the latter case, the extra energy is transferred to the motion of the cold plasma and a more compact distribution of fast ions is established. According to the Liouville theorem, two-dimensional collisionless motion of the guiding centers (provided that μ is conserved) is incompressible because the transverse coordinates of a guiding center constitute a canonically conjugate pair of variables.

It is because of the above incompressibility that the theory developed in [9] cannot be directly applied to the interpretation of the experimental results under discus-

sion, because the distribution of the injected guiding centers does not have a distinct dip.

The limitations imposed by the Liouville theorem can be removed when considering a three-dimensional problem. The corresponding three-dimensional theory is currently under development. Here, we only present some estimates.

In a three-dimensional case, transverse compression is possible due to the broadening of the distribution function over longitudinal velocities if there is a mechanism for energy exchange between the longitudinal and transverse components. Such a mechanism appears in a finite-β plasma when the azimuthal fast-ion rotation velocity $\omega_{azim} \sim v_i \beta \rho / a^2$ (where ρ is the Larmor radius) becomes comparable to the ion bounce frequency $\omega_b \sim v_i / L$. In this case, the presence of perturbations that break the axial symmetry can lead to the overlapping of the resonances and to the efficient transport of fast ions. Using the Chirikov criterion [15], we can derive the resonance overlapping condition $\sqrt{\beta\tilde{\beta}} > a^2/(L\rho)$, where $\tilde{\beta}$ is the characteristic amplitude of the resonant perturbations of β. For fast ions with a Larmor radius of $\rho \sim a$, this condition is satisfied for rather small perturbation amplitudes. The overlapping of the resonances results in the efficient transverse transport of fast ions within the finite-β plasma region. In this case, the radial displacement of the guiding centers is accompanied by a redistribution between the longitudinal and transverse ion energies. (Note that the corresponding broadening of the region where the fast-ion density is peaked should be comparable to the broadening caused by the difference between the longitudinal magnetic field profiles at different radii in a finite-β plasma. For this reason, rather fine measurements are required to prove this effect experimentally.)

Thus, while transferring their energy to the cold plasma motion, fast ions can acquire a minimum-energy distribution corresponding to a narrower spatial profile, without reducing their volume in phase space.

6. CONCLUSIONS

The radial profile of the DD fusion products has been measured near the turning points of fast ions in the GDT device. The FWHM of the profile is found to be $a_{DD} = 12$ cm. The radial fast-ion density profile near the turning points with a mirror ratio of $R = 2$ has been measured using a charge-exchange neutral analyzer with an active target. For ions with an energy close to the injection energy ($E = 20$ keV), the profile width is found to be $a_{CX} = 30$ cm, whereas for ions with an energy of $E = 13$–16 keV, it is nearly half as large ($a_{CX} = 16$–18 cm). Experiments with a movable limiter have shown that the loss of fast ions from the plasma periphery is insignificant. This is also confirmed by an analysis of the fast-ion energy balance. Possible mechanisms for the formation of a narrow fast-ion density profile have been discussed.

ACKNOWLEDGMENTS

We are grateful to V.N. Borodkin for his assistance in experiments. This work was supported in part by the US Civilian Research and Development Foundation for the Independent States of the Former Soviet Union, project no. RP1-2553-NO-03.

APPENDIX

BRIEF DESCRIPTION OF THE MCFIT CODE

The MCFIT code used to calculate the fast-ion distribution is described in detail in [7]. Here, we only present a brief description of the code, following [4].

The MCFIT code is designed to simulate the relaxation and transport of high-energy ions produced during NBI for given parameters of the magnetic field and target plasma. The code uses the Monte Carlo method and is intended for solving the following problems:

(i) Three-dimensional simulations of the behavior of fast ions with allowance for Coulomb collisions and charge exchange, taking into account the energy and time dependences for these effects.

(ii) Acquisition of a detailed information on the GDT.

The code is based on the conventional Monte Carlo scheme; i.e., it simulates statistically independent histories of fast ions. The result is obtained by summing the contributions from different ions to the parameter of interest. For N simulated particle histories, the final result for each of the parameters is calculated as the average of the values obtained in each history, and the statistical error of the final result is calculated from the root-mean-square deviation of an individual parameter from its average. The main drawback of this method is that the statistical error decreases very slowly (as $N^{-1/2}$) with increasing N. The code simulates the following processes:

(i) the generation of neutrals at the surfaces of the ion-optical systems of neutral injectors and their flight to the plasma;

(ii) the ionization of the beam neutrals in the plasma by charge exchange, by electron impact, and by their stripping in the interaction with ions;

(iii) ion motion in a given magnetic field;

(iv) the interaction of ions with a target plasma (deceleration and angular scattering); and

(v) the charge-exchange interaction of ions with a neutral gas and the production of fast neutrals.

As input data, along with the parameters of the magnetic field and target plasma, the MCFIT code uses the spatial distribution of the neutral gas in the region occupied by fast ions. The time evolution of the spatial dis-

tribution of neutrals during an experiment is calculated using the NEUSI code [16].

The MCFIT code allows simulations in a wide range of physical parameters. The results of simulations are discrete parameter distributions on a phase space mesh at given time instants. The main calculated parameters are the energy of the fast-ion component, the trapped neutral beam power, the charge-exchange loss power, the power of the target plasma heating, and the fast-ion distribution over energies and pitch angles. Knowing the distribution function of fast ions, it is easy to compute their spatial density distribution and also the spatial profiles of the charge-exchange neutral fluxes with different energies.

It is worth noting that the MCFIT code allows one to simulate the behavior of fast ions taking into account variations in the magnetic field under the action of the fast-ion pressure. For this purpose, a self-consistent problem is solved with allowance for the diamagnetic effect of hot ions. Note also that the MCFIT code has been developed over more than ten years in parallel with the development of the GDT experiments. The code was tested by thoroughly comparing the results of numerical simulations to the experimental data (see, e.g., [4]).

REFERENCES

1. V. V. Mirnov and D. D. Ryutov, Vopr. At. Nauki Tekh., Ser. Termoyadernyĭ Sintez, No. 1, 57 (1980).
2. E. P. Kruglyakov, A. A. Ivanov, and Yu. A. Tsidulko, Trans. Fusion Sci. Technol. **43**, 315 (2003).
3. V. I. Davydenko, G. V. Roslyakov, and V. Ya. Savkin, Vopr. At. Nauki Tekh., Ser. Termoyadernyĭ Sintez, No. 2, 67 (1983).
4. A. V. Anikeev, P. A. Bagryansky, A. A. Ivanov, *et al.*, Nucl. Fusion **40**, 753 (2000).
5. P. A. Bagryansky, A. A. Ivanov, E. P. Kruglyakov, *et al.*, Fusion Eng. Des. **70**, 13 (2004).
6. A. A. Ivanov, A. V. Anikeev, P. A. Bagryansky, *et al.*, Phys. Rev. Lett. **90**, 105002 (2003).
7. K. Noack, G. Otto, and S. Collatz, Trans. Fusion Technol. **35**, 218 (1999).
8. D. D. Ryutov, Preprint No. 85-32 (Inst. of Nuclear Physics, Siberian Division, USSR Acad. Sci., Novosibirsk, 1985).
9. Yu. A. Tsidulko, Phys. Plasmas **11**, 4420 (2004).
10. V. N. Kornilov and V. V. Maximov, Prib. Tekh. Éksp., No. 2, 96 (2001).
11. V. V. Maximov, A. V. Anikeev, P. A. Bagryansky, *et al.*, Nucl. Fusion **44**, 542 (2004).
12. Yu. N. Dnestrovskii and D. P. Kostomarov, *Numerical Simulation of Plasmas* (Mir, Moscow, 1982; Springer-Verlag, New York, 1986).
13. S. A. Korepanov, P. A. Bagryansky, P. P. Deichuli, *et al.*, Trans. Fusion Technol. **35**, 345 (1999).
14. A. V. Anikeev, P. A. Bagryansky, A. A. Ivanov, *et al.*, Nucl. Fusion **40**, 753 (2000).
15. B. V. Chirikov, At. Énerg. **6**, 630 (1959).
16. S. Collatz and K. Noack, Trans. Fusion Technol. **35**, 375 (1999).

Translated by N.F. Larionova

Plasma Physics Reports, Vol. 31, No. 11, 2005, pp. 908–918. Translated from Fizika Plazmy, Vol. 31, No. 11, 2005, pp. 978–988.

PLASMA DYNAMICS

Measurements of the Azimuthal Magnetic Field within Imploding Multiwire Arrays in the Angara-5-1 Facility

G. G. Zukakishvili[1], K. N. Mitrofanov[1], V. V. Aleksandrov[1], E. V. Grabovskiĭ[1], G. M. Oleĭnik[1], I. Yu. Porofeev[1], P. V. Sasorov[2], and I. N. Frolov[1]

[1] *Troitsk Institute for Innovation and Fusion Research, Troitsk, Moscow oblast, 142190 Russia*

[2] *Institute of Theoretical and Experimental Physics, Bol'shaya Cheremushkinskaya ul. 25, Moscow, 117218 Russia*

Received January 12, 2005; in final form, April 5, 2005

Abstract—Results are presented from measurements of the azimuthal magnetic fields within imploding multiwire tungsten arrays in the Angara-5-1 facility at currents of 2.5–4 MA. It is shown that the penetration of the magnetic field into the axial region of the wire array lags behind the discharge current pulse. The current of a precursor produced at the array axis prior to the implosion of the bulk array mass is measured. It is found that the magnetic field in the initial stage of implosion is azimuthally nonuniform. The mass distribution inside the array is calculated from the measured magnetic field. © *2005 Pleiades Publishing, Inc.*

1. INTRODUCTION

Z-pinches produced from cylindrical wire arrays have been studied since the 1970s, when experimental facilities with a current pulse duration of a few hundred nanoseconds were created. Such Z-pinches (in contrast to hydrogen and deuterium pinches) were used to generate X-ray pulses. It was expected that, at the instant of maximum compression, a wire cylinder imploding under the action of the magnetic self-field would release the stored kinetic and magnetic energy in the form of an X-ray pulse. It was shown in the late 1980s [1–4] that the implosion of an array composed of several wires differs significantly from that predicted by the conventional snowplow model. Instead of the acceleration of the wire material as a whole, the plasma was continuously generated from the wires and flowed toward the array axis. Long before the implosion of the bulk array mass, a current precursor was observed at the axis. A relatively long X-ray pulse lasted over two to three tens of nanoseconds. An analysis of these results stimulated the use other kinds of cylindrical loads: annular gas puffs and foam liners. In the middle 1990s, it was shown, however, that the use of multiwire arrays consisting of a large number (from a few tens to a few hundred) of wires enables the generation of nanosecond X-ray pulses [5, 6]. This created renewed interest in studying wire arrays. It was shown in [7, 8] that the phenomena observed in the early studies also take place in experiments with multiwire tungsten arrays. A model describing these phenomena in the limit of an infinitely large number of wires was proposed in [9]. In experiments with currents of 3–4 MA, X-ray pulses with a duration of 6 ns were obtained. This points to a similarity between the processes occurring in the Angara and Z facilities [5, 6], although discharge currents in them are very different. The main factor governing the implosion of multiwire arrays is the process of prolonged plasma production.

By the term *prolonged plasma production*, we mean not merely the process of ionization but the formation of a highly conductive plasma that is capable of intercepting a major fraction of the discharge current and whose ohmic resistance is lower than the internal resistance of the generator and is comparable to (or even less than) the resistance related to variations in the array inductance. During prolonged plasma production, the current-carrying plasma flows continuously toward the array axis, thereby giving rise to a plasma shell whose thickness is much larger than the skin depth and that is entirely penetrated by the current and magnetic field. In the initial stage of implosion, the plasma shell can be discontinuous in the azimuthal direction. In this case, the plasma is accelerated towards the axis by the Ampère force $\mathbf{j} \times \mathbf{B}/c$, which is nearly uniform over the entire cross section of the plasma shell, rather than by a magnetic piston, which acts on the outer plasma boundary and gives rise to strong instabilities. Such plasma liners are less subject to the Rayleigh–Taylor instability as compared to thin plasma shells with a thickness on the order of the skin depth.

However, the elasticity of such a "thick" plasma shell penetrated by the current may significantly reduce the plasma compression ratio. Obviously, there is an optimal shell thickness that is large enough for instabilities to be suppressed but is still sufficiently small to ensure compact plasma compression.

To verify theoretical results and to acquire data on the implosion of wire arrays, we have developed a

1063-780X/05/3111-0908$26.00 © 2005 Pleiades Publishing, Inc.

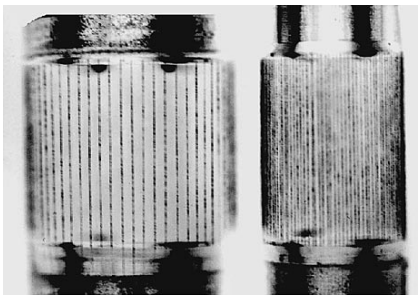

Fig. 1. General view of wire arrays with diameters of 20 and 8 mm.

method for measuring the magnetic field within a wire array with the help of microprobes. In [10], microprobes were used to measure the magnetic field at the front of a collisionless shock wave in plasma. In our case, the plasma energy density is much higher and the microprobes are destroyed in each shot. To enable reliable measurements of the magnetic field, a probe with a size of about 300 μm was composed of two oppositely wound loops: when the signals from these loops coincided (with allowance for their different polarities), the measurements were seen to be correct. An important advantage of this technique is that the experimental data on the magnetic field can be compared to the results of computer simulations, a rare occasion in studies on Z-pinches. We assume that the signal from such a microprobe is proportional to the time derivative of the magnetic field at the probe location. The magnetic field perturbations caused by the probe are relatively low when the probe size is less than the skin depth in the surrounding plasma. This question will be discussed in more detail in a separate paper.

The azimuthal magnetic field, which was produced by the axial current, was measured by the microprobes whose loops were parallel to the pinch axis.

In our experiments, we used wire arrays like those shown in Fig. 1. An array consisted of two cylindrical metal electrodes of the same diameter, placed coaxially at a height of 10–15 mm from one another. Identical wires were set equidistantly between these electrodes to form a kind of a squirrel wheel with a diameter of 20 mm. The experiments described below were performed with tungsten wire arrays.

The arrays consisted of 8–600 tungsten wires with diameters of 5–8 μm, the interwire distance being from 0.1 to 8 mm. The current generator was the Angara-5-1 facility—an eight-module pulsed current generator with an internal resistance of 0.25 Ω, each module being a double pulse-forming line with water insulation. The current pulse was delivered to the load via vacuum transmission lines with magnetic self-insulation [11]. The current amplitude in the load was 2.5–4.5 MA, and the current rise time was 100–120 ns.

2. MEASUREMENTS OF THE AZIMUTHAL MAGNETIC FIELD IN THE PLASMA OF A MULTIWIRE ARRAY

The arrangement of the microprobes measuring the azimuthal magnetic field is shown in Fig. 2a. The probes can be set both beyond the array (to measure the current flowing through it) and at different radii within the array. All the probes were inserted in the interelec-

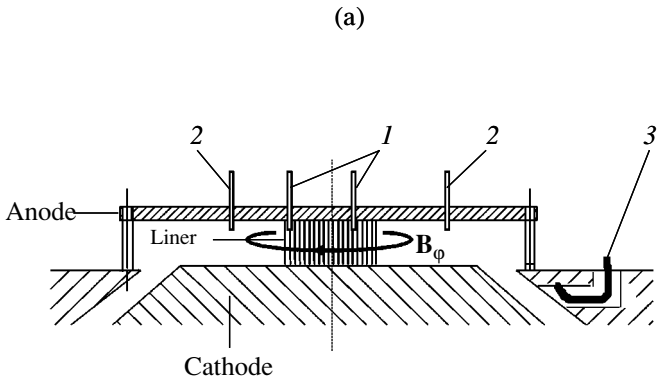

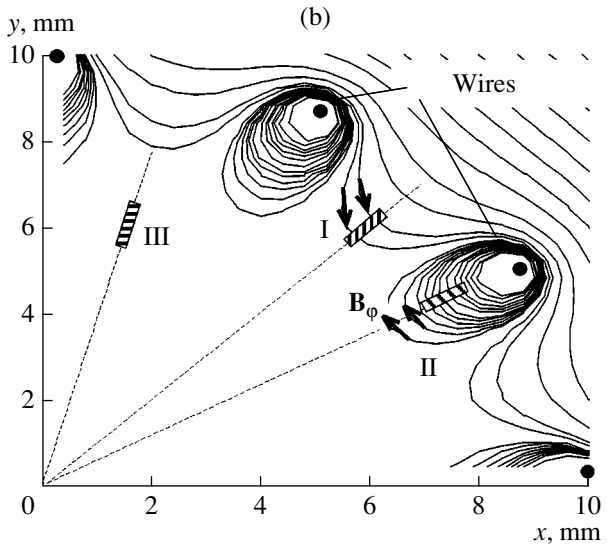

Fig. 2. (a) Arrangement of the magnetic probes in the Angara-5-1 facility: probes *1* for measuring the azimuthal field are set at radii of 5 and 8.5 mm, probes *2* are set at a radius of 30 mm, and eight-loop detector *3* of the total current flowing through the wire array is set at a radius of 55 mm (only one loop is shown). (b) Calculated configuration of the azimuthal magnetic field of the wire array at the time $t = 3$ ns from the beginning of the discharge (at this instant, almost the entire current flows in a narrow skin layer located near the initial array radius R_0). Roman numerals show the locations of the magnetic probes.

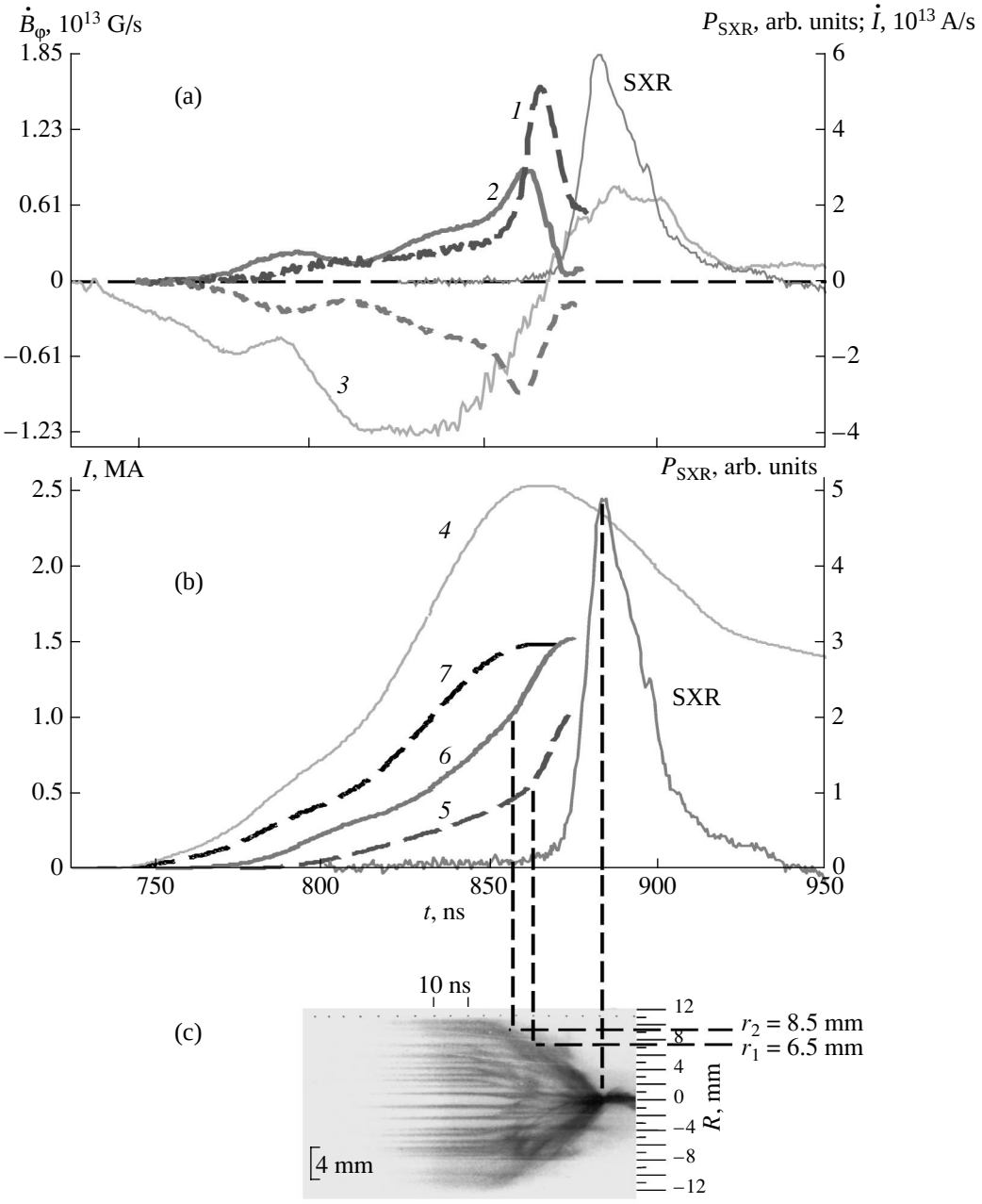

Fig. 3. Measurements of the azimuthal magnetic field within a multiwire array (shot no. 3974): (a) the time derivatives of the magnetic field measured by probes P_2 and P_1 set at radii of 6.5 mm (curve *1*) and 8.5 mm (curves *2*), respectively, and the time derivative of the current within the radius of 20 mm (curve *3*); (b) the currents within the radii of 30, 6.5, and 8.5 mm (curves *4*, *5*, and *6*, respectively) and the current within the radius of 30 mm reduced by a factor of $\sqrt{3}$ ($I = I_0/\sqrt{3}$) (curve *7*); and (c) an optical streak image (negative) synchronized with plots (a) and (b). In plots (a) and (b), the SXR signal is also shown.

trode gap to a depth of 2–3 mm. The measurements of the magnetic field beyond the array are in good agreement with the current measurements by the conventional Angara-5-1 technique, in which the total current was measured using eight loops placed at a radius of 55 mm in front of each module. The loop signals were averaged and integrated [12]. Below, we will describe measurements of the magnetic field within a wire array. The arrangement of the microprobes relative to the array wires is shown in Fig. 2b.

Figure 3 shows typical waveforms of (*4*) the current pulse through the array, the soft X-ray (SXR) intensity, and (*2*) the signals from the two loops of the same microprobe. The SXR intensity was calculated by the signals from the three to four vacuum X-ray diodes

placed behind different filters [13]. It can be seen that the signals obtained from the two oppositely wound loops (curves *2*) coincide with an accuracy of up to 5%.

Figure 3 shows signals measured in experiments with a 20-mm-diameter 15-mm-high wire array consisting of forty 20-mm-long 6-μm-diameter tungsten wires. The linear mass density of the array was 220 μg/cm. In Fig. 3c, an optical streak image obtained in a shot with an identical wire array is shown. Two magnetic probes P_1 and P_2 were set at points I and III (at radii of 8.5 and 6.5 mm, respectively) at an angle of 90° with respect to one another (see Fig. 2b). The currents whose waveforms are shown in Fig. 3 flowed within the radii at which probes P_2 and P_1 were located (curves *5*, *6*, respectively). The currents were calculated by the formula $I = r_p B_\varphi/0.2$ (where r_p [cm] is the radius of the probe location and B_φ [G] is the induction of the azimuthal component of magnetic field measured by the probe) under the assumption that the distribution of magnetic field was axisymmetric.

Figure 3 shows only a fraction of the waveforms within a time interval during which the signals from each of the two probe loops coincide with one another. The azimuthal magnetic flux penetrates into the wire array in the early stage of implosion. It can be seen that the currents calculated from the probe signals become appreciable only 30–40 ns after the beginning of the discharge. Until the onset of the SXR pulse, the currents steadily increase to a level of 0.6 (for probe P_1) and 0.4 (for probe P_2) of the current amplitude. The experiments showed that, ~100 ns after the beginning of the discharge (the implosion duration being 150 ns), the plasma residing within the radius of 5.0–6.5 mm carries from 3 to 15% of the total current. About 20 ns before the maximum of the SXR pulse, the signals from the loops of the same probe begin to differ from one another, which indicates that the probe is damaged. It can be seen from the optical streak image shown in Fig. 3c that the visible size of the array remains constant up to t = 860 ns and then begin to decrease. Between 875 and 895 ns, when the emission power is maximum, one can see the traces of the substance approaching the axis after the bulk of the glowing plasma has already been accumulated near the axis.

Figure 4 shows waveforms of the currents measured in two different shots by probes set at points I and II (Fig. 2b). The wire array consisted of forty 8-μm-diameter tungsten wires set equidistantly at a radius of 10 mm. The array height was 15 mm, and the linear mass density was 380 μg/cm. As in Fig. 3, the signals became unreliable when the SXR pulse appeared. Probe P_1 was set at a radius of 8.5 mm in front of a wire, and probe P_3 was set between two wires. The behavior of the signals is similar to that in Fig. 3; however, the polarity of the signal from probe P_3 during the first 35 ns is opposite to the polarity of the main signal. An enlarged fragment of this signal is shown in Fig. 4c (curve *8*).

The signal of opposite polarity is related to the initial topology of the magnetic field of the wire array (see Fig. 2b). The arrows show the direction of the magnetic field lines. It can be seen that the lines of the magnetic field produced by one wire cross the probe loop in the direction opposite to that of the lines of the total magnetic field produced by all the wires (see positions II and I).

An X-ray backlighting photograph of the wire plasma obtained using X-pinch radiation with a photon energy of >1 keV (see [14]) is shown in Fig. 4d. It can be seen that, by the time t = 75 ns from the beginning of the discharge, the wires have expanded approximately threefold and have formed quite a dense core absorbing X-pinch radiation.

Thus, during the first 35 ns, the distribution of the current at the periphery of the wire array is azimuthally nonuniform. At t = 75 ns, the plasma distribution at the periphery of the wire array is also azimuthally nonuniform.

3. DISCUSSION OF THE MEASUREMENT RESULTS OF THE AZIMUTHAL MAGNETIC FIELD

In the model proposed in [9], the wire array is regarded as an axisymmetric cylinder with a radius equal to the initial radius R_0 of the array. The cylinder generates plasma at the rate

$$\dot{m}(t) = 0.2\left(\frac{I(t)}{R_0}\right)^{1.8} \frac{\mu g}{cm^2\ ns}, \quad (1)$$

where $I(t)$ is the array current in MA and R_0 is in cm. According to [9], the plasma is accelerated in a thin boundary layer with a radius close to R_0. Under our conditions, the thickness of this layer is a few hundred microns. The plasma is accelerated here almost up to the local Alfvén velocity. The momentum acquired by the plasma accelerated toward the array axis is equal to the difference between the magnetic field pressures at the outer and inner surfaces of the boundary layer,

$$\frac{B_{ext}^2}{8\pi} - \frac{B_{int}^2}{8\pi} = (\rho V_A)V_A,$$

where B_{ext} and B_{int} are the fields outside and inside the array, respectively, just beyond the boundary layer. Assuming that the velocity at the inner boundary is equal to the local Alfvén velocity $V_A = B_{int}/\sqrt{4\pi\rho}$, we obtain

$$B_{int} = \frac{B_{ext}}{\sqrt{3}} \approx 0.58 B_{ext}. \quad (2)$$

When deriving this expression, we ignored variations in ρ and V_A during the acceleration; i.e., it was assumed that plasma acceleration in the layer was steady-state in character.

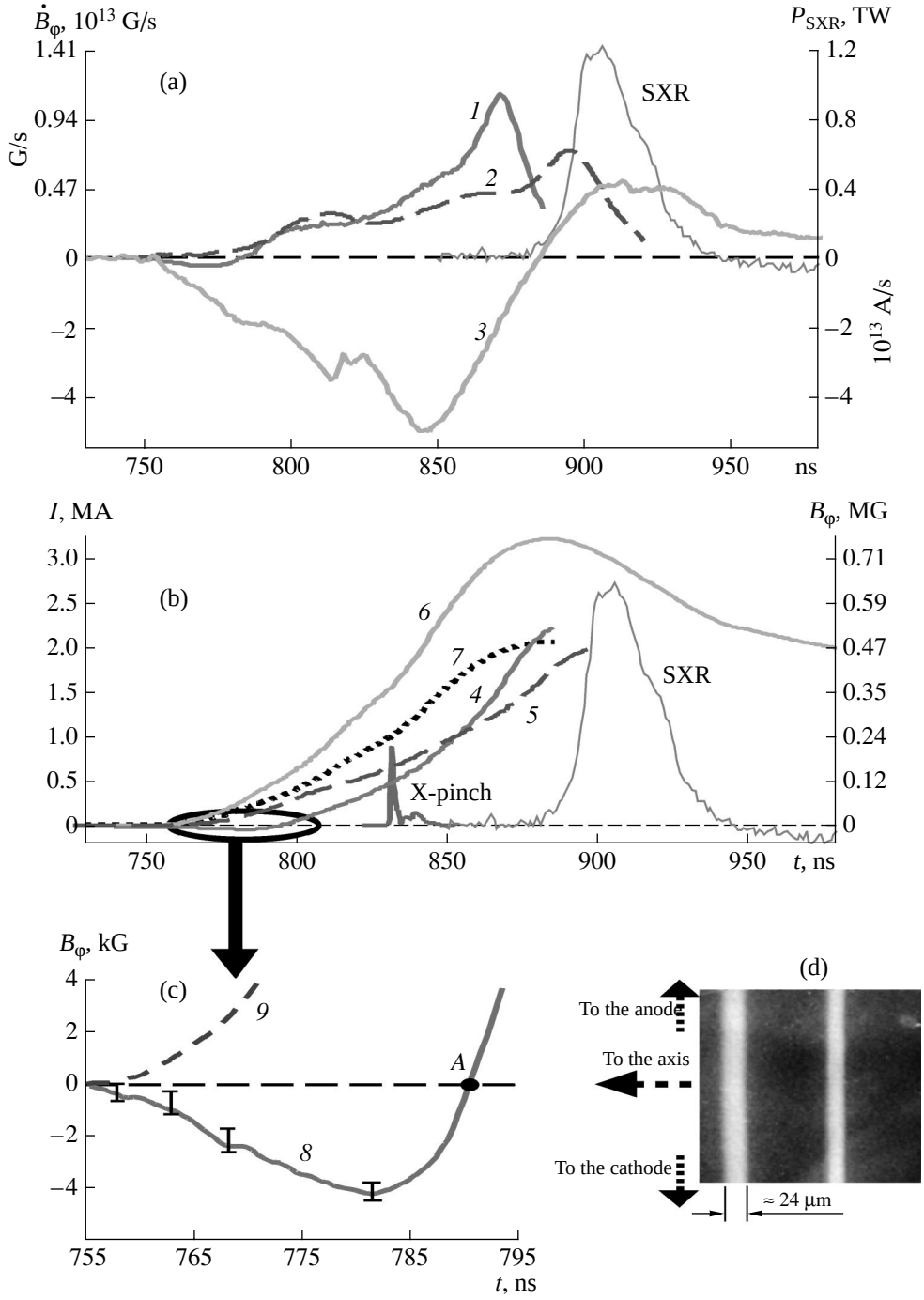

Fig. 4. Measurements of the azimuthal magnetic field near the wires of a multiwire array (shot nos. 3910, 3912): (a) the time derivatives of the magnetic field measured at a radius of 8.5 mm in front of a wire (curve *1*) and between the wires (curve *2*) and the time derivative of the current within the radius of 30 mm (curve *3*); (b) the currents within the radius of 8.5 mm measured in front of a wire (curve *4*) and between the wires (curve *5*), the current within the radius of 30 mm (curve *6*), and the same current reduced by a factor of $\sqrt{3}$ ($I = I_0/\sqrt{3}$) (curve *7*); (c) the magnetic field measured at a radius of 8.5 mm in front of a wire (curve *8*) and between the wires (curve *9*); and (d) a backlighting photograph of a wire array taken in X rays with photon energies of $h\nu > 1$ keV at $t =$ 75 ns (a fragment of the negative). On the right ordinate axis in plot (b), the azimuthal magnetic field at the probe location is plotted. In plots (a) and (b), the SXR signal is also shown.

The currents calculated by the signals from the probes set at the radius of 8.5 mm (see Figs. 3, 4; curves *7*) are in fair agreement with relationship (2). Note that this relationship remains valid even when the visible plasma radius in the optical streak image becomes less than 8.5 mm (see Fig. 3c). A possible reason is that a certain

amount of plasma that is invisible in the streak image stays beyond the 8.5-mm radius and carries ≈40% of the total current. It follows from expressions (1) and (2) that the jump in the magnetic field across the boundary layer depends only slightly on ρ. Hence, this low-density plasma, slightly emitting in the optical range, is able to carry up to ≈40% of the total current at the radius R_0 as long as the plasma is being produced (regardless of the plasma production rate).

Let us estimate the minimum plasma density that is required for the plasma to be capable of carrying an appreciable fraction of the current within the plasma production zone. The plasma velocity cannot be higher than

$$V_A < c\frac{E}{B_{\text{int}}} \Rightarrow \rho > \frac{B_{\text{int}}^4}{4\pi c^2 E^2}, \qquad E = \frac{U}{h}, \tag{3}$$

where U is the voltage across the array and h is the array height. In our experiments, $U \approx$ 300–400 kV, h = 15 mm, and $B_{\text{int}} \approx 0.5$ MG. Therefore, we find that the plasma with a mass density of $\rho > 10$ μg/cm^3 is capable of carrying an appreciable fraction of the discharge current within the plasma production zone.

Figure 5 illustrates the results of 1D simulations of the magnetic field evolution within the array (see [9] for details) for the experimental conditions corresponding to Fig. 3. The time behavior of the plasma production rate $\dot{m}(t)$ was deduced by comparing the calculated curves to the time evolution of the azimuthal magnetic field measured at different radii (r_p = 6.5 and 8.5 mm) within the wire array. The time dependence $\dot{m}(t)$ was then used to calculate the time evolution of the radial profiles of the current $I(<r_p, t)$ flowing within the radius r_p of the probe location, the plasma mass density $\rho(r, t)$, and the radial plasma velocity $v_r(r, t)$ during the implosion of the wire array.

The calculated dependences $I(<r_p, t)$, $\rho(r, t)$, and $v_r(r, t)$ show that, in the early stage of implosion, a certain fraction of the plasma penetrates into the array with a velocity of $(1.5–2.5) \times 10^7$ cm/s and reaches the array axis long before the beginning of the SXR pulse. This leads to the formation of an emitting precursor at the array axis. The linear mass of the precursor (the plasma mass within the radius $0.1R_0$, see Fig. 5c) was calculated as

$$m_{fr}(t) = 2\pi\left(R_0\int_0^t \dot{m}(\tau)d\tau - \int_{0.1R_0}^{R_0} \rho(r, t)r dr\right) \text{ μg/cm}.$$

The estimated precursor mass at the time t = 110 ns from the beginning of the discharge (30 ns before the SXR maximum) is 1–2% of the initial array mass (220 μg/cm). At this time, the outer visible boundary of the plasma is still at rest and the estimated current flowing within the radius $0.1R_0$ is about 300–400 kA. Since the visible diameter of the precursor is 1–2 mm, the current and mass of the precursor should be less than or on the order of the above estimates, which are close to the corresponding estimates made in [1–4]. It can be seen from Fig. 5b that, up to the onset of the SXR pulse, nearly one-half of the total current flows outside the region with a radius equal to one-half of the initial array radius ($0.5R_0 < r < R_0$). The reason for this is that the current-carrying plasma still continuous to move at this instant.

Note that the signals from the probes set between the wires and in front of the wires (see Fig. 4) are similar to one another (except for the first 35 ns). Therefore, the azimuthal modulation of the magnetic field is small over almost the entire implosion process (at least within the radius of the probe location). Nothing definite can be said, however, about the azimuthal modulation of the plasma pressure. Although the pressure must be equalized along the magnetic field lines, the propagation time of the sound waves across the interwire gap can be long enough for the pressure between the wires to differ significantly from that in front of the wires.

Measurements of the azimuthal field show that the plasma continues to be accelerated after the visible plasma radius has already decreased (see Fig. 3c). Therefore, a question arises of what the visible boundary in the optical streak image is.

Figure 6 shows the distribution of the plasma mass density in the (r, t) plane calculated by the 1D model. It can be seen that the time evolution of the visible plasma radius in Fig. 3c is in good agreement with the calculated time evolution of the radius corresponding to the plasma density maximum. In these calculations, we used the radial profiles of the plasma mass density shown in Fig. 5c.

We believe that the position of the outer visible boundary of the plasma in the optical streak image corresponds to the maximum of the plasma density associated with the maximum of the plasma production rate.

In [9], the plasma production rate $\dot{m}(t)$ calculated by formula (1) increased approximately as the current squared. It was assumed in [9] that $\dot{m}(t)$ vanished after the wires were entirely evaporated. The evaporation time T is determined by the expression

$$2\pi R_0\int_0^T \dot{m}(t)dt = M_0,$$

where M_0 is the initial linear mass of the wire array. However, the jump in the magnetic field between the inner and outer boundaries of the wire array in the stage when the visible plasma radius decreases indicates that $\dot{m}(t) \neq 0$. A reduction in $\dot{m}(t)$ at times later than or close to T, which is somehow related to a decrease in the mass of the wire cores, leads to a decrease in the

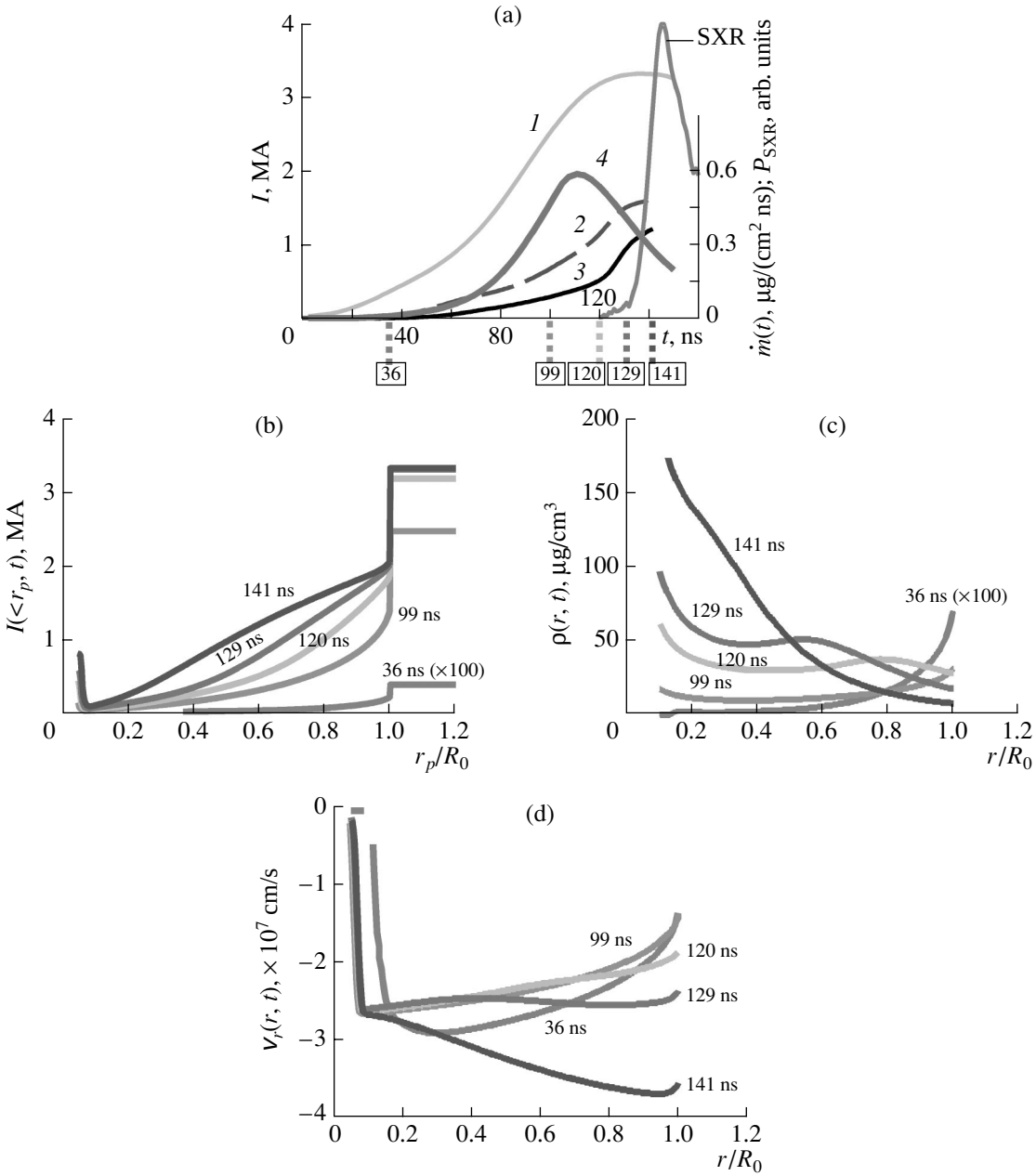

Fig. 5. (a) Waveforms of the current within the radius of 55 mm (curve *1*), the currents within the radii r_p = 8.5 and 6.5 mm calculated by the 1D model (curves *2* and *3*, respectively), the plasma production rate $\dot{m}(t)$ calculated by the 1D model (curve *4*), and the measured SXR signal; (b) calculated radial distributions of the current $I(<r_p, t)$ within the radius r_p at different times, (c) calculated radial distributions of the plasma mass density at different times; and (d) calculated radial distributions of the radial component of the plasma velocity at different times.

density of the plasma layers moving toward the axis and, consequently, in their brightness.

A decrease in $\dot{m}(t)$ at times close to T was studied in [15] using a 1D model. The behavior of $\dot{m}(t)$ when it tends to zero determines the plasma distribution beyond the Z-pinch produced at the array axis and can thus affect the stability and compactness of the compressed plasma.

Let us consider the initial portion of the signal from the probe set in front of a wire (Fig. 4c, curve *8*). Over the first ≈20 ns from the beginning of the discharge, this signal is proportional to the signal measured by the probe set at a radius of 8.5 mm between the wires. This result is quite natural if we assume that the wires are infinitely thin filaments carrying the same currents. The structure of the magnetic field produced by such a system of filamentary currents is shown in Fig. 2b. Starting

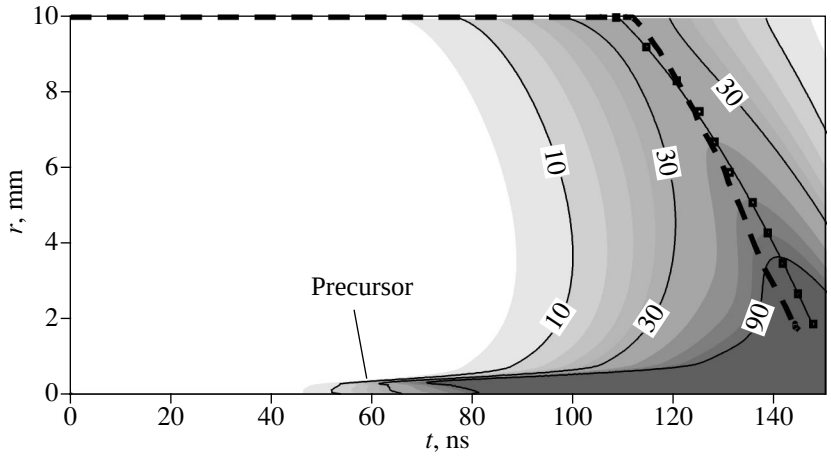

Fig. 6. Distribution of the plasma mass density in the (r, t) plane calculated by the 1D model. The line marked by squares shows the calculated time evolution of the radius corresponding to the maximum plasma density, and the dashed line shows the measured time evolution of the visible radius of the wire array plasma obtained from the optical streak image (see Fig. 3c). The relief of the plasma mass density is shown by shades of gray; the numerals by the contour lines show the values of the plasma mass density in units of $\mu g/cm^3$.

from the time ≈20 ns from the beginning of the discharge, the signals from a probe set in front of a wire and that set between the wires begin to differ from one another: the polarity of the former changes at t = 35 ns (Fig. 4c, point *A* on curve *8*). This points to a change in the magnetic field distribution within the region lying between the radius R_0 and the radius of the probe location (see Fig. 7). The structure of the magnetic field produced by the current-carrying plasma jets emerging from each wire was calculated in [3]. Although our measurements are insufficiently accurate to determine the parameters of these jets, it is obvious that, starting from 20–30 ns, the current flows through the jets moving from each wire toward the array axis. In this case, the magnetic separatrix (the line that separates the field lines enclosing the array axis within the array from those enclosing individual jets emerging from each wire) shifts toward the array axis. Figure 7 show the structure of the magnetic field at times of 21 and 36 ns after the beginning of the discharge. These structures were calculated with allowance for the calculated radial current distributions (along each jet) obtained in 1D simulations (similar distributions are shown in Fig. 5b). The change in the magnetic field structure from that shown in Fig. 2b to that shown in Fig. 7b leads to the change in the polarity of the probe signal in Fig. 4c.

These measurements provide an estimate of the velocity with which the separatrix (or the current-carrying part of the jet) is displaced toward the array axis. According to [16], where the parameters of the wire arrays were close to those in our experiments, the plasma jet begins to emerge from a wire when a plasma corona forms around it. Assuming that the time during the corona forms is about 10 ns and the distance from the probe to the nearest wire is $\Delta r \approx 1.5 \pm 0.5$ 0.5 mm and taking into account that the probe signal changes its polarity at ≈35 ns (Fig. 4c, point *A* on curve *8*), we obtain the velocity with which the separatrix is displaced toward the axis: $V_{\text{displ}} \approx (0.4\text{–}0.6) \times 10^7$ cm/s.

It follows from the above considerations that the time evolution of the magnetic field within a wire array is, to a great extent, determined by the time behavior of the plasma production rate $\dot{m}(t)$. Therefore, the measurements of the magnetic field inside a wire array provide important data on the physics of the entire implosion process. These data can be used to optimize the parameters of wire arrays and to increase the SXR yield.

4. MEASUREMENTS OF THE AZIMUTHAL MAGNETIC FIELD BEYOND THE MULTIWIRE ARRAY PLASMA

In large controlled fusion devices (such as the Angara-5-1 and Z facilities), the energy of separate modules is supplied to the load using 3D vacuum concentrators based on magnetically insulated transmission lines (MITLs). Nonsynchronous operation of the modules, nonuniformities of the transmission lines, and terawatt X-ray emission generated in the course of implosion can reduce the efficiency of energy transportation to the load because of an increase in the pulse duration and a break in magnetic self-insulation.

To determine the position and instant of break in magnetic self-insulation, we measured the magnetic field (current) beyond the plasma at different points of the MILTs using magnetic probes set at a distance of 30 mm from the array axis and loops placed at a radius of 55 mm.

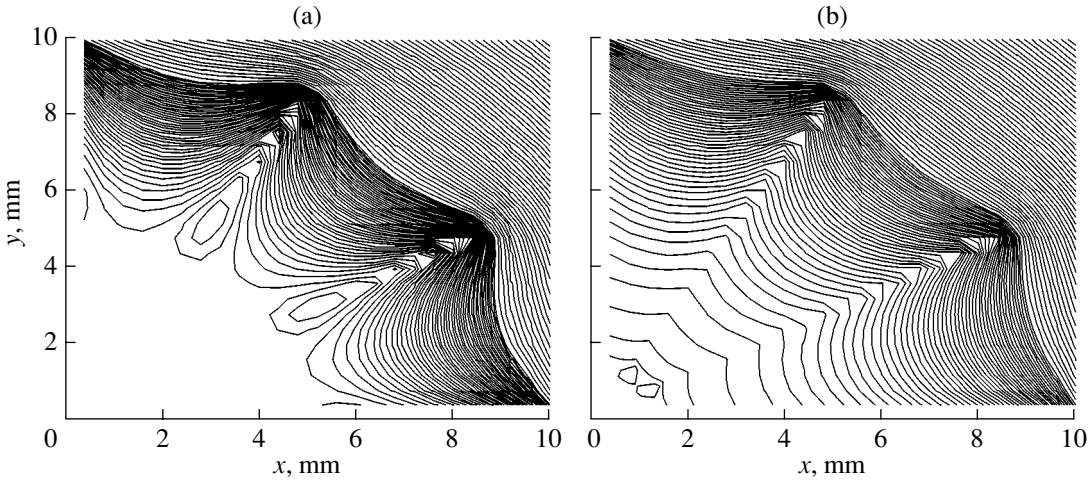

Fig. 7. Calculated configurations of the azimuthal magnetic field in a 20-mm-diameter wire array consisting of twelve wires at times of (a) 21 ns after the beginning of the discharge, when the current flows within the region between the radii $0.5R_0$ and R_0, and (b) 36 ns after the beginning of the discharge, when the current flows within the region between the radii $0.15R_0$ and R_0. The magnetic field lines are calculated under the assumption that the wires are infinitely thin current-carrying filaments. The radial current distributions are calculated by the 1D model (see, e.g., Fig. 5b).

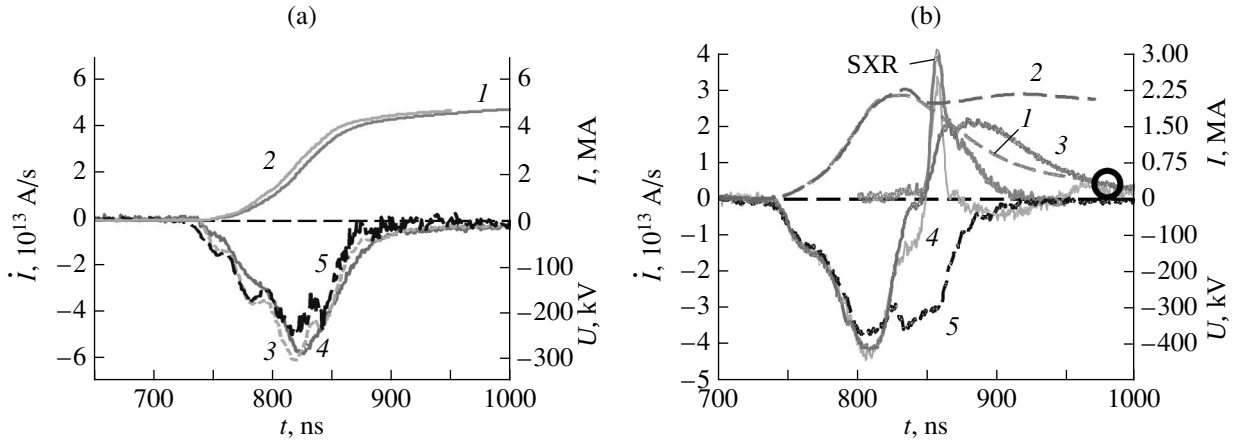

Fig. 8. Waveforms of the currents within the radii of 30 and 55 mm (curves *1* and *2*, respectively), the time derivatives of the currents within the radii of 30 and 55 mm (curves *3* and *4*, respectively), and the voltage at the separatrix (curve *5*) in the cases of (a) a massive 20-mm diameter cylindrical copper load and (b) a load in the form of a nested wire array. In plot (b), the SXR signal (in arbitrary units) is also shown.

The geometry of the experiment is shown in Fig. 2a. Signals from a magnetic probe set at a radius of 30 mm were compared to signals from a standard set of current loops installed in MILTs at a radius of 55 mm. Such a comparison provided data on the physical processes within the region between the probe and the loops.

Figure 8a shows the waveforms of the current and current time derivatives at radii of 30 and 55 mm and the concentrator voltage. In this case, a massive 20-mm-diameter copper cylinder was used as a load. It can be seen that the waveforms of the current time derivatives at radii of 30 and 55 mm and the concentrator voltage agree well with one another, as it should be in the case of a motionless load. No leakage current is observed (or it is too low). Figure 8b shows waveforms of the current and voltage measured with a load in the form of a nested wire array. The outer array consisted of forty 5-μm-diameter tungsten wires positioned at a radius of 6 mm, the total linear mass being 160 μg/cm. The inner array consisted of forty 8-μm-diameter tungsten wires placed at a radius of 3 mm, the total linear mass being 380 μg/cm. The waveforms of the current time derivatives (as well as of the currents themselves) at radii of 30 and 55 mm coincided with one another up to the instant of the SXR maximum (100–110 ns from the beginning of the discharge). After the SXR maxi-

mum, the current time derivatives at radii of 30 and 55 mm began to differ from one another. This indicates the onset of the leakage current in the region between these radii. The factors provoking leakage currents in the MITLs are high-power SXR emission and an increase in the interelectrode voltage due to an increase in the load impedance.

The presence of leakage currents points to the splitting of the magnetic flux: one part of the magnetic flux is concentrated between the generator and the leakage currents (circuit I), whereas the other part, between the leakage currents and the load axis (circuit II).

The electromagnetic energy stored in circuit II is converted into the internal energy of the Z-pinch plasma and SXR emission (the current somewhat decreases during the SXR pulse; see Fig. 8b, curve *1*).

The induction of circuit I is determined by the MILT design and is equal to $L_I \approx 8$ nH. The ohmic resistance of this circuit, R_I, is mainly determined by the resistance of the plasma in the interelectrode gap, where magnetic flux is split off. According to the Spitzer theory, this resistance is on the order of 1–10 mΩ. The time constant of the current decay in circuit I is $\tau_I = L_I/R_I \approx 1$–5 μs, which agrees with the characteristic duration of the current pulse (a plateau after the SXR maximum; see Fig. 8b, curve *2*) measured by the loops placed at a radius of 55 mm.

Then, 125–150 ns after the SXR maximum, the current time derivatives at radii of 30 and 55 mm again begin to coincide with one another (in Fig. 8b, this time is marked by a circle). This indicates that active dissipation of electromagnetic energy by the plasma load in circuit I has already terminated by this time.

Thus, measurements of the azimuthal magnetic field near a wire array have allowed us to monitor leakage currents arising in the MILTs and the total discharge current flowing through the load. Studying the effect of the inductance of the 3D concentrator on the emergence of leakage currents is beyond the scope of this study; this problem will be considered in a separate paper.

5. CONCLUSIONS

The measurements of the azimuthal magnetic field made it possible to compare the experimental data to the results of 1D simulations [9], to calculate the time evolution of the plasma production rate *dm*/*dt*, and thereby to determine the radial profiles of the azimuthal magnetic field and the plasma density during the implosion of a wire array. The results obtained can be formulated as follows:

(i) The measurements of the azimuthal magnetic field confirm the validity of the model of prolonged plasma production.

(ii) The azimuthal magnetic field is frozen in the plasma produced during the implosion of a wire array.

(iii) The magnetic field is discontinuous at the initial boundary of the wire array (a boundary layer).

(iv) The azimuthal magnetic flux penetrates into the array in the early stage of implosion. Starting from $t \approx$ 20–30 ns, the current flows through the plasma jets emerging from each wire and flowing toward the array axis.

(v) Thirty nanoseconds before the SXR maximum, the current within a region of radius 5 mm (for an array radius of 10 mm) amounts to 100–400 kA (from 3 to 15% of the total discharge current). The velocity of the plasma carrying this current is $(1.5–2.5) \times 10^7$ cm/s. The upper estimate of the mass of this plasma is 1–2% of the total array mass, which agrees with the results of X-ray measurements of the plasma mass in the axial region of the array [17].

(vi) During the first 35–40 ns after the beginning of the discharge, the current distribution at the periphery of the wire array is azimuthally nonuniform.

(vii) Seventy-five nanoseconds after the beginning of the discharge, the distribution of matter at the array periphery is found to be azimuthally nonuniform.

(viii) Until the onset of the X-ray pulse, about one-half of the total current flows outside the region with a radius equal to one-half of the initial array radius ($0.5R_0 < r < R_0$). Up to this instant, the current-carrying plasma still continues to move toward the array axis.

ACKNOWLEDGMENTS

This study was supported in part by the Russian Foundation for Basic Research, project no. 01-02-17319.

REFERENCES

1. I. K. Aĭvazov, V. D. Vikharev, G. S. Volkov, *et al.*, Fiz. Plazmy **14**, 197 (1988) [Sov. J. Plasma Phys. **14**, 110 (1988)].
2. M. B. Bekhtev, V. D. Vikharev, S. V. Zakharov, *et al.*, Zh. Éksp. Teor. Fiz. **95**, 1653 (1989) [Sov. Phys. JETP **68**, 955 (1989)].
3. I. K. Aĭvazov, M. B. Bekhtev, V. V. Bulan, *et al.*, Fiz. Plazmy **16**, 645 (1990) [Sov. J. Plasma Phys. **16**, 373 (1990)].
4. N. A. Bobrova, T. L. Razinkova, and P. V. Sasorov, Fiz. Plazmy **14**, 1053 (1988) [Sov. J. Plasma Phys. **14**, 617 (1988)].
5. T. W. L. Sanford, G. O. Allshouse, B. M. Marder, *et al.*, Phys. Rev. Lett. **77**, 5063 (1996).
6. R. B. Spielman, C. Deeney, G. A. Chandler, *et al.*, Phys. Plasmas **5**, 2105 (1998).
7. A. V. Branitskii, E. V. Grabovskii, M. V. Frolov, *et al.*, in *Proceedings of the 12th International Conference on High-Power Particle Beams, Haifa, 1998*, p. 599.
8. S. V. Lebedev, F. N. Beg, S. N. Bland, *et al.*, Phys. Plasmas **8**, 3734 (2001).

9. V. V. Aleksandrov, A. V. Branitskiĭ, G. S. Volkov, *et al.*, Fiz. Plazmy **27**, 99 (2001) [Plasma Phys. Rep. **27**, 89 (2001)].
10. A. N. Babenko, É. P. Kruglyakov, R. Kh. Kurtmulaev, *et al.*, in *Plasma Diagnostics*, Ed. by S. Yu. Luk'yanov (Atomizdat, Moscow, 1973), Vol. 3, p. 509 [in Russian].
11. Z. A. Al'bikov, E. P. Velikhov, A. I. Veretennikov, *et al.*, At. Energ. **68**, 26 (1990).
12. G. S. Volkov, E. V. Grabovskiĭ, V. I. Zaĭtsev, *et al.*, Prib. Tekh. Eksp., No. 2, 74 (2004).
13. A. V. Branitskiĭ and G. M. Oleĭnik, Prib. Tekh. Eksp., No. 4, 58 (2000).
14. V. V. Alexandrov, E. V. Grabovsky, K. N. Mitrofanov, *et al.*, in *Proceedings of the International Conference on Advanced Diagnostics for Magnetic and Inertial Fusion, Varenna, 2001*, Ed. by P. E. Stott *et al.* (Kluwer Academic, New York, 2002), p. 419.
15. V. V. Alexandrov, I. N. Frolov, E. V. Grabovsky, *et al.*, IEEE Trans. Plasma Sci. **30**, 559 (2002).
16. V. V. Aleksandrov, A. G. Alekseev, V. N. Amosov, *et al.*, Fiz. Plazmy **29**, 1114 (2003) [Plasma Phys. Rep. **29**, 1034 (2003)].
17. G. S. Volkov, E. V. Grabovskiĭ, K. N. Mitrofanov, and G. M. Oleĭnik, Fiz. Plazmy **30**, 115 (2004) [Plasma Phys. Rep. **30**, 99 (2004)].

Translated by N.N. Ustinovskiĭ

Plasma Physics Reports, Vol. 31, No. 11, 2005, pp. 919–926. Translated from Fizika Plazmy, Vol. 31, No. 11, 2005, pp. 989–996.

PLASMA DYNAMICS

Nanosecond Electric Explosion of a Tungsten Wire in Different Media

A. E. Ter-Oganesyan[1], S. I. Tkachenko[2], V. M. Romanova[1], A. R. Mingaleev[1], T. A. Shelkovenko[1], and S. A. Pikuz[1]

[1] *Lebedev Physical Institute, Russian Academy of Sciences, Leninskiĭ pr. 53, Moscow, 119991 Russia*

[2] *Institute for High Energy Densities, Associated Institute for High Temperatures, Russian Academy of Sciences, Izhorskaya ul. 13/19, Moscow, 127412 Russia*

Received November 18, 2004

Abstract—The effect of surrounding media of different densities and electric strengths on the heating dynamics of a micron wire during its nanosecond electric explosion is investigated. Tungsten wires with diameters of $d = 25$–50 μm were exploded in air and water at a current rise time of $(dI/dt) \sim 10^{10}$ A/s. The diagnostic complex is described. © *2005 Pleiades Publishing, Inc.*

1. INTRODUCTION

Although nanosecond electric explosions of wires are fairly widely studied in the physics of high-temperature plasma, the initial stage of this process is still very poorly understood. Experiments on laser and X-ray probing of exploding wires that were performed in such facilities as Angara-5 [1], Z [2], MAGPIE [3], and XP [4] provide information on the late stage of the explosion, when ohmic heating of the wire has already come to an end. This is why it is rather difficult to develop an adequate theoretical model of the initial (prebreakdown) stage of electric explosion. In particular, there are no experimental data that can be used to develop a physical concept of the intense heating of a condensed matter (the effect of the electron–ion system being in a nonequilibrium state, the influence of nonequilibrium processes related to the development of defects in the melting zone, etc.), as well as of an abrupt change in the wire resistance and density. For this reason, both the properties of the matter and the physical models are usually extrapolated. Multiphase states of matter in the initial stage of explosion also deserve thorough investigation.

The main factor determining the properties of a condensed matter is the energy deposited in it. It was shown in [4] that the energy deposited in a wire in the ohmic heating stage also determines the expansion velocity and uniformity of the plasma produced. Thus, to widen the range of the parameters and processes under study, it is necessary to avoid an early breakdown of the discharge gap at a high deposited energy. According to the nucleation mechanism for the loss of phase stability [5], the deposited energy can, in principle, be increased to a level corresponding to the sublimation energy. To do this, it is necessary to delay the process of plasma production by suppressing surface discharges. This can be done by placing the wire into an arc-extinguishing medium. It is in this way that the duration of the prebreakdown stage was increased in [6–10] when studying the thermophysical and electrophysical properties of substances. In [11], where wire explosions in vacuum were investigated, the duration of the ohmic heating stage was increased by using an insulating coating.

This paper is devoted to experimental study of the initial stage of the electric explosion of tungsten wires in water and air.

2. EXPERIMENTAL SETUP AND MEASUREMENT TECHNIQUE

Experiments on the fast explosion of fine wires were carried out in a capacitor-based setup (see Fig. 1) with a storage capacitance of $C = 0.1$ μF, $U_{max} = 35$ kV, and $L = 10$ nH. The working voltage was 20 kV. The capacitor was connected to the discharge gap via several parallel air strip lines. The intrinsic inductance of the capacitor was small compared to the inductance of a single line. This allowed us to vary the total inductance of the discharge circuit and, accordingly, the maximum current growth rate by varying the number of lines.

The capacitor was switched to the load via a gas-filled trigatron spark gap. To reduce noise signals in the discharge circuit, the trigger pulse was applied to the central electrode through a low-inductance 5-kΩ TVO-5 resistor.

Besides electric diagnostics, we also used laser shadowgraphy and X-pinch radiography. Since the facility design did not allow us to use these methods simultaneously, the optical and X-ray images were obtained in different shots. The process under study can easily be synchronized with the laser pulse because the jitters in the triggering times of both the spark gap and the laser were no more than a few nanoseconds. Using

1063-780X/05/3111-0919$26.00 © 2005 Pleiades Publishing, Inc.

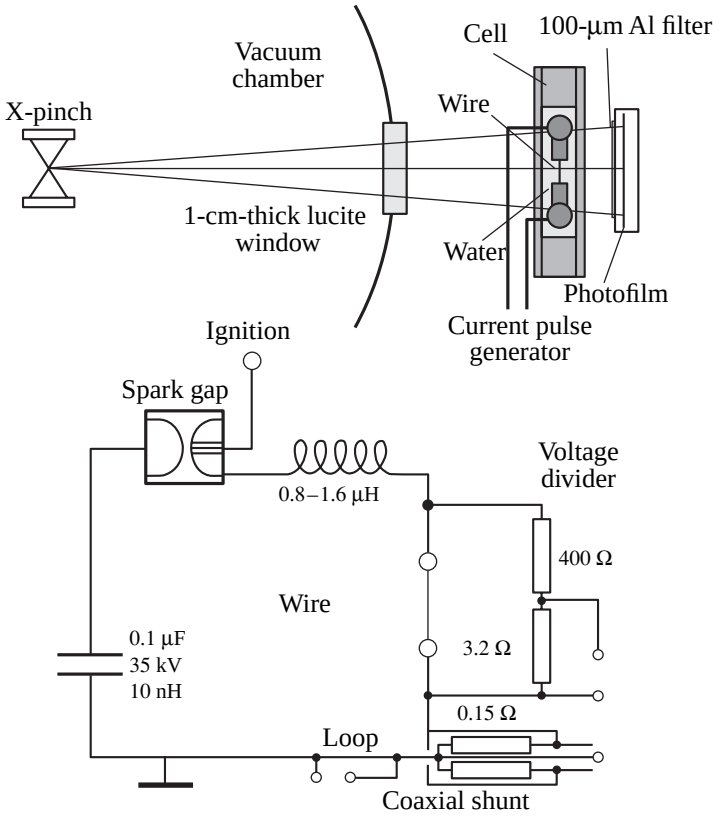

Fig. 1. Scheme of the experimental setup.

a time-delay circuit, we could control the time at which the wire was imaged and, thus, monitor different stages of the wire explosion. A more complicated problem was to synchronize the wire explosion with the X-ray pulse generated using the BIN facility, because the jitter in the BIN triggering time could be as high as several microseconds. The BIN facility is a high-power nanosecond current generator designed by the classical scheme of power sharpening: Marx generator (MG)–intermediate capacitor–forming line–vacuum diode, which are connected to one another via uncontrolled switches. The largest contribution to the total jitter was brought by the MG, whereas jitters in the triggering times of all the other units were relatively small. To improve synchronization in radiography experiments, the spark gap in the wire explosion circuit was triggered by one of the high-voltage pulses formed by the BIN facility, either by the pulse from the shunt of the charging current of the intermediate capacitor or by the pulse from the voltage divider in the forming line. Without going into detail, we note that, in the former case, the probing X-ray pulse was delayed relative to the beginning of the discharge current through a wire by up to 1.5 μs with a jitter of 30–50 ns, whereas, in the latter case, the time delay was up to 300 ns with a jitter of 5–10 ns.

2.1. Electric Measurements

Electric measurements were aimed at determining the time evolution of the discharge current through the wire and the ohmic component of the voltage across it. Based on these data, we calculated the resistance of the discharge channel and the energy deposited in the wire.

The voltage was measured with a resistive divider made of low-inductance resistors. To reduce electromagnetic interferences on the recorded signals, the resistance of the upper arm of the divider was chosen to be relatively low (400 Ω), which was, however, larger than the maximum resistance of the exploding wire. For a reasonable division factor of ~10^2, the resistance of the lower arm was much less than the wave impedance of the cable. To decrease the inductance of the lower arm, it was made of three 10-Ω resistors connected in parallel and carefully shielded to reduce noise signals. The divider was tested using an I1-7 generator of voltage pulsed with an amplitude of 10 V, a pulse duration of 100 ns, and a rise time shorter than 1 ns (Fig. 2). The signals were recorded by a Tektronix TDS 3054B oscilloscope with a bandwidth of 500 MHz.

The current was measured with a 0.15-Ω coaxial shunt connected to the grounded electrode of the discharge gap. The shunt design excluded the influence of

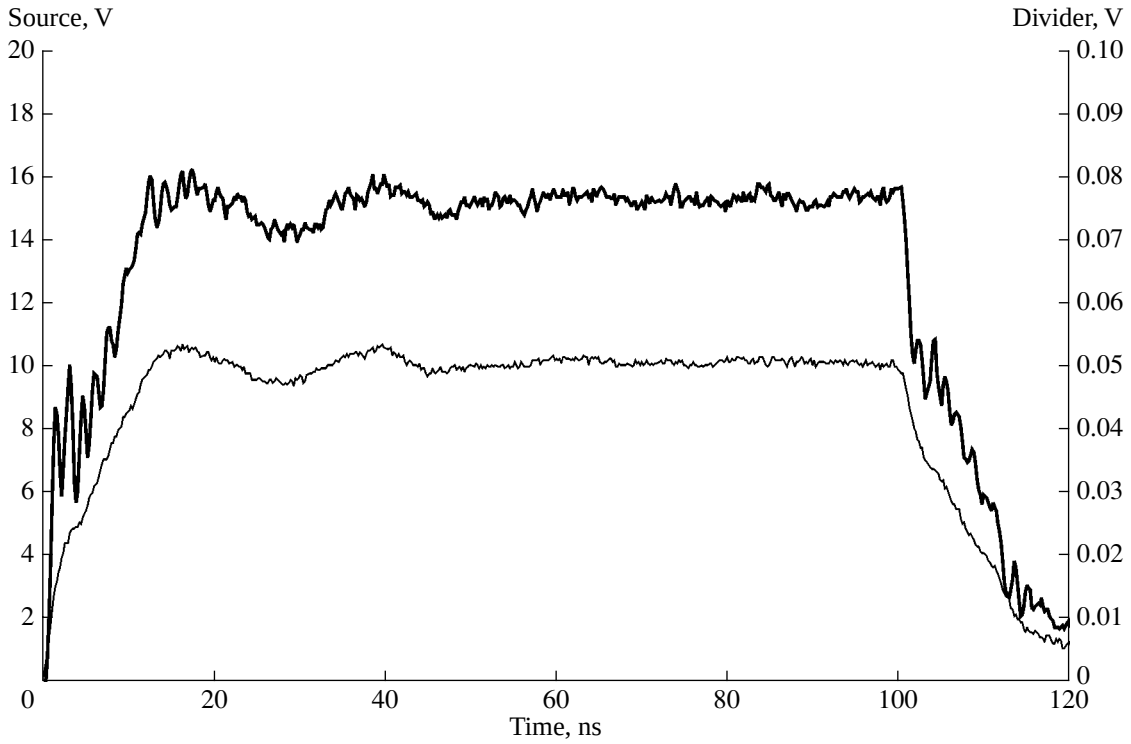

Fig. 2. Waveforms of the source and divider voltages in the case of short-circuited electrodes. The light line shows the source voltage, and the heavy line shows the divider voltage.

any electromagnetic interferences. The shunt was also tested using an I1-7 generator with a load of 75 Ω.

The inductive loop (see Fig. 3) was calibrated by discharging the capacitor through the discharge circuit, the discharge gap being short-circuited with a 1-mm-diameter copper wire (in this case, the ohmic component of the voltage could be ignored; i.e., $U \approx LdI/dt$). It was proved experimentally that the signal from the inductive loop followed the divider signal fairly well. This allowed us to recalculate the loop signal into the inductive voltage component measured by the divider. The ohmic component of the voltage across the wire was then found by the formula $U_r = RI = U - LdI/dt$.

2.2. Optical Diagnostics

Shadow images of the exploding wire were obtained using a diagnostic laser facility based on an IZ-25 generator with radiation conversion into the second harmonics (λ = 532 nm). The duration of the laser pulse was 10 ns, and the pulse energy was 0.03 J. The optical scheme of single-frame laser shadowgraphy is shown in Fig. 4.

Laser output window *1* was projected (with a magnification) by long-focus lens *2* onto objective plane *3*. Lens *4* with a focal length of 40 cm formed a wire image on photofilm *7* with a magnification of 1.3. The self-radiation from the exploding wire was cut off by SZS-21 colored filter *6*. A significant fraction of the self-radiation was also cut off by 1-mm diaphragm *5* placed at the focus of lens *4*. For useful radiation, the diaphragm acts as a schlieren hole—a shield that blocks the light rays deflected due to refraction. As a result, a conventional shadow image of the object is superimposed by a schlieren image of the expanding wire and the surrounding medium.

The laser, whose operation was monitored using an FD102 photodiode, which intercepted a fraction of laser radiation, was synchronized with the wire explosion by using the control signal of the laser Q-switch: one part of this signal triggered the spark gap of the capacitor (thus initiating the wire explosion), whereas the other part, after passing through a time-delay circuit, triggered the laser.

2.3. X-ray Diagnostics

For the radiography of the exploding wire, we used hard radiation from an electron beam generated in an X-pinch minidiode. X-pinch was produced by exploding two (or more) wires crossed in the diode of a high-current accelerator. In the crossing area, a micropinch develops that emits in a wide wavelength range, which depends on the material and diameter of the wire, as well as on the parameters of the current pulse [11]. Under certain conditions, X-pinch emits very short X-ray pulses in the photon energy range of 1–10 keV. Such pinches are widely used in shadow radiography as

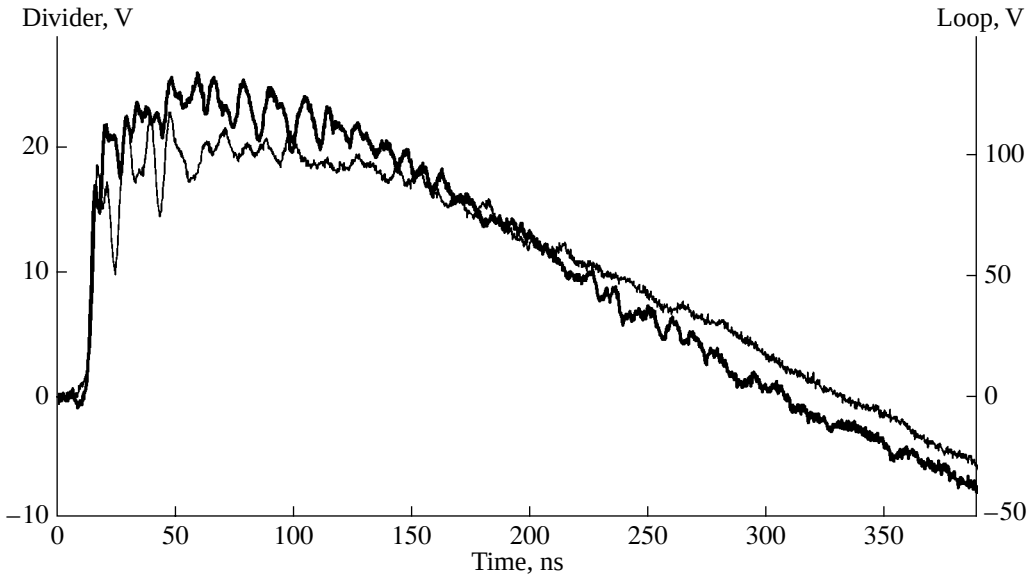

Fig. 3. Waveforms of the voltages at the divider and inductive loop in the case of short-circuited electrodes. The light line shows the loop voltage, and the heavy line shows the divider voltage.

point radiation sources [12–14]. The sensitivity of the method depends on the absorption of radiation in the object under study, i.e., by the amount of matter along a ray.

Immediately after the X-ray burst, the plasma neck in the X-pinch breaks [13], which is accompanied by the generation of high-energy (10–100 keV) electrons. The size of this electron source is 0.1–1 mm [15]. The radiation caused by the electron beam can also be used for the radiography of dense plasma objects. Since this radiation is rather hard, it can be extracted from the vacuum chamber and used to take images in condensed media [11].

In our experiments, a relatively large object was placed at a distance of 30–150 cm from the radiation source and its image was recorded on an X-ray film without magnification (the so-called contact image). We used a lucite filter with a thickness of 10–12 mm and cutoff energy of 10 keV. At a large distance from the radiation source, the spatial resolution of the method was limited only by the resolution of the photofilm.

A scheme of the radiography diagnostics beyond the vacuum chamber of the BIN generator is shown in Fig. 1.

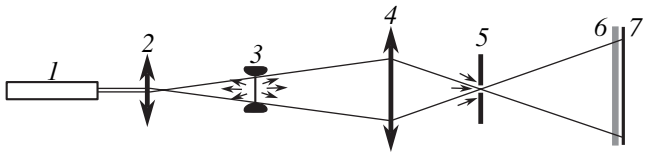

Fig. 4. Scheme of optical shadowgraphy (see text for details).

3. EXPERIMENTAL RESULTS

Most of the experiments were carried out beyond the vacuum chamber, in air and other media.

Figure 5 shows the waveforms of the current $I(t)$ and voltage $U_r(t)$ obtained in explosions of 25-μm tungsten wires in water and air. It can be seen that, up to ~80 ns after the beginning of the current pulse, the waveforms of the current and voltage in different media are similar to one another. In air, breakdown (a sharp increase in the current in Fig. 5a) occurs just after 80 ns, whereas in water, it occurs only after 220 ns. Note that breakdown in air is accompanied by a sharp decrease in the discharge voltage (Fig. 5b). Breakdown in water is preceded by a long-lasting (~100 ns) current pause, during which the current is as low as 100–200 A and the voltage changes only slightly. Therefore, in this stage, the resistance of the discharge gap is very high. Such a difference between the electric characteristics of the wire explosion in water and air can be related to the high electric strength of water. Indeed, the breakdown voltage in water is almost half again as high as that in air (see table).

Figure 5c shows the time evolution of the resistance $R(t)$ of wires exploding in water and air. The curves begin to differ from one another after ~70 ns: in water, the resistance keeps increasing, whereas in air, it decreases. Hence, we can conclude that, up to this time, the processes in the discharge gap depend only on the wire material and the parameters of the current pulse and are independent of the parameters of the surrounding medium, whose influence begins to manifest itself in the later stage.

Parameters of explosions of 25-μm tungsten wires in different media: w_d is the energy deposited in the wire before breakdown, w_s is the sublimation energy, and U_d and R_d are the voltage and resistance at the instant of breakdown

Medium	5-μm polyimide shell	Plasticine	Glycerin	Epoxy glue	Transformer oil	Water	Air
w_d/w_s	0.9 ± 0.2	1.8 ± 0.2	1.5	2.1 ± 0.2	1.7 ± 0.1	1.8 ± 0.2	1.1 ± 0.1
U_d, kV	12.8 ± 3.2	15.3 ± 1.3	16.5	15.9 ± 0.9	14.3 ± 0.4	15.3 ± 1	9.2 ± 1.9
R_d, Ω	23 ± 5	190 ± 60	210	150 ± 60	110 ± 30	90 ± 30	19 ± 5

Figure 5d shows the time evolution of the specific deposited energy w, which was determined from the measured current and voltage by the formula

$$w(t) = m^{-1}\int_0^t I(\tau)U_r(\tau)d\tau; \quad (1)$$

where m is the wire mass. The data are again given for explosions in water and air. The horizontal marks show the instants of breakdown, i.e., the end of the ohmic stage of energy deposition. It can be seen that, in water, the deposited energy changes only slightly during the current pause.

Figure 5e shows the resistivity ρ as a function of the energy deposited in the wire. The resistivity was determined from the measured current and voltage by the formula

$$\rho(t) = \frac{U_r(t)}{I(t)}\frac{\pi a_0^2}{l}; \quad (2)$$

where a_0 is the initial wire radius and l is the wire length (the wire resistivity was determined without allowance for thermal expansion). The specific deposited energy (normalized to the sublimation energy) of ~0.2 corresponds to a melted state of the tungsten wire. Until the deposited energy reaches this value, the resistivity increases according to the law $\rho/\rho_0 = 1 + \beta\Delta T$, which corresponds to the heating of a solid wire. After this, the resistivity of the tungsten wire, which is in a liquid state because the specific deposited energy exceeds the melting energy, varies only slightly over a long time period. This agrees with the literature data (see, e.g., [7, 9]): since the temperature coefficient of the resistivity for liquid tungsten is very low ($\beta \sim 10^{-5}$ K^{-1}), the resistivity of liquid tungsten is often assumed to be constant. In our experiments, the resistivity varied within the range $\rho \sim (1.3–1.6) \times 10^{-6}$ Ω m, whereas the deposited energy varied approximately fivefold. When the specific deposited energy becomes comparable to or larger than the sublimation energy, the calculated resistivity is no longer a characteristic of the wire material alone but also depends on the interaction of the explosion products with the surrounding medium.

We obtained (using both optical and X-ray diagnostics) well-resolved images of exploding wires in the later stage of the explosion, i.e., after breakdown. Figure 6 presents an image of a 25-μm tungsten wire exploding in air. The image was obtained by using optical diagnostics at 350 ns from the beginning of the discharge. It can be seen that the shock wave in air propagates without breaking its cylindrical symmetry. Hence, up to the instant corresponding to this image, spatial nonuniformities had no time to develop in the wire. Nonuniformities that are clearly seen in the electrode regions point to the significant effect of the electrodes on the initial stage of the wire explosion.

Figures 7a and 7b illustrate the explosion of a 50-μm tungsten wire in water and air, respectively. The water chamber in which the wire was exploded was placed at a distance of 120 cm from the X-pinch. Since X-pinch radiation passed through a 10-mm lucite window of the vacuum chamber, 1-m air gap, 1-mm plastic wall of the water chamber, and 10 mm of water with a total cutoff energy about 12 keV, we used four-wire tungsten or molybdenum X-pinches emitting in the photon energy range of higher than 12 keV. X-ray images of both unexploded and exploded wires are shown in Figs. 7c and 7e as an illustration of the spatial resolution and sensitivity of the diagnostics. In Fig. 7e, one can see a wire core (expanded up to 2.3 mm) with a well-resolved structure. The density distributions inferred from the densitograms of the cores shown in Figs. 7a and 7b are presented in Figs. 7d and 7f, respectively. It can be seen from these density distributions that the core of a wire exploding in water is tubular in structure. The mean expansion velocity of the tungsten wire core is about 0.9×10^5 cm/s in water and 2.8×10^5 cm/s in air. The lower expansion velocity of the core in water (as compared to that in air) can be related to the higher specific density of water: the higher the density, the higher the resistance to expansion. It is also seen from the X-ray images that, in air, the outer boundary of the core begins to lose its cylindrical symmetry, whereas in water, it is still cylindrically symmetric. From rough estimates of the density of the tungsten wire core shown in Fig. 7e (assuming the distribution of the matter to be uniform), it follows that the sensitivity of the method is better than 2.3×10^{-4} g/cm^2 (or 10^{18} cm^{-2}).

4. DISCUSSION

The results of experiments on the electric explosion of 25-μm tungsten wires in different media are summarized in the table, which presents the normalized specific energy deposited in the wire before breakdown

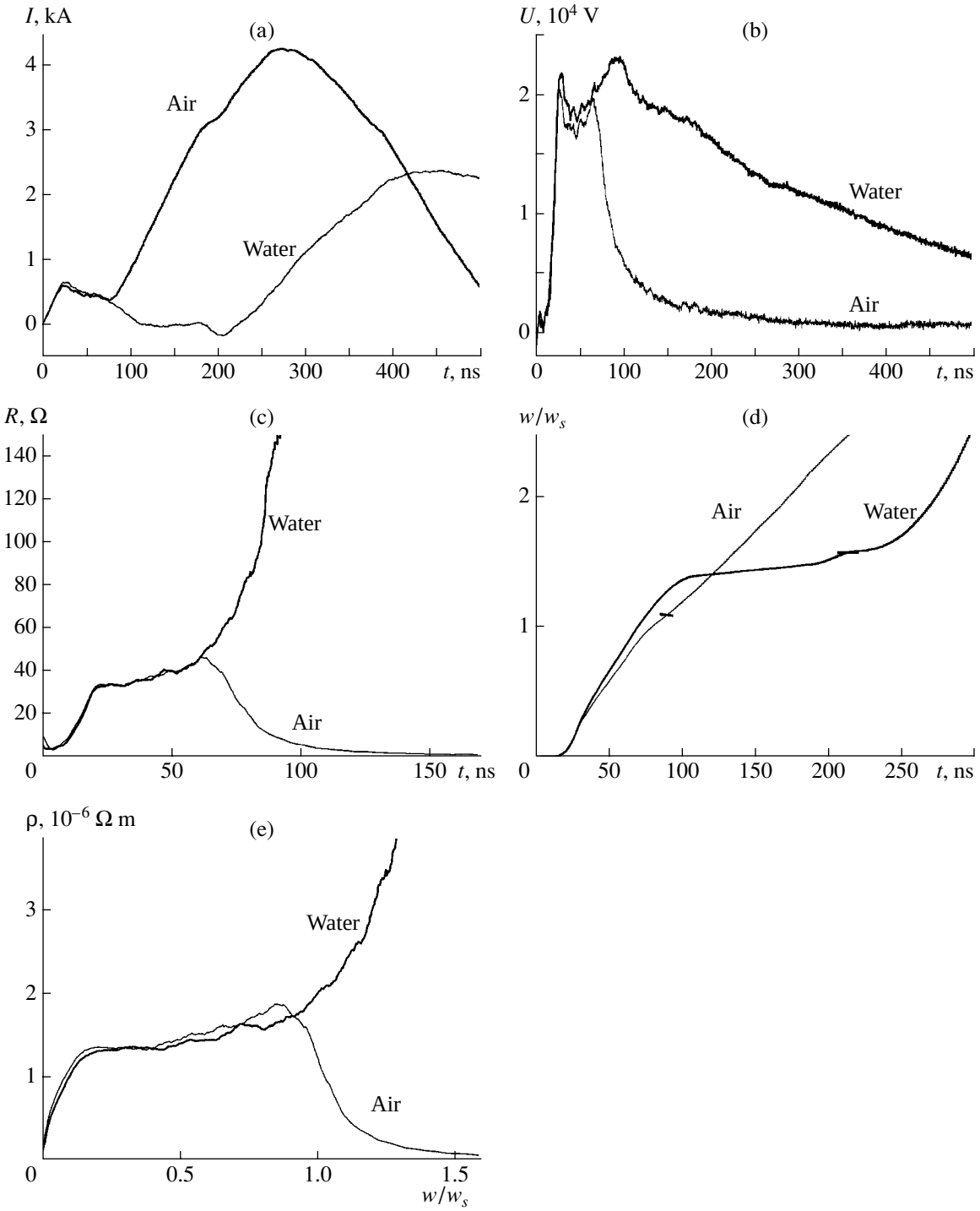

Fig. 5. Waveforms of the (a) current and (b) voltage, time dependence of the (c) wire resistance and (d) deposited energy, and (e) wire resistivity as a function of the deposited energy for explosions of 25-μm tungsten wires in water and air.

(a sharp increase in the discharge current), as well as the voltage and resistance at the instant of breakdown. It can be seen that the energy deposited in the wire in the ohmic heating stage is larger in a dense medium: in water, it is almost twice as large as that in air. The energy deposited in the wire during explosions in other condensed media (transformer oil, alcohol, glycerin, epoxy glue, plasticine, and lucite) was comparable to that deposited during an explosion in water. This energy is large enough to heat the wire to the melting temperature, to melt it, and then to heat it up to the subcritical temperature. Note that, in the case of a vacuum

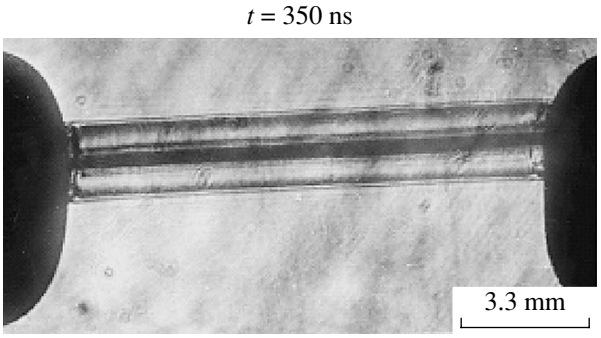

Fig. 6. Laser shadowgraph of a 25-μm tungsten wire exploding in open air at $t = 350$ ns.

explosion, the energy deposited in a bare tungsten wire was less by one order of magnitude [11]. When a tungsten wire was covered by an ~5 μm insulating polyimide film, the explosion parameters were close to those in air. Evidently, such a thin cover did not affect the processes occurring in the wire during its explosion.

In all of the condensed media under study, the breakdown voltages were close to one another, being more than half as high again as that in air. Therefore, we may suppose that the instant of breakdown in condensed media is mainly determined by the properties of wire material and the parameters of the current pulse. This is also confirmed by the experimental data on the explosion of a tungsten foil placed between two glass plates [8]. In those experiments, the breakdown voltage was $E_b \approx 1.1$ kV/mm, which is within the range of breakdown voltages measured in our experiments with condensed media, 1–1.3 kV/mm (recall that, in air, $E_b \approx 0.75$ kV/mm).

When a wire is exploded in a condensed medium, the resistance of the discharge gap is higher than in air. Such an increase in the resistance can occur when a "liquid wire–vapor" conducting system transforms into a dispersed (and, hence, a poorly conducting) "liquid drops in vapor" state. According to the measured resistance of the discharge gap, the breakdown conditions in air are reached before the wire transforms into a dispersed state. For the same reason, the recovered density profiles in Figs. 7d and 7f differ from one another. Thus, the formation of a tubular structure in the case of a wire explosion in water can be related to the expansion of drops (which are not held together by the Ampére force) during a prolonged current pause preceeding breakdown and the formation of a current-carrying shell that prevents further expansion. Breakdown in air occurs earlier; hence, the generated current-carrying shell prevents the expansion of the wire material before a significant amount of it is dispersed. As a result, the central part of the wire remains a bit denser even in the later stage of expansion.

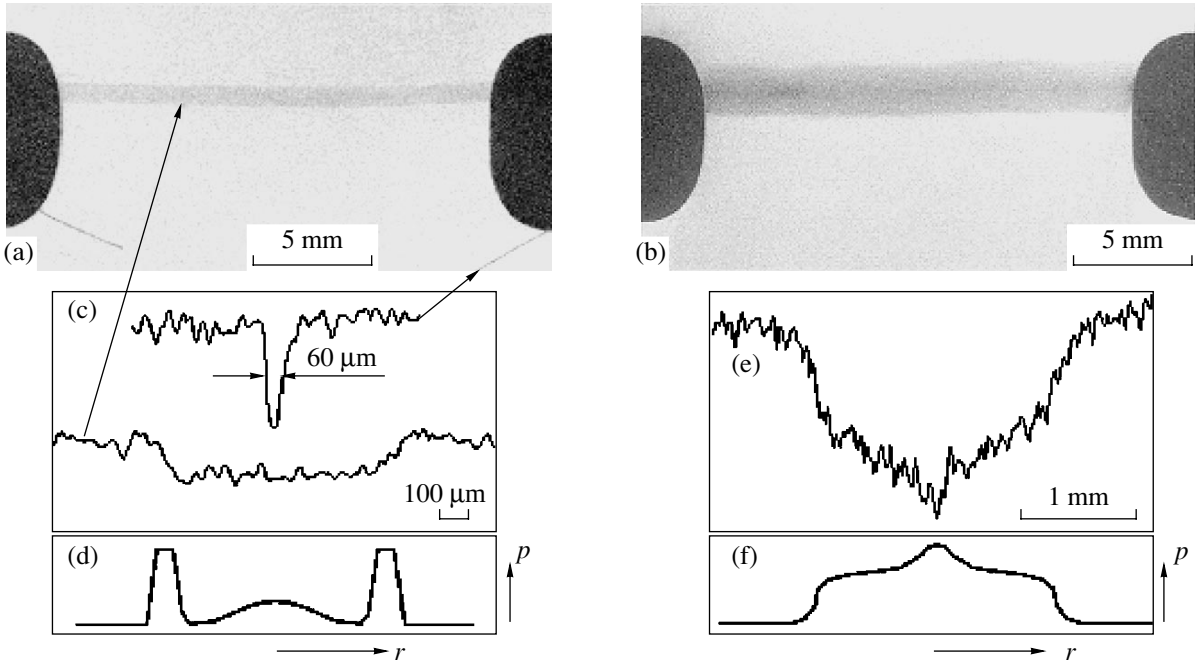

Fig. 7. Radiographs of a 50-μm tungsten wire exploding in (a) water (at $t = 960$ ns) and (b) air (at $t = 850$ ns). The radiographs were obtained using an X-pinch radiation source with a photon energy of higher than 12 keV. (c, e) Densitograms of the exploding wires and (d, f) reconstructed density profiles (in arbitrary units). In plot (c), a densitogram of a segment of the wire before its explosion is also shown to illustrate spatial resolution.

ACKNOWLEDGMENTS

We are grateful to G.V. Ivanenkov, S.Yu. Gus'kov, A.V. Agafonov, and A.G. Russkikh for useful discussions. This study was supported in part by the International Science and Technology Center (grant no. 2151), the Russian Foundation for Basic Research (project nos. 04-02-17292, 05-02-17532, and 05-02-17533), and Cornell University (subcontract under project no. DE-PC03-2NA 00057).

REFERENCES

1. V. V. Aleksandrov, A. V. Branitskiĭ, G. S. Volkov, *et al.*, Fiz. Plazmy **27**, 99 (2001) [Plasma Phys. Rep. **27**, 89 (2001)].
2. R. B. Spielmen, C. Deeney, G. A. Chandler, *et al.*, Phys. Plasmas **5**, 2105 (1998).
3. S. V. Lebedev, I. H. Mitchell, R. Aliaga-Rossel, *et al.*, Phys. Rev. Lett. **81**, 4152 (1998).
4. S. A. Pikuz, T. A. Shelkovenko, D. B. Sinars, *et al.*, Phys. Rev. Lett. **83**, 4313 (1999).
5. S. I. Tkachenko, V. S. Vorob'ev, and S. P. Malyshenko, Appl. Phys. Lett. **82**, 4047 (2003).
6. S. V. Lebedev and A. I. Savvatimskiĭ, Usp. Fiz. Nauk **144**, 215 (1984) [Sov. Phys. Usp. **27**, 749 (1984)].
7. S. V. Koval', N. I. Kuskova, and S. I. Tkachenko, Teplofiz. Vys. Temp. **35**, 876 (1997).
8. V. N. Korobenko, A. D. Rakhel', A. I. Savvatimskiĭ, and V. E. Fortov, Fiz. Plazmy **28**, 1093 (2002) [Plasma Phys. Rep. **28**, 1008 (2002)].
9. R. S. Hixson and M. A. Winkler, Int. J. Thermophys. **11**, 709 (1990).
10. V. I. Oreshkin, R. B. Baksht, A. Yu. Labetsky, *et al.*, Zh. Tekh. Fiz. **74** (7), 38 (2004) [Tech. Phys. **49**, 843 (2004)].
11. D. B. Sinars, Hu Min, K. M. Chandler, *et al.*, Phys. Plasmas **8**, 216 (2001).
12. T. A. Shelkovenko, D. B. Sinars, S. A. Pikuz, and D. A. Hammer, Phys. Plasmas **8**, 1305 (2001).
13. T. A. Shelkovenko, D. B. Sinars, S. A. Pikuz, *et al.*, Rev. Sci. Instrum. **72**, 667 (2001).
14. G. V. Ivanenkov, A. R. Mingaleev, S. A. Pikuz, *et al.*, Fiz. Plazmy **22**, 403 (1996) [Plasma Phys. Rep. **22**, 363 (1996)].
15. T. A. Shelkovenko, S. A. Pikuz, V. M. Romanova, *et al.*, Proc. SPIE **5156**, 36 (2004).

Translated by N.N. Ustinovskiĭ

Plasma Physics Reports, Vol. 31, No. 11, 2005, pp. 927–937. Translated from Fizika Plazmy, Vol. 31, No. 11, 2005, pp. 997–1008.

PLASMA INSTABILITIES

Laboratory Modeling of Nonstationary Processes in Space Cyclotron Masers: First Results and Prospects

A. V. Vodop'yanov, S. V. Golubev, A. G. Demekhov, V. G. Zorin, D. A. Mansfel'd, S. V. Razin, and V. Yu. Trakhtengerts

Institute of Applied Physics, Russian Academy of Sciences, ul. Ul'yanova 46, Nizhni Novgorod, 603600 Russia

Received January 12, 2005

Abstract—Results are presented from laboratory modeling of the dynamics of space cyclotron masers. A self-oscillatory mode of cyclotron instability in the nonequilibrium plasma of an ECR discharge in a magnetic mirror trap is found. The plasma comprises two electron populations: the background population with a density of $N_e \sim 10^{13}$–10^{14} cm^{-3} and temperature of $T_e \approx 300$ eV and the energetic population with a density of $N_e \sim 10^{10}$ cm^{-3} and temperature of $T_e \approx 10$ keV. Quasi-periodic pulsed precipitation of energetic electrons from the trap, accompanied by microwave bursts at frequencies below the electron gyrofrequency in the center of the trap, is detected. The study of the microwave plasma emission and the energetic electrons precipitated from the trap shows that the precipitation is related to the excitation of whistler-mode waves propagating nearly parallel to the trap axis. The observed instability has much in common with phenomena in space magnetic traps, such as radiation belts of magnetized planets and solar coronal loops. The experimental results demonstrate the opportunity of laboratory modeling of space cyclotron masers. The main tasks and possibilities of such modeling are discussed. © *2005 Pleiades Publishing, Inc.*

1. INTRODUCTION

Resonant interaction between particles and waves (in particular, cyclotron interaction) significantly affects the dynamics of many processes in space plasma. Investigations of these processes, which began as early as the 1960s [1–4], led to the development of the space cyclotron maser (SCM) concept. A substantial contribution to this field of research was made by works on the self-consistent theory of cyclotron instability (CI) in the Earth's magnetosphere [5, 6].

The SCM operation governs the population of the radiation belts of the Earth and planets with energetic particles [5] and the generation of high-power magnetosphere radiation, such as ELF/VLF chorus emissions in the Earth's magnetosphere [7–9], the Earth's kilometric radiation [10, 11], and the Jovian decametric radiation [12].

The SCM operation has much in common with that of laboratory cyclotron resonance masers (CRMs) and lasers. Distinguishing features of SCMs are a decisive influence of the plasma on the dispersion properties of the excited waves, a substantial nonuniformity of the plasma and the magnetic field, and the wide energy and angular spectra of the charged particles exciting the instability.

The SCM parameters in different systems differ substantially from one another and also from the parameters of laboratory systems; nevertheless, the dynamics of such systems is governed by the same nonlinear mechanisms. These mechanisms can be divided into two groups:

(i) The quasilinear and nonlinear modification of the distribution function of energetic particles under the action of the generated radiation and the associated change in the instability growth rate.

(ii) The nonlinear change in both the surface and body parameters of the electrodynamic system.

The common physical mechanisms underlying the operation of laboratory and space masers make possible laboratory modeling of SCMs. The importance of such modeling is related to the difficulties in studying space phenomena because of their large scales and sporadic character and a great number of mutually dependent uncontrolled factors that are difficult to take into account. Therefore, there are many unresolved problems (both quantitative and qualitative) concerning the generation of electromagnetic radiation in SCMs and its influence on the dynamics of energetic particles in space plasmas. As applied to the Earth's magnetosphere, the current state of these problems is reviewed in [13–16] (see also [8, 17, 18]).

SCMs can be divided into several types. The first type (which is most similar to laboratory electronic devices) comprises low-density ($\omega_{pe} \ll \omega_{He}$, where ω_{pe} and ω_{He} are the electron plasma frequency and the electron gyrofrequency, respectively) systems in which the density of the energetic (hot) electron component N_h can be comparable to or even higher than the density of the cold component N_c. Under these conditions, electromagnetic waves with a wave vector **k** almost perpendicular to the external magnetic field **B** are efficiently excited at frequencies near the electron gyrofrequency.

1063-780X/05/3111-0927$26.00 © 2005 Pleiades Publishing, Inc.

It is these systems that generate, e.g., the Earth's kilometric radiation and the Jovian decametric radiation.

The second type of SCMs occurs in the flux tubes of trap configurations filled with a fairly dense cold plasma ($\omega_{pe} \gtrsim \omega_{He}$) containing a small additive of energetic electrons or ions. A characteristic feature of energetic particles in magnetic traps is that their average transverse kinetic energy $T_\perp$ is higher than their longitudinal energy $T_\parallel$. This is explained by the presence of a loss cone and the action of various acceleration mechanisms (such as the betatron acceleration operating when a particle moves toward a higher magnetic field or when the magnetic field increases with time). The energetic particles can efficiently generate electromagnetic waves at small angles to **B** at frequencies below the gyrofrequency ($\omega < \omega_H$). These waves play an important role in the plasma dynamics in space magnetic traps (such as the Earth's radiation belts and solar flare loops), because (i) they can be reflected from conjugate regions of the ionosphere and can thus repeatedly return to the equatorial region, where their interaction with energetic particles is most intense; (ii) they have a large magnetic component, which leads to the efficient diffusion of energetic particles over pitch angles, so that these particles can fall into the loss cone and leave the trap; and (iii) the instability condition for them is satisfied along the entire flux tube.

We can also distinguish space plasma-wave generators whose operation is based on trapped particles or on the particle beams produced by space accelerators (e.g., by solar flares). It is also worth mentioning generators of large-scale oscillations (with a wavelength comparable to the system size) that can be excited by energetic particles under the drift or bounce resonance conditions. These oscillations can play an important role in the transport and acceleration of energetic particles in the magnetospheres of the Earth and planets.

Laboratory experiments make it possible to perform repeated measurements with a controllable variation in the parameters. At the same time, laboratory modeling has its inherent problems stemming from too small spatial and temporal scales of the modeled processes in comparison to those characteristic of space phenomena.

Because of a considerable difference between the above types of SCMs, the problems of their modeling should be considered separately. In what follows, we consider (unless otherwise specified) the CI of the electromagnetic waves that are generated by trapped energetic particles and propagate at small angles to the external magnetic field. The problems concerning the modeling of other types of SCMs (in particular, those operating in a low-density plasma and similar to laboratory gyrotron systems) deserve separate consideration.

Note that the generation of CI whistler-mode waves was observed in laboratory experiments with magnetic traps as early as the 1965–1990s [19–24]. In those experiments (like in typical space plasmas), the plasma contained two electron components: the main cold component and a low-density hot component, which comprised most of the plasma energy. It was pointed out that the onset of CI of whistler-mode waves was accompanied by short radiation bursts and by escape of energetic electrons through the loss cone. The mechanism for the formation of short radiation bursts was not discussed. In [25], it was suggested for the first time that the specific features of one of the above experiments [21] were related to the nonlinearity of the Q factor of the resonator formed in a magnetic trap. The plasma itself can serve as a nonlinear element in such a resonator, because it determines the main characteristics of the wave propagation and ensures rapid change in the Q factor in the course of the generation of electromagnetic radiation. An attempt to explain the results of all of the above experiments on the common basis of a self-consistent theory of CI was made in [26].

In this paper, we discuss the possibility of using laboratory magnetic traps to model linear and nonlinear mechanisms of CI in space plasmas. The problem of experimentally achieving the required values of the characteristic dimensionless parameters determining the role of various nonlinear mechanisms is considered. The first results are presented from experiments on laboratory modeling of the SCM dynamics that were performed at the Institute of Applied Physics by using a high-power (80-kW) 8-mm (37.5-GHz) gyrotron radiation to produce a plasma with an energetic electron component. The use of high-power short-wavelength radiation allowed us to achieve a higher energy of the hot electron component and to ensure an almost quasi-optical propagation of CI-driven waves in the plasma (as is the case in actual space plasmas).

2. RELATIONS BETWEEN THE PARAMETERS OF SPACE AND LABORATORY PLASMA CYCLOTRON MASERS

Under laboratory conditions, the most commonly used method for producing plasma with an energetic electron component is electron cyclotron resonance (ECR) breakdown and heating. This method allows one to obtain a hot electron component with characteristic energies from 100 eV to a few hundred keV (depending on the microwave power, magnetic field, gas pressure, and other parameters) and to control the fraction of energetic electrons over a wide range. For energetic electrons in such a plasma, collisions are usually of minor importance over times on the order of the period T_b of oscillations of these electrons between magnetic mirrors ($\nu_e T_b \ll 1$, where ν_e is the electron collision frequency). This is also true for energetic electrons in space magnetic traps, such as the Earth's and Jovian magnetospheres and solar flare loops.

An anisotropic velocity distribution with $T_\perp > T_\parallel$ gives rise to the CI of electromagnetic waves [3, 4]. The

linear stage of instability is characterized by the net growth rate, which is determined by the resonance interaction of energetic particles with waves and different mechanisms for wave energy losses. Space plasmas usually have smooth particle velocity distributions; in this case, the initial stage of instability is kinetic in character. The frequency dependence of the growth rate of the kinetic CI of waves with $\widehat{\mathbf{kB}} \ll 1$ is primarily determined by two dimensionless parameters [5]: the anisotropy index of the particle distribution over pitch angles, $A = T_\perp/T_\parallel - 1$, and the parameter $\beta_* \approx kv_0/\omega_H$, where $v_0 = (2W_0/m)^{1/2}$ is the characteristic velocity of energetic particles, W_0 is their average energy, and k is the characteristic wavenumber. For whistlers, we have $\beta_* \simeq (\omega_p^2/\omega_H^2)v_0^2/c^2$. The parameter A determines the upper frequency boundary of the instability domain, $\omega_{\max}/\omega_H = A/(A+1)$, and β_* determines the number of resonant particles. For $\beta_* \gg 1$ and $A + 1 \sim 1$, which is typical for the Earth's outer radiation belt, the CI growth rate is maximum at a frequency of $\omega \approx \omega_{HL}/\beta_* \ll \omega_{HL}$ (where the subscript L stands for the values at the center of the trap). The maximum growth rate can be roughly estimated at [5]

$$\gamma_{\max}/\omega_{HL} \approx 0.2AN_h/N_c, \quad (1)$$

where N_h and N_c are the number densities of hot and cold electrons, respectively.

In the case of ECR heating, the density of the plasma produced is limited by the condition $\omega_{pr} \lesssim \omega_{Hr}$, which is related to the efficiency of the field penetration into the plasma and the field absorption in the plasma (here, subscript r stands for the values in the ECR region). For a quasi-longitudinal launching of microwaves, the limitation on the plasma density is less rigid; moreover, in this case, the ratio ω_p/ω_H usually increases toward the center of the trap. However, this ratio is typically $\omega_p/\omega_H \lesssim 3$–4. Under these conditions, we have $\beta_* \sim 1$, so the CI growth rate is maximum near the upper boundary frequency $\omega_{\max}$ [5]. The above estimate for the maximum CI growth rate should be corrected to reduce this value by the factor $\exp(-\beta_*^{-1})$. Another characteristic feature of laboratory magnetic traps is a relatively low (in comparison, e.g., to the Earth's radiation belts) magnetic mirror ratio ($\sigma \sim 2$–10). For this reason, the anisotropy of the particle pitch-angle distribution related to the presence of a loss cone (i.e., the parameter A) is fairly high. This leads to an increase in the upper frequency boundary of unstable whistlers, $\omega_{\max} = \omega_{HL}A/(A+1)$.

In space magnetic traps, the inequality $l/\lambda \gg 1$ is usually satisfied, where λ is the wavelength and l is the characteristic scale of the plasma nonuniformity along the magnetic field (the length of the system). Under laboratory conditions (even in unique devices), the ratio l/λ, which depends on the device dimensions and the plasma density ($\omega_p \sim \omega_H$), is substantially less than in space traps. Nevertheless, in laboratory devices, the condition $l/\lambda \gg 1$ is also usually satisfied ($l/\lambda \sim 10$–20).

The most interesting and important problems that may be solved using laboratory modeling are related to the nonlinear mechanisms governing the dynamics of waves and particles during the development of CI. For the Earth's magnetosphere, the problems of interest are the self-modulation of cyclotron maser radiation due to, e.g., a quasilinear change in the CI growth rate [27–30]; the nonlinear turning of the resonator mirrors [31, 32]; and the interaction with the oscillatory motion of flux tubes [33, 34]. For solar flare loops, a situation may occur [25] in which the collisional damping of waves is nonlinearly reduced because of plasma heating by the generated radiation [35]. Particular attention is currently given to the origin of discrete (quasi-monochromatic) radiation [9, 15]. Let us briefly discuss conditions under which these mechanisms can operate and the possibility of studying them in laboratory devices.

In addition to the above circumstances, the dynamics of these processes is affected by the following factors: (i) the ratio between the characteristic length a of the system and the length of linear amplification $l_{CI} \sim v_g/\gamma$, (ii) the ratio between the CI growth rate γ and the collisional damping rate ν_{coll}, (iii) the value and nonlinearity of the reflection coefficient, and (iv) the pitch-angle characteristics of the particle source.

Using formula (1) and the dispersion relation for whistlers, $kc \simeq \omega_p[\omega/(\omega_H - \omega)]^{1/2}$, we can write the dimensionless parameter $\Gamma_{CI} = a/l_{CI} = \gamma a/v_g$ (the optical thickness of the system with respect to amplification) in the form

$$\Gamma_{CI} \approx 0.1A\frac{N_h}{N_c}\frac{a\omega_{pe}}{c}\beta_*^{1/2}, \quad (2)$$

where, as in Eq. (1), we take into account that $\omega \approx \omega_{HL}/\beta_* \ll \omega_{HL}$. For estimates, we use the parameters of the experiment that will be discussed below: $N_c \sim 10^{14}$ cm^{-3}, $N_h \sim 5 \times 10^{10}$ cm^{-3}, $W_0 \sim 10$ keV, $a \sim 10$ cm, and $A \sim 2$. As a result, we obtain $\Gamma_{CI} \sim 2 \times 10^{-2}$ (in this case, $\beta_* \lesssim 1$; therefore, formulas (1) and (2) can be used only for rough estimates). Hence, under laboratory conditions, the onset of CI is typically determined by reflections from the ends of the plasma resonator. In order to achieve a single-pass amplification regime ($\Gamma_{CI} \sim 5$–10), the anisotropy should be increased severalfold or the system length should be increased by one order of magnitude (the other parameters being fixed).

The collisional damping rate of whistlers is equal to

$$\nu_{coll} \simeq \frac{\omega}{\omega_H}\nu_{ei}, \quad (3)$$

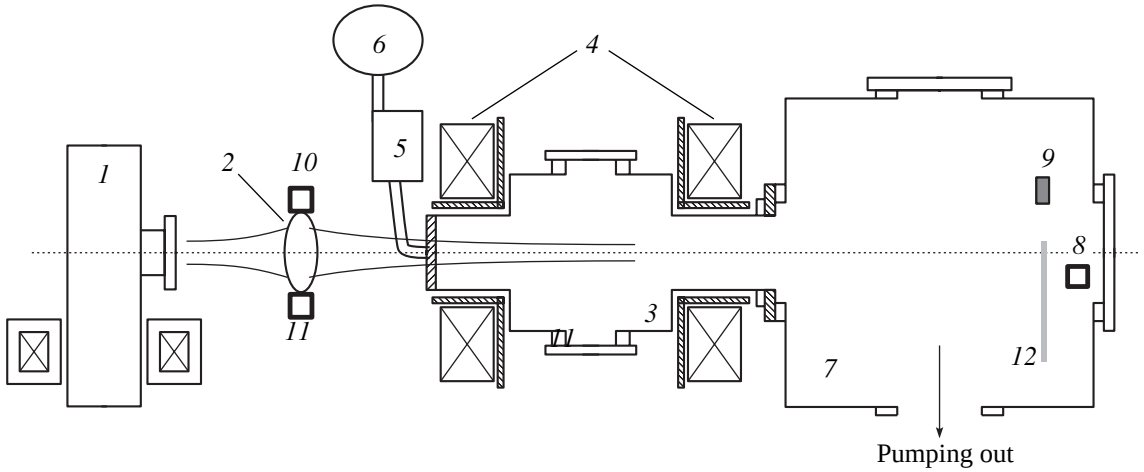

Fig. 1. Schematic of the experimental setup: (*1*) gyrotron, (*2*) focusing lens, (*3*) discharge chamber, (*4*) solenoids, (*5*) pulsed valve, (*6*) working-gas tank, (*7*) diagnostic chamber, (*8*) p-i-n diode, (*9*) Langmuir probe; (*10*, *11*) coaxial–waveguide junctions, and (*12*) aluminum filters.

where ν_{ei} is the electron–ion collision frequency. For estimates, we use the expression $\nu_{ei} \simeq 4.5 \times 10^{-5} N_i Z^2 W_c^{-3/2}$, where Z is the ion charge number (here and in the subsequent estimates, the density and energy are in cm^{-3} and eV, respectively). A comparison between Eqs. (1) and (3) yields the estimate

$$\gamma/\nu_{coll} \approx 70A \frac{N_h}{10^{10}} \left(\frac{10^{13}}{N_c}\right)^2 \left(\frac{T_c}{10^2}\right)^{3/2} B_L Z^{-2}, \qquad (4)$$

where B_L is in T. It follows from this estimate that the ratio γ/ν_{coll} in a laboratory trap can be larger or less than unity; i.e., at a sufficiently low temperature and high density of the background plasma, the onset of CI can be caused by a nonlinear reduction in the collision frequency. In particular, the collisional damping rate is on the order of the growth rate if, for the above plasma parameters, we have $T_c \lesssim 10^2$ eV.

Self-oscillatory modes of CI that are related to a nonlinear change in the distribution function of energetic particles depend on the distribution of the source particles over pitch angles θ [29]. Such modes can occur in the case of both a monotonic distribution with a peak at $\theta = \pi/2$ and a butterfly-type (sloshing-electron) distribution with a maximum at an intermediate pitch angle between 0° and 90° [28]. Both these types of distribution can occur in space and laboratory plasmas. From the standpoint of laboratory modeling, the method of ECR breakdown and heating is convenient because it allows one to change the distribution over pitch angles by shifting the resonance region inside the trap. When breakdown occurs in the center of the trap, the distribution has a maximum at $\theta = \pi/2$. By shifting the resonance region, a butterfly-type distribution can be produced.

The above estimates indicate that the linear and nonlinear mechanisms that are invoked to explain the dynamics of SCMs can also operate in laboratory traps. Therefore, the most fruitful approach to the laboratory modeling of SCMs consists in a qualitative and quantitative interpretation of the results of laboratory experiments and natural observations on the basis of the same concepts and models and, as a result, in an extension of the applicability region of the available models.

The most difficult problems can arise in modeling processes with characteristic times on the order of or less than the bounce times of electrons and wave packets in a magnetic trap. In moderate laboratory traps ($l \sim$ 20 cm), these times can amount to several nanoseconds and even to a fraction of a nanosecond. This requires much effort for their resolution.

3. RESULTS OF LABORATORY EXPERIMENTS

3.1. Experimental Setup

Experiments were carried out in the SMIS 37 device (see Fig. 1). Linearly polarized microwave radiation from gyrotron *1* with a frequency of 37.5 GHz, peak power of 80 kW, and pulse duration of 1–1.5 ms was focused by dielectric lens *2* into the center of discharge chamber *3*. The radiation intensity in the focal plane was on the order of 10 kW/cm^2. The plasma was heated at the fundamental harmonic of the electron gyrofrequency. The discharge chamber with a characteristic transverse size of 70 mm was placed in an axially symmetric mirror trap. The magnetic field in the trap was produced by two solenoids *4*. The duration of the magnetic field pulse was about 13 ms, the maximum magnetic field in the mirror region was $B_{0max} = 3.5$ T, and the mirror ratio was $\sigma = 4$ or 10. The mirror-to-mirror distance was $l = 25$ cm. The working gas (argon or nitrogen) was fed into the discharge chamber through

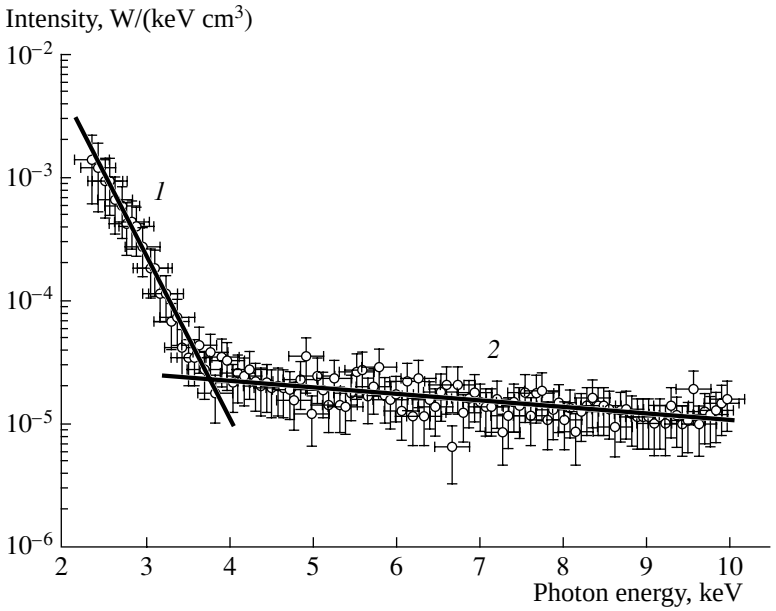

Fig. 2. Spectrum of X-ray emission from the plasma. Straight lines correspond to Maxwellian energy distributions: (*1*) background plasma (T_c = 327 eV, $N_c = 2.6 \times 10^{13}$ cm^{-3}) and (*2*) hot electrons (T_h = 8.4 keV, $N_h = 5.5 \times 10^{10}$ cm^{-3}).

pulsed valve *5* from tank *6* with a regulated gas pressure. The use of pulsed gas puffing allowed us to maintain the gas pressure in the discharge chamber at a level of 10^{-5}–10^{-3} torr during the heating microwave pulse, whereas the pressure in diagnostic chamber *7* was substantially lower (on the order of 10^{-6} torr). In this case, distortion of the energy spectrum of the electrons escaping from the trap was minimal.

The energetic electrons precipitated from the magnetic trap were measured with the help of mobile SPPD-11-04 silicon p-i-n diode *8* located at a distance of 60 cm from the center of the trap. When an electron falls through the input window of the p-i-n diode into the i-zone, depleted of charge carriers, it produces charge carriers (electrons and holes) drifting toward the diode contacts under the action of the electric field. As a result, a current pulse with an amplitude proportional to the electron energy is generated in the electric circuit. The p-i-n diode used in our experiments is capable of detecting electrons with energies in the range from 7 to 500 keV. The lower energy limit depends on the thickness of the dead layer produced in the diode during its treatment, whereas the upper energy limit is determined by the size of the depleted zone. The time resolution of the detector (a few nanoseconds) is determined by the drift time of charge carriers across the sensitive region.

The operating conditions and the plasma parameters in the diagnostic chamber were monitored using Langmuir probe *9*.

To record and roughly analyze the spectrum of the plasma microwave emission, we used coaxial–waveguide junctions (CWJs) *10* and *11* with different dimensions of the waveguide sections. The CWJs were mounted outside the vacuum chamber, near the system axis. The transverse size of the receiver aperture determines the lowest frequency of the detected electromagnetic radiation. The boundary frequencies of the four CWJs used in our experiments were 2.2, 5.4, 8.2, and 11.8 GHz. The detector was connected to the CWJ output through a 2-m-long microwave cable in order to protect the detector from the action of high-power gyrotron radiation.

Signals from the microwave detectors, the Langmuir probe, and the p-i-n diode were fed to a Gould 6000 multichannel digital oscilloscope and were stored in a computer.

3.2. Experimental Results

3.2.1. Plasma parameters. As was shown in [36], the ECR heating at the fundamental harmonic of the electron gyrofrequency in our device produces a plasma with a two-temperature electron energy distribution. To determine the plasma temperature and density, we measured the spectrum and absolute intensity of the plasma X-ray bremsstrahlung. From the X-ray plasma emission spectrum shown in Fig. 2, it can be seen that the plasma comprises two electron populations: the temperature of the first (cold) population is $T_c \sim$ 300–400 eV, whereas the temperature of the second (hot) population is $T_h \sim$ 7–10 keV. From the measured absolute intensity of the X-ray plasma emission, we can determine the densities of both electron populations. The density of the low-temperature population is $N_c \sim 5 \times 10^{13}$ cm^{-3}, and the density of the hot population

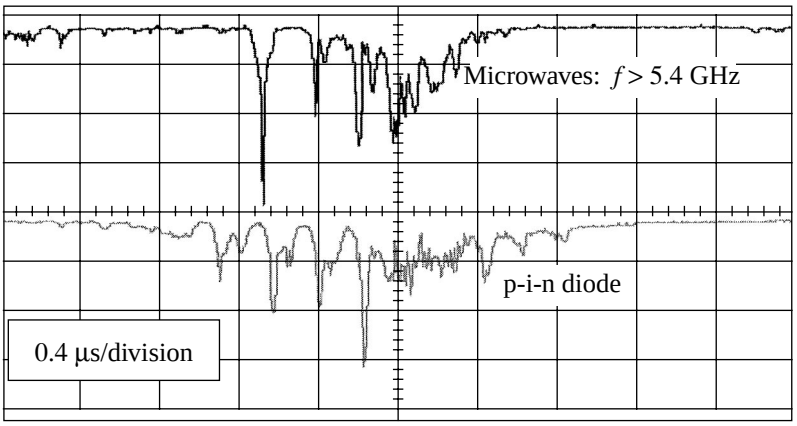

Fig. 3. Oscillograms of the plasma microwave radiation and the signal from the p-i-n diode.

is $N_h \sim 10^{10}$–10^{11} cm^{-3}. The error in determining the temperature is about 15%, whereas the error in determining the density is on the order of the density itself [36].

3.2.2. Properties of instability. Under certain conditions that will be discussed below, we observed the onset of instability characterized by a pulsed precipitation of energetic electrons from the trap and short microwave bursts at frequencies of 2–11 GHz (the electron gyrofrequency at the center of the trap was $f_{HL} \approx 15$ GHz).

The instability usually showed up as a quasi-periodic sequence of radiation pulses (the self-oscillatory mode). Sometimes, a nonperiodic time modulation and single pulses with significantly larger amplitudes (giant pulses) were observed.

Figure 3 shows a typical oscillogram of the plasma microwave emission and the current of the p-i-n diode, detecting the precipitation of energetic electrons. This oscillogram was obtained under the following conditions: the magnetic mirror ratio was $\sigma = 4$, the magnetic field at the center of the trap was $B_L = 0.5$ T, and the argon pressure in the discharge chamber was $p_0 \sim 10^{-4}$ torr. It can be seen that instability in this case manifests itself as quasi-periodic (with a period of up to 200 ns) synchronous microwave bursts and p-i-n diode current pulses with a characteristic duration of 30 ns.

A closer examination of these signals showed that almost every pulse of the precipitated energetic electrons was accompanied by a microwave burst. The converse, however, was not true; i.e., microwave bursts were often observed that were not accompanied by electron precipitation. This was presumably related to different measurement conditions: the receiving microwave antenna had a wide directional pattern, whereas the p-i-n diode detected electrons that escaped from the trap almost along the magnetic field, in the vicinity of one magnetic field line. This means that the transverse structure of electron precipitation can change from pulse to pulse. Another possible explanation is that there is an energy threshold in the spectral sensitivity of the particle detector ($W_{min} \simeq 7$ keV).

Our experiments showed that the instability developed in a certain limited range of the plasma electron densities, $N_{e\,min} < N_e < N_{e\,max}$. This is clearly seen from the oscillogram presented in Fig. 4, in which the upper and lower traces correspond to the plasma microwave emission and the probe ion current, respectively. The detected plasma microwave emission is seen as a sequence of short bursts. Under standard operating conditions, the probe current is proportional to the plasma density in the trap. As the plasma density is increased monotonically, pulsed electron precipitation and microwave bursts appear when the plasma density exceeds $N_{e\,min}$ and disappear when N_e becomes higher than $N_{e\,max}$.

In Fig. 5, the number of microwave bursts (at frequencies of $f > 5.4$ GHz) per gyrotron pulse is plotted as a function of the gas pressure p_0 before breakdown. It can be seen that instability develops in a limited range of p_0. This is obviously related to an increase in the maximum value of N_e with increasing p_0. Probably, as N_e exceeds a certain value, the hot electron population gradually disappears because of both an increase in collisional energy losses and a decrease in the heating efficiency due to the shielding of the resonance region by the plasma. On the other hand, at low p_0 (and, hence, N_e), the density of energetic electrons is too low for the onset of instability.

3.2.3. Microwave spectrum. Our diagnostics did not allow us to perform high-accuracy time-resolved measurements of the spectrum of the plasma microwave emission. Some idea of the shape of the emission spectrum can be provided by CWJ signals measured in several frequency ranges. Figure 6 shows the time-integrated (over a gyrotron pulse) signals of the microwave plasma emission in different frequency ranges as a function of the magnetic field B_L at the center of the trap

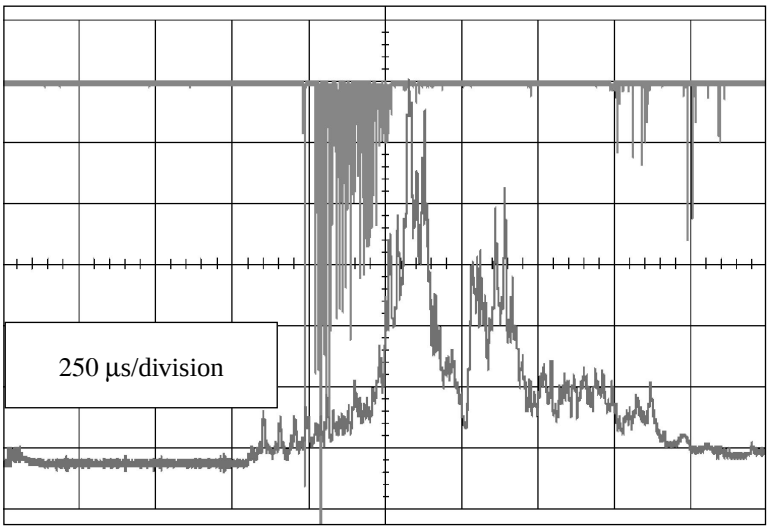

Fig. 4. Oscillograms of the plasma microwave radiation (the upper trace) and the Langmuir probe current characterizing the plasma density (the lower trace).

for the optimal initial gas pressure ($p_0 \simeq 10^{-4}$ torr) and a mirror ratio of $\sigma = 4$. We note that the curves corresponding to different frequency ranges are not calibrated relative one another and cannot thus be used to construct the emission spectrum. However, from Fig. 6, we can conclude that (i) the emission is concentrated in the frequency range $2 < f < 11$ GHz and (ii) the spectrum shifts toward higher frequencies with increasing magnetic field. In the shortest wavelength channel ($f >$ 11.8 GHz), no microwave signals were observed.

Similar results were obtained at a mirror ratio of $\sigma =$ 10; in this case, the electron gyrofrequency at the center of the trap was 10 GHz and no microwave emission was observed at frequencies above 8 GHz.

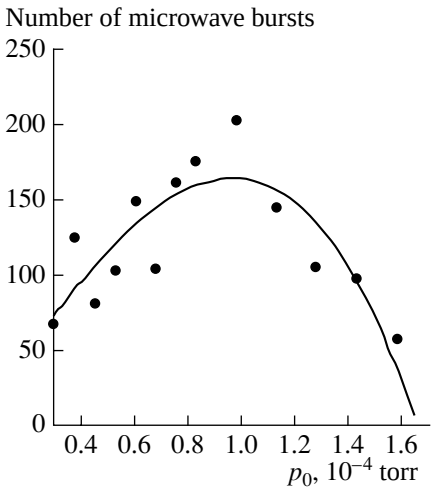

Fig. 5. Number of microwave bursts per gyrotron pulse as a function of the gas pressure in the chamber.

When the microwave receivers were oriented at a certain angle to the system axis, the amplitude of the microwave signals decreased, and no microwave emission was detected when the receivers were oriented across the trap. Hence, the observed microwave emission was generated nearly along the magnetic field and only at frequencies below f_{HL}.

3.2.4. Energy spectrum of the precipitated electrons. To obtain information on the energy spectrum of the precipitated electrons, we measured the energy distribution function of energetic electrons. For this pur-

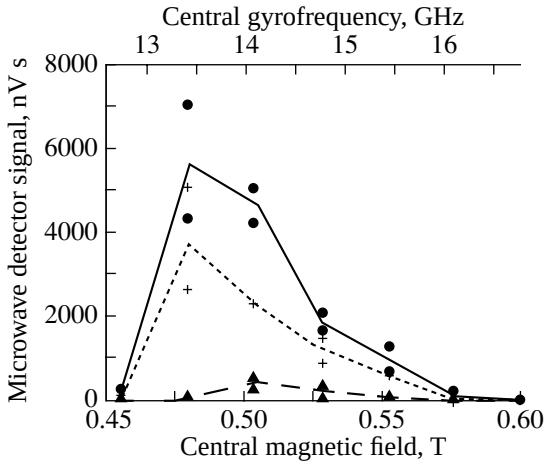

Fig. 6. Time-integrated (over a gyrotron pulse) intensity of plasma microwave radiation in different frequency ranges as a function of the magnetic field in the center of the trap. The crosses and the dotted line correspond to the frequency range $f > 2$ GHz, the circles and the solid line correspond to $f > 5.4$ GHz, and the triangles and the dashed line correspond to $f > 8.2$ GHz.

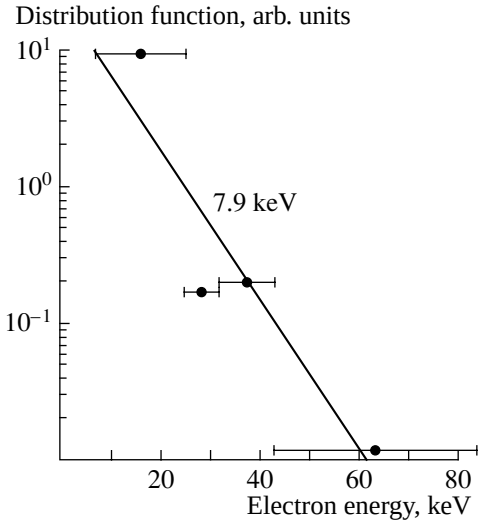

Fig. 7. Energy spectrum of the particles producing p-i-n diode signals (energetic electrons precipitated from the trap).

pose, a set of aluminum filters of different thickness was placed in front of the window of the p-i-n diode. We used 2-, 4-, 8-, and 30-μm-thick filters. The filter thickness determined the minimum energy the electron should have to pass through the filter. Taking into account the sensitivity of the p-i-n diode (7 keV), the minimum electron energies for these filters were found to be 25, 32, 43, and 84 keV, respectively.

The measured energy distribution function of energetic electrons is shown in Fig. 7. The straight line corresponds to a Maxwellian distribution with T_e = 7.9 keV. This agrees well with X-ray bremsstrahlung measurements of the temperature of energetic electrons [36]. These data also shows that the bulk energetic electrons have energies from 7 to 10 keV.

It should be noted that the p-i-n diode is sensitive not only to energetic electrons but also to X-ray photons with energies of up to 40 keV. We performed test experiments with a permanent magnet that was placed near the p-i-n diode and deflected the precipitated electrons. In this case, the diode signal was almost zero; this indicates that, in the absence of a magnet, the diode recorded only electrons.

4. DISCUSSION

The observed precipitation of energetic electrons from the trap and the generation of microwave bursts can naturally be related to the onset of CI of whistler-mode waves propagating at small angles to the magnetic field. The frequency of the excited waves is proportional to ω_{HL}; this explains why the emission spectrum shifts toward higher frequencies with increasing magnetic field. For the same reason, the spectrum shifts toward lower frequencies as the mirror ratio is increased, because this is done by decreasing the magnetic field in the center of the trap, whereas the field in the mirror region is changed only slightly.

4.1. Wave Amplification

Let us estimate the growth rate and gain factor of CI in the experiment under discussion by using available data on the parameters of the background and energetic electron components (Figs. 2, 7). Instead of approximate formula (1), we will use more exact expressions that allow us to obtain the gain factor as a function of frequency. We take into account that, for the above plasma parameters, we have $\beta_* \lesssim 0.2$. When $\beta_* < 1$, the whistler-mode growth rate is very sensitive to both the electron distribution anisotropy and the background plasma density. Since we do not know the exact values of the plasma parameters (we have no information on the electrons with energies below 2.5 keV and do not know the electron distribution over pitch angles), we will calculate the gain factor for different limiting values of the plasma parameters.

According to [5], in the case of $\beta_* \lesssim 1$ and a Maxwellian electron distribution over longitudinal velocities, the logarithmic single-pass amplitude gain of whistlers with $\mathbf{k} \parallel \mathbf{B}$ can be calculated by the formula

$$\Gamma(\omega) = \frac{\pi}{2^{3/2}} \frac{N_{cL}}{n_{hL}} \frac{a\omega_{pL}}{c} \frac{A-(A+1)\tilde{\omega}}{[\tilde{\omega}(1+\tilde{\omega}/2)]^{1/2}} \exp\left[-\frac{(1-\tilde{\omega})^3}{\tilde{\omega}\beta_*}\right]. \quad (5)$$

Here, $\tilde{\omega} \equiv \omega/\omega_{HL}$ and the dependence of the magnetic field on the longitudinal coordinate z is assumed to be parabolic: $B(z) = B_L(1 + z^2/a^2)$ (for the experiment under discussion, $a \simeq 7$ cm). The wavelength of the recorded radiation in plasma is $\lambda \sim 4$ mm; hence, we can use the geometric-optics approximation to estimate the gain factor.

The use of formula (5) is justified because the amplification of axially propagating whistlers depends primarily on the integral characteristics of the distribution function, such as the anisotropy index A and the characteristic energy, which (along with the total plasma density and the magnetic field) determines the parameter β_*. ECR heating in the resonance region ($B = B_{res}$) leads to diffusion over transverse velocities. Hence, the pitch angles of the particles that have gained a sufficiently large energy at the center of the trap are close to $\theta_L = \theta_{res} = \arcsin(\sigma_{res}^{-1/2})$, where $\sigma_{res} = B_{res}/B_L$. Due to nonresonant processes (in particular, collisional diffusion over pitch angles), electrons fall into the region $\theta_L > \theta_{res}$. The same processes lead to the isotropization of the electron distribution. At the same time, at smaller pitch angles, the energetic electrons interacting with a high-power gyrotron radiation fall into the loss cone and rapidly escape from the trap. Therefore, when estimating anisotropy, we will assume that ener-

getic electrons are absent at $\theta_L < \theta_{res}$ and that the distribution over pitch angles at $\theta_L > \theta_{res}$ is almost uniform. For such a distribution, the isotropy index is equal to $A = (\sigma_{res} + 0.5)/(\sigma_{res} - 1)$.

Figure 8 shows the results of calculations by formula (5). ECR heating at the fundamental harmonic ($\sigma_{res} = 2.67$) corresponds to $A = 0.9$. The densities of the cold and energetic components were chosen according to Fig. 2. For this distribution, the maximum gain factor $\Gamma_{max} \leq 5 \times 10^{-4}$ is attained at the frequency $\tilde{\omega}_{opt} \approx 0.4$ and the upper boundary frequency is $\tilde{\omega}_{max} = 0.47$. It is unlikely that whistler-mode waves can be excited in an actual plasma system at such a small gain, because this would require a reflection coefficient of $R > 0.999$. Even if the actual densities of the cold and hot plasma components were twice as large as the measured ones (taking into account possible experimental errors; see section 3.2), the situation would not alter radically.

Hence, in order for CI to develop, the pitch-angle anisotropy of the energetic electron component must be substantially larger than that of the electrons sloshing within the ECR regions. We assume that parasitic heating at the second harmonic of the electron gyrofrequency takes place in our experiment. The condition for the second-harmonic ECR is satisfied in the central region of the trap, into which a small fraction of gyrotron radiation can penetrate because of refraction at the plasma boundaries and reflection from the chamber wall. This radiation penetrates into the resonance region at large angles in the form of extraordinary waves (only these waves can propagate here because $\omega_{pe} \approx 3\omega_{He}$).

If the ECR heating of the energetic electrons in our experiment occurs predominantly at the second harmonic of the gyrofrequency, then we have $A \simeq 4$ ($\sigma_{res} \simeq 1.34$). In this case, the single-pass gain is about 5% (or even 12%, taking into account possible errors in measuring the electron density).

In the case of $A = 4$, we obtain the frequency dependence of the gain factor that is more consistent with our observations (in this case, we have $\tilde{\omega}_{opt} \simeq 0.65$–$0.7$ and $\tilde{\omega}_{max} = 0.8$, which, under our experimental conditions, corresponds to $f_{opt} \simeq 9.1$–9.8 GHz and $f_{max} \simeq 11.2$ GHz). In this case, the gain factor $\Gamma_{max} \sim 0.05$–0.12 is sufficient for the onset of instability at a reflection coefficient of $R > 0.88$–0.95 and a twofold increase in the densities of the background and energetic electron components substantially affects the conditions for the onset of instability.

Thus, the calculations of the gain of whistler-mode waves show that the CI of these waves in our experiment can be explained by the large anisotropy of the velocity distribution of energetic electrons, $A \simeq 4$, which corresponds to the heating of energetic electrons at the second harmonic of the gyrofrequency near the center of the trap. The CI growth rate averaged over the period of the wave propagation through the trap is $\gamma = \Gamma/T_g \approx 5 \times 10^7$ s^{-1}, where T_g is the period of oscillations of wave packets between the magnetic mirrors. This agrees in order of magnitude with the experimental results (for brevity, we do not describe here the measurements of the growth rate; the temporal characteristics of the observed instability will be discussed in more detail in a separate paper).

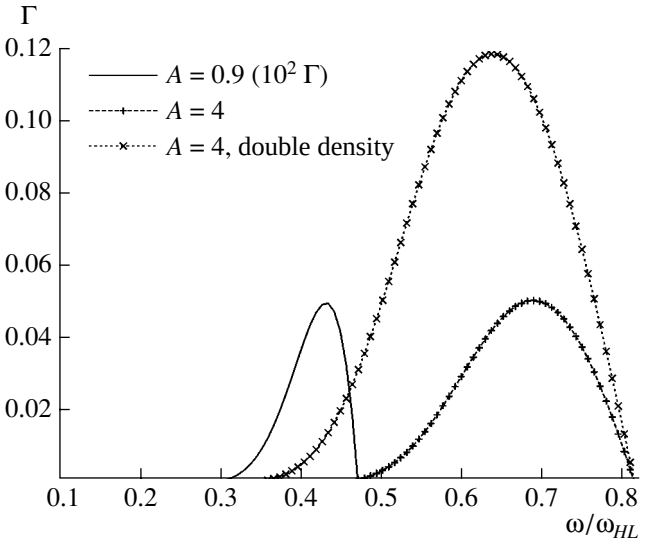

Fig. 8. Single-pass gain factor of whistler-mode waves for two values of the anisotropy index A of energetic electrons. For $A = 0.9$, Γ multiplied by a factor of 10^2 is shown. For $A = 4$, a curve is also shown that was obtained with allowance for possible errors in measuring the densities of the cold and energetic electrons.

4.2. Mechanism for the Onset of a Self-Oscillatory CI Mode

The above estimates show that the single-pass gain factor of whistler-mode waves in the trap is rather small, so the generation of waves requires their efficient reflection from the ends of the trap. This is also confirmed by the parameters of microwave signals: it can be seen from the oscillograms in Fig. 3 that the characteristic duration of microwave bursts is $\tau \gtrsim 50$ ns, whereas the oscillation period of wave packets between the mirrors is $T_g \sim 5$ ns.

The collisional damping of the generated waves in our experiment is of minor importance because $\nu_{coll} \sim 2 \times 10^5 \ll \gamma$. The plasma pressure is also low in comparison to the magnetic field pressure ($\beta = 8\pi NT/B_0^2 \sim 5 \times 10^{-3}$); this allows us to discard the self-modulation of precipitation due to the interaction of energetic electrons with flux tube oscillations. Hence, among mechanisms for the onset of a self-oscillatory CI mode that were listed in Section 2, only two mechanisms can operate under our experimental conditions: (i) the non-

linear modulation of the distribution function and the CI growth rate and (ii) nonlinear variations in the reflection coefficient of waves from the ends of the trap. Most likely, the latter mechanism does not operate in our experiment because the observed electron losses are not accompanied by a substantial decrease in the plasma density. For this reason, we believe that the observed self-oscillations are related to the modification of the distribution function during the development of CI [29]. In this case, pauses between pulses are determined by the time required to restore the free energy that is necessary for the onset of instability and that is lost during the pulse. The CI threshold in this case is associated with wave losses from the system. Note that the relaxation of the system to a subthreshold state and its return to an unstable state are not necessarily related to a change in the particle density in the trap but can occur when the particle distribution over pitch angles changes at relatively small density variations.

Such an interpretation does not contradict our observations; nevertheless, it calls for a more serious justification (both theoretical and experimental). In particular, a self-consistent model should take into account the specific features of the ECR source of energetic particles—the source itself has its origin in quasilinear diffusion under the action of gyrotron radiation; i.e., it does not supply particles with a specified distribution over pitch angles. Note that this diffusion is also responsible for the entrance of the particles into the loss cone and their escape from the trap. This process is especially efficient for electrons passing through the region of ECR at the fundamental harmonic of ω_H; i.e., it depends strongly on the particle pitch-angle distribution, which can change in the course of CI. Note that p-i-n diode signals corresponding to the precipitation of energetic electrons are almost absent (to within the detector noise) in the absence of plasma microwave emission. This indicates the low rate of quasilinear diffusion over pitch angles in pauses between pulses; i.e., the free-energy source is rather weak. As for the experiment, it is necessary to investigate the dependence of the temporal parameters of instability on the pumping power, which, apparently, determines the power of the source of energetic particles.

5. CONCLUSIONS

The CI dynamics has been studied experimentally in a straight magnetic trap filled with an ECR-heated microwave-discharge plasma. The observed quasi-periodic pulsed precipitation of energetic electrons from the trap is accompanied by microwave bursts at frequencies below the electron gyrofrequency in the center of the trap. The generated microwave radiation is found to propagate nearly parallel to the trap axis. These results can be explained by the onset of CI of whistler-mode waves. This is confirmed by calculations of the growth rate and gain factor of CI for the plasma parameters typical of our experiments. The most probable mechanism for the onset of the observed self-oscillations is similar to that for the generation of quasi-periodic (with periods of $T \sim 10^2$ s) radiation in the Earth's magnetosphere.

Our experimental results and their comparison to theory raise the hope that future experiments will provide a more detailed modeling of SCM phenomena that play an important role in the dynamics of geospace, planetary, and solar plasmas.

ACKNOWLEDGMENTS

This work was supported in part by the Russian Foundation for Basic Research (project nos. 02-02-17092 and 03-02-17100) and the Physical Science Department of the Russian Academy of Sciences under the Basic Research Program "Solar Wind: Generation and Interaction with the Earth and Other Planets." One of the authors (D.A. Mansfel'd) is grateful to the Dynasty Foundation for their financial support.

REFERENCES

1. A. A. Andronov and V. Yu. Trakhtengerts, Geomagn. Aéronom. **4**, 233 (1964).
2. C. F. Kennel and H. E. Petschek, J. Geophys. Res. **71**, 1 (1966).
3. V. Yu. Trakhtengerts, Geomagn. Aéronom. **3**, 442 (1963).
4. R. Z. Sagdeev and V. D. Shafranov, Zh. Éksp. Teor. Fiz. **39**, 181 (1960) [Sov. Phys. JETP **12**, 130 (1960)].
5. P. A. Bespalov and V. Yu. Trakhtengerts, *Alfvén Masers* (IPF AN SSSR, Gorki, 1986) [in Russian].
6. P. A. Bespalov and V. Yu. Trakhtengerts, in *Reviews of Plasma Physics*, Ed. by M. A. Leontovich (Atomizdat, Moscow, 1980; Consultants Bureau, New York, 1986), Vol. 10.
7. W. J. Burtis and R. A. Helliwell, Planet. Space Sci. **24**, 1007 (1976).
8. O. Santolik, D. A. Gurnett, J. S. Pickett, *et al.*, J. Geophys. Res. **108**, 1278 (2003).
9. V. Y. Trakhtengerts, Ann. Geophys. **17**, 95 (1999).
10. E. A. Benediktov, G. G. Germantsev, Yu. A. Sazonov, and A. F. Tarasov, Kosm. Issl. **3**, 614 (1965).
11. R. F. Benson and W. Calvert, Geophys. Res. Lett. **6**, 479 (1979).
12. V. V. Zaĭtsev, E. Ya. Zlotnik, and V. E. Shaposhnikov, Pis'ma Astron. Zh. **11**, 208 (1985) [Sov. Astron. Lett. **11**, 83 (1985)].
13. V. Y. Trakhtengerts and M. J. Rycroft, J. Atmos. Sol.–Terr. Phys. **62**, 1719 (2000).
14. A. G. Demekhov, V. Y. Trakhtengerts, M. M. Mogilevsky, and L. M. Zelenyi, Adv. Space Res. **32** (3), 355 (2003).
15. A. G. Demekhov and V. Yu. Trakhtengerts, Izv. Vyssh. Uchebn. Zaved., Radiofiz. **44**, 111 (2001).
16. V. Y. Trakhtengerts, A. G. Demekhov, and M. J. Rycroft, in *Strong Microwaves in Plasmas*, Ed. by A. G. Litvak

(Inst. of Applied Physics, Nizhni Novgorod, 3003), Vol. 2, p. 453.

17. V. Y. Trakhtengerts, M. J. Rycroft, D. Nunn, and A. G. Demekhov, J. Geophys. Res. **108**, 1138 (2003).
18. R. B. Horne and N. P. Meredith, J. Geophys. Res. **108**, 1016 (2003).
19. W. A. Perkins and W. L. Barr, in *Proceedings of the 2nd International Conference on Plasma Physics and Controlled Nuclear Fusion Research, Culham, 1965* (IAEA, Vienna, 1966), Vol. 2, p. 115.
20. J. Jacquinot, C. LeLoup, J. P. Poffe, *et al.*, in *Proceedings of the 3rd International Conference on Plasma Physics and Controlled Nuclear Fusion Research, Novosibirsk, 1968* (IAEA, Vienna, 1969), Vol. 2, p. 347.
21. V. V. Alikaev, V. M. Glagolev, and S. A. Morosov, IEEE Trans. Plasma Sci. **10**, 753 (1968).
22. H. Ikegami, H. Ikezi, M. Hosokawa, *et al.*, Phys. Fluids **11**, 1061 (1968).
23. W. B. Ard, R. A. Dandl, and R. F. Stetson, Phys. Fluids **9**, 1498 (1966).
24. R. C. Garner, M. E. Mauel, S. A. Hokin, *et al.*, Phys. Rev. Lett. **59**, 1821 (1987).
25. A. V. Gaponov-Grekhov, V. M. Glagolev, and V. Yu. Trakhtengerts, Zh. Éksp. Teor. Fiz. **80**, 2198 (1981) [Sov. Phys. JETP **53**, 1146 (1981)].
26. A. G. Demekhov and V. Yu. Trakhtengerts, Izv. Vyssh. Uchebn. Zaved., Radiofiz. **29**, 1117 (1986).
27. A. G. Demekhov and V. Y. Trakhtengerts, J. Geophys. Res. **99**, 5831 (1994).
28. D. L. Pasmanik, A. G. Demekhov, V. Y. Trakhtengerts, *et al.*, Ann. Geophys. **22**, 3561 (2004).
29. P. A. Bespalov, Pis'ma Zh. Éksp. Teor. Fiz. **33**, 192 (1981) [JETP Lett. **33**, 182 (1981)].
30. P. A. Bespalov, Zh. Éksp. Teor. Fiz. **87**, 1894 (1984) [Sov. Phys. JETP **60**, 1090 (1984)].
31. P. P. Belyaev, S. V. Polyakov, V. O. Rapoport, and V. Yu. Trakhtengerts, Geomagn. Aéron. **27**, 652 (1987).
32. A. G. Demekhov, S. V. Isaev, and V. Y. Trakhtengerts, in *Proceedings of the 25th Apatity Seminar on Physics of Auroral Phenomena, Apatity, 2002*, p. 69.
33. F. V. Coroniti and C. F. Kennel, J. Geophys. Res. **75**, 1279 (1970).
34. P. A. Bespalov, Fiz. Plazmy **4**, 177 (1978) [Sov. J. Plasma Phys. **4**, 103 (1978)].
35. V. Yu. Trakhtengerts, Izv. Vyssh. Uchebn. Zaved., Radiofiz. **39**, 699 (1996).
36. A. V. Vodop'yanov, S. V. Golubev, V. G. Zorin, *et al.*, Pis'ma Zh. Tekh. Fiz. **25** (14), 90 (1999) [Tech. Phys. Lett. **25**, 588 (1999)].

Translated by N.F. Larionova

Plasma Physics Reports, Vol. 31, No. 11, 2005, pp. 938–952. Translated from Fizika Plazmy, Vol. 31, No. 11, 2005, pp. 1009–1025.

PLASMA ELECTRONICS

Experimental and Theoretical Investigations of Stochastic Oscillatory Phenomena in a Nonrelativistic Electron Beam with a Virtual Cathode

Yu. A. Kalinin, A. A. Koronovskiĭ, A. E. Khramov, E. N. Egorov, and R. A. Filatov

Chernyshevsky Saratov State University, Astrakhanskaya ul. 83, Saratov, 410026 Russia

Received December 23, 2004; in final form, February 24, 2005

Abstract—Results are presented from experimental investigations of oscillatory phenomena in an electron beam with a virtual cathode in a diode gap with a decelerating field. Experiments have revealed a stochastic broadband generation of the microwave oscillations of a virtual cathode in a decelerating field. Numerical simulations based on a simple one-dimensional model have shown that the onset of the stochastic generation and the broadening of the oscillation spectrum with increasing beam deceleration rate are governed by the processes of regrouping of the electrons in a beam with a virtual cathode. © *2005 Pleiades Publishing, Inc.*

1. INTRODUCTION

A new class of devices of high-power microwave electronics—one in which an electron beam with a virtual cathode (VC) is used as an active medium—was proposed in the late 1970s and early 1980s [1–4] and is still a subject of active research [5–8]. Even the first experiments and numerical simulations revealed the complicated unsteady dynamics of radiation from vircators, i.e., microwave oscillators with a VC [9–13]. Quite a number of theoretical and experimental papers were devoted to studying the stochastic generation of radiation in vircators [5–7, 13–17], the processes responsible for the onset of coherent spatiotemporal structures in an electron beam with a VC and for their interaction [16, 18–21], and the mutual synchronization of VC-based devices [6, 22–25]. In particular, by applying different methods for separating out coherent structures, it was shown theoretically [18–20, 26] that the complication of the spectral composition of radiation from a vircator is closely related to the formation of electron structures in a beam with an overcritical current. However, no detailed experimental investigations of the stochastic generation of radiation in VC-based systems, as well as of the physical mechanisms governing the complicated behavior of an electron beam with a VC, were carried out, largely because of the difficulties in diagnosing relativistic electron beams (REBs).

One of the simplest systems for studying the formation of a VC and its unsteady stochastic oscillations is a Pierce diode [17, 27–29]—a system of two infinitely wide parallel equipotential grids penetrated by an electron beam with an overcritical current. A system like this, in which the electron motion is thought of as being one-dimensional, can be regarded as a model of the drift space and can also serve to investigate the nonlinear dynamics of the processes in such high-power electronic devices as vircators [29]. In recent years, a model of this type has also attracted attention as one of the simplest models of a distributed self-oscillating electron–plasma system for studying stochastic oscillations [17, 26, 29–31].

Note that experimental investigation and practical development of VC-based oscillators is a rather difficult task because of the necessity of using intense REBs with overcritical currents, i.e., with currents above the limiting vacuum current [32]. This is why a detailed study of the parameters of the generation of radiation in vircators, as well as of the physical processes occurring in an electron beam with a VC, is impossible. The conditions of experiments on microwave generation by a VC can be "relaxed," e.g., by using systems with additional electron deceleration; in this case, an unsteady VC forms at comparatively low beam currents in a decelerating field with a strength above a certain critical value.

In this context, it is of great interest to investigate a modified Pierce diode in the form of a drift gap in which an unsteady oscillating VC forms at the expense of strong beam deceleration (an electron beam with an overcritical perveance). In such a system, a VC can form and a stochastic broadband signal can be generated at low electron beam currents and densities, which makes possible a detailed experimental study of the physical processes occurring in a beam with a VC with the help of experimental methods used in microwave electronics [33]. Note that this type of system with a decelerated electron beam has not yet been studied theoretically or experimentally.

The objective of the present paper is to experimentally investigate the oscillatory phenomena in a nonrelativistic electron beam formed by an electron optical system in a diode gap with a decelerating potential and

1063-780X/05/3111-0938$26.00 © 2005 Pleiades Publishing, Inc.

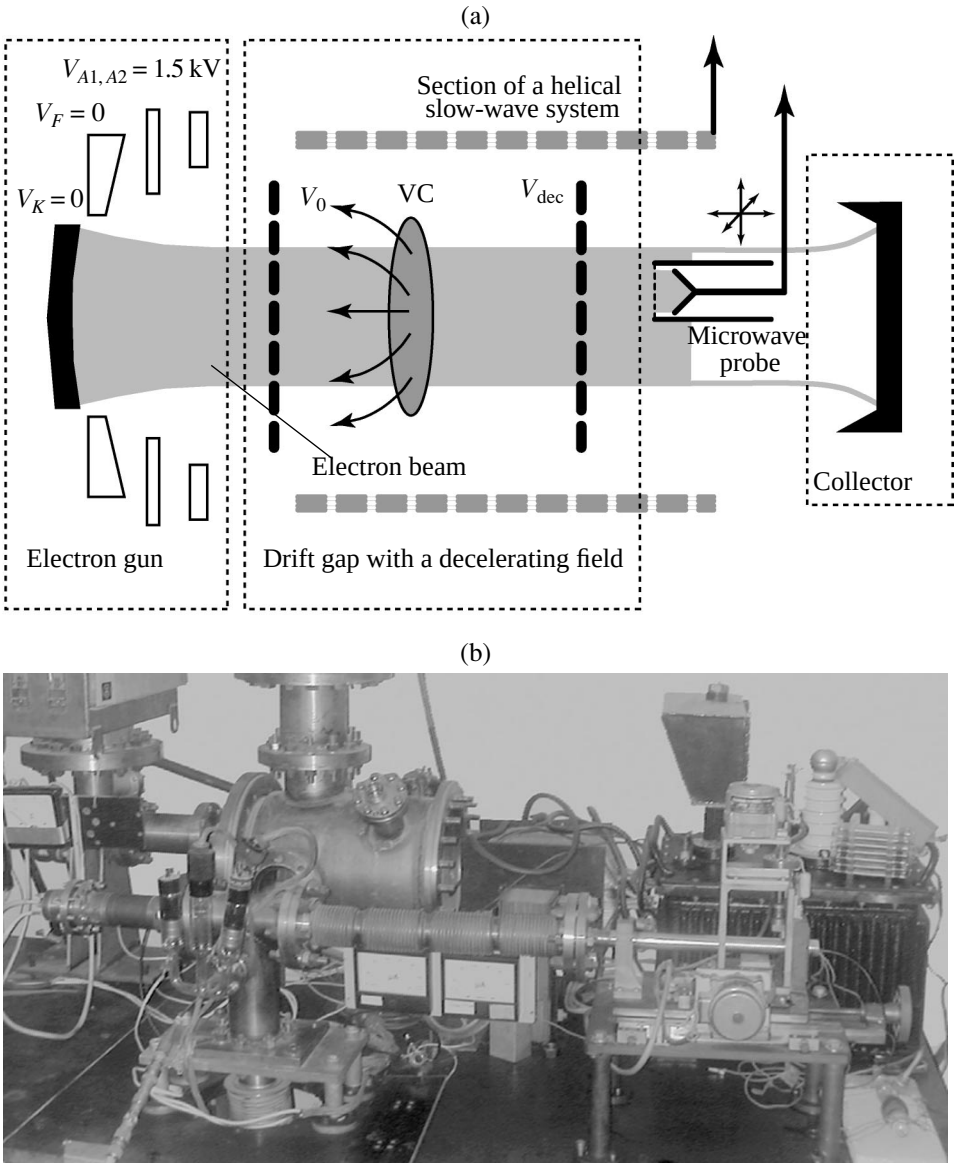

Fig. 1. (a) Schematic and (b) external view of the experimental device for investigating stochastic oscillations in an electron beam with a VC in a system with an overcritical perveance.

to analyze the behavior of an electron beam in a drift gap with a decelerating field by means of numerical simulations.

2. EXPERIMENTAL TECHNIQUES

As an object for experimental investigations of oscillations in an electron beam with a VC, we chose a diode scheme in which a beam formed by an electron optical system (EOS) was injected into a diode consisting of two grid electrodes (Pierce diode) with a decelerating field (a schematic of the experimental setup is shown in Fig. 1a). The decelerating field was produced by applying a negative (with respect to the first (entrance) grid) potential V_{dec} to the second (exit) grid.

The electron source was a hot cathode whose current was limited by the space charge. The EOS formed an axisymmetric cylindrical converging electron beam in the drift space, which was surrounded by a solenoid creating a guiding longitudinal magnetic field. The magnetic field was varied from 0 to 250 G; the voltage used to accelerate an electron beam was equal to 1.5 kV; and the beam current at the exit from the EOS was varied over a range of 50–100 mA, depending on the cathode heating voltage and on the accelerating potential. The spread in electron velocities at the exit from the EOS was very small (less than 0.2%), so the electron beam could be considered monoenergetic.

The electron beam formed by the EOS entered the region between the grids (the diode gap). The potential

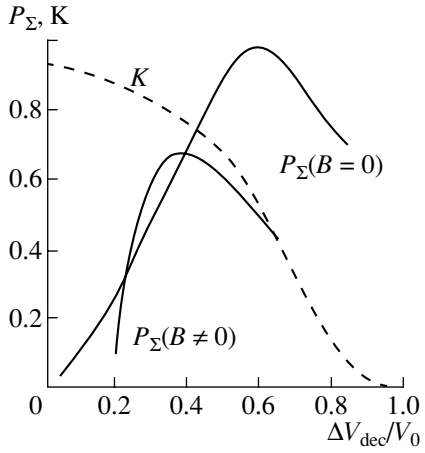

Fig. 2. Global interaction power P_Σ (for different magnetic field strengths) and the coefficient K of current transmission through the diode (at a magnetic field strength of $B = 220$ G) as functions of the normalized potential difference $\Delta V_{dec}/V_0$ between the grids.

V_0 of the first grid was equal to the anode potential V_A (the accelerating voltage), and the potential of the second grid, $V_{dec} = V_0 - \Delta V_{dec}$, was varied from values such that $V_{dec}/V_0 = 1$ ($\Delta V_{dec} = 0$, the electron beam was not decelerated at all) to $V_{dec}/V_0 = 0$ ($\Delta V_{dec} = V_0$, the electron beam was decelerated to a complete stop). The quantity ΔV_{dec} has the meaning of the potential difference between the grids: it produces the decelerating field in the diode gap. Note that the operating regime with a zero decelerating potential, $\Delta V_{dec} = 0$, corresponds to that of a "classical" vircator, and the operating regime with $\Delta V_{dec}/V_0 = 1$ is that of a reflex triode [6, 34].

An increase in the decelerating potential of the second grid can be considered as an increase in the perveance of the electron beam in the diode gap:

$$p = I/\bar{V}^{3/2}, \quad (1)$$

where $\bar{V} = (V_0 + V_{dec})/2$ is the effective potential.

As the decelerating potential difference ΔV_{dec} between the grids of the diode gap was increased, a VC was observed to form in the system at a certain critical value of the beam perveance, $p = p_{cr}$. The electron beam was modulated by the temporal and spatial oscillations of the VC; moreover, some of the electrons were reflected from the VC back toward the entrance grid. As a result, the VC was observed to execute stochastic oscillations, whose shape and power depended substantially on the potential difference ΔV_{dec} between the grids of the diode gap.

The noisy oscillations in an electron beam were analyzed using a broadband section of a helical slow-wave system (HSS) loaded on an absorbing insertion and on an energy extraction unit, and also using a section of a broadband coaxial line loaded on a resistance—an RF probe that could be moved in three mutually perpendicular directions [33]. The coaxial probe was equipped with a decelerating grid in order to analyze the distribution of charged particles over longitudinal velocities. Within the diode gap, a velocity- and density-modulated electron beam excited the broadband section of the HSS, the signals from which were processed by an SCh-60 spectrum analyzer. This made it possible to determine the spectral power density of the noisy oscillations generated by an electron beam with a VC.

Experimental investigations were carried out using a sectional vacuum device with continuous pumping-out (the minimum residual gas pressure being about 10^{-6}–10^{-7} torr). A photograph of the experimental device is presented in Fig. 1b.

3. EXPERIMENTAL RESULTS

Oscillations in the system under examination are governed by the presence of a VC in the diode gap with a decelerating field. This is why it is very important to study how the processes occurring in an electron beam with a VC depend on the decelerating potential of the second grid. The generation processes in a system with a VC are also highly sensitive to the strength of the external focusing magnetic field, [35, 36] (this question, too, will be discussed in the present section).

Figure 2 shows the normalized global oscillation power as a function of the normalized potential difference $\Delta V_{dec}/V_0$ between the grids in the presence and in the absence of a magnetic field ($B = 220$ and 0 G, respectively). We can see that there is an optimum value of the decelerating potential at which the global power P_Σ of oscillations in a beam with a VC is maximum. Analyzing Fig. 2, we also note that the oscillation power depends strongly on the external focusing magnetic field. The power of the oscillations generated by the VC in the absence of a magnetic field ($B = 0$) is substantially higher and is maximum at a decelerating potential of $\Delta V_{dec}/V_0 \sim 0.5$. In the presence of the focusing magnetic field, the global power of the oscillations generated by the VC is lower. The stronger the magnetic field, the lower the potential difference ΔV_{dec} between the grids at which the global oscillation power in the beam is maximum.

Figure 2 also shows the coefficient K of current transmission through the diode gap as a function of the potential difference between the grids in the presence of the external magnetic field ($B = 220$ G). The current transmission coefficient is defined as the ratio of the current that has passed through the second grid, I_{out}, to the current I_0 of the beam formed by the electron gun: $K = I_{out}/I_0$. It can be seen that, in contrast to the global oscillation power P_Σ, the current transmission coefficient K decreases as the decelerating potential increases. This indicates that an increase in the decelerating potential difference ΔV_{dec} is accompanied by an increase in the number of electrons reflected from the

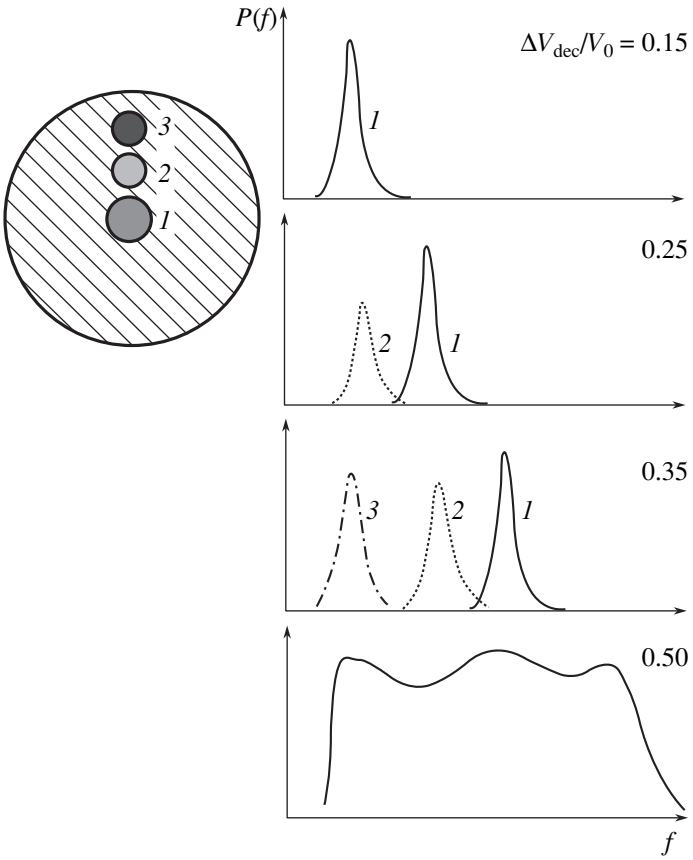

Fig. 3. Qualitative shapes of the spectra of the beam current oscillations recorded by an RF probe at different radial positions within the beam (shown schematically on the left) for different values of the decelerating potential difference.

VC (or from the diode region behind the VC) back toward the entrance grid.[1] At a certain, sufficiently high, potential difference ΔV_{dec} between the grids (whose magnitude depends weakly the strength of the external focusing magnetic field), almost all of the beam electrons are seen to be reflected from the VC, so the current transmission coefficient becomes nearly zero, $K \approx 0$. This is the case only when the additional electron deceleration is sufficiently strong, i.e., when the decelerating potential difference is comparable to the accelerating voltage, $\Delta V_{dec}/V_0 \approx 1$. In this case, almost all of the beam electrons that have passed through the potential barrier of an unsteady VC are turned by the high decelerating potential V_{dec} at the second grid back to the injection plane, so the current transmission coefficient becomes rather small, $K \approx 0$. As the decelerating potential difference increases, the VC tends to be displaced toward the injection plane.

Let us now consider how the generation process in an electron beam in the diode gap develops when the decelerating potential difference (i.e., the perveance p of the beam in the space between the grids) is increased. To do this, we analyze the spectra of the high-frequency current oscillations recorded by an RF probe at different radii r_b within the beam at several values of the decelerating potential difference, each next being larger than the previous one. The results of the analysis of the development of the generation process are illustrated in Fig. 3, where we schematically show the radial positions within the beam at which high-frequency current oscillations were recorded and for which the power spectra were obtained with the help of the spectrum analyzer. An analysis of the results presented in Fig. 3 allows us to draw the following conclusions.

At small values of the decelerating potential difference between the grids in the diode gap, i.e., when the perveance p of the electron beam is lower than a critical value p_{cr}, no beam oscillations were recorded. As the decelerating potential difference (i.e., the ratio $\Delta V_{dec}/V_0$) increases, the beam perveance reaches a certain critical value p_{cr} at which a VC forms in the system. The VC begins to reflect some electrons back toward the first grid of the diode, so the coefficient K of the transmission of the electron beam through the diode gap begins to decrease. The most important effect here is that the high-frequency current oscillations are recorded only at the center of the beam (see Fig. 3,

[1] Recall that an increase in the decelerating potential ΔV_{dec} corresponds to a decrease in the potential V_{dec} of the second grid, so the electron beam is decelerated to a complete stop at $V_{dec} = 0$.

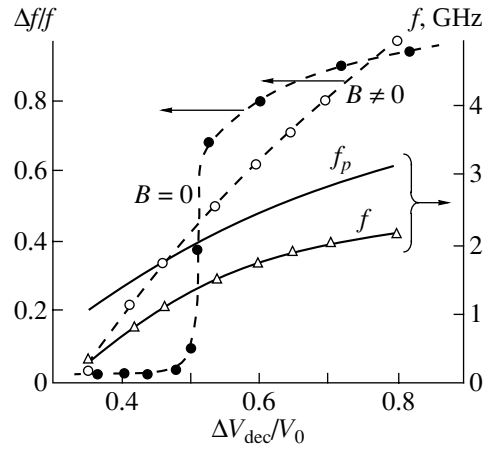

Fig. 4. Characteristic frequency and bandwidth of stochastic oscillations in a beam with a VC as functions of the potential difference $\Delta V_{dec}/V_0$ between the grids. Theoretical dependence (2) of the plasma frequency f_p of the electron beam in the space between the grids of the diode gap is also shown.

point *1* and curve *1*, which refer to the case $\Delta V_{dec}/V_0 = 0.15$). At larger radii in the beam cross section, no high-frequency current oscillations were observed; consequently, at a low deceleration rate, i.e., for a low beam perveance, $p \gtrsim p_{cr}$), a VC first arises at the center of the electron beam. As the beam deceleration rate becomes faster, the frequency of oscillations of the beam current at the beam center increases (cf. the positions of curve *1* for $\Delta V_{dec}/V_0 = 0.15$ and 0.25 in Fig. 3) and the beam current begins to oscillate at larger beam radii. An analysis of the power spectra for $\Delta V_{dec}/V_0 = 0.25$ and 0.35 shows that, as the beam deceleration rate increases, the beam current begins to oscillate first at radial position *2* and then at radial position *3* in the cross section of the electron beam. In this case, the high-frequency current oscillations at the periphery of the beam (i.e., in the beam's external layers) become more intense as the decelerating potential ΔV_{dec} (and, consequently, the electron beam perveance) increases. This indicates that, within the diode gap, the VC is distributed in both space (in the transverse direction) and time. As the decelerating potential increases, an unsteady electron-reflecting VC forms first at the center of the electron beam and then begins to expand radially. Following [8, 37], this can be interpreted as the formation of a VC in an electron beam that has the shape of a cup in the radial direction and is convex toward the injection plane. In terms of this radial structure of the VC, it is possible to explain why the oscillation frequency is different at different beam radii. Specifically, the larger the radius, the greater the longitudinal dimension of the potential well in the electron beam and, consequently, the lower the frequency of oscillations of the VC.

A further increase in the electron deceleration rate was accompanied by the onset of broadband noisy oscillations whose spectrum was found to be essentially the same at different radial positions (i.e., over the entire beam cross section). A representative spectrum of the beam current oscillations for $\Delta V_{dec}/V_0 = 0.5$ is illustrated qualitatively in Fig. 3. In this case, the electrons in the beam execute oscillations over its entire cross section. After being reflected by the VC, the electrons can occur at arbitrary radii of the beam, giving rise to developed stochastic oscillations. A fundamentally important point here is that a description of this operating regime requires at least a two-dimensional theory of the dynamics of an electron beam in the VC region.

In view of such complications in the oscillation spectrum of a beam with a VC as the electron deceleration rate (i.e., the perveance of the beam in the diode gap) is increased, it is necessary to consider the parameters of these spectra in more detail. Figure 4 shows the normalized frequency bandwidths $\Delta f/f$ of the generated oscillations that were measured from the oscillation power spectra recorded by a portion of a helix in the VC region at different strengths of the external magnetic field. Figure 4 also shows the characteristic generation frequency (i.e., the frequency at which the power in the spectrum is generated most intensely) in the system as a function of the decelerating potential difference $\Delta V_{dec}/V_0$. The frequency bandwidth Δf was determined at a level of 3 dB in the oscillation power spectrum.

From Fig. 4 it follows that the characteristic generation frequency in a VC-based system increases monotonically with increasing decelerating potential difference $\Delta V_{dec}/V_0$ (or equivalently beam perveance). In [38, 39], it was shown theoretically that the characteristic frequency of oscillations of the VC is proportional to the plasma frequency of the electron beam, $f_{VC} \propto f_p$. In addition, Fig. 4 shows the theoretical dependence of the reduced plasma frequency f_p of an electron beam on the potential difference between the grids of the diode gap:

$$f_p^2 = \frac{2^{3/2}\pi\sqrt{\eta}}{\varepsilon_0}\frac{p\bar{V}}{r^2}, \qquad (2)$$

where p and r are the perveance of the electron beam and its radius, $\bar{V} = (V_0 + V_{dec})/2$, $\eta = \frac{e}{m_e}$ is the electron charge-to-mass ratio, and ε_0 is the dielectric constant. A comparison between the characteristic generation frequencies shows that the frequency of oscillations of the VC is related to the plasma frequency by

$$f_{VC} = k f_p, \qquad (3)$$

where $k \approx 0.5$ is a numerical factor. Note that, in [13, 38], when investigating the dependence of the frequency of oscillations of a VC on the plasma frequency in systems without additional electron deceleration, the numerical factor was found to be equal to $k \approx 2$. It can be suggested that the discrepancy between the values of the numerical factors k that were obtained empirically

in the experiment and were found in [13, 38] can be attributed to the additional deceleration of the electron beam. Note also that, according to formula (2), the dependence of the frequency f_{VC} on the decelerating potential is described by the relationship $f_{VC} \propto p\sqrt{\bar{V}}$, which agrees well with experiment.

The normalized frequency bandwidth $\Delta f/f$ of the oscillations generated in a beam with a VC also increases as decelerating potential difference in the diode gap increases. However, the dependence $\Delta f/f(V_{dec})$ at a strong focusing magnetic field (B = 220 G) differs from that in the absence of a magnetic field ($B = 0$). In the first case, the generation frequency bandwidth increases monotonically with the decelerating potential difference ΔV_{dec}. When the magnetic field is absent, the generation frequency bandwidth increases in a jumplike manner at $\Delta V_{dec}/V_0 \approx 0.3$. A further increase in the decelerating potential of the second grid of the diode gap (i.e., in the perveance of the electron beam) is accompanied by a monotonic increase in the frequency bandwidth $\Delta f/f$.

Hence, we can speak of two characteristic operating regimes of the electron–wave VC-based oscillator under consideration: the regime of the generation of nearly regular narrowband oscillations, which occurs when the beam perveance is slightly above the critical value (i.e., when the deceleration rate of the beam in the diode gap is slow), and the regime of the generation of stochastic oscillations with a broadband spectrum, which occurs when the electron beam perveance is high (i.e., when the beam deceleration is strong).

An important property of the VC-based oscillator under consideration is its ability to generate microwave radiation in the absence of an external magnetic field. The operating regime without a magnetic field is characterized by the generation of a stochastic broadband signal with a slightly irregular spectrum within the electron beam. This circumstance can be very useful in creating sources of broadband noisy signals with more than an octave bandwidth. Therefore, it is important to analyze how the global power of oscillations in an electron beam with a VC depends on the strength of the external magnetic field. The above experimental results (see Fig. 2) show that the maximum global oscillation power increases with decreasing magnetic field.

Figure 5 shows the normalized global power P_Σ of oscillations in a beam with a VC as a function of the magnetic field in the regimes of the narrowband generation (the normalized decelerating potential of the second grid is equal to $\Delta V_{dec}/V_0 = 0.2$) and of the stochastic broadband generation (for $\Delta V_{dec}/V_0 = 0.5$). We can see that, in the regime of the weakly stochastic narrowband generation, the global oscillation power P_Σ is maximum at a certain magnetic field strength, whereas, in the broadband generation regime, the power P_Σ is maximum in the absence of a magnetic field ($B = 0$).

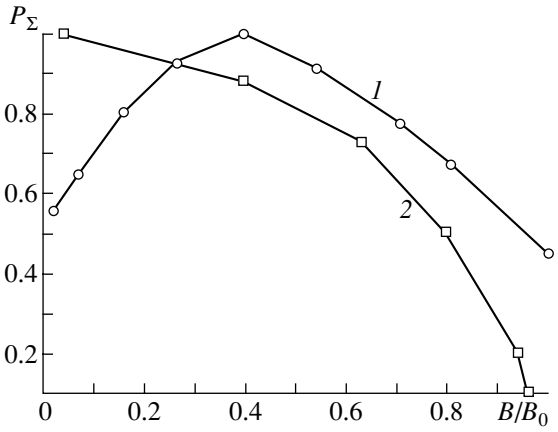

Fig. 5. Global powers of (*1*) narrowband and (*2*) broadband oscillations in an electron beam as functions of the external magnetic field (B_0 = 250 G).

Let us now consider distinctive features of the physical processes in an electron beam with a VC. An important characteristic that makes it possible to analyze the state of the beam in the VC region and which can be obtained experimentally is the velocity distribution of the beam electrons that have passed through the VC and have reached the second grid.

Figure 6 presents the velocity distribution functions of the electrons behind the second grid for different values of $\Delta V_{dec}/V_0$. The distributions were recorded by an RF probe placed at the exit from the drift space. Figure 7 displays the mean electron velocities v_{mean} and the normalized velocity spread $\Delta v/v_{mean}$ calculated for several values of the potential difference $\Delta V_{dec}/V_0$ from the experimentally measured electron velocity distribution functions. We can see that the shape of the electron distribution function changes radically as the oscillations of the VC grow with increasing deceleration rate of the electron beam in the diode gap. The most important effects here are the broadening of the velocity distribution function $\Delta v/v_{mean}$ and the increase in its irregularity as the beam deceleration rate increases and, consequently, the stochastic oscillations in a beam with a VC become more complicated. Such behavior of the electron velocity distribution with increasing beam perveance can be attributed to the formation of several electron structures (bunches) in the VC region [16]. For instance, when the beam deceleration rate is slow, i.e., when the oscillations in the system are nearly regular, the electron distribution function is close to a δ function. This indicates that the only structure that forms in the system is a VC. As the beam deceleration rate increases, the electron velocity distribution becomes rather complicated (acquires a multipeak structure); this points to the regrouping of electrons and, consequently, the formation of electron structures (bunches) in the VC region.

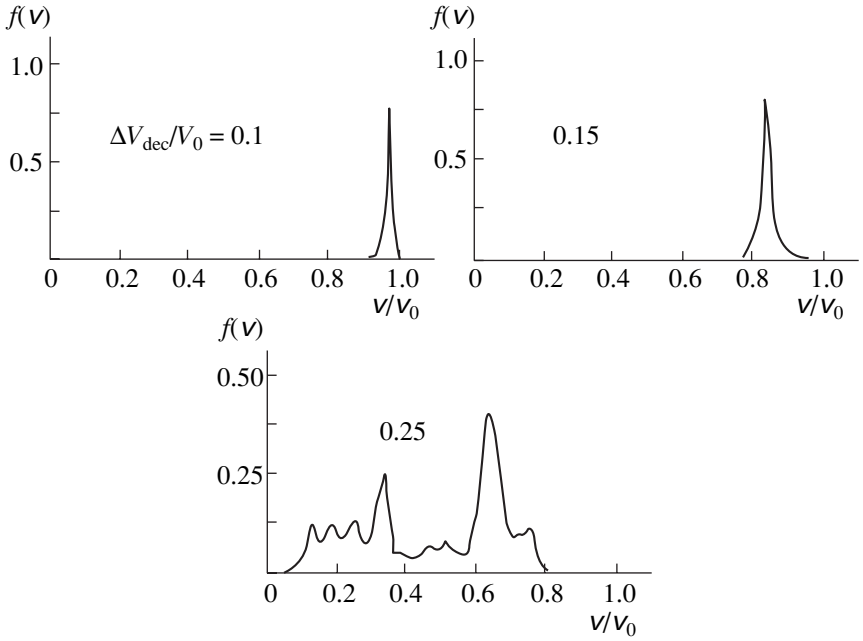

Fig. 6. Electron velocity distribution function at the exit from the second grid for different values of the decelerating potential $\Delta V_{dec}/V_0$.

Finally, we consider the experimentally measured parameters of microwave generation by an electron beam with a VC when there are positively charged ions in the drift space. The presence of positive ions (which corresponds to a higher pressure of the residual gas), on the one hand, decreases the electron density and partially neutralizes the space charge of the electron beam, thereby preventing the formation of a VC [29], and, on the other hand, gives rise to additional ion oscillations (such as relaxation, plasma, and radial oscillations) [40]. This, according to the experiment, makes the power spectra of the noisy oscillations in such beams more regular. Figure 8 shows how the modulation depth N (defined as $N = P_{max}/P_{min}$, where P_{max} and P_{min} are the maximum and minimum spectral powers in the working frequency band) of the oscillation spectrum of an electron beam with a VC depends on the pressure of the residual gases in the interaction space of the oscillator. The potential of the second grid was equal to $\Delta V_{dec}/V_0 = 0.5$. It is clear from Fig. 8 that, at a pressure of $P \sim 5 \times 10^{-7}$ torr, the modulation depth is about 7–8 dB, whereas at a pressure of $P \sim 10^{-5}$ torr, it is about 3 dB. We thus can see that an increase in the pressure of the residual gases in the drift space of an electron–wave VC-based oscillator leads to an improvement in the spectral parameters of the noisy broadband generation: the continuous spectrum of the generated noisy broadband radiation becomes more regular and, accordingly, more uniform.

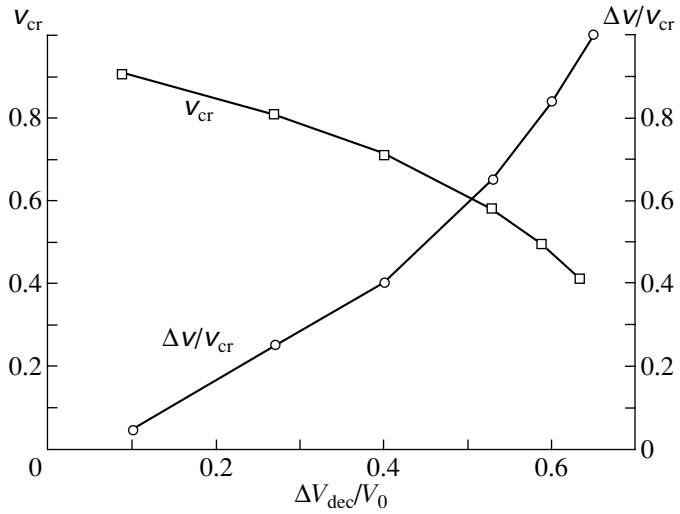

Fig. 7. Mean velocity v_{mean} of the electrons that have passed through the second grid and the spread in its values, $\Delta v/v$, for different values of the decelerating potential difference $\Delta V_{dec}/V_0$ between the grids of the diode gap.

4. NUMERICAL SIMULATIONS OF THE OSCILLATIONS OF A VIRTUAL CATHODE IN A PIERCE DIODE WITH A DECELERATING FIELD

Here, we consider the results from numerical simulations of unsteady processes by means of a simple model of an electron beam with a VC. We also compare the theoretical and experimental results on the oscillations of the VC.

The unsteady nonlinear processes occurring in a charged particle beam with a VC were simulated in terms of a one-dimensional model of a drift gap with a decelerating field by the particle-in-cell (PIC) method [41, 42]. Of course, the assumption of one-dimensional motion of the electron beam is not valid for all operating regimes of the experimental electron–wave VC-based oscillator under consideration. It might be supposed, however, that the main physical mechanisms for the formation of a VC in a diode gap with a decelerating field in the one-dimensional case would be qualitatively similar to those in a more complicated case of two-dimensional motion of an electron beam with a VC.

Let us briefly outline the scheme for numerical simulations. In plane geometry, the electron beam is modeled as a system of macroparticles (charged plane sheets) injected into the interaction space with a constant velocity at equal time intervals. We switch from the dimensional parameters, namely, the potential φ, the space charge field E, the electron density ρ, the electron velocity v, the spatial coordinate x, and the time t, to the following dimensionless variables, which are marked by a prime:

$$\varphi = (v_0^2/\eta)\varphi', \quad E = (v_0^2/L\eta)E', \quad \rho = \rho_0\rho', \quad v = v_0 v', \quad x = Lx', \quad t = (L/v_0)t', \tag{4}$$

where $\eta = e/m_e$, v_0 and ρ_0 are the static (unperturbed) electron beam velocity and electron density, and L is the length of the drift gap. In what follows, the primes by the dimensionless variables will be omitted.

For each of the charged sheets (macroparticles), we solve the dimensionless nonrelativistic equations of motion

$$\frac{d^2x_i}{dt^2} = -E(x_i), \tag{5}$$

where x_i is the coordinate of the ith sheet and $E(x_i)$ is the space charge field at the point with the coordinate x_i.

In order to calculate the strength of the space charge field and its potential and also the charge density, we introduce a uniform spatial mesh with a spacing Δx. In the quasistatic approximation, the potential of the space charge field is determined from the one-dimensional Poisson's equation

$$\frac{\partial^2\varphi}{\partial x^2} = \alpha^2\rho(x), \tag{6}$$

where $\alpha = \omega_p L/v_0$ is the so-called Pierce parameter [27]. In Eq. (6), the density of the positive ion background is assumed to be low enough to be ignored in simulating the oscillatory processes in an electron beam. The space charge field E is calculated by numerically integrating the values of the potential that have been obtained from Poisson's equation.

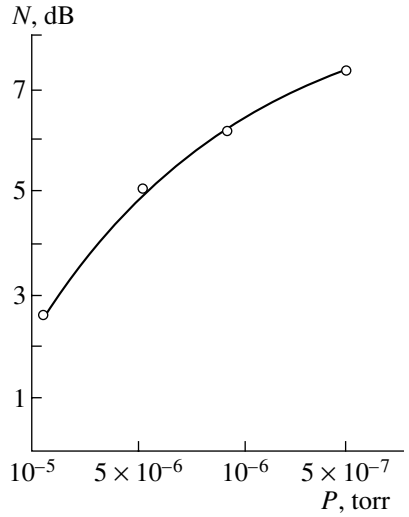

Fig. 8. Dependence of the modulation depth N of the oscillation spectrum on the residual gas pressure in the diode gap.

Poisson's equation (6) is supplemented with the boundary conditions

$$\varphi(x = 0) = \varphi_0, \quad \varphi(x = 1) = \varphi_0 - \Delta\varphi, \tag{7}$$

where φ_0 is the accelerating potential (in the dimensionless units used here, it is equal to $\varphi_0 = 1$) and $\Delta\varphi$ is the decelerating potential difference between the grids.

The space charge density is calculated using the PIC method, i.e., by linearly weighing the contributions of macroparticles (charged sheets) to its mesh values—a technique that reduces the noise introduced in computations by the mesh [42]. In this method, the space charge density in the jth mesh point, i.e., at the point with the coordinate $x_j = j\Delta x$, is expressed as

$$\rho(x_j) = \frac{1}{n_0}\sum_{i=1}^{N}\Theta(x_i - x_j). \tag{8}$$

Here, x_i is the coordinate of the ith macroparticle; N is the total number of macroparticles; the parameter n_0 of the computational scheme is equal to the number of macroparticles in a cell in an unperturbed state; and

$$\Theta(x) = \begin{cases} 1 - |x|/\Delta x, & |x| < \Delta x, \\ 0, & |x| > \Delta x \end{cases} \tag{9}$$

is a piecewise-linear form function, which determines the procedure of weighting the contribution of a macroparticle on a spatial mesh with the spacing Δx.

The macroparticles that have reached the exit grid, as well as those that have been reflected from the VC and have reached the first (entrance) grid, are absorbed at the boundaries. This, in fact, corresponds to the reditron model of a VC-based oscillator [6, 43]. It should be noted, however, that the use of the reditron model in

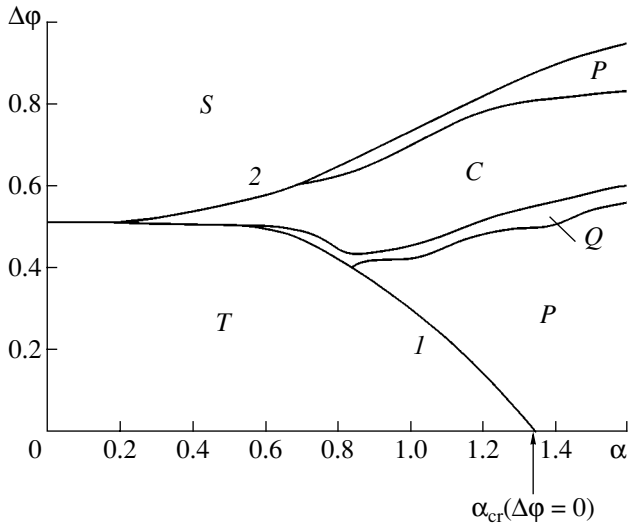

Fig. 9. Characteristic regimes of the behavior of an electron beam inside a diode gap with a decelerating field in the "Pierce parameter–decelerating potential difference" plane: (*C*) stochastic oscillations in a beam with a VC, (*Q*) quasi-periodic (two-frequency) oscillations of the VC, (*P*) periodic oscillations of the VC, (*S*) steady VC, and (*T*) total transmission of the electron beam through the diode gap. The arrow shows the parameter value $\alpha_{cr} = 4/3$ at which an unsteady VC forms in a system without a decelerating field, curve *1* is the boundary at which the steady single-stream state loses its stability (i.e., an unsteady VC forms), and curve *2* is the boundary at which a steady VC forms in a beam that reflects all the beam electrons.

numerical simulations brings about simplifying assumptions because, in a model experimental device, the electrons can repeatedly pass from the accelerating gap to the deceleration region.

The main parameters of the numerical scheme—the number N_C of points in the spatial mesh and the number n_0 of macroparticles in a cell in an unperturbed state—were chosen to be $N_C = 800$ and $n_0 = 24$ (which correspond to $N = 19\,200$ macroparticles in the computation region in an unperturbed state). These values of the parameters of the numerical scheme were chosen so as to provide the required accuracy and reliability of calculations aimed at analyzing complicated nonlinear processes (including deterministic chaos) in the electron-plasma system under investigation [42, 44]. The equations of motion were solved by a leap-frog scheme of second-order accuracy [42], and Poisson's equation was integrated by the error-correction method [45].

Figure 9 illustrates the characteristic regimes of oscillations of the electron beam in the diode gap in the plane of the parameters α and Δφ, which are, respectively, the Pierce parameter and the decelerating potential difference between the grids. Let us discuss these regimes in more detail, by referring to Figs. 9 and 10, if necessary. Figure 10 presents the oscillation power spectra $P(f)$ and the phase portraits (obtained by the Takens method [46]) of the electric field oscillations $E(x = 0)$ at the first (entrance) grid of the diode gap for a Pierce parameter equal to $\alpha = 0.9$ and for different values of the decelerating potential difference Δφ.

Domain *T* in Fig. 9 refers to the regime in which the electron beam is fully transmitted through the drift gap; in this case, no VC forms in the electron beam and no oscillations are excited there. Curve *1* corresponds to the critical values of the control parameters (the Pierce parameter α and potential difference Δφ) at which the system becomes unstable and an unsteady VC, oscillating in both space and time, arises in the beam. When the beam is not decelerated ($\Delta\varphi = 0$), the critical value of the Pierce parameter at which an unsteady VC forms in the system is equal to $\alpha_{cr} = 4/3$ [29] (in Fig. 9, this critical value α_{cr} at the abscissa is indicated by the arrow). As the decelerating potential difference Δφ increases, the boundary of the region in which an unsteady VC can appear in the parameter space is displaced toward smaller values of the Pierce parameter. This makes it possible, by increasing the decelerating potential at the second grid of the diode, to achieve microwave generation by a VC at beam currents lower than those in a system without electron deceleration (a "classical" scheme of a VC-based oscillator [6]).

Curve *2* in Fig. 9 corresponds to the values of the control parameters at which the oscillations in the system are suppressed and a steady VC forms in the beam that reflects all the electrons that were injected into the diode gap. This regime, which is denoted by the symbol *S* in Fig. 9, corresponds to the strong deceleration of the electron beam; it can be described analytically in terms of the steady-state theory of electron beams with an overcritical current (see, e.g., [47]).

Domains *P*, *Q*, and *C* in Fig. 9 correspond to different characteristic oscillation regimes of an electron beam with a VC. Analyzing the pattern of the regimes, we can conclude that, as the decelerating potential in the system increases, an electron beam with a VC sequentially evolves through different oscillations regimes. Let us examine these regimes in more detail.

Two domains *P* correspond to the regimes of regular oscillations of the VC. In the lower of these two regions, regular oscillations in a system with a decelerated electron beam occur at low decelerating potentials of the second grid (i.e., when the beam perveance *p* only slightly exceeds the critical value p_{cr} at which a VC appears in the system). For this regime with a slow deceleration rate of the electron beam, the parameters of the electric field oscillations are shown in Fig. 10a. In the upper region, regular oscillations occur at high deceleration rates of the electron beam (i.e., in Fig. 9, they occur near curve *2*, corresponding to a transition of the system to a state with a steady VC). The parameters of the regular oscillations for this case are shown in Fig. 10c, which was obtained for a high decelerating potential difference, $\Delta\varphi = 0.625$, between the grids of the diode gap. A comparison between Figs. 10a and 10c leads to the conclusion that, qualitatively, the shape of

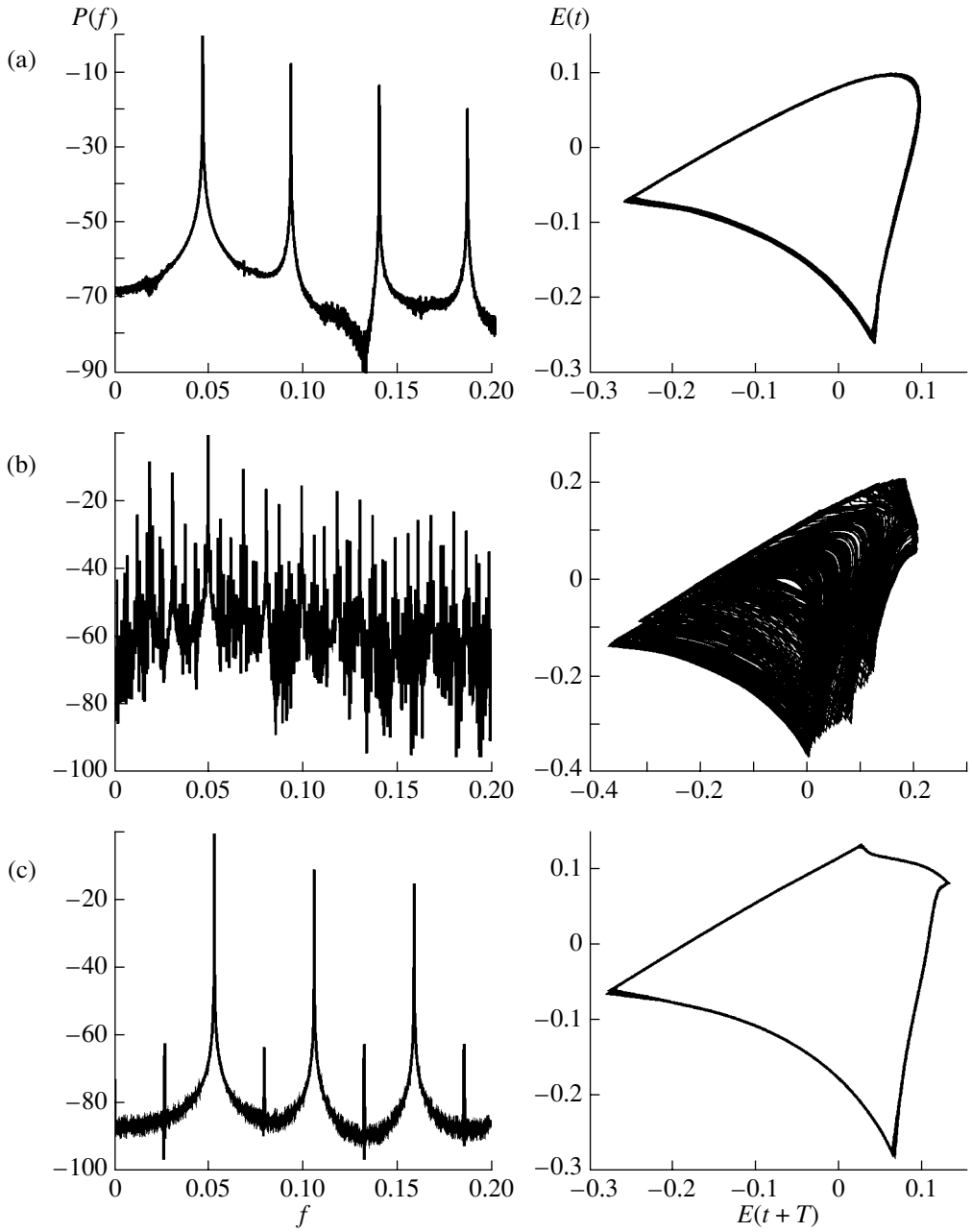

Fig. 10. Oscillation power spectra $P(f)$ and phase portraits of the electric field oscillations $E(t)$ at the entrance grid of the diode gap for a Pierce parameter equal to $\alpha = 0.9$ and for different values of the decelerating potential difference: $\Delta\varphi$ = (a) 0.37, (b) 0.47, and (c) 0.625.

the oscillations, as well as their spectral composition, differs only slightly between these two regimes. Analyzing the corresponding phase portraits, however, we can say that, in the second regime, the oscillations are more nonlinear (i.e., their cycles are far more complicated in shape) than those at slow electron beam deceleration rates.

For a larger decelerating potential difference, $\Delta\varphi \approx 0.5$, the system evolves from the regime of regular oscillations to the regime of stochastic generation (Fig. 9, domain *C*). The parameters of the electric field oscillations in the stochastic generation regime at a potential difference of $\Delta\varphi = 0.47$ are shown in Fig. 10b. We can see that, in regime *C*, the oscillation power spectrum becomes continuous, although highly irregular. The phase portrait in this case corresponds to a stochastic attractor. The system evolves from the regime of periodic oscillations to the regime of stochastic microwave generation by the VC through the regime of quasiperiodic oscillations (Fig. 9, domain *Q*). The quasiperiodic oscillation regime is characterized by oscillations at two incommensurable base frequencies, whose

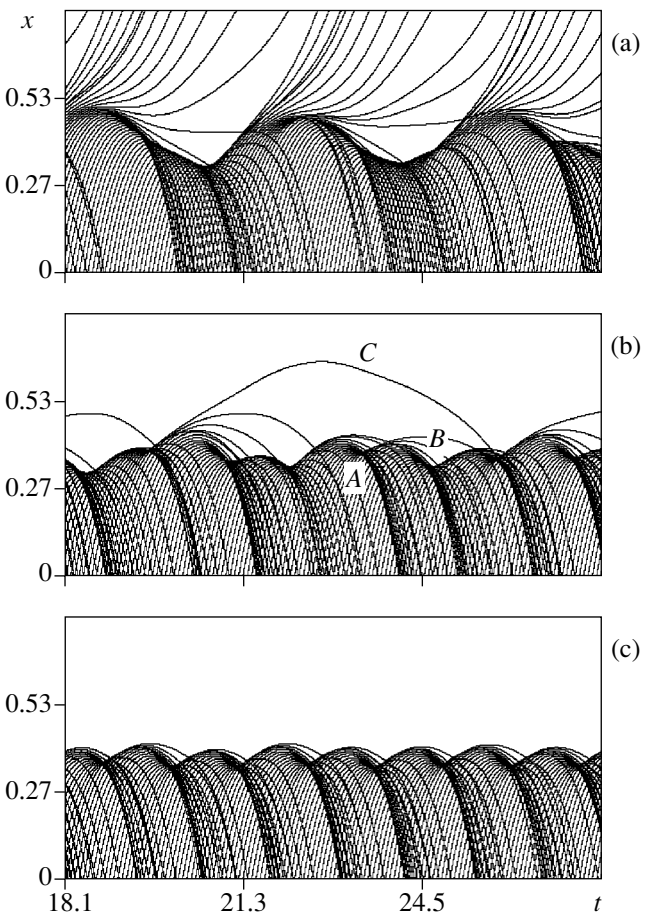

Fig. 11. Spatiotemporal diagrams of the dynamics of an electron beam in a diode gap for a Pierce parameter equal to $\alpha = 0.9$ and for different values of the decelerating potential difference: $\Delta\varphi$ = (a) 0.37, (b) 0.47, and (c) 0.625.

image in phase space is a two-dimensional torus. Accordingly, the system evolves to the stochastic generation regime in a classical way—through the disruption of quasi-periodic oscillations (and of the torus in phase space) [48].

This scenario agrees well with the data of experimental investigations reported in the previous section of the paper. Thus, as the decelerating potential difference ΔV_{dec} between the grids in the model experimental device was increased, we observed the excitation of nearly regular oscillations; as the beam deceleration rate was further increased, the oscillations became more complicated. At large values of ΔV_{dec}, we observed stochastic broadband microwave generation. Such behavior is qualitatively similar to that observed experimentally. A good qualitative agreement with experiment was achieved for slow deceleration rates of the electron beam—the case in which two-dimensional effects in the beam are unimportant and a one-dimensional model describes well the unsteady dynamics of an electron beam with a VC in the model experimental device.

Note that the numerically calculated dependence of the oscillation frequency in a beam with a VC on the decelerating potential is also in good qualitative agreement with that obtained experimentally (see Fig. 4). Numerical simulations, as well as experimental investigations, show that an increase in the decelerating potential difference $\Delta\varphi$ leads to an increase in the generation frequency, proportional to the plasma frequency of the beam electrons, which, in turn, increases with $\Delta\varphi_0$ (i.e., with the beam perveance).

Let us now consider the cause of such a complicated dynamics of an electron beam with an overcritical perveance in a diode gap with a decelerating field. To do this, we analyze the physical processes occurring in an electron beam with a VC in a decelerating field by examining the spatiotemporal diagrams of the electron beam and also by reconstructing the electron velocity distribution functions for the regimes of regular and of stochastic oscillations of the VC.

Figure 11 shows the spatiotemporal diagrams of the beam electrons in the dimensionless coordinates (t, x) for the same values of the control parameters α and φ_0 as in Fig. 10. Recall that, in this section, we are working in the reditron model, in which the effect of the electrons reflected from the VC on the beam in the region ahead of the first grid, as well as the possibility that the beam electrons can repeatedly pass from the accelerating gap to the deceleration region, is ignored. Since the influence of the reflected electrons on the injected beam in the region ahead of the first (entrance) grid is ignored, the reditron model cannot describe some effects that may occur in the interaction of the reflected electrons with the injected ones, in particular, the possible additional velocity modulation of the injected electron beam. In Fig. 11, the coordinate $x = 0$ corresponds to the first grid of the diode gap and the coordinate $x = 1$ shows the position of the second grid. Each curve in the diagrams presents the trajectory of a charged macroparticle used in numerical simulations. The diagrams show the trajectories of only some macroparticles that were injected into the interaction space with the same velocity at equal time intervals. The concentration of the trajectories of the charged macroparticles corresponds to the compression—the onset of an electron structure (bunch)—in the electron beam.

An analysis of the spatiotemporal diagrams of charged macroparticles in a beam with an overcritical perveance shows that the electron velocity in the diode gap becomes lower (the slope angle of the trajectories of charged macroparticles decreases) and, at a certain spatial point in the interaction space, the electrons stop moving and turn back, so the beam passes over to a two-stream state. The turning point of the electrons can be regarded as the coordinate x_{VC} of the VC. The figures show that, during the characteristic period of oscillations, the plane from which the electrons are reflected and, consequently, the position of the VC are displaced toward the injection plane. In other words, the potential

barrier becomes high enough to reflect the electrons in a region far from the injection plane and then moves toward this plane, thereby oscillating within the diode gap in both time and space.

In the regime of regular oscillations at a slow beam deceleration rate (see Fig. 11a), the trajectories of the charged macroparticles in the diode gap are seen to be concentrated only in the VC region. This indicates that, in the regime of regular oscillations, only one compact dense electron bunch (structure)—a VC—forms in the system. The space charge density within the VC region is substantially higher than that in the remaining region of the interaction space. When the space charge density in the VC region becomes higher than a certain critical value, the charge is ejected from the interaction space back toward the injection plane and the space charge density in the interaction space decreases rapidly; as a result, the depth of the decelerating potential well (the VC) decreases, so the VC opens the door for the electrons, which thus easily overcome the potential barrier. The transit electrons that appear in the system are accumulated in the spatial region between the grids; as a consequence, the space charge in this region becomes higher and the depth of the potential well increases, giving rise to a VC, which begins to reflect electrons. Thereby, the process repeats itself periodically. Figure 11a shows three characteristic time periods of oscillations of the VC.

The conclusion that only one spatiotemporal structure forms in an electron beam with a VC at slow beam deceleration rates is confirmed by Fig. 12, which displays the velocity distribution functions $f(v)$ of charged macroparticles in the regime of regular oscillations, or more precisely, the electron velocity distribution functions of the electrons at the exit from the second grid (i.e., those that have passed through the VC) and the electrons at the exit from the first grid (i.e., those that have been reflected from the VC). We see from Fig. 12a that the electron velocity distribution function at the exit from the second grid in the regime of regular oscillations has only one maximum. This agrees well with the experimentally obtained single-peaked electron velocity distribution at the exit from the second grid held at a low decelerating potential at which oscillations are generated predominantly at a single frequency (cf. Fig. 6, the case $\Delta V_{dec}/V_0 = 0.1$). The velocity distribution function of the electrons reflected from the VC is more complicated in shape: in the case at hand, it has three pronounced peaks.

In the regime of stochastic oscillations (Fig. 9, domain *C*), the internal dynamics of an electron beam in a diode gap with a decelerating field is more complicated than in the previous case. Let us analyze the stochastic generation regime by referring to the spatiotemporal diagram of the electron beam (see Fig. 11b) and to the electron velocity distribution functions at the exit from the system (see Fig. 12).

From the spatiotemporal diagram we see that, during one characteristic period of oscillations in the system, two electron structures, or equivalently two VCs, form in a beam. In the diagram in Fig. 11b, they correspond to two regions of concentration of electron trajectories and are denoted by *A* and *B*. It is clearly seen that each of the electron structures reflects some electrons. The electron structures (VCs) are strongly coupled to one another by the electrons reflected from them. The electrons reflected from one of the structures (e.g., structure *A* in Fig. 11b) affect the potential distribution in the injection region (i.e., in the region of the first grid) and, therefore, bring additional changes in the velocities of the electrons that enter into the interaction space and form the second structure (structure *B*). In turn, the electrons reflected from the secondary structure change the "starting" conditions for the formation of the first VC in the next period of oscillations.

Such a complicated internal dynamics of the beam can be interpreted as being due to the onset of a distributed feedback in a VC-based system with an overcritical current, with the result that the system begins to generate stochastic microwave radiation (analogous results can be found in [16, 19, 20, 26]).

The complex internal dynamics of an electron beam, as well as the formation of several electron structures and the interaction between them, is also confirmed by the shapes of the velocity distribution functions of charged macroparticles in the case of a fast electron deceleration rate (see Fig. 12). In this case, the velocity distributions are more complicated in shape than those in the case of regular dynamics of an electron beam with a VC. This indicates that an electron beam in a diode gap with a decelerating field is rapidly thermalized due to the strong interaction between several electron structures near the entrance grid of the diode and, accordingly, that the nonlinear unsteady processes in the system become far more complicated [13, 49].

Note also that, in the regime of stochastic oscillations, some charged macroparticles in the system remain within the interaction space during several oscillation periods (in Fig. 11b, the trajectory of one such "long-lived" particles is denoted by *C*). Since the characteristic transit times of these particles exceed the period of oscillations of the VC, they may be thought to be responsible for the onset of the low-frequency components in the spectra of the generated oscillations when the decelerating potential of the second grid in a system with a VC is increased.

At a very large decelerating potential difference $\Delta\varphi$, the beam dynamics again is regular. The corresponding spatiotemporal diagram of an electron beam with a VC for this case is shown in Fig. 11c. We see from this diagram that the amplitude of the spatial oscillations of the VC is small and the reflected electrons are weakly modulated in velocity; as a result, at a very fast electron deceleration rate, the stochastic dynamics is suppressed. As the potential difference $\Delta\varphi$ increases fur-

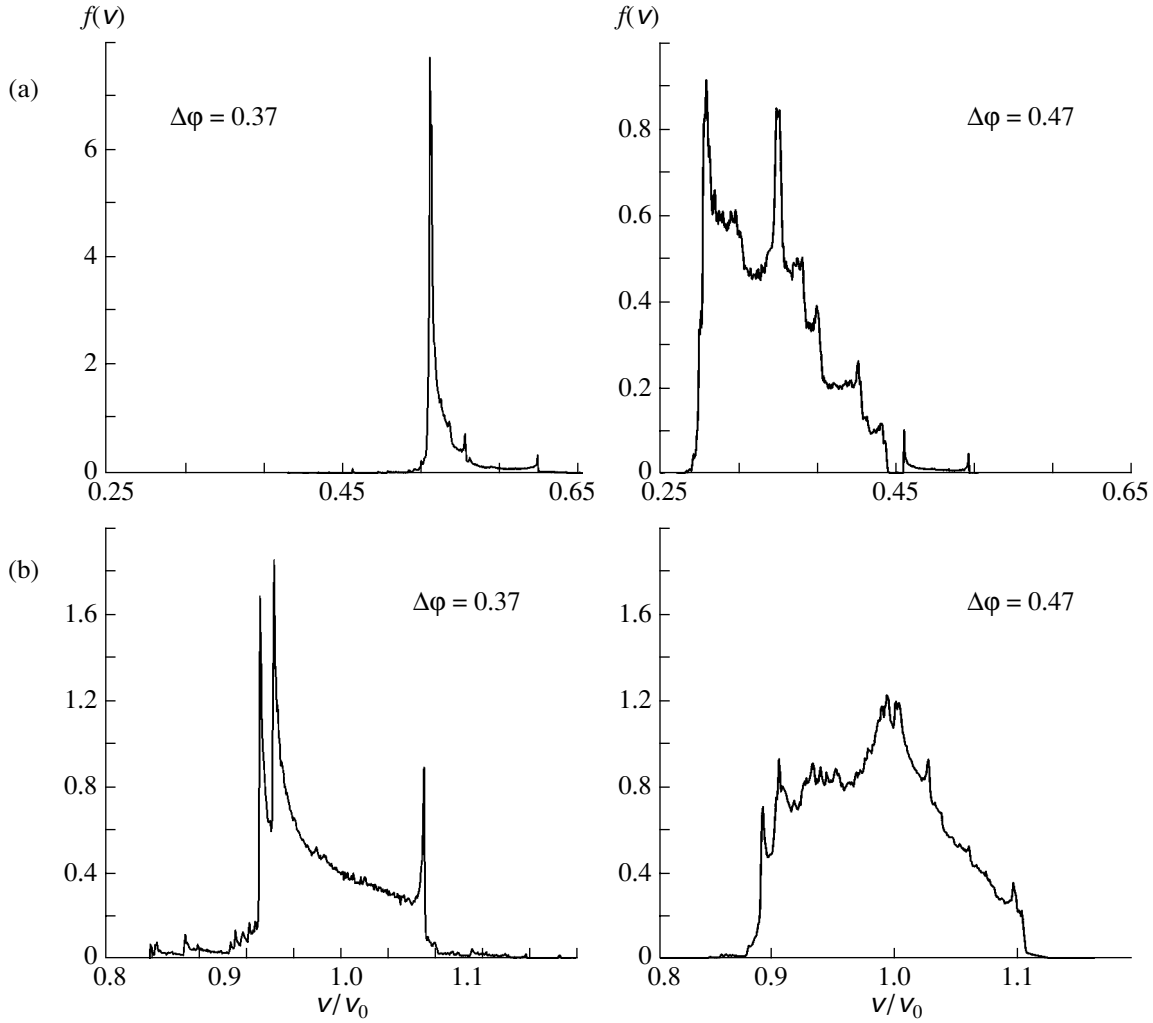

Fig. 12. Velocity distribution functions (a) of the electrons at the exit from the second grid (i.e., those that have passed through the VC) and (b) of the electrons at the exit from the first grid (i.e., those that have been reflected from the VC) for a Pierce parameter equal to $\alpha = 0.9$ and for $\Delta\varphi = 0.37$ and 0.47.

ther, the amplitude of the oscillations of the VC rapidly decreases and the system evolves into regime *C* (see Fig. 9), in which the VC is steady and reflects all of the beam electrons back toward the injection plane.

5. DISCUSSION OF THE THEORETICAL AND EXPERIMENTAL RESULTS

Hence, our experimental investigations show that the broadband noisy oscillations observed in the drift gap with a decelerating potential are generated by a VC that forms in a nonrelativistic electron beam in a decelerating field. Numerical simulations show that the stochastic oscillations are of a dynamic nature and are governed by the processes of the formation of electron structures in a beam with an overcritical perveance and of the interaction between them. The broadening of the oscillation spectrum with increasing beam deceleration rate is attributed to the onset of secondary electron structures after the formation of the main electron structure—the VC. The secondary structures are grouped bunches of the electrons that have passed through the unsteady VC region and, correspondingly, have been modulated at a frequency close to the plasma frequency of the beam in the drift gap with a decelerating field. The appearance of the low-frequency components in the spectra of oscillations generated by a beam with an overcritical perveance can be associated with the dynamics of the electrons that remain within the interaction space during several periods of oscillations of the VC.

At a qualitative level, the results of one-dimensional numerical simulations confirm the experimental data fairly well. However, a comparison with experiment shows that the one-dimensional theory is only capable of describing regular oscillation regimes at a slow beam deceleration rate and some characteristic features of the evolution of the system into the stochastic generation

regime with increasing decelerating potential. In particular, the one-dimensional theory does not provide an analytic description of the experimentally revealed effect—the change in the spectral composition of oscillations in a beam with a VC when the decelerating potential of the second grid is increased (see Fig. 3). According to [8, 37], the experimentally revealed characteristic features of the change in the spectral composition of oscillations in different cross sections of the beam with increasing decelerating potential are explained as being due to the complicated radial structure of a VC, which has the shape of a cup in the radial direction and is convex toward the injection plane. This allows us to conclude that, in order to analyze and describe the dynamics of an electron beam with a VC in a strong decelerating field (corresponding to the experimentally observed regimes of developed stochastic oscillations), it is necessary to take into account two-dimensional effects, which can be described only in terms of a two-dimensional numerical model. Such two-dimensional numerical analysis seems to be very important and it will be the subject of our further theoretical studies of electron–wave devices in which stochastic oscillations are generated by a VC that forms in an electron beam with an overcritical perveance.

It is also necessary to point out the following important effect, which was revealed by analyzing a numerical model of a diode gap with an additional deceleration of an electron beam with a VC. In [29], it was shown that, when a monoenergetic electron beam with an overcritical current (i.e., with an overcritical value of the Pierce parameter, $\alpha > \alpha_{cr} = 4/3$ [39]) is injected into a diode gap with a zero decelerating potential, it excites only regular (periodic) oscillations, no matter how much the Pierce parameter is above its critical value. With an additional nonzero decelerating potential, the dynamics of an electron beam in the diode gap becomes far more complicated: the system can even pass into the regimes of developed stochastic generation. This indicates that applying a decelerating potential to the second grid of the diode makes the regime of stochastic oscillations of the VC easier to achieve—an important point for the practical development of VC-based oscillators of stochastic microwave radiation. In our opinion, the complications of the beam dynamics in a system with a decelerating field can be attributed to the fact that the coupling between the structures forming in an electron beam with an overcritical current (perveance) becomes stronger because of the additional electron deceleration and, accordingly, because of an increasingly large number of electrons that are reflected from the secondary electron structure (the secondary VC) and return to the injection plane, thereby ensuring additional distributed feedback in the beam. On the other hand, it should be noted that our numerical simulations were carried out based on the reditron model, in which the effect of the electrons reflected from the VC on the beam in the region ahead of the first grid, as well as the possibility that the beam electrons can repeatedly pass from the gap between the electron gun and the first (entrance) grid to the deceleration region, was ignored. In Section 4, it was already mentioned that, in the reditron model, no account is taken of the effect that is exerted upon the injected beam by the reflected electrons and that may lead, e.g., to an additional velocity modulation of the injected electron beam. These factors will be the subject of our further investigations; taking them into account may be very important for achieving a better agreement between the simulation results and the experimental data (this concerns, first of all, such parameters of the spectral composition of the stochastic oscillations as the frequency bandwidth of the spectrum and its modulation depth) in the case of low decelerating potentials at the second grid and of strong guiding magnetic fields (when two-dimensional effects are insignificant).

Note in conclusion that the mechanism for generating broadband noisy oscillations that has been considered here both experimentally and theoretically can be used to create controlled microwave oscillators of high- and moderate-power broadband signals.

ACKNOWLEDGMENTS

We are grateful to Prof. D.I. Trubetskov, corresponding member of the Russian Academy of Sciences, for his interest in this study, useful discussions, and valuable critical remarks. This work was supported in part by the Russian Foundation for Basic Research (project nos. 05-02-16273 and 05-02-16286), the Department of Atomic Science and Technology of the RF Ministry of Atomic Industry, and the US Civilian Research and Development Foundation for the Independent States of the Former Soviet Union (grant no. BRHE REC-006), the Dynasty Foundation, and the International Center for Fundamental Physics in Moscow.

REFERENCES

1. R. A. Mahaffey, P. A. Sprangle, J. Golden, and C. A. Kapetanakos, Phys. Rev. Lett. **39**, 843 (1977).
2. A. N. Didenko, Ya. E. Krasik, S. F. Perelygin, and G. P. Fomenko, Pis'ma Zh. Tekh. Fiz. **5**, 321 (1979) [Sov. Tech. Phys. Lett. **5**, 128 (1979)].
3. D. J. Sullivan, US Patent No. 4 345 220, 17.08.82, H 03 B 9.01.
4. A. N. Didenko, A. G. Zherlitsyn, A. S. Sulakshin, *et al.*, Pis'ma Zh. Tekh. Fiz. **9**, 1510 (1983) [Sov. Tech. Phys. Lett. **9**, 647 (1983)].
5. D. I. Trubetskov and A. E. Khramov, *Lectures on Microwave Electronics for Physicists* (Nauka, Moscow, 2003), Vol. 1 [in Russian].
6. A. E. Dubinov and V. D. Selemir, Radiotekh. Élektron. (Moscow) **47**, 575 (2002).
7. A. E. Dubinov, I. Yu. Kornilova, and V. D. Selemir, Usp. Fiz. Nauk **172**, 1225 (2002) [Phys. Usp. **45**, 1109 (2002)].

8. A. E. Dubinov, I. A. Efimov, I. Yu. Kornilova, *et al.*, Fiz. Élem. Chast. At. Yadra **35** (2), 462 (2004).
9. H. E. Brandt, IEEE Trans. Plasma Sci. **13**, 513 (1985).
10. H. Sze, J. Benford, and B. Harteneck, Phys. Fluids **29**, 5875 (1986).
11. A. M. Afonin, A. N. Didenko, A. F. Pautkin, and A. S. Roshal', Radiotekh. Élektron. (Moscow) **37**, 1889 (1992).
12. A. P. Privezentsev, N. I. Sablin, N. M. Filipenko, and G. P. Fomenko, Radiotekh. Élektron. (Moscow) **37**, 1242 (1992).
13. V. D. Selemir, B. V. Alekhin, V. E. Vatrunin, *et al.*, Fiz. Plazmy **20**, 689 (1994) [Plasma Phys. Rep. **20**, 621 (1994)].
14. V. E. Vatrunin, A. E. Dubinov, V. D. Selemir, and N. V. Stepanov, in *Proceedings of the 10th Winter School on Microwave Electronics and Radiophysics, Saratov, 1996*, Ed. by D. I. Trubetskov (GosUNTs "Kolledzh," Saratov, 1996), Vol. 2, p. 89 [in Russian].
15. Tsang-Lang Lin, Wen-Ting Chen, Wen-Chung Liu, and Yuan Hu, J. Appl. Phys. **68**, 2038 (1990).
16. V. G. Anfinogentov and A. E. Khramov, Izv. Vyssh. Uchebn. Zaved., Radiofiz. **41**, 1137 (1998).
17. A. E. Hramov and I. S. Rempen, Int. J. Electron. **91**, 1 (2004).
18. A. P. Privezentsev and G. P. Fomenko, Izv. Vyssh. Uchebn. Zaved., Prikl. Nelin. Dinam. **2** (5), 56 (1994).
19. D. I. Trubetskov, V. G. Anfinogentov, N. M. Ryskin, *et al.*, Radiotekhnika **63** (4), 61 (1999).
20. A. E. Khramov, Radiotekh. Élektron. (Moscow) **44**, 551 (1999).
21. A. E. Khramov, Radiotekh. Élektron. (Moscow) **47**, 860 (2002).
22. H. Sze, D. Price, and B. Harteneck, J. Appl. Phys. **67**, 2278 (1990).
23. K. J. Hendricks, R. Adler, and R. C. Noggle, J. Appl. Phys. **68**, 820 (1990).
24. A. E. Khramov, Radiotekh. Élektron. (Moscow) **44**, 211 (1999).
25. A. E. Dubinov, V. D. Selemir, and A. V. Tsarev, Izv. Vyssh. Uchebn. Zaved., Radiofiz. **43**, 709 (2000).
26. A. A. Koronovskiĭ and A. E. Khramov, Fiz. Plazmy **28**, 722 (2002) [Plasma Phys. Rep. **28**, 666 (2002)].
27. J. Pierce, J. Appl. Phys. **15**, 721 (1944).
28. B. B. Godfrey, Phys. Fluids **30**, 1553 (1987).
29. D. I. Trubetskov and A. E. Khramov, *Lectures on Microwave Electronics for Physicists* (Nauka, Moscow, 2004), Vol. 2 [in Russian].
30. P. A. Lindsay, X. Chen, and M. Xu, Int. J. Electron. **79**, 237 (1995).
31. H. Matsumoto, H. Yokoyama, and D. Summers, Phys. Plasmas **3**, 177 (1996).
32. M. V. Kuzelev and A. A. Rukhadze, *Electrodynamics of Dense Electron Beams in Plasma* (Nauka, Moscow, 1990) [in Russian].
33. Yu. A. Kalinin and A. D. Esin, *Methods and Instruments of Physical Experiment in Vacuum Microwave Elecronics* (SGU, Saratov, 1991) [in Russian].
34. A. A. Rukhadze, S. D. Stolbetsov, and V. P. Tarakanov, Radiotekh. Élektron. (Moscow) **37**, 385 (1992).
35. W. Jiang, H. Kitano, L. Huang, *et al.*, IEEE Trans. Plasma Sci. **24**, 187 (1996).
36. Yu. A. Kalinin, A. A. Koronovskiĭ, I. S. Rempen, *et al.*, in *Proceedings of the 14th International Conference on Microwave Engineering and Telecommunication Technology, Sevastopol, 2004* (Veber, Sevastopol, 2004), p. 593 [in Russian].
37. V. S. Voronin, A. N. Lebedev, and Yu. T. Zozulya, Zh. Tekh. Fiz. **42**, 546 (1972) [Sov. Phys. Tech. Phys. **17**, 432 (1972)].
38. A. N. Didenko and V. I. Rashchikov, Fiz. Plazmy **18**, 1182 (1992) [Sov. J. Plasma Phys. **18**, 616 (1992)].
39. V. L. Granatstein and I. Alexeff, High-Power Microwave Sources (Artech House Microwave Library, Boston, 1987).
40. E. K. Kolesnikov, A. S. Manuĭlov, and B. V. Filippov, *Dynamics of Charged Particle Beams in Gas-Plasma Media* (SPbGU, St. Petersburg, 2002) [in Russian].
41. A. S. Roshal', *Simulation of Charged Particle Beams* (Atomizdat, Moscow, 1979) [in Russian].
42. Ch. K. Birdsall and A. B. Langdon, *Plasma Physics via Computer Simulations* (McGraw-Hill, New York, 1985; Énergoatomizdat, Moscow, 1989).
43. H. A. Davis, R. R. Bartsch, T. J. T. Kwan, *et al.*, IEEE Trans. Plasma Sci. **16**, 192 (1988).
44. V. G. Makhan'kov and Yu. G. Pollyak, Zh. Tekh. Fiz. **46**, 439 (1976) [Sov. Phys. Tech. Phys. **21**, 250 (1976)].
45. P. J. Roach, *Computational Fluid Dynamics* (Hermosa, Albuquerque, 1976; Mir, Moscow, 1980).
46. F. Takens, in *Lectures Notes in Mathematics*, Ed by D. Rand and L. S. Young (Springler-Verlag, New York, 1981), p. 366.
47. A. P. Privezentsev, G. P. Fomenko, and N. M. Filipenko, Zh. Tekh. Fiz. **51**, 1161 (1981) [Sov. Phys. Tech. Phys. **26**, 659 (1981)].
48. S. P. Kuznetsov, *Dynamic Chaos* (Fizmatlit, Moscow, 2001) [in Russian].
49. V. D. Selemir, A. E. Dubinov, and I. G. Prikhod'ko, Vopr. At. Nauki Tekh., Ser. Teor. Prikl. Fiz., No. 1, 22 (1993).

Translated by G.V. Shepekina

Plasma Physics Reports, Vol. 31, No. 11, 2005, pp. 953–960. Translated from Fizika Plazmy, Vol. 31, No. 11, 2005, pp. 1026–1033.

PARTICLE ACCELERATION IN PLASMA

Mechanism for Ion Acceleration along the Normal to the Axis of a Beam–Plasma Discharge in a Weak Magnetic Field

N. V. Isaev[1], A. A. Rukhadze[2], and E. G. Shustin[1]

[1] *Institute of Radio Engineering and Electronics (Fryazino Branch), Russian Academy of Sciences, pl. Vvedenskogo 1, Fryazino, Moscow oblast, 141190 Russia*

[2] *Prokhorov Institute of General Physics, Russian Academy of Sciences, ul. Vavilova 38, Moscow, 119991 Russia*

Received December 15, 2004

Abstract—The mechanism responsible for the previously discovered phenomenon of acceleration of an ion flow along the normal to the axis of a beam–plasma discharge in a weak magnetic field is investigated. It is suggested that the ions are accelerated in the field of a helicon wave excited in the discharge plasma column. It is shown theoretically that, under actual experimental conditions, a helicon wave can be excited at the expense of the energy of an electron beam. The spectral parameters and spatial structure of the waves excited in a beam–plasma discharge in the frequency ranges of Langmuir and helicon waves are studied experimentally and are shown to be related to the parameters of the ion flow. Theoretical estimates are found to agree well with the experimental results. © *2005 Pleiades Publishing, Inc.*

1. INTRODUCTION

In [1, 2], the experimentally discovered effect was described of acceleration of the ions that escape from a beam–plasma discharge in a weak magnetic field ($\Omega_e < \omega_{Le}$, where Ω_e is the electron gyrofrequency and ω_{Le} is the electron Langmuir frequency) in a direction normal to the discharge axis. The ion energy was found to be certainly greater than the energy the ion can acquire in the electrostatic field between the plasma column and the wall of the discharge chamber. Hence, the question naturally arises of what might be the mechanism responsible for this ion acceleration.

High-frequency oscillations at frequencies close to the electron Langmuir frequency have no effect on the acceleration process: they cannot trap and accelerate ions because their velocities are incommensurate with the ion velocities. The maximum energy to which an ion can be accelerated by the ponderomotive force of high-frequency oscillations is equal to $(mu^2/2)(n_b/n_p)^{1/3}m/M$ (where m and M are the electron and ion masses, respectively; u is the electron beam velocity; and n_b and n_p are the electron beam density and plasma density). In experiments, this energy is on the order of 10^{-2} eV. It is thus clear that this mechanism cannot ensure ion acceleration to the experimentally observed energies.

It can be suggested that, in a weakly magnetized plasma, the acceleration mechanism in question is associated with the Cherenkov excitation of two branches of quasistatic (almost potential) oscillations by an electron beam, namely, a high-frequency ($\omega \approx \omega_{Le}$) Langmuir mode and a so-called Trivelpiece–Gould (TG) mode, i.e., a bulk-mode low-frequency ($\omega < \Omega_e$) E-wave of the plasma waveguide. In this case, in spite of its fast growth rate, the generated short-wavelength ($\lambda_z \le 1$ cm) high-frequency mode does not prevent the excitation of a long-wavelength ($\lambda_z \ge 10$ cm) TG mode. The long-wavelength TG mode in a weakly magnetized plasma, in turn, can excite another mode, namely, a so-called helicon (or a helical wave), whose phase velocity has a transverse component much less than the beam velocity (and even the electron thermal velocity). It is this latter mode that is responsible for the ion acceleration observed in [1, 2].

2. THEORY

Here, we develop an analytic theory of the excitation of low-frequency oscillations in a weakly magnetized plasma by a nonrelativistic electron beam. The theoretical results presented below make it possible to qualitatively estimate whether the mechanism proposed can operate under the experimental conditions of [2].

The simultaneous excitation of both modes of the low-frequency waves by an electron beam is very difficult to calculate analytically. This is why we assume that the modes are coupled weakly enough so that the processes of their excitation can be analyzed separately. The conditions under which this approach can be used to study the excitation of two low-frequency oscillation modes in a weakly magnetized plasma are [3]

$$\frac{c^2k^2}{\omega_{Le}^2} \ll 1, \quad \frac{\omega}{\Omega_e} < \frac{\omega^2}{c^2k_z^2}\varepsilon_\perp \cong \frac{\omega_{Le}^2\omega^2}{\Omega_e^2c^2k_z^2} \ll 1. \qquad (1)$$

1063-780X/05/3111-0953$26.00 © 2005 Pleiades Publishing, Inc.

Here, $k \approx \left(\frac{\pi^2 n^2}{L_0^2} + \frac{\mu_{ls}^2}{R^2}\right)^{1/2}$, where L_0 and R are the length of the discharge plasma column and its radius and n and μ_{ls} are the longitudinal and transverse wavenumbers of a wave with the frequency ω and $k_z = \frac{\pi n}{L_0}$. It is under conditions (1) that the TG mode and helicon are weakly coupled to one another. When conditions (1) are not satisfied, the axisymmetric TG and helicon modes in cylindrical geometry should be described by the following strongly coupled equations:

$$\left(\tilde{k}_z^2 + \frac{g^2\omega^2}{\varepsilon_\perp c^2}\right)\Delta_\perp E_z - \hat{\xi}\frac{\varepsilon_\parallel}{\varepsilon_\perp}E_z = \frac{\omega}{c}\frac{g}{\varepsilon_\perp}\Delta_\perp\frac{\partial B_z}{\partial z}$$
$$= i\frac{\omega}{c}\frac{g}{\varepsilon_\perp}k_z\Delta_\perp B_z, \qquad (2)$$
$$\tilde{k}_z^2\Delta_\perp B_z - \hat{\xi}B_z = -\frac{\omega}{c}g\Delta_\perp ik_z E_z.$$

Here,

$$\Delta_\perp = \frac{1}{r}\frac{\partial}{\partial r}r\frac{\partial}{\partial r}, \quad \tilde{k}_z^2 = k_z^2 - \frac{\omega^2}{c^2}\varepsilon_\perp, \quad \hat{\xi} = \tilde{k}_z^2 - g\frac{\omega^2}{c^2}, \qquad (3)$$

and the elements $\varepsilon_\perp$, g, and $\varepsilon_\parallel$ of the plasma dielectric tensor

$$\varepsilon_{ij}(\omega) = \begin{pmatrix} \varepsilon_\perp & ig & 0 \\ -ig & \varepsilon_\perp & 0 \\ 0 & 0 & \varepsilon_\parallel \end{pmatrix} \qquad (4)$$

are given by the expressions

$$\varepsilon_\perp = 1 + \frac{\omega_{Le}^2}{\Omega_e^2}\left(1 + i\frac{\nu_e}{\omega}\right),$$
$$g = \frac{\omega_{Le}^2}{\omega\Omega_e}\left(1 + i\frac{\omega\nu_e}{\Omega_e^2}\right), \qquad (5)$$
$$\varepsilon_\parallel = 1 - \frac{\omega_{Le}^2}{\omega^2}\left(1 - i\frac{\nu_e}{\omega}\right) - \frac{\omega_b^2}{(\omega - k_z u)^2},$$

where $\omega_b = \sqrt{\frac{4\pi e^2 n_b}{m}}$ is the Langmuir frequency of a beam of density n_b and ν_e is the effective collision frequency between the electrons and heavy particles.

Equations (2) and formulas (4) and (5) are obtained under the general restrictions

$$\omega \gg \nu_e > k_z V_{Te}, \quad \omega_{Le} \gg \Omega_e > k_\perp V_{Te}, \qquad (6)$$

where $k_\perp \sim \frac{\mu_{ls}}{R}$ and $V_{Te} = \sqrt{\frac{T_e}{m}}$ is the thermal velocity of the plasma electrons.

Under conditions (1), Eqs. (2) can be solved by the method of successive approximations; specifically, the field E_z of the TG mode (in the saturation stage of the beam–plasma instability) can be determined from the first of Eqs. (2) and then, in the second of the equations, this field can be treated as a source of the field B_z of the helicon.

Hence, a simplified set of equations of the analytic model developed here has the form

$$\varepsilon_\perp\Delta_\perp E_z - k_z^2\varepsilon_\parallel E_z = 0,$$
$$\Delta_\perp B_z + \frac{\omega^4 g^2}{c^4 k_z^2}B_z = -\frac{i\omega g}{k_z c}\Delta_\perp E_z. \qquad (7)$$

This set of equations will be solved below.

The first of Eqs. (7) contains the source term, which describes the excitation of waves by an electron beam. The beam excites a TG mode in which

$$E_z = \frac{k_z}{k_\perp}E_r. \qquad (8)$$

The solution to the first of Eqs. (7) can be sought in the form

$$E_z(r) = E_{0z}J_0\left(\frac{\mu}{R}r\right), \qquad (9)$$

where $\frac{\mu}{R} = k_\perp$ and the quantity μ describes the radial profile of the wave field. Substituting expression (9) into the first of Eqs. (7) yields the dispersion relation

$$k_\perp^2\frac{\omega_{Le}^2}{\Omega_e^2} - k_z^2\left(\frac{\omega_{Le}^2}{\omega^2} + \frac{\omega_b^2}{(\omega - k_z u)^2}\right) = 0. \qquad (10)$$

For a low-density beam ($n_b \ll n_p$), this dispersion relation gives the frequency ω of the TG mode and the complex correction δ to this frequency,

$$\omega = k_z u = \frac{k_z}{k_\perp}\Omega_e, \quad \delta = \omega\left(\frac{n_b}{2n_p}\right)^{1/3}\frac{-1 + i\sqrt{3}}{2}. \qquad (11)$$

These expressions show, in particular, that the mode in question can be excited only under the resonance condition

$$k_\perp u = \frac{\mu}{R}u = \Omega_e. \qquad (12)$$

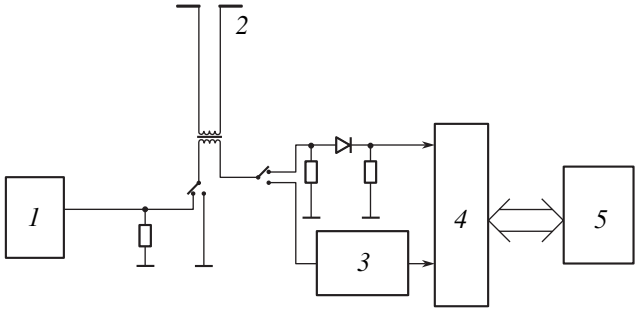

Fig. 1. Scheme for detecting oscillations in a discharge plasma column: (*1*) sweep generator, (*2*) dipole probe, (*3*) spectrum analyzer, (*4*) interface plate, and (5) PC.

Taking into account relationship (8) and expressions (11), we obtain the following condition for the field components of the TG mode:

$$\frac{E_{z0}}{E_{r0}} = \frac{\omega}{\Omega_e} \ll 1. \quad (13)$$

Let us now estimate the TG mode amplitude that is established as a result of the onset of instability. This amplitude is found from the condition for the beam electrons to be trapped by the wave potential [4],

$$\frac{E_{r0}^2}{4\pi n_b \frac{mu^2}{2}} \approx \left(\frac{n_b}{2n_p}\right)^{1/3} \frac{\Omega_e^2}{4\omega_p^2}. \quad (14)$$

For a beam with an energy of ≈1 keV and a density of $n_b \sim 10^8$ cm^{-3} (such that we have $\frac{n_b}{n_p} \sim 10^{-3}$ and $\frac{\Omega_e}{\omega_p} \approx 0.2$), expression (14) yields the estimates $E_{r0} \approx 10$ V/cm and $E_{z0} \approx 2$–3 V/cm ($E_{\varphi 0} \approx 0$).

According to the second of Eqs. (7), the beam-excited quasi-longitudinal TG mode is a source of the helicon field. Inserting representation (9) into the second of Eqs. (7), we obtain

$$B_z = B_{z0}^H J_0\left(\mu \frac{r}{R}\right), \quad (15)$$

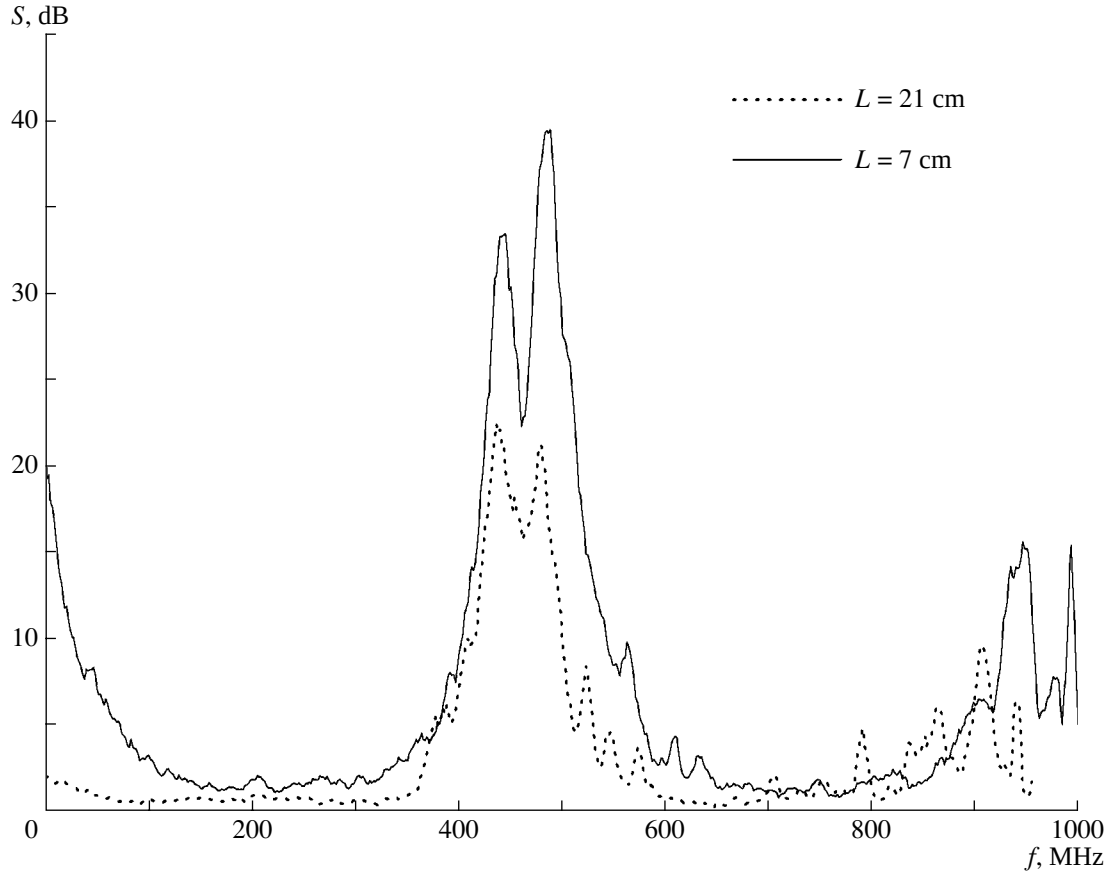

Fig. 2. Total spectrum of the field component E_z recorded by a probe in the discharge plasma column at different distances L from the electron collector. The experimental parameters were as follows: the beam accelerating voltage was U_b = 2 kV, the beam current was I_b = 150 mA, the magnetic field was H = 38 Oe, and the pressure in the discharge chamber was p = 0.3 mtorr.

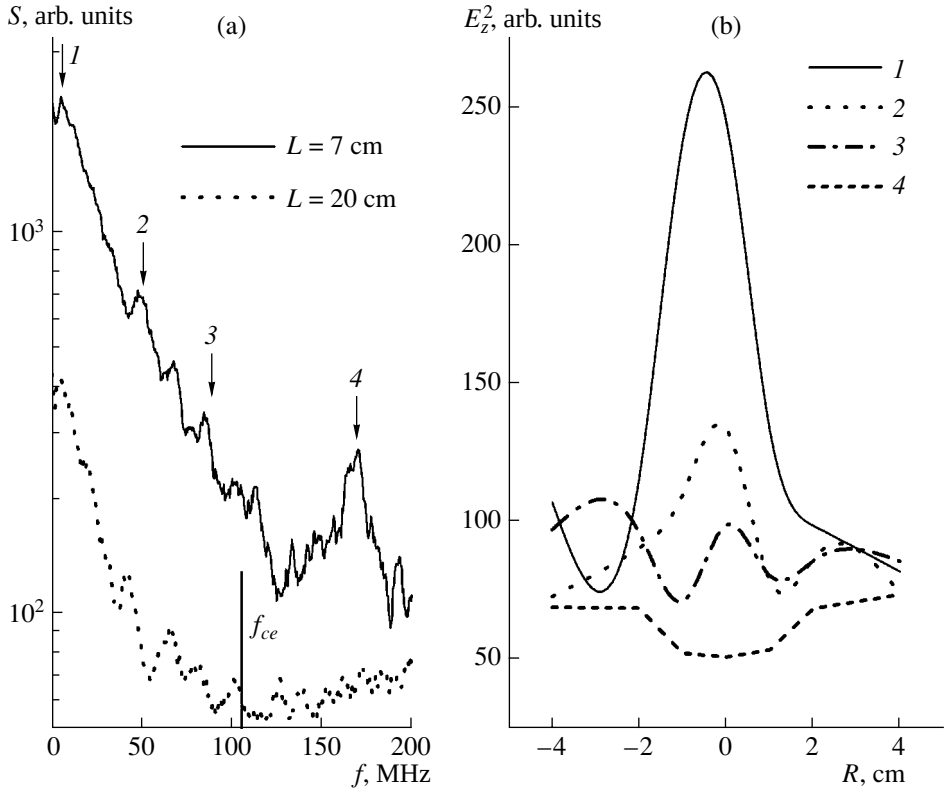

Fig. 3. (a) Spectrum of oscillations generated in the low-frequency range and (b) radial profiles of the field intensity at different frequencies (denoted by the arrows in plot (a)).

where

$$B_{z0}^H = i\frac{\omega_{Le}^2}{k_z c\Omega_e}\frac{\mu^2}{R^2}\frac{E_{z0}}{\dfrac{\omega^2\omega_{Le}^4}{c^4k_z^2\Omega_e^2}-\dfrac{\mu^2}{R^2}}. \quad (16)$$

Along with B_z^H, a helicon has nonzero field components E_r^H and E_φ^H:

$$E_\varphi^H \approx \frac{\omega}{c\dfrac{\mu}{R}}B_z^H, \quad E_r^H \approx \frac{\omega_{Le}^2\omega}{c^2k_z^2\Omega_e}E_\varphi^H. \quad (17)$$

From formula (15) we see that, under the resonance condition

$$\omega^2 = \frac{\mu^2k_z^2c^4\Omega_e^2}{R^2\omega_{Le}^4} \quad (18)$$

and when collisional dissipation is ignored, the helicon field components B_z^H, E_r^H, and E_φ^H increase without bound even when the longitudinal fields are very weak. Unfortunately, resonance condition (18) and beam instability condition (12) cannot be satisfied simultaneously. This, however, is not because of physical reasons but is the result of using conditions (1), with which it was possible to construct a simple analytic theory. (Note that numerical simulations are free of this constraint.) In the case under consideration, the first term in the denominator in expression (16) is much larger than the second term (the resonance conditions is not satisfied). Even in this case, however, estimates yield $B_z^H \sim$ 1 G and show that the field components E_r^H and E_φ^H are comparable in strength to the corresponding field components of the TG mode. Finally, a very important point is that the phase velocity of the helicon satisfies the condition

$$\frac{V_{ph}^H}{u} \approx \frac{\omega}{\Omega_e} \geq 10^{-1}.$$

This indicates that the velocity of the excited wave is sufficiently high (in comparison to the ion thermal velocity), which ensures ion acceleration to superthermal energies. The density of the ions accelerated by this mechanism is determined by the helicon field amplitude. According to a very rough estimate based on Poisson's equation,

$$4en_{acc} \sim E_r^H/R, \quad (19)$$

it may be as high as $n_{acc} \sim (1\text{–}3) \times 10^6$ cm^{-3}.

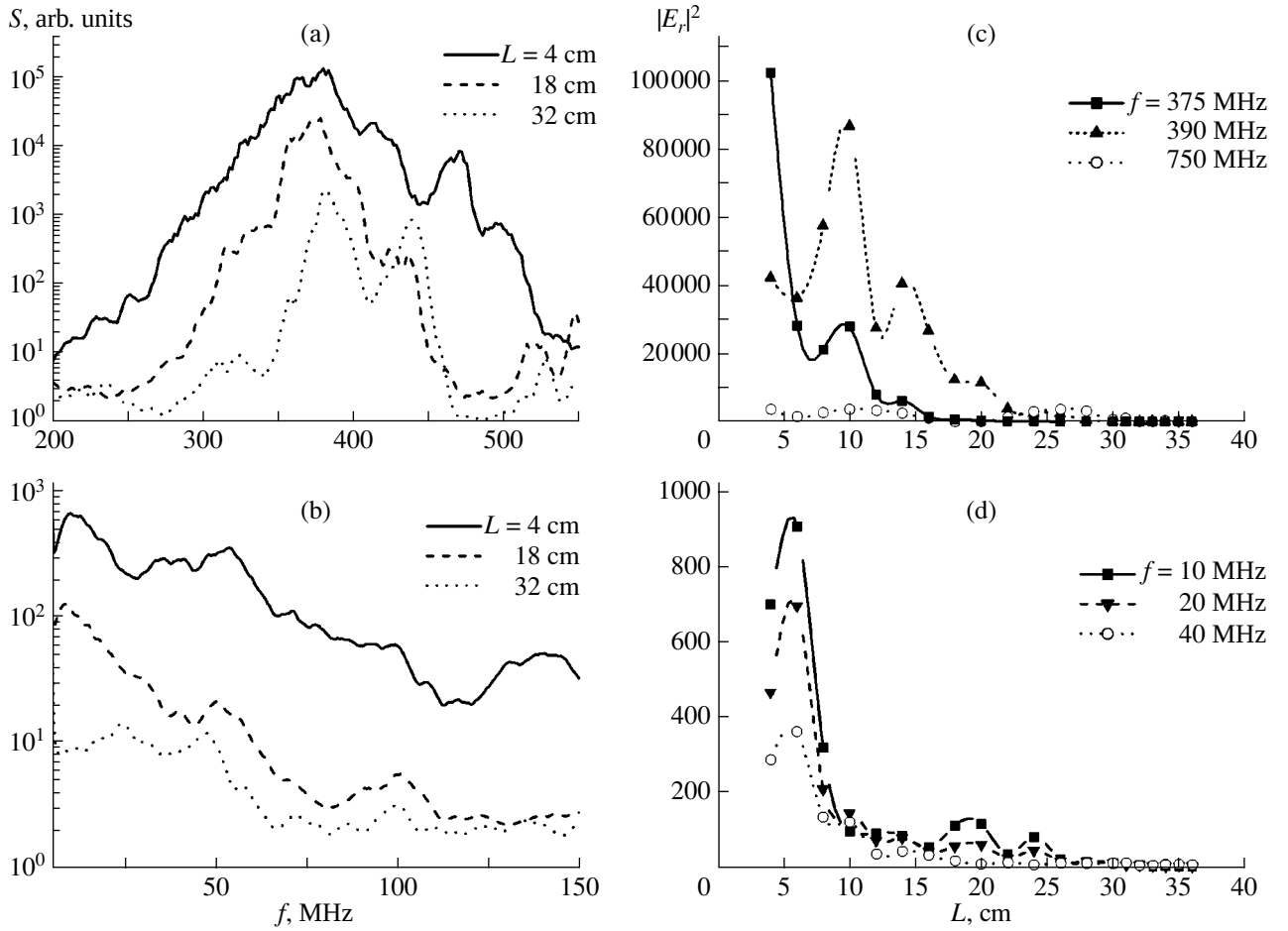

Fig. 4. Spectra of the field component E_r in the (a) high- and (b) low-frequency ranges and longitudinal profiles of the individual components of the spectrum in the (c) high- and (d) low-frequency ranges. The experimental parameters are the same as in Figs. 2 and 3, except for the beam current, which is equal to I_b = 350 mA.

3. EXPERIMENTAL TECHNIQUE

In order to check the hypothesis that was proposed above to explain the mechanism whereby the ions are accelerated, we carried out a series of experimental investigations of the spectra and spatial structure of the waves generated in a beam–plasma discharge in the helicon frequency range.

The experimental scheme was described in [2]. The main difference of the experiments reported here from those performed in [2] is that, in place of a single Langmuir probe, we used a double floating probe (Fig. 1). The double probe had the form of a symmetric dipole 7 mm in length and 0.2 mm in diameter. The probe was loaded with a transformer through a 12-cm-long two-wire line. A TC-4WT transformer (manufactured by the Mini-Circuits Company) with a bandwidth of 3–800 MHz and a resistance conversion factor of 4 symmetrized the probe load, decoupled the probe from the chamber wall, and converted the wave impedance of the coaxial line of the measuring circuit (50 Ω) into the impedance of the probe load (200 Ω) in order to minimize plasma perturbations caused by the probe current. The coaxial cable and the transformer output (through a hermetically sealed connector in the discharge chamber wall) were connected to the input of a C4-60 spectrum analyzer.

The voltage U_{in} at the entrance to the spectrum analyzer is related to the electric field $\bar{E}$ in the probe region (this field is assumed to be uniform along the probe) by the relationship

$$U_{in} = \frac{1}{2}\bar{E}l\frac{Z_{t1}\sqrt{Z_{t2}/Z_{t1}}}{Z_p + Z_{t2}}, \qquad (20)$$

where Z_{t1} = 200 Ω is the input impedance of the transformer, Z_{t2} = 50 Ω is its output impedance, l is the probe length, and Z_p is the equivalent impedance of the probe.

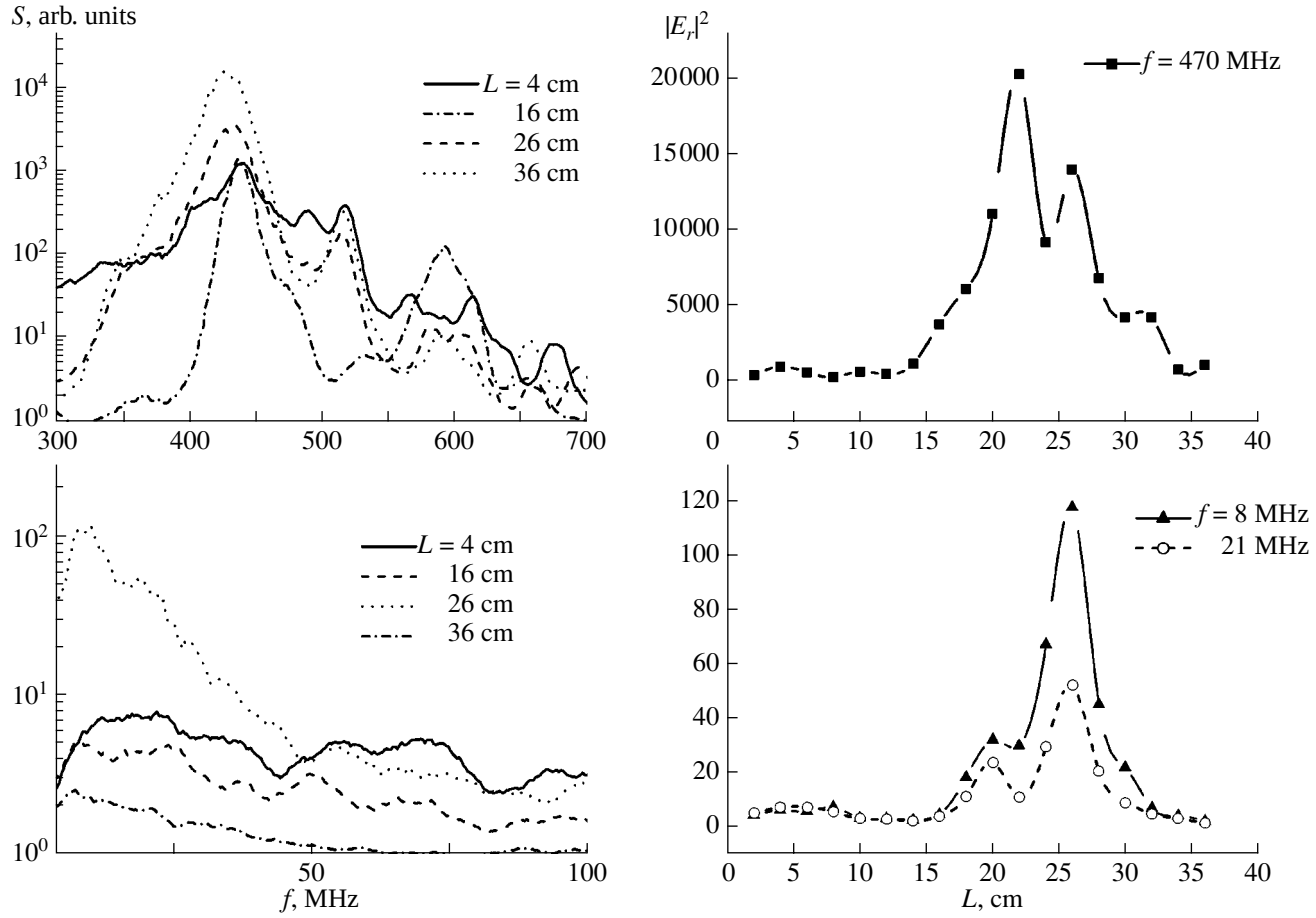

Fig. 5. The same as in Fig. 4, but for H = 23 Oe, p = 0.3 torr, U_b = 1.3 kV, and I_b = 160 mA.

The impedance of the probe at low frequencies ($\omega < \omega_{Li}$) can be determined from the static probe characteristic,

$$Z_p = (dI_p/dU|_{U = U_p})^{-1},$$

where U_p is the potential of the floating probe. In the frequency range of interest to us, however, the probe characteristic and, accordingly, the probe impedance are certainly nonstatic. This is why we estimated the probe impedance $Z_p(f)$ by calibration, namely, by comparing the currents of the transformer loaded with the probe in situations in which resistors with known resistances were connected to the probe and in which the probe was immersed in the plasma, a known voltage from an X1-42 sweep generator being applied to the secondary winding of the transformer. Our measurements yielded Z_p = 1–2 kΩ, depending on the plasma density.

The spectra of oscillations were measured in two frequency ranges, 300–1000 MHz and 5–200 MHz. The first range corresponds to the excitation of Langmuir waves ($\omega \sim \omega_{Le}$), and the second is the frequency range of the TG mode and helicon waves ($\omega < \Omega_e$). The spectra were recorded at different positions of the probe, which could be moved along and across the plasma column. When moving the probe along the radius, we monitored the extent to which it perturbed the system. The perturbation was identified by a change in the level and spectrum of the signal measured by an immovable probe placed at the periphery of the plasma column. From the measured spectra, we plotted longitudinal and transverse profiles of the signal intensity at fixed frequencies (the frequencies of the spectral peaks).

4. EXPERIMENTAL RESULTS

Figure 2 shows the characteristic oscillation spectra recorded by the probe oriented along the system axis over the entire frequency range from 0 to f_p ($f_p = \omega_{Le}/2\pi$, $f_c = \Omega_e/2\pi$). Figure 3a gives an enlarged fragment of the spectrum in the frequency range $f < f_c$. From Fig. 2 we can see that oscillations in the plasma column are indeed excited in two frequency ranges. The oscillations in the range $f \le f_p$ are more intense; their spectrum contains one peak or they have a multipeak spec-

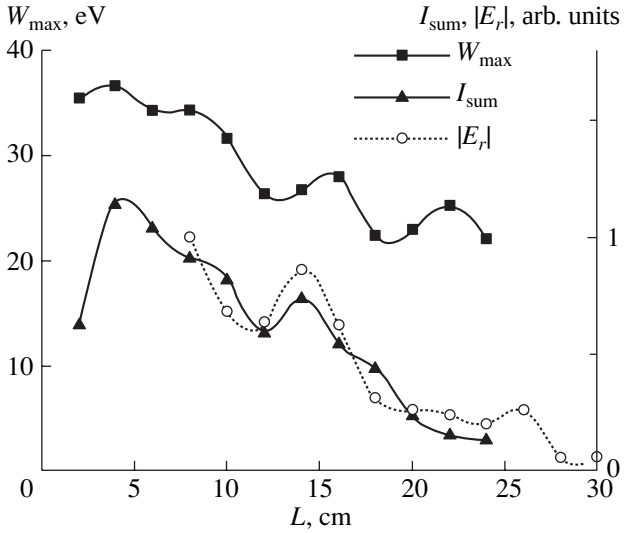

Fig. 6. Integral parameters of the ion flow: the energy W_{max} corresponding to the peak of the distribution function and the total ion flux density $I_{sum} = \int f(W)dW$ as functions of the position of the input window of the spectrum analyzer along the chamber axis for the same experimental parameters as in Fig. 4. The dashed curve shows the longitudinal profile of the amplitude of the field component E_r in the peak of the spectrum.

trum. The intensity of broadband oscillations in the range $f < f_c$ is two to three orders of magnitude lower. In this frequency range, the spectrum has several peaks, each with a width of about 5 MHz, and, as a rule, contains a continuous component, decreasing toward higher frequencies.

The radial profile of the field component E_z (see Fig. 3b) in the high-frequency range has a shape characteristic of the fundamental mode of bulk waves, $E_z = E_0 J_0(k_\perp r)$. In the low-frequency range, the radial field profiles are different at different frequencies. The shapes of the profiles measured at frequencies corresponding to the spectral peaks in the range $f < 30$ MHz are characteristic of the fundamental mode of bulk waves. The radial profiles in the frequency range $30 < f < 100$ MHz correspond to bulk waves (in particular, axially asymmetric modes); they have two to three peaks, reflecting the presence of high spatial modes. The profiles at frequencies above the electron cyclotron frequency correspond to surface waves.

We also tried to measure the radial profiles of the electric field component E_r by the same probe. The length of the radially oriented dipole, however, was comparable to the radial scale of the field nonuniformity, so that the probe could not be considered point-

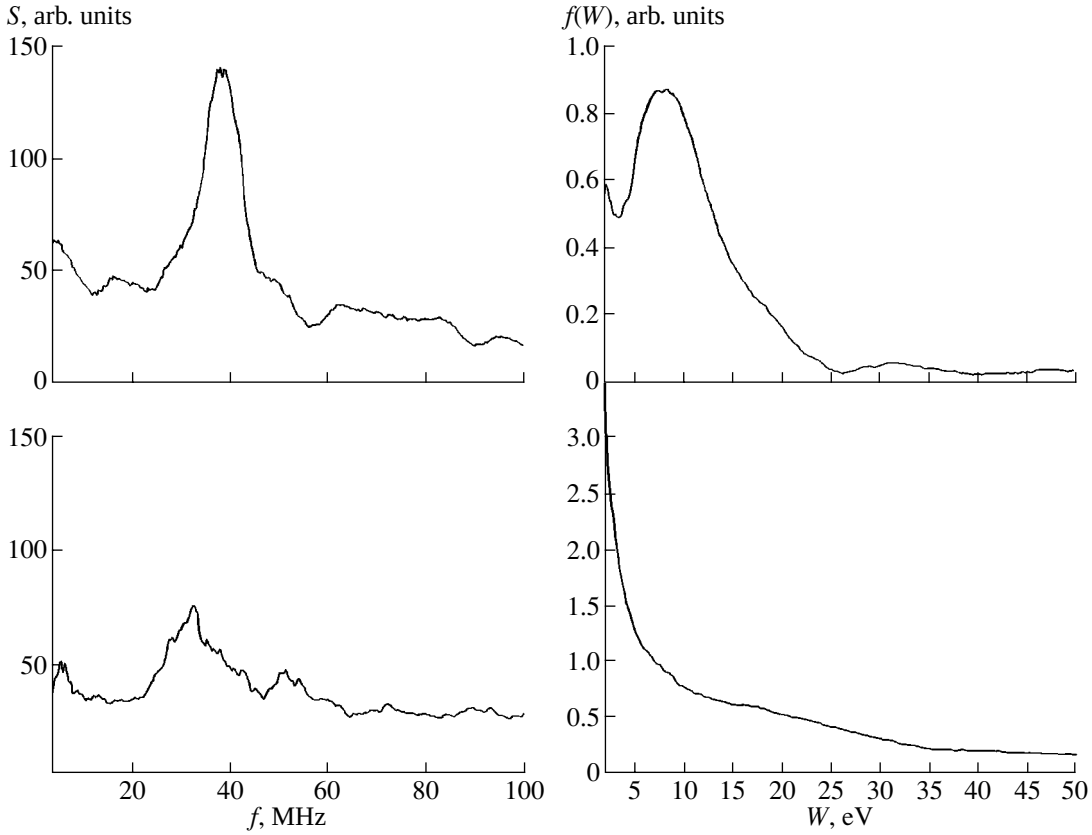

Fig. 7. Low-frequency oscillation spectra and the corresponding energy distribution functions of the ion flow. The upper and lower panels present the measurement results for $H = 38$ and 23 Oe, respectively, the pressure being $p = 0.5$ mtorr.

like. Nevertheless, the radial profiles so estimated clearly show spatial oscillations in the signal intensity, which provide qualitative evidence for the presence of bulk-mode waves with different numbers of peaks (from one for the fundamental mode to three for high spatial modes).

Together with the spectra recorded at different positions of the probe along the interaction region, Figs. 4 and 5 also show the longitudinal profiles of the field intensity at characteristic frequencies. From these figures we can see that, at a low plasma density and relatively high beam velocity (the two parameters that govern the characteristic scale length—the length of the wave amplified at the Langmuir frequency), the field intensity at frequencies $f \sim f_p$ increases from the electron gun toward the electron collector. This increase is nonmonotonic and is accompanied by pronounced oscillations. As the beam velocity decreases and/or the plasma density increases, the region of the maximum field intensity at these frequencies is displaced toward the gun; from this region toward the collector, the field decreases. At frequencies $f < f_c$, the field intensity is, as a rule, seen to increase in the region where rf oscillations are saturated.

Measurements carried out with an ion energy analyzer that was oriented perpendicular to the chamber axis and was moved along the chamber near its wall showed that the ion flow is most intense and hottest in the region where the electric field in both frequency ranges is maximum (see Fig. 6). The fact that the longitudinal profiles of $|E_r|$ and I_{sum} essentially coincide confirms the validity of estimate (19) and thus offers evidence in support of the ion acceleration mechanism proposed here.

The maximum radial field strength estimated from formula (19) with allowance for the probe impedance measured in the same regime was found to be about 10 V/cm (in the region where the energy of the accelerated ions was the highest).

Finally, the relation between the ion acceleration and the excitation of helicon waves is clearly (although only qualitatively) illustrated by Fig. 7, from which we can see that the accelerated ions cease to be generated concurrently with the breakdown of generation of an intense wave in the frequency range $f < f_c$.

5. CONCLUSIONS

In the present paper, we have proposed a possible mechanism for ion acceleration in a direction normal to the axis of a beam–plasma discharge in a weak longitudinal magnetic field. Our experimental studies confirmed the relation between the observed ion acceleration and the generation of a helicon wave. In order to additionally check the hypothesis proposed here, it is desirable to experimentally analyze the dispersion of the excited low-frequency waves and also examine the effect of the intensity and spectrum of these waves on the parameters of the ion flow (e.g., by exciting a helicon wave in a discharge by some external means). These investigations are planned to be done in subsequent study.

It should be noted that the possibility of the excitation of a helicon wave in the interaction of an electron beam with a plasma was considered under the assumption that the motion of the beam electrons is purely longitudinal. Taking into account their transverse motion may help to reveal new additional mechanisms for the generation of low-frequency modes of a plasma waveguide.

ACKNOWLEDGMENTS

We are grateful to A.I. Chmil' for creating programs for automating experiments and processing measurement data and also to A.I. Arsenin, V.G. Leĭman, V.P. Tarakanov, and S.P. Chikin for fruitful discussions of the results obtained. This work was supported in part by the Russian Foundation for Basic Research and the government of Moscow oblast ("Naukograd-2004" grant no. 04-02-97257).

REFERENCES

1. N. V. Isaev, L. Yu. Kochmarev, and E. G. Shustin, Fiz. Plazmy **23**, 966 (1997) [Plasma Phys. Rep. **23**, 891 (1997)].
2. N. V. Isaev, A. I. Chmil', and E. G. Shustin, Fiz. Plazmy **30**, 292 (2004) [Plasma Phys. Rep. **30**, 263 (2004)].
3. K. V. Vavilin, V. Yu. Plaksin, M. Kh. Ri, and A. A. Rukhadze, Fiz. Plazmy **30**, 739 (2004) [Plasma Phys. Rep. **30**, 687 (2004)].
4. R. I. Kovtun and A. A. Rukhadze, Zh. Éksp. Teor. Fiz. **58**, 1709 (1970) [Sov. Phys. JETP **31**, 915 (1970)].

Translated by O.E. Khadin

Plasma Physics Reports, Vol. 31, No. 11, 2005, pp. 961–964. Translated from Fizika Plazmy, Vol. 31, No. 11, 2005, pp. 1034–1037.

PLASMA OPTICS

Formation of a Cylindrical Ion Beam in the Field of an Axisymmetric System of Ring Currents at a Low Hall Current

V. P. Shumilin

Lenin All-Russia Electrotechnical Institute, Krasnokazarmennaya ul. 12, Moscow, 111250 Russia

Received November 10, 2004

Abstract—A study is made of the structure of an accelerating layer with a closed Hall current and the geometry of an ion beam in an external magnetic field created by an arbitrary axisymmetric system of ring currents under conditions such that the Hall current can be ignored. It is shown that the ion trajectories are perpendicular to the magnetron cutoff surface for electrons and that the cathode plasma boundary coincides with a magnetic field line. A magnetic field configuration is found in which the cutoff surface is a plane surface perpendicular to the axis of the system. It is shown that, for a small ratio of the gyroradius of the electrons (in terms of the maximum energy acquired by them in the layer) to the characteristic size of the structure, such a configuration provides sufficient means to ensure the formation of slightly converging ion beams or those that are essentially parallel to the system axis. © *2005 Pleiades Publishing, Inc.*

1. It is known [1–3] that, under certain conditions, a quasineutral plasma flow is reflected from a transverse magnetic field. This occurs when the plasma momentum flux density Mnv^2 (where M is the mass of an ion, n is the ion density, and v is the ion flow velocity) is low in comparison to the magnetic pressure $H^2/8\pi$. In fact, in the boundary layer between the plasma flow and the magnetic field, a potential difference is established that is determined by the ion kinetic energy. The electric field decelerates the ions over a distance on the order of the electron gyroradius calculated in terms of the maximum energy the electrons can acquire in the layer. Since the equations of motion of the particles are invariant under the operation of time reversal, the problem of the structure of such boundary layers is equivalent to that of the acceleration of the ions that originate with a zero velocity at the surface where the decelerated plasma flow comes to a complete stop (the magnetron cutoff surface for electrons). This is why problems of the reflection of a plasma flow from a magnetic field [1–3] played an important role in the development of plasma physics, in particular, the theory of Hall-current plasma accelerators [4–8].

For $Mnv^2 \ll H^2/8\pi$, the magnetic field in the boundary layer varies insignificantly (the Hall current is low). In this case, the motion of the particles can be analyzed without involving the equation for the magnetic field, $\nabla \times \mathbf{H} = 4\pi\mathbf{j}/c$. In my recent paper [9], this approximation was used to investigate the structure of an accelerating layer and the geometry of an ion beam in an external magnetic field with nonzero radial ($H_r \sim 1/r$) and longitudinal (H_z = const) components. In the present paper, the results obtained in [9] are generalized to the case of an external magnetic field created by an arbitrary system of axisymmetric ring currents. It is clear that these currents ought to be sufficiently high. Indeed, since the thickness of the accelerating layer is on the order of the gyroradius of the electrons in terms of their total energy, $\rho_e(\varphi_0) = mc\sqrt{2e\varphi_0/m}/(eH_0)$ (where e and m are the charge and mass of an electron, φ_0 is the accelerating voltage, and H_0 is the characteristic magnetic field strength), the condition for the layer thickness to be small in comparison to the characteristic size of the system, $\rho_e(\varphi_0) \ll R_0$, yields

$$H_0 \gg \frac{mc}{eR_0}\sqrt{\frac{2e\varphi_0}{m}},$$

or

$$J_0 \gg \sqrt{\frac{mc^4\varphi_0}{8e}}$$

(where $J_0 = cR_0H_0/4$ is the characteristic magnitude of the external current), i.e.,

$$J_0 \gg 8.4\sqrt{\varphi_0}.$$

Here, the current and potential are expressed in amperes and volts, respectively.

2. As in [9], we consider an analogue of the Chapman–Ferraro problem, namely, the problem of a cylindrical ion beam in the magnetic field of an arbitrary axisymmetric system of ring currents. In this case, the vector potential of the magnetic field in cylindrical coordinates (r, ϕ, z) has only an axial component,

$$A_r = A_z = 0, \quad A_\phi = A_\phi(r, z).$$

1063-780X/05/3111-0961$26.00

We again assume that the ions originate exclusively at the magnetron cutoff surface for electrons and that the electrons and ions move in nested cylindrical surfaces of radii $r(z)$ and have the same radial and longitudinal velocities. We also assume that, at the cutoff point (i.e., at $r = r_0$ and $z = z_0$), the following conditions are satisfied:

$$\dot{r}(r_0, z_0) = 0, \quad \dot{z}(r_0, z_0) = 0, \tag{1}$$

where the superior dot denotes differentiation over time. Hence, by analogy with [9], we are interested in a class of solutions for which $r_e(t) = r_i(t) \equiv r(t)$ and $z_e(t) = z_i(t) \equiv z(t)$.

Let us consider one of the nested surfaces, and let the coordinates $r = r_c$ and $z = z_c$ correspond to the cathode plasma boundary. The equations of motion for the electrons have the form

$$\ddot{r} - r\dot{\phi}^2 = -\frac{eE_r}{m} - \frac{e}{mc}\dot{\phi}\frac{\partial(rA_\phi)}{\partial r}, \tag{2a}$$

$$r\ddot{\phi} + 2\dot{r}\dot{\phi} = \frac{e}{mc}\dot{z}\frac{\partial A_\phi}{\partial z} + \frac{e}{mc}\frac{\dot{r}}{r}\frac{\partial(rA_\phi)}{\partial r}, \tag{2b}$$

$$\ddot{z} = -\frac{eE_z}{m} + \frac{e}{mc}r\dot{\phi}\frac{\partial A_\phi}{\partial z}. \tag{2c}$$

Since the magnetic field has essentially no impact on the heavy ions, the equations of ion motion can be written as

$$\ddot{r} = \frac{e}{M}E_r, \tag{3a}$$

$$\ddot{z} = \frac{e}{M}E_z. \tag{3b}$$

Because of the smallness of the ratio m/M, we can ignore the terms with $\ddot{r}$ and $\ddot{z}$ in Eqs. (2a) and (2c). From Eq. (2b) we readily obtain

$$r^2\dot{\phi} - \frac{e}{mc}rA_\phi = \text{const}.$$

Since the time derivative of the axial coordinate at the cathode plasma boundary $z = z_c$ vanishes, $\dot{\phi} = 0$, we have

$$\dot{\phi} = \frac{e}{mc}\frac{1}{r^2}[rA_\phi(r, z) - r_cA_\phi(r_c, z_c)].$$

For the electric field components, we then obtain the expressions

$$E_r = \frac{e}{mc^2}\frac{1}{r}\left\{\frac{1}{r}[rA_\phi(r, z) - r_cA_\phi(r_c, z_c)]^2 - [rA_\phi(r, z) - r_cA_\phi(r_c, z_c)]\frac{\partial}{\partial r}(rA_\phi)\right\},$$

$$E_z = -\frac{e}{mc^2}\frac{1}{r}[rA_\phi(r, z) - r_cA_\phi(r_c, z_c)]\frac{\partial A_\phi}{\partial z}.$$

Hence, the sought-for surface $r(z)$ is described parametrically by the set of equations

$$\frac{d^2\rho}{d\tau^2} = \frac{1}{\rho^2}\left\{\frac{1}{\rho}[\rho A(\rho, \zeta) - \rho_cA(\rho_c, \zeta_c)]^2 - [\rho A(\rho, \zeta) - \rho_cA(\rho_c, \zeta_c)]\frac{\partial}{\partial\rho}(\rho A)\right\}, \tag{4a}$$

$$\frac{d^2\zeta}{d\tau^2} = -\frac{1}{\rho}[\rho A(\rho, \zeta) - \rho_cA(\rho_c, \zeta_c)]\frac{\partial A}{\partial\zeta}, \tag{4b}$$

where we have introduced the dimensionless variables

$$\rho = \frac{r}{R_0}, \quad \zeta = \frac{z}{R_0}, \quad \tau = \frac{t}{T}, \quad T = \sqrt{\frac{M}{m}}\left(\frac{mcR_0}{eA_0}\right), \quad A = \frac{A_\phi}{A_0},$$

with $A_0 = H_0R_0$ being the characteristic value of the vector potential. In accordance with conditions (1), the boundary conditions for Eqs. (4) have the form

$$\rho(0) = \rho_0, \quad \zeta(0) = \zeta_0, \quad \left.\frac{d\rho}{d\tau}\right|_{\tau=0} = 0, \quad \left.\frac{d\zeta}{d\tau}\right|_{\tau=0} = 0. \tag{5}$$

The set of Eqs. (4) has the first integral

$$\left(\frac{d\rho}{d\tau}\right)^2 + \left(\frac{d\zeta}{d\tau}\right)^2 + 2\psi(\rho, \zeta) = 2\psi(\rho_0, \zeta_0),$$

where

$$\psi(\rho, \zeta) = \frac{1}{2\rho^2}[\rho A(\rho, \zeta) - \rho_cA(\rho_c, \zeta_c)]^2 \tag{6}$$

is the dimensionless electric field potential.

We are now to find an equation for the cutoff surface $\rho_0(\zeta_0)$. Since the potential at this surface has the form

$$\psi(\zeta_0) = \psi(\rho_0(\zeta_0), \zeta_0),$$

we obtain

$$\frac{d\psi}{d\zeta_0} = \left.\frac{\partial\psi}{\partial\rho}\right|_{\rho_0, \zeta_0}\frac{d\rho_0}{d\zeta_0} + \left.\frac{\partial\psi}{\partial\zeta}\right|_{\rho_0, \zeta_0}.$$

On the other hand, expression (6) yields the relationships

$$\frac{\partial\psi}{\partial\rho} = -\frac{1}{\rho}\left\{2\psi(\rho,\zeta) - \sqrt{2\psi(\rho,\zeta)}\frac{\partial}{\partial\rho}(\rho A)\right\},$$

$$\frac{\partial\psi}{\partial\zeta} = \sqrt{2\psi(\rho,\zeta)}\frac{\partial A}{\partial\zeta}.$$

Therefore, if the potential distribution over the cutoff surface, $\psi(\zeta_0)$, is prescribed, this surface satisfies the equation

$$\rho_0(\zeta_0)[u_0(\zeta_0) - A(\zeta_0)] = \text{const},$$

where

$$u_0(\zeta_0) = \sqrt{2\psi(\zeta_0)}$$

is the dimensionless ion velocity at the cathode boundary of the layer. For definiteness, we set

$$A(1, \zeta_{00}) = 1, \tag{7}$$

and, as a result, obtain

$$\rho_0(\zeta_0)[u_0(\zeta_0) - A(\rho_0, \zeta_0)] = u_0(\zeta_{00}) - 1. \tag{8}$$

The equation for the equipotential cutoff surface, $u_0(\zeta_0) = u_0 = \text{const}$, has the form

$$\rho_0(\zeta_0)A(\rho_0, \zeta_0) = \rho_0(\zeta_0)u_0 - u_0 + 1. \tag{9}$$

Using this equation and also relationship (6), which, for the equipotential cutoff surface, has the form

$$\rho_c(\zeta_c)A(\rho_c, \zeta_c) = \rho_0(\zeta_0)A(\rho_0, \zeta_0) - \rho_0(\zeta_0)u_0,$$

we arrive at the equation for the cathode plasma boundary,

$$\rho_c(\zeta_c)A(\rho_c, \zeta_c) = 1 - u_0. \tag{10}$$

From this equation we see that, when the cutoff surface is equipotential, the plasma boundary always coincides with a magnetic field line.

In the context of the above results, the particular case of a vector potential of the form

$$\frac{h\rho}{2} - \frac{\zeta}{\rho}$$

was considered in [9]. Here, $h = H_z/H_0$, with $H_z = \text{const}$ being a constant longitudinal magnetic field.

The tangent of the angle of inclination of the ion trajectories at the cutoff surface to the z axis is equal to

$$\tan\alpha_0 = \frac{\ddot{\rho}(0)}{\ddot{\zeta}(0)} = -\frac{1}{\rho_0\left.\dfrac{\partial A}{\partial\zeta}\right|_{\rho_0,\zeta_0}}\left[u_0 - \left.\frac{\partial}{\partial\rho}(\rho A)\right|_{\rho_0,\zeta_0}\right].$$

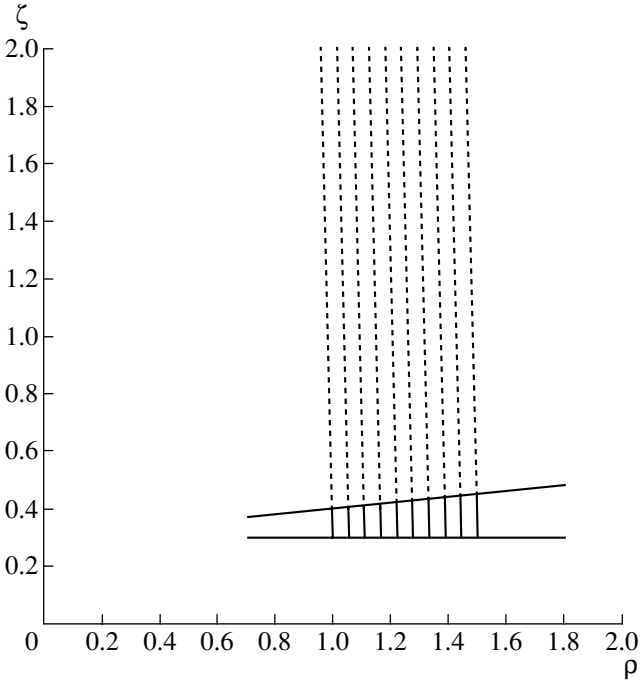

Fig. 1. Ion trajectories for $u_0 = 0.1$ and $\zeta_{00} = 0.3$.

On the other hand, Eq. (9) implies that the tangent of the angle of inclination of the cutoff surface itself is equal to

$$\frac{d\rho_0(\zeta_0)}{d\zeta_0} = \frac{\rho_0\left.\dfrac{\partial A}{\partial\zeta}\right|_{\rho_0,\zeta_0}}{u_0 - \left.\dfrac{\partial}{\partial\rho}(\rho A)\right|_{\rho_0,\zeta_0}},$$

so that the ion trajectories are always perpendicular to this surface.

3. Let us require that the cutoff surface coincide with the plane $\zeta_0 = \zeta_{00}$, i.e., that the condition $\tan\alpha_0 = 0$ be satisfied. Under this condition, the following equation should be valid in a certain spatial region near the cutoff surface:

$$\frac{\partial}{\partial\rho}(\rho A) = u_0. \tag{11}$$

This equation has the solution

$$A(\rho, \zeta) = u_0 + \frac{f(\zeta)}{\rho}, \tag{12}$$

where $f(\zeta)$ is an arbitrary function. The shape of the plasma boundary depends on the form of the function $f(\zeta)$, and the dimensionless magnetic field components can be written as

$$H_\rho = -\frac{\partial A}{\partial\zeta} = -\frac{1}{\rho}\frac{df}{d\zeta}, \quad H_\zeta = \frac{1}{\rho}\frac{\partial}{\partial\rho}(\rho A) = \frac{u_0}{\rho}. \tag{13}$$

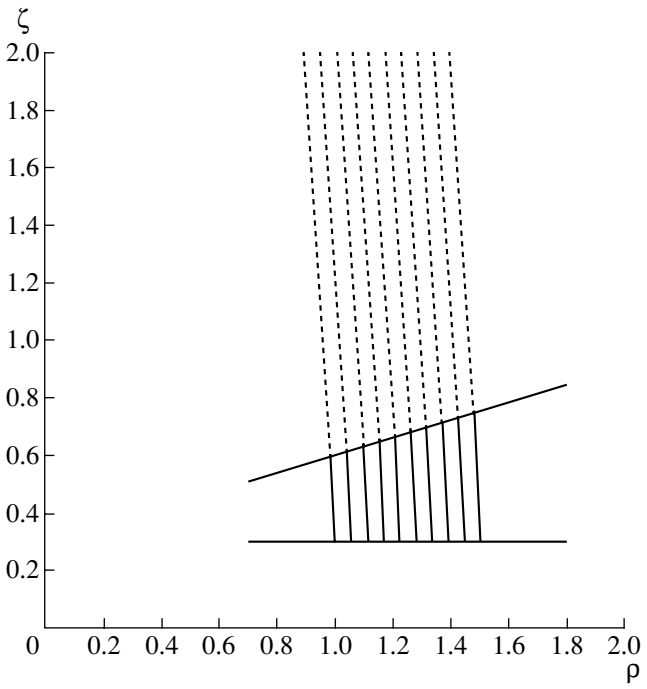

Fig. 2. Ion trajectories for $u_0 = 0.3$ and $\zeta_{00} = 0.3$.

For instance, for $df/d\zeta = -1$, taking into account relationship (7), we obtain

$$A(\rho, \zeta) = u_0 + \frac{1 - u_0 + \zeta_{00} - \zeta}{\rho}. \qquad (14)$$

The ion trajectories that were calculated in dimensionless coordinates by numerically solving the set of Eqs. (4) with boundary conditions (5) for vector potential (14) with $u_0 = 0.1$ and $\zeta_{00} = 0.3$ and with $u_0 = 0.3$ and $\zeta_{00} = 0.3$ are shown in Figs. 1 and 2, respectively. We see that, for small values of the parameter u_0, the ion beam is essentially parallel to the ζ axis. We also see that, as this parameter increases, the beam becomes slightly convergent to the axis. The parameter u_0, which determines the maximum dimensionless ion velocity, is equal to the ratio of the gyroradius of the electrons with energy $e\varphi_0$ in a constant magnetic field H_0 (in the case at hand, this is the radial magnetic field component at the point with the coordinates $r = R_0$ and $z = \zeta_{00}R_0$) to the radius of the system R_0, $u_0 = \rho_e(\varphi_0)/R$. In the units in which the potential difference is expressed in volts, the magnetic field strength is in gausses, and the radius is in centimeters, this parameter is

$$u_0 \approx 3.37\frac{\sqrt{\varphi_0}}{H_0 R_0}.$$

Thus, for $R_0 = 2.6$ cm and $\varphi_0 = 250$ V, we have $u_0 \approx 0.315$ for $H_0 = 65$ G and $u_0 \approx 0.103$ for $H_0 = 200$ G.

To summarize, in the present paper, it has been shown that, with magnetic field configuration (13) created by an axisymmetric system of ring currents, it is possible to make the electron cutoff surface planar and perpendicular to the system axis and, accordingly, to form slightly converging ion beams or those that are essentially parallel to the system axis.

ACKNOWLEDGMENTS

I am grateful to A.V. Zharinov for formulating this problem and for fruitful discussions and to A.N. Ermilov for his sympathetic attitude and encouragement of the work.

This work was supported in part by the Russian Foundation for Basic, project nos. 05-02-08030 and 05-02-16081.

REFERENCES

1. S. Chapman and V. C. A. Ferraro, Terr. Magn. Atmos. Elect. **45** (3), 245 (1940).
2. V. C. A. Ferraro, J. Geophys. Res. **57**, 15 (1952).
3. L. A. Artsimovich, *Controlled Thermonuclear Reactions*, Ed. by A. Kolb and R. S. Pease (Fizmatgiz, Moscow, 1961; Gordon & Breach, New York, 1964).
4. A. I. Morozov, in *Encyclopedia of Low-Temperature Plasma*, Ed. by V. E. Fortov (Nauka, Moscow, 2000), Vol. 3, p. 383 [in Russian].
5. S. D. Grishin, in *Encyclopedia of Low-Temperature Plasma*, Ed. by V. E. Fortov (Nauka, Moscow, 2000), Vol. 4, p. 291 [in Russian].
6. A. I. Morozov, Fiz. Plazmy **29**, 261 (2003) [Plasma Phys. Rep. **29**, 235 (2003)].
7. A. V. Zharinov and Yu. S. Popov, Zh. Tekh. Fiz. **37**, 294 (1967) [Sov. Phys. Tech. Phys. **12**, 208 (1967)].
8. M. A. Vlasov, A. V. Zharinov, and Yu. A. Kovalenko, Zh. Tekh. Fiz. **71** (12), 34 (2001) [Tech. Phys. **46**, 1522 (2001)].
9. V. P. Shumilin, Fiz. Plazmy **31**, 453 (2005) [Plasma Phys. Rep. **31**, 412 (2005)].

Translated by O.E. Khadin

Plasma Physics Reports, Vol. 31, No. 11, 2005, pp. 965–977. Translated from Fizika Plazmy, Vol. 31, No. 11, 2005, pp. 1038–1050.

LOW-TEMPERATURE PLASMA

Self-Consistent Simulation of Pulsed and Continuous Microwave Discharges in Hydrogen

V. A. Koldanov, A. M. Gorbachev, A. L. Vikharev, and D. B. Radishchev

Institute of Applied Physics, Russian Academy of Sciences, ul. Ul'yanova 46, Nizhni Novgorod, 603600 Russia

Received November 9, 2004; in final form, December 10, 2004

Abstract—Results are presented from numerical simulations of pulse-periodic and continuous microwave discharges in hydrogen that are used in CVD reactors for chemical vapor deposition of diamond films. Attention is focused on the processes that should be taken into account in order to construct the simplest possible adequate numerical model. It is shown that the processes of vibrational excitation of hydrogen molecules, as well as chemical reactions, play an important role in the establishment of energy balance within the discharges. The results of numerical simulations are compared to the experimental data. *© 2005 Pleiades Publishing, Inc.*

1. INTRODUCTION

The process of chemical vapor deposition (CVD) of diamond films in microwave discharge plasmas has been actively studied in recent years [1]. In CVD reactors, the working gas mixture is hydrogen with a small addition of carbon-containing gas (usually methane). One purpose of this research is to seek conditions for synthesizing diamond films (DFs) at faster rates than those achievable in existing reactors. The DF growth rate is determined by the rates of production of radicals within the plasma and of their transport to the substrate, as well as by the rates of surface reactions. It is difficult to improve the technology of plasma synthesis of DFs without developing a model that would adequately describe the processes occurring in CVD reactors. Although there are a number of papers devoted to constructing models of a CVD reactor [2–6], the problem is still far from being completely resolved. The reason for this is that, even in the simplest case of a microwave discharge in pure hydrogen, it is very difficult to consider all the processes that occur in the discharge plasma. Another difficulty is that the lack of experimental data on the cross sections and rate constants of the processes raises the probability of error. This is why the model should be tested against its capability of predicting the experimentally measurable parameters (such as the gas temperature and the degree of hydrogen dissociation).

In the present paper, a numerical model is constructed by using the experimental results reported in [7]. For simulations, we chose a CVD reactor based on a cylindrical cavity excited at an axisymmetric TM_{013} mode by a magnetron with an operating frequency of 2.45 GHz and a power of 1–5 kW (Fig. 1). The reactor is similar in design to that developed in the Michigan State University (United States) [1]. In such a reactor, microwave discharges are initiated in a quartz dome placed in the bottom part of the cavity. The flange on which the quartz dome is mounted has holes for supplying and pumping out the gas mixture. The movable upper wall of the cavity makes possible the tuning to the working frequency. In the experiments of [7], DFs were synthesized in both pulse-periodic (with a pulse duration of 5 ms and repetition rate of 100 Hz) and continuous regimes of microwave discharge maintenance in hydrogen–methane mixtures at the same average microwave power. Some of the experiments were carried out with a working gas mixture containing 1–5% of argon or nitrogen for diagnostic purposes.

In [7], the gas-discharge plasma was diagnosed by the optical emission spectroscopy (OES) method. Radiation from the plasma was focused onto the vertical entrance slit of a monochromator, i.e., emission was recorded from a relatively thin (of thickness on the order of 1 mm) vertical discharge layer, as is shown schematically in Fig. 2. The OES method was used to determine the degree of dissociation of molecular hydrogen, the gas temperature, and the intensities of the spectral lines of argon and atomic hydrogen. The microwave power reflected from the cavity was also recorded in the experiments. These parameters were used to check the adequacy of the model.

This work is a continuation of [8], which was aimed at developing a self-consistent numerical model of a microwave discharge in a CVD reactor. The main requirements for the model are rapid computations and correct predictions of the measured values over a broad range of external parameters. These somewhat contradictory requirements can only be met by taking into account the processes that really play an important role. The primary goal of the present paper is to choose the processes that are indeed necessary for the construction of the model. This is done by detailed comparisons of the simulation results to the experimental data. Attention is focused on pulse-periodic microwave discharges, because studying dynamic processes in them

1063-780X/05/3111-0965$26.00

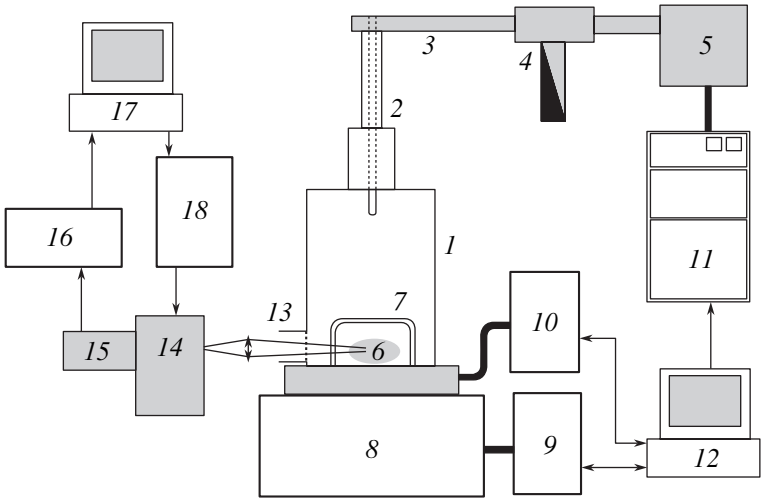

Fig. 1. Schematic of the experimental device: (*1*) cylindrical cavity, (*2*) cavity tuner, (*3*) waveguide line, (*4*) circulator with an absorber of the reflected microwave power, (*5*) magnetron, (*6*) microwave discharge region, (*7*) quartz tube, (*8*) buffer vacuum volume, (*9*) pumping-out system, (*10*) gas supply system, (*11*) magnetron power supply system, (*12*) control computer, (*13*) diagnostic window, (*14*) MDR-41 monochromator, (*15*) photomultiplier, (*16*) digital oscilloscope, (*17*) computer, and (*18*) monochromator control system.

provides more information than can be obtained from investigating continuous discharges.

2. DESCRIPTION OF THE MODEL

Since the reactor under consideration is axisymmetric, it can be described by a two-dimensional model. The two-dimensional self-consistent model that was developed for describing a microwave discharge in hydrogen can be conventionally divided into the following modules:

(i) The electrodynamic module for calculating the electromagnetic fields in a reactor by the finite-difference time-domain (FDTD) method [9], in which the plasma is accounted for in terms of the conduction currents. This module yields the distribution of the rms microwave field over the discharge volume and the reflected microwave power (averaged over the microwave field period).

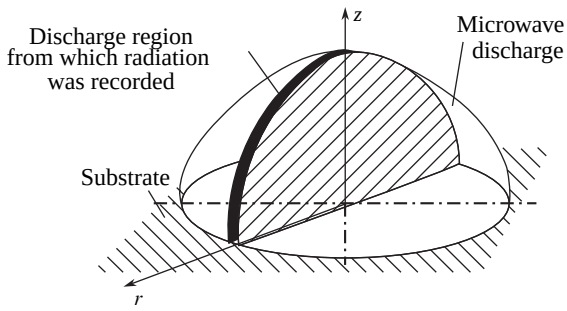

Fig. 2. Schematic representation of a discharge in the microwave cavity.

(ii) The plasma module for calculating the plasma density in the discharge on the basis of the electron balance equation under the assumption of a local relationship between the electron temperature and the microwave field and with allowance for diffusion and plasma transport by gas flows. The rate constants of reactions involving electrons are determined based on the data on the electron distribution function that were calculated in [10].

(iii) The gas-dynamic module for calculating the density, temperature, and velocity of a neutral gas.

(iv) The module for calculating the density of atomic hydrogen in a discharge from the balance equation with allowance for diffusion and plasma transport by gas flows.

(v) The module for calculating the discharge parameters associated with the vibrational kinetics of molecular hydrogen. This module takes into account the *e–V* and *V–T* relaxation processes and calculates the vibrational temperature of hydrogen molecules, the electron-impact dissociation of hydrogen molecules in vibrationally excited states, and the energy expended on gas heating.

(vi) The module for calculating the averaged discharge parameters that are measured in experiments.

This division of the model into modules is rather conventional. As will be seen below, the processes that are taken into account in the model exert considerable influence on each other. Only the first two modules may be regarded as relatively independent of the others: being related to one another, they are only slightly cou-

pled to the remaining modules. Let us now describe each module in more detail.

2.1. Electrodynamic and Plasma Modules

As in [8], the electromagnetic field distributions in a cylindrical cavity are calculated from Maxwell's equations by the FDTD method [9], in which the effect of the plasma is accounted for by introducing the conduction currents:

$$\begin{aligned} \nabla \times \mathbf{E} &= -\frac{1}{c}\frac{\partial \mathbf{H}}{\partial t}, \\ \nabla \times \mathbf{H} &= \frac{1}{c}\frac{\partial \mathbf{E}}{\partial t} + \frac{4\pi}{c}\mathbf{j}, \\ \frac{\partial \mathbf{j}}{\partial t} &= \frac{e^2}{m}N_e\mathbf{E} - \nu_m(N)\mathbf{j}, \end{aligned} \tag{1}$$

where $\mathbf{j}$ is the current density; $\nu_m(N)$ is the electron–molecule collisions frequency, which depends on the gas density N; c is the speed of light; and e and m are the charge and mass of an electron. This calculation method provides high accuracy and makes it possible to describe the effect of the plasma on the electromagnetic field distribution in a fairly simple way.

The electron density is obtained from the ionization–recombination balance equation

$$\begin{aligned} \frac{\partial N_e}{\partial t} &= k_i(T_e)NN_e - \alpha N_e^2 + \nabla \cdot (D_a \nabla N_e) \\ &\quad - \nabla \cdot (\mathbf{u}N_e), \end{aligned} \tag{2}$$

where $k_i(T_e)$ is the constant of the electron-impact ionization [10], $\alpha\left[\frac{\text{cm}^3}{\text{s}}\right] = 2.3 \times 10^{-7}\sqrt{300/T_e\,[\text{K}]}$ is the constant of the electron dissociative recombination [4], and $D_a\left[\frac{\text{cm}^3}{\text{s}}\right] = \frac{11.1T^2\,[\text{K}]}{4 \times 10^3 p\,[\text{torr}]}\left(1 + \frac{T_e}{T}\right)$ is the ambipolar diffusion coefficient [4]. It was shown in [11] that the main ions in a hydrogen plasma are the H_3^+ ions produced from the primary ions H_2^+ in the fast reaction $H_2^+ + H_2 \longrightarrow H_3^+ + H$. The effective electron temperature is given by the relationship $T_e\,[\text{K}] = T_V\,[\text{K}] + 390E_e/N\,[\text{Td}]$, which was obtained by approximating the dependence of the electron temperature on the reduced electric field E/N and on the vibrational gas temperature T_V (see [10]). For microwave fields, the effective field is equal to $E_e\,[\text{V/cm}] = \frac{E}{\sqrt{1 + \omega^2/\nu_m^2}}$, where E is the rms field. The last term on the right-hand side of Eq. (2) describes plasma transport by neutral gas flows; in this equation, $\mathbf{u}$, p, T, and N are, respectively, the velocity, pressure, temperature, and density of the neutral gas. Equation (2) is supplemented with the boundary conditions $\left.\frac{\partial N_e}{\partial r}\right|_{r=0} = 0$ and $N_e|_S = 0$, where S is the area of the surface enclosing the discharge volume.

2.2. Gas-Dynamic Module

The structure and parameters of the discharge are determined, to a great extent, by the neutral gas heating processes. The full set of gas-dynamic equations for an ideal gas has the form

$$\begin{aligned} \frac{\partial N}{\partial t} &= -\nabla \cdot (N\mathbf{u}) + \frac{1}{2}\frac{\partial [\text{H}]}{\partial t}, \\ \frac{\partial \mathbf{u}}{\partial t} + (\mathbf{u} \cdot \nabla)\mathbf{u} &= -\frac{\nabla p}{\rho} + \mathbf{g} + \frac{\eta(T)}{\rho}\Delta\mathbf{u}, \\ \frac{\partial p}{\partial t} + (\mathbf{u} \cdot \nabla)p + \gamma p \nabla \cdot \mathbf{u} &= (\gamma - 1)\{Q_\Sigma + \nabla \cdot (\lambda(T)\nabla T)\}, \\ T &= p/Nk_B, \end{aligned} \tag{3}$$

where ρ is the mass density, $\eta(T)$ is the dynamic viscosity, γ is the adiabatic index, $\lambda(T)$ is the gas thermal conductivity, $\mathbf{g}$ is the gravitational acceleration, and Q_Σ is an external source for gas heating. The last term on the right-hand side of the first of Eqs. (3) describes the change in the gas density via the dissociation and recombination of hydrogen. In the model described in [8], the term Q_Σ is calculated by a simplified method from the formula

$$Q_\Sigma = \delta\sigma E^2, \tag{4}$$

where δ is the fraction of the absorbed microwave power that is spent on gas heating, σ is the plasma conductivity, and E is the rms electric field. The calculations were usually carried out for $\delta = 0.4$. Such a description is very rough, however. It will be shown below that, in order to evaluate the source term Q_Σ correctly, it is necessary to take into account the energy balance in the chemical reactions occurring in the reactor and also the vibrational kinetics of molecular hydrogen.

The set of Eqs. (3) is extremely difficult to analyze, and its numerical integration also runs into serious difficulties. Specifically, an explicit computational scheme becomes unstable in calculating the nascent acoustic and shock waves [12]. In order to make the scheme stable, the time step should be substantially shortened, which markedly reduces the computational speed. Accounting for gas viscosity fails to achieve the desired effect because, on the one hand, hydrogen viscosity is very low and, on the other, an artificial increase in the viscosity appreciably changes the velocities of the established flows.

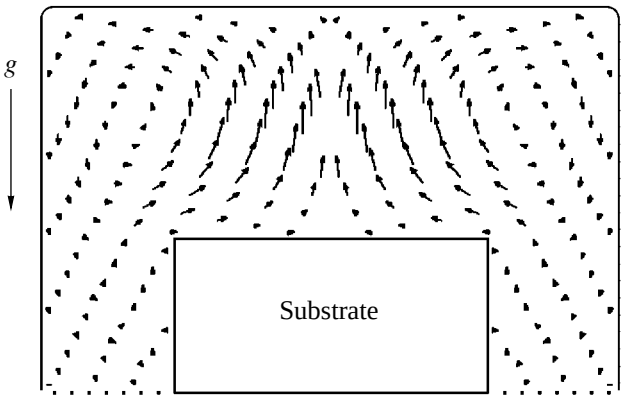

Fig. 3. Schematic diagram of the established gas flows in a CVD reactor.

Equations (3) can be simplified by examining them in the isobaric approximation. Estimates show that this approximation is valid for characteristic gas heating times longer than or about 1 ms (which corresponds to about ten transits of an acoustic wave across the discharge volume). In the isobaric approximation, the set of gas-dynamic equations reads

$$\begin{aligned} \frac{\partial N}{\partial t} &= -\nabla \cdot (N\mathbf{u}) + \frac{1}{2}\frac{\partial [\mathrm{H}]}{\partial t}, \\ \gamma p \nabla \cdot \mathbf{u} &= (\gamma - 1)\{Q_\Sigma + \nabla \cdot (\lambda(T)\nabla T)\}, \\ T &= p/Nk_B. \end{aligned} \tag{5}$$

In order to determine the gas velocity **u**, the second of Eqs. (5) can be written in terms of the velocity potential φ [13]

$$\begin{aligned} \mathbf{u} &= -\nabla\varphi, \\ \Delta\varphi &= -\frac{\gamma - 1}{\gamma p}\{Q_\Sigma + \nabla \cdot (\lambda(T)\nabla T)\}. \end{aligned} \tag{6}$$

The main drawback of Eqs. (5) and (6) is that they do not take into account vortex flows (in particular, those associated with convection). In addition, the calculation of the velocity potential in two-dimensional geometry takes a large amount of computer time.

This is why the main purpose in constructing the gas-dynamic module of the model was to find such a method for solving the gas-dynamic equations that would keep the explicit scheme stable, would provide its rapid convergence, would make it possible to calculate the convective flows, and would satisfy the isobaric approximation.

In this way, set of gas-dynamic equations (3) was reduced to the form

$$\begin{aligned} \frac{\partial \mathbf{u}}{\partial t^*} &= -\frac{\nabla \tilde{p}}{\rho} + \mathbf{g} + \frac{\eta(T)}{\rho}\Delta\mathbf{u}, \\ \frac{\partial \tilde{p}}{\partial t^*} &+ \gamma p \nabla \cdot \mathbf{u} \\ &= (\gamma - 1)\{Q_\Sigma + \nabla \cdot (\lambda(T)\nabla T)\} - \nu_{\mathrm{eff}}\tilde{p}, \end{aligned} \tag{7}$$

where $\tilde{p}$ is a small deviation from the equilibrium pressure p, $\tilde{p} \ll p$; $\nu_{\mathrm{eff}} = \dfrac{1}{10\partial t^*}$ is the artificially introduced damping rate of acoustic waves, and t^* is the effective time with which to implement the iterative process.

It is important to note that the set of Eqs. (7) can be integrated numerically by the FDTD method, which is commonly used to determine microwave fields in electrodynamic systems. In accordance with this method, either one of the components of the gas velocity or the deviation of the gas pressure from its equilibrium value was calculated at a point of the numerical grid. In this case, the conditions at the boundaries of the computation region implied that the walls of the cavity were impenetrable by the gas, $(\mathbf{u} \cdot \mathbf{n})_S = 0$, where **n** is the normal to the boundary. The only exception was the lower boundary of the computation region (Fig. 3), through which the gas could flow freely into the buffer volume (Fig. 1) and at which the boundary condition was $\tilde{p} = 0$. Additional gas flows associated with the pumping of gas through the reactor were not accounted for in the model. The temperature at the boundary of the discharge region was treated as an external parameter. In calculations, the temperature of the quartz dome was usually assumed to be equal to 700 K and the temperature of the substrate was taken to be that measured by an IR pyrometer.

The solution to Eqs. (7) rapidly converges to that for an isobaric gas flow because all pressure perturbations are damped by an artificially introduced viscosity. In computations, we used the effective time step $\partial t^* =$ 100 ns, which was chosen to satisfy the stability condition for the difference scheme, $\partial t^* < h/u_c$, where h is the spatial grid spacing and u_c is the maximum speed of sound. The established values of the gas flow velocities that were calculated from Eqs. (7) were used to find the new values of the gas density and temperature from the continuity equation (the first of Eqs. (3)) and the equation of state of an ideal gas (the last of Eqs. (3)).

Hence, the method proposed here is, in essence, a version of the well-known method of separate sweeps [12]. In contrast to Eqs. (5) and (6), it allows one to take into account the vortex (in particular, convective) flows occurring in the reactor. Figure 3 shows a schematic diagram of established gas flows in a CVD reactor for an incident microwave power of 1.5 kW at a pressure of

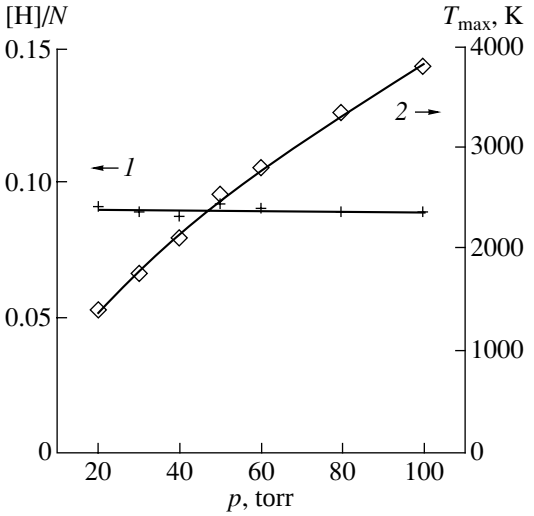

Fig. 4. (*1*) Degree of hydrogen dissociation and (*2*) the maximum gas temperature in the discharge vs. gas pressure at an absorbed microwave power of 2 kW [8].

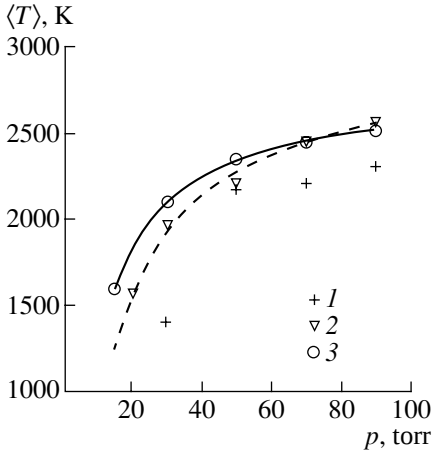

Fig. 5. Gas temperature vs. gas pressure in a continuous discharge at an absorbed microwave power of 1.5 kW: (*1*) experimental data and results of calculations (*2*) without and (3) with allowance for the vibrational kinetics of molecular hydrogen.

20 torr. It should be noted that, under the conditions in question, the velocities of the convective flows are lower than 10 cm/s, so the flows do not have any significant influence on the discharge structure. In addition, the method proposed allows the speed of the calculation to be substantially increased (by two to three times) in comparison to the case in which the solution is found in terms of the velocity potential from Eqs. (5) and (6).

2.3. Module for Calculating Atomic Hydrogen Density

Initially, the atomic hydrogen density in a discharge was calculated without allowance for the vibrational kinetics of hydrogen. In the balance equation for the atomic hydrogen density, account was taken of such processes as the electron-impact dissociation of hydrogen molecules from the ground state, the diffusion of atomic hydrogen and its transport by gas flows, and also (in contrast with the model of [8]) the thermal dissociation and three-body recombination. That the last two processes should be taken into account follows immediately from the simulation results of [8]. For instance, the results obtained in [8] show that the maximum gas temperature increases rapidly with pressure and becomes as high as 3000–4000 K (see Fig. 4). At such high temperatures, however, the production of atomic hydrogen should be dominated by the reaction of the thermal decomposition of hydrogen [14, 15], which was not accounted for in the model of [8]:

$$H_2 + N \longleftrightarrow H + H + N. \quad (8)$$

With allowance for reaction (8), the atomic hydrogen density in a discharge is described by the expression

$$\frac{\partial [H]}{\partial t} = 2(k_d(T_e)N_e + k_T(T)N)[H_2] - 2k_R(T)[H]^2 N + \nabla \cdot \left(\frac{D_H(T)}{T}\nabla(T[H])\right) - \nabla \cdot ([H]\mathbf{u}). \quad (9)$$

Here, k_d is the electron-impact dissociation constant; D_H is the coefficient of diffusion of atomic hydrogen in molecular hydrogen; and k_T and k_R are the thermal dissociation (direct reaction (8)) and three-body recombination (reverse reaction (8)) constants, respectively [14, 15]. Equation (9) is supplemented with the same boundary conditions as those used to calculate the electron density.

It should be noted that direct reaction (8) releases an energy equal to $\varepsilon_{dis} = 4.8$ eV, which may play an important role in the overall energy balance. With allowance for reaction (8), the resulting specific power going into gas heating is given by the formula

$$Q_\Sigma = \delta\sigma E^2 - Q_{dis}, \quad (10)$$

where the term $Q_{dis} = \varepsilon_{dis}(k_T(T)[H_2] - k_R(T)[H]^2)N$ describes the energy balance in reaction (8).

It was found that the results computed with allowance for the above additional reactions differ substantially from those presented in [8] (see Fig. 4). Figure 5 shows how the experimental and calculated gas temperatures depend on the gas pressure in a continuous microwave discharge. We can see that, when the energy losses due to hydrogen dissociation were taken into account, the calculated gas temperature at high pressures was significantly lower, providing much better

agreement with the experimental data. In fact, this energy loss mechanism is so efficient that it limits the gas temperature to a level of 2500–2700 K. The overall energy balance and the energy transport mechanisms will be discussed in more detail below.

2.4. Module for Calculating Hydrogen Vibrational Kinetics

For characteristic values of the reduced electric field, $E/N \sim 50$ Td, the main mechanism for heating a molecular gas in the CVD reactor under consideration is the *V–T* relaxation process. The reason is that, in molecular gases, the electrons most efficiently transfer their energy to the vibrational degrees of freedom of the molecules. As a result, the fraction δ of the absorbed microwave power that goes into gas heating depends on the plasma state at each point of the discharge region. In addition, the vibrational excitation of hydrogen molecules markedly changes the rate of their dissociation. This is why the gas temperature and atomic hydrogen density in the discharge should be calculated with allowance for the vibrational kinetics of molecular hydrogen.

In the model proposed here, the vibrational excitation of hydrogen molecules in the discharge was described without allowance for the anharmonicity of the molecular vibrations under the assumption that the *V–V* exchange is the fastest process [16]. The distribution of hydrogen molecules over the vibrational degrees of freedom at energies lower than the dissociation energy was assumed to be a Boltzmann distribution with the temperature T_V:

$$[\mathrm{H}_2(v)] = [\mathrm{H}_2]\frac{1-\exp(-\varepsilon_{\mathrm{vib}}/T_V)}{1-\exp(-\varepsilon_{\mathrm{dis}}/T_V)}\exp(-v\varepsilon_{\mathrm{vib}}/T_V) \quad \text{for} \quad v\varepsilon_{\mathrm{vib}} < \varepsilon_{\mathrm{dis}}, \tag{11}$$

where v is the number of the vibrational level and $\varepsilon_{\mathrm{vib}}$ is the vibrational quantum energy. In the *V–T* and *e–V* processes, only transitions from the zeroth to the first vibrational level and back were taken into account. This is justified because the rate of excitation of the vibrational levels decreases rapidly with increasing v and also when $T_V \ll \varepsilon_{\mathrm{dis}}$,

$$\begin{aligned}\mathrm{H}_2(v=0) + e &\longleftrightarrow \mathrm{H}_2(v=1) + e\\ \mathrm{H}_2(v=0) + \mathrm{M} &\longleftrightarrow \mathrm{H}_2(v=1) + \mathrm{M}.\end{aligned} \tag{12}$$

When the vibrational temperature is not too high, $T_V \ll \varepsilon_{\mathrm{dis}}$, the balance equation for the energy stored in molecular vibrations has the form

$$\begin{aligned}\frac{\partial W_{\mathrm{vib}}}{\partial t} &= Q_e - Q_{VT}^{\mathrm{H}_2} - Q_{VT}^{\mathrm{H}} - Q_{\mathrm{dis}}^{\mathrm{vib}}\\ &+ \nabla\cdot(\alpha_V \nabla W_{\mathrm{vib}}) - \nabla\cdot(W_{\mathrm{vib}}\mathbf{u}),\end{aligned} \tag{13}$$

where $W_{\mathrm{vib}} = \dfrac{\varepsilon_{\mathrm{vib}}[\mathrm{H}_2]}{\exp(\varepsilon_{\mathrm{vib}}/T_V)-1}$ is the vibrational energy density.

The first three terms on the right-hand side of Eq. (13) describe the following processes: the excitation and quenching of vibrations in collisions with electrons (*e–V* relaxation) [16],

$$\begin{aligned}Q_e &= \varepsilon_{\mathrm{vib}} N_e\{k_{0-1}^e(T_e)[\mathrm{H}_2(v=0)]\\ &- k_{1-0}^e(T_e)[\mathrm{H}_2(v=1)]\};\end{aligned} \tag{14}$$

the excitation and quenching of vibrations in collisions with hydrogen molecules (*V–T* relaxation) [16],

$$\begin{aligned}Q_{VT}^{\mathrm{H}_2} &= \varepsilon_{\mathrm{vib}}[\mathrm{H}_2]\{k_{0-1}^{\mathrm{H}_2}(T)[\mathrm{H}_2(v=1)]\\ &- k_{1-0}^{\mathrm{H}_2}(T)[\mathrm{H}_2(v=0)]\};\end{aligned} \tag{15}$$

and the excitation and quenching of vibrations in collisions with hydrogen atoms (*V–T* relaxation) [16],

$$\begin{aligned}Q_{VT}^{\mathrm{H}} &= \varepsilon_{\mathrm{vib}}[\mathrm{H}]\{k_{0-1}^{\mathrm{H}}(T)[\mathrm{H}_2(v=1)]\\ &- k_{1-0}^{\mathrm{H}}(T)[\mathrm{H}_2(v=0)]\}.\end{aligned} \tag{16}$$

The fourth term describes vibrational energy losses due to hydrogen dissociation (N is the total density of neutral particles):

$$\begin{aligned}&Q_{\mathrm{dis}}^{\mathrm{vib}}\\ &= \sum_v v\varepsilon_{\mathrm{vib}}\{k_e(T_e, v)N_e + k_T(T, v)N\}[\mathrm{H}_2(v)].\end{aligned} \tag{17}$$

The last two terms on the right-hand side of Eq. (13) describe diffusive transport of the vibrational energy (α_V being the hydrogen self-diffusion coefficient) and its transport by gas flows, respectively. It was assumed that, at the boundaries of the computation region, the vibrational temperature is equal to the gas temperature.

Hence, with allowance for the vibrational kinetics of molecular hydrogen, the resulting specific energy input into the gas is given by the expression

$$Q_\Sigma = Q_{VT}^{\mathrm{H}_2} + Q_{VT}^{\mathrm{H}} + Q_{\mathrm{elastic}} - Q_{\mathrm{dis}}^{T}. \tag{18}$$

Here, Q_{elastic} is the energy flux transferred to the gas in electron–molecule elastic collisions and the term $Q_{\mathrm{dis}}^{T} = \varepsilon_{\mathrm{dis}}\sum_v 2k_T(T, v)N[\mathrm{H}_2(v)] - 2k_R(T)[\mathrm{H}]^2 N - Q_{\mathrm{dis}}^{\mathrm{vib}}$ describes the fraction of thermal energy that goes into gas heating with allowance for the change in the rate of direct reaction (12) due to the excitation of the vibrational levels.

With allowance for the dissociation of hydrogen molecules in vibrationally excited states, the atomic hydrogen density is described by the equation

$$\frac{\partial[\mathrm{H}]}{\partial t} = \sum_{v} 2(k_e(T_e, v)N_e + k_T(T, v)N)[\mathrm{H}_2(v)] - 2k_R(T)[\mathrm{H}]^2 N + \nabla\cdot(D_\mathrm{H}(T)\nabla[\mathrm{H}]) - \nabla\cdot\left(\frac{D_\mathrm{H}(T)[\mathrm{H}]}{N}\nabla N\right) - \nabla\cdot([\mathrm{H}]\mathbf{u}). \quad (19)$$

Here, the sum accounts for the processes of the electron and thermal dissociation of hydrogen molecules in vibrationally excited states; the second term describes the three-body recombination processes; and the third, fourth, and fifth terms describe the processes of diffusion, thermal diffusion, and transport of hydrogen atoms by gas flows, respectively. It should be noted that the thermal diffusion has little effect on the density of atomic hydrogen, probably because its gradients in the discharge are much steeper than the temperature gradients (see Section 3 for details).

The dissociation rate constants were set equal to

$$k_e(T_e, v) = A_e\exp\left(-\frac{I_e^* - v\varepsilon_\mathrm{vib}}{T_e}\right),$$
$$k_T(T, v) = A_T\exp\left(-\frac{I_T^* - v\varepsilon_\mathrm{vib}}{T}\right), \quad (20)$$

where the quantities A_e, A_T, I_e^*, and I_T^* were taken from [14, 15]. It was thus assumed that the vibrational excitation only changes the threshold of the reaction. Note that this assumption is not quite correct because the cross section for electron-impact dissociation depends on the vibrational excitation of molecules, which can considerably change the reaction rate constant. We failed to find reliable data on this dependence, however.

The results of calculations of the gas temperature and the degree of hydrogen dissociation as functions of the gas pressure for a continuous microwave discharge with allowance for the vibrational kinetics of hydrogen molecules are illustrated in Figs. 5 and 6. With the hydrogen vibrational kinetics taken into account, the model yielded the gas temperatures that differ only slightly from those obtained by calculating the specific energy input into the gas from simplified formula (10). As before, the energy loss in thermal dissociation reaction (8) is the main factor that restricts the gas temperature. It should be noted that the vibrational temperature exceeds the gas temperature only slightly because of the rapid *V–T* relaxation processes. From Fig. 6 it can be seen, however, that, when the vibrational excitation of hydrogen molecules is taken into account, the degree of hydrogen dissociation is several times higher. Hence, the vibrational kinetics has essentially no effect on the thermal dissociation rate but increases the electron-impact dissociation rate due to the dissociation of hydrogen molecules in vibrationally excited states. This is the main mechanism for producing atomic hydrogen.

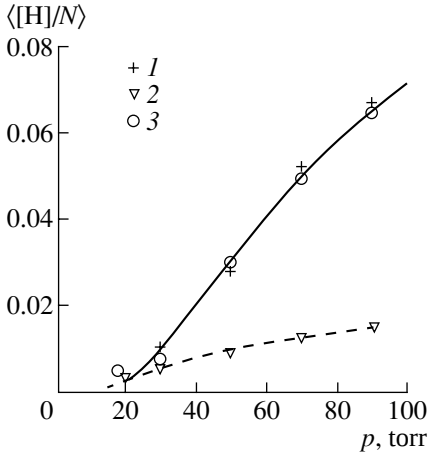

Fig. 6. Degree of hydrogen dissociation vs. gas pressure in a continuous discharge at an absorbed microwave power of 1.5 kW: (*1*) experimental data and results of calculations (*2*) without and (3) with allowance for the vibrational kinetics of molecular hydrogen.

2.5. Module for Calculating Dissociative Electron Attachment

It is known [16] that hydrogen is an electronegative gas and that, at high pressures, the threshold for breakdown in hydrogen is governed by the dissociative electron attachment reaction

$$\mathrm{H}_2 + e \longrightarrow \mathrm{H} + \mathrm{H}^- - 3.7\ \mathrm{eV}. \quad (21)$$

The rate of reaction (21) depends on the electron temperature and also on the vibrational excitation of molecular hydrogen [16]. Negative H^- ions are mainly lost in the reactions [4]

$$\mathrm{H}^- + \mathrm{H} \longrightarrow \mathrm{H}_2 + e, \quad (22)$$

$$\mathrm{H}^- + \mathrm{H}_3^+ \longrightarrow 2\mathrm{H}_2. \quad (23)$$

With allowance for the vibrational excitation of hydrogen molecules, as well as their diffusion and transport by gas flows, the density of negative H^- ions is described by the equation

$$\frac{\partial[\mathrm{H}^-]}{\partial t} = \sum_{v} k_{da}(T_e, v)[\mathrm{H}_2(v)]N_e - k_{\mathrm{H}+\mathrm{H}^-}[\mathrm{H}][\mathrm{H}^-] - k_{\mathrm{H}_3^+ + \mathrm{H}^-}[\mathrm{H}_3^+][\mathrm{H}^-] + \nabla\cdot(D_\mathrm{H}(T)\nabla[\mathrm{H}^-]) - \nabla\cdot([\mathrm{H}^-]\mathbf{u}). \quad (24)$$

Here, the sum describes the processes of dissociative electron attachment to hydrogen molecules in vibrationally excited states and k_{H+H^-} and $k_{H_3^+ + H^-}$ are the rate constants of reactions (22) and (23), respectively. The last two terms on the right-hand side of Eq. (24) describe the diffusion of H^- ions and their transport by gas flows, respectively. The boundary conditions for Eq. (24) were taken to be the same as those for the electron density equation.

Accordingly, the equations for the electron density and atomic hydrogen density were supplemented with the terms that describe the processes involving negative hydrogen ions. Taking into account the effect of the vibrational excitation of molecular hydrogen on the rate of reaction (21) makes the model far more complicated. The calculated results, however, were found to differ insignificantly from the previous ones. In all simulated regimes, the concentration of negative hydrogen ions was relatively low (about several percent of the electron density), so they did not have any significant influence on the processes in the discharge plasma (see Section 3).

2.6. Method for Comparing the Simulation Results to the Experimental Data

The adequacy of the model was checked against the experimental data obtained by the OES method [7]. This method provides measurements of the parameters averaged over the volume of the observed plasma layer (see Fig. 2). Therefore, the calculated results generally are difficult to test against the experimental data without any preprocessing. Usually, the experimental data are used to reconstruct the spatial distributions of the plasma parameters and then to compare them to the calculated distributions [4, 5]. In the present paper, we propose to take an opposite approach: to simulate the signals recorded by measuring devices and then to compare the simulated signals to the experimental ones. We think that this method of comparison is preferable.

The simulations were carried out under the following assumptions: the plasma is optically thin, the radiating levels are excited from the ground state by direct electron impact, and the main mechanism for depopulating these levels is collisional quenching. Estimates show that, under such conditions, a radiating level is populated practically instantaneously as compared to the temporal scales of the other discharge parameters. In this case, the relative intensity of a spectral line emitted from the plasma layer is calculated by the formula

$$I(N_j) = \int_V J_j(z, r)dV. \quad (25)$$

Here, the quantity $J_j(z, r) = \dfrac{k_{ext}(T_e)N_eN_j}{k_q(T)N}$ is proportional to the intensity of the spectral line emitted by the particles of species N_j in a unit volume and $k_{ext}(T_e)$ and $k_q(T)$ are the rate constants for the excitation and quenching of the emitting level. In simulations, the collisional quenching cross section was assumed to be constant and the temperature dependence of the quenching rate constant had the form $k_q(T) \propto N\sqrt{T} \propto T^{-1/2}$. The integration was carried out over the discharge region available for measurements (the hatched region in Fig. 2).

In order to compare the numerical results to the experimental data, we simulated the dynamics of the intensity of hydrogen and argon atomic lines and the degree of hydrogen dissociation. In calculations, as well as in experiments, the latter parameter was determined by the actinometric method, i.e., from the ratio of the intensities of the spectral lines of hydrogen and argon atoms that have the same excitation threshold,

$$\langle [H]/[N] \rangle \sim I(H)/I(N). \quad (26)$$

The gas temperature was measured from the distribution of the intensity of emission from the unresolved rotational structure of the 0–0 band of the transition $C^3\Pi_u \longrightarrow B^3\Pi_g$ of nitrogen molecules [7]. It was found that the main contribution to the gas temperature comes from the brightest discharge regions. Accordingly, in our model, the gas temperature was averaged over the volume of the plasma layer with a weighting factor equal to the emission intensity of nitrogen molecules,

$$\langle T \rangle = \frac{1}{I(N_2)}\int_V T(z, r)J_{N_2}(z, r)dV. \quad (27)$$

The model was also tested against the experimental data obtained from measurements of the microwave power reflected from the cavity in the pulse-periodic regime of discharge maintenance.

3. SIMULATION RESULTS AND DISCUSSIONS

3.1. Comparison of Simulation Results to Experimental Data

The results of calculations carried out for a continuous microwave discharge in a CVD reactor have already been presented in Figs. 5 and 6 (see the description of the model in Sections 2.3 and 2.4). In this work, our attention is mainly focused on the pulse-periodic regime of discharge maintenance, which make it possible to investigate dynamic processes and thereby to provide a more adequate comparison between simulations and experiments.

Pulse-periodic microwave discharges were simulated for the actual experimental parameters, namely, for a pulsed microwave power of 3 kW, pulse duration of 5 ms, and repetition rate of 100 Hz. Figure 7 illustrates the dynamics of the gas temperature and vibrational temperature throughout a microwave pulse. At a pressure of 30 torr, the vibrational temperature in the

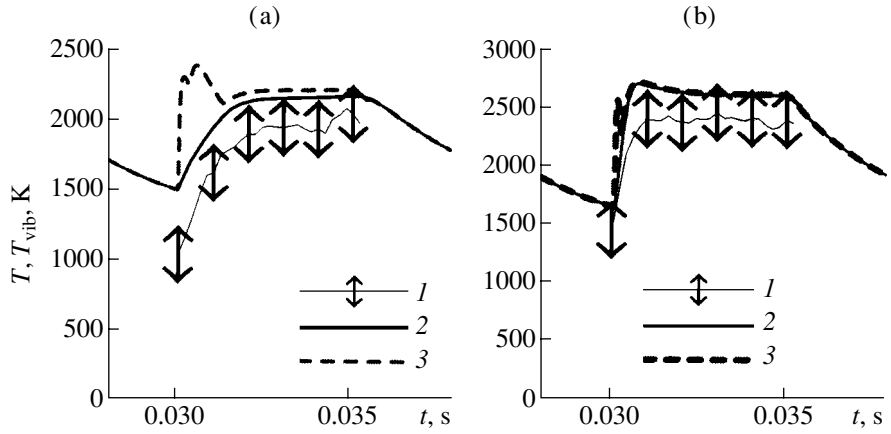

Fig. 7. Dynamics of different temperatures at gas pressures of (a) 30 and (b) 70 torr: (*1*) experimental data and results of calculations of (*2*) the gas temperature and (*3*) vibrational temperature.

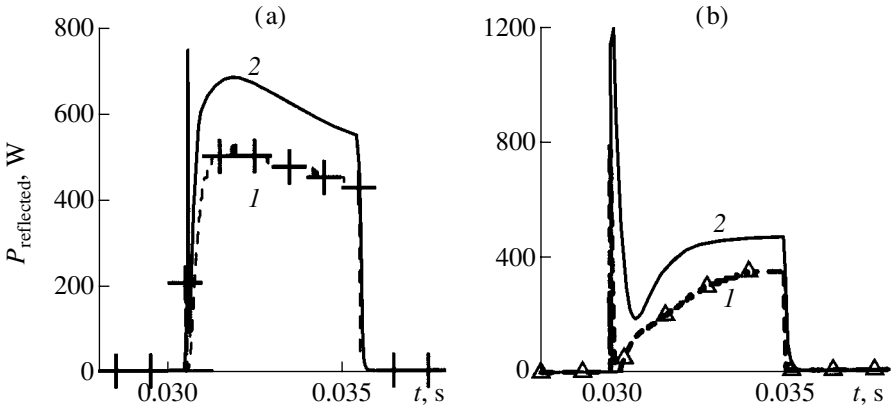

Fig. 8. Dynamics of the microwave power reflected from the cavity at gas pressures of (a) 30 and (b) 70 torr: (*1*) experimental data and (*2*) calculated results.

initial stage of the pulse is seen to become substantially higher than the gas temperature (Fig. 7a). At higher pressures (Fig. 7b), the efficiency of the *V–T* relaxation increases and the vibrational temperature becomes approximately equal to the gas temperature.

Figure 8 illustrates the dynamics of the microwave power reflected from the cavity at pressures of 30 and 70 torr. We can see that the calculated and measured signals have essentially the same shape but their intensities are appreciably different. It should be noted that, in simulations, we were unable to achieve the same coupling between the cavity and the microwave transmission line as that in the experiment, presumably because the dimensions of the cavity were varied in discrete steps equal to the spacing of the spatial grid (in the case at hand, the grid spacing was 2 mm). The calculations, however, correctly describe most of the tendencies in the behavior of the discharge, in particular, an improvement in the coupling between the cavity and the microwave transmission line and a delayed onset of the microwave breakdown at high gas pressures.

Figures 9 and 10 show the dynamics of the intensities of the spectral lines of argon and atomic hydrogen at a pulsed microwave power of 3 kW. The intensity of the argon spectral lines has a maximum at the beginning of the microwave pulse and decreases as the gas is heated (Fig. 9). The reason for this is that the argon concentration in the discharge is proportional to the density of the neutral gas. Thus, the fact that the argon line intensities behave in the same manner indicates that the gas-dynamic processes are correctly incorporated in our model. On the other hand, atomic hydrogen is produced in the discharge plasma and the intensity of line emission from hydrogen atoms is seen to increase throughout the microwave pulse (Fig. 10). The calculated dependence of the intensity of the spectral lines of

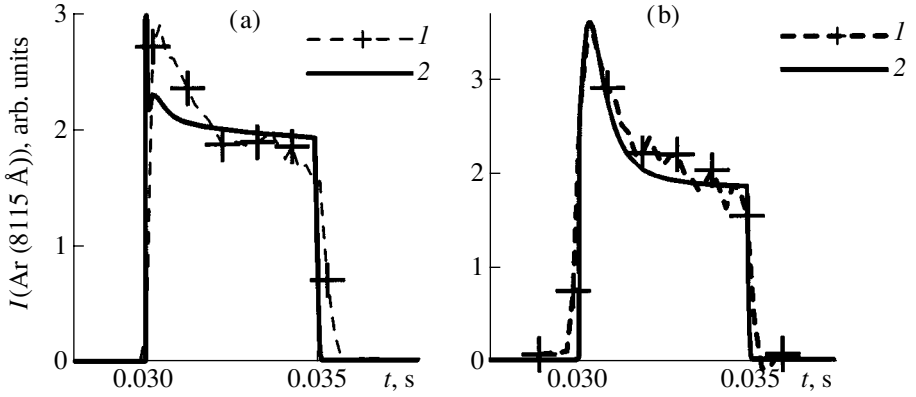

Fig. 9. Dynamics of the intensity of the Ar 8115-Å spectral line at gas pressures of (a) 30 and (b) 70 torr: (*1*) experimental data and (*2*) calculated results.

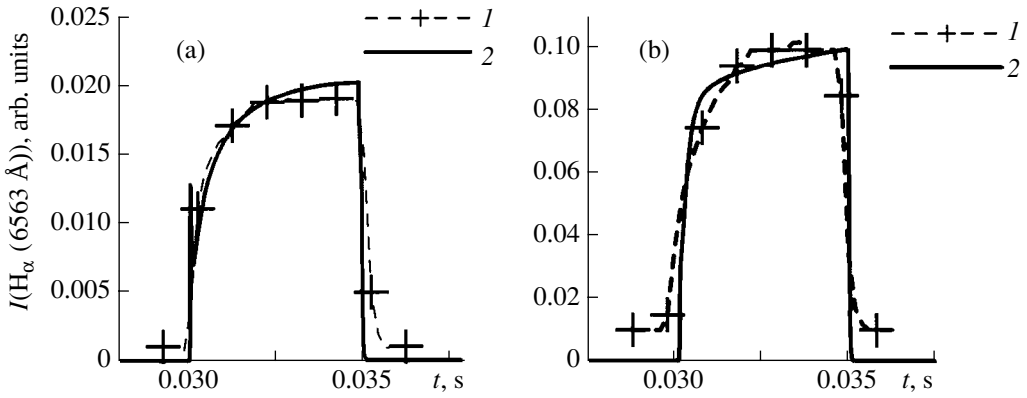

Fig. 10. Dynamics of the intensity of the H_α spectral line at gas pressures of (a) 30 and (b) 70 torr: (*1*) experimental data and (*2*) calculated results.

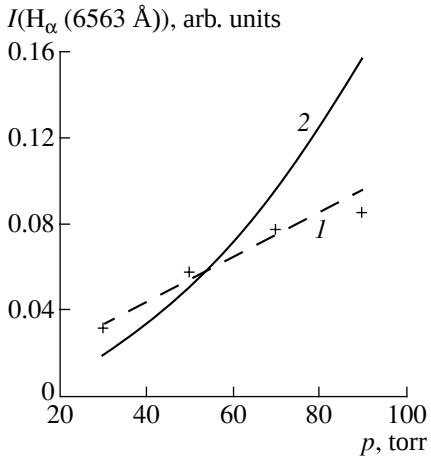

Fig. 11. Intensity of the H_α spectral line at the end of a microwave pulse vs. gas pressure: (*1*) experimental data and (*2*) calculated results.

argon and atomic hydrogen on the gas pressure correctly reflects the main tendencies in the experimentally observed behavior of the discharge (see Figs. 11, 12). The discrepancy between the calculated and experimental results may indicate that the rate of collisional quenching of the excited levels depends on the discharge parameters in a more complicated fashion than it is assumed in our model.

The results of simulations carried out with allowance for negative H^- ions show that, at low pressures, the density of these ions is fairly high in comparison to the electron density (Fig. 13a). As the pressure increases, the density of H^- ions changes insignificantly (Fig. 13b), whereas the electron density increases and remains approximately equal to the critical collisional density. In all cases, the rapid increase in the density of H^- ions at the beginning of the microwave pulse is followed by its decrease at later pulse stages because, at high concentrations of atomic hydro-

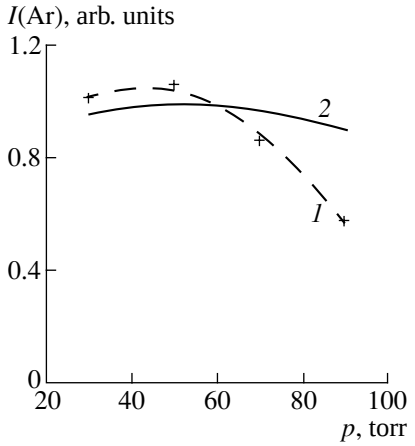

Fig. 12. Intensity of the Ar 8115-Å spectral line at the end of a microwave pulse vs. gas pressure: (*1*) experimental data and (*2*) calculated results.

gen in a microwave discharge, reaction (22) proceeds more efficiently. Hence, our simulations show that, at pressures higher than 20 torr, the dissociative electron attachment has a negligible effect on the evolution of microwave discharges in hydrogen.

3.2. Energy Transport Mechanisms in a Continuous Microwave Discharge

As was pointed out in Section 2.2, the reaction of the thermal dissociation of hydrogen absorbs a great deal of energy and thereby limits the gas temperature. This is possible, however, only when there are mechanisms for the rapid transport of energy from the region where it is released. Accordingly, it is of interest to compare the efficiencies of different energy transport mechanisms in the discharge.

The main fraction of the energy that is released in the discharge plasma eventually goes into heating the gas and producing various radicals (in particular, atomic hydrogen). In a steady discharge, the power absorbed by the plasma is balanced by the losses of energy due to its transport out of the CVD reactor. In this section, we compare the fluxes of the energy transported by gas heat conduction, $\mathbf{q}_T = -\lambda(T)\nabla T$, and by atomic hydrogen diffusion, $\mathbf{q}_\mathrm{H} = -\frac{1}{2}\varepsilon_\mathrm{dis} D_\mathrm{H}(T)\nabla[\mathrm{H}]$. We assume that each hydrogen atom carries the energy equal to half the dissociation energy. Our calculations show that, at pressures above 20 torr, other energy transport mechanisms (such as the vibrational energy transport) are far less efficient than the two mechanisms just mentioned.

The radial profiles of the plasma parameters and the energy fluxes by heat conduction and diffusion in the established regime of a microwave discharge are presented in Fig. 14. It can be seen from Fig. 14 that the discharge volume can be conventionally divided into two regions. In the central region, the gas temperature gradients are low and the main energy transport mechanism is the diffusion of atomic hydrogen. The peripheral region is dominated by the heat conduction mechanism.

As the gas pressure increases, the plasma volume decreases and the specific power and atomic hydrogen density increase substantially. The gas temperature, however, does not increase because the thermal energy is expended on dissociating hydrogen. In fact, this thermal-energy loss mechanism is so efficient that it limits the gas temperature to a level of 2500–2700 K. The gas temperature can increase further only after hydrogen has been completely dissociated. Accordingly, the effect of atomic hydrogen on the energy transport in a microwave discharge increases considerably. It is this mechanism that equalizes the gas temperature over the

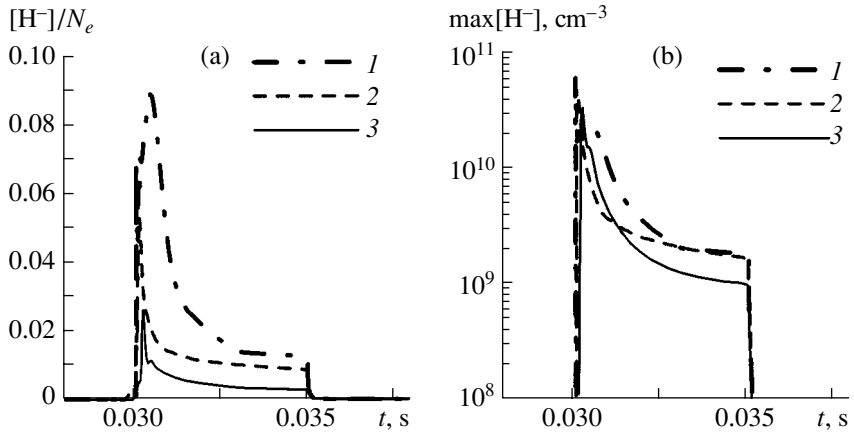

Fig. 13. Dynamics of (a) the relative density of negative H^- ions and (b) their maximum density in the discharge plasma during a microwave pulse at an absorbed power of 3 kW and gas pressures of (*1*) 30, (*2*) 50, and (*3*) 90 torr.

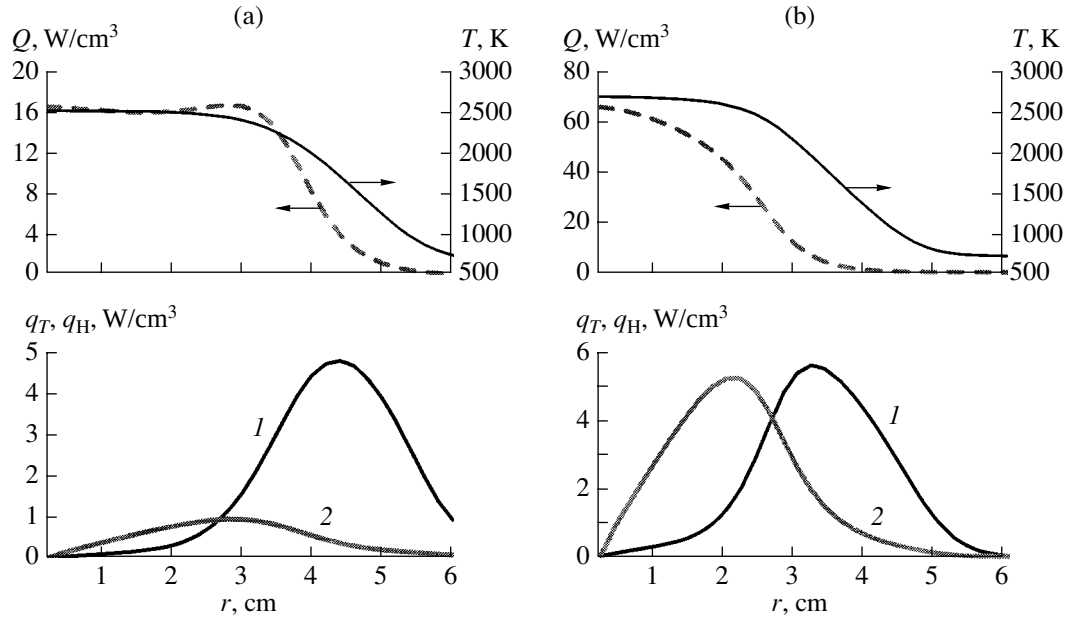

Fig. 14. Radial profiles of the plasma parameters and of the energy fluxes q_T (curves *1*) and q_H (curves *2*) at a height of 12 mm above the substrate, at an absorbed microwave power of 3 kW, and at gas pressures of (a) 60 and (b) 120 torr.

entire discharge volume. At high pressures, the volume of a uniformly heated gas is much larger than that of the visible discharge region.

4. CONCLUSIONS

In the present paper, we have shown that, in order to construct a model capable of adequately simulating a microwave discharge in hydrogen at pressures of 20–200 torr and a power of several kilowatts, it is necessary to take into account not only the processes that were described in [8] but also the energy balance in the chemical reactions of thermal dissociation and recombination of hydrogen, as well as the vibrational excitation of hydrogen molecules. At pressures above 20 torr, negative H^- ions play an insignificant role. We have demonstrated that vibrationally excited hydrogen molecules have a substantial influence on the electron-impact dissociation rate and, consequently, on the degree of hydrogen dissociation in a microwave discharge. We have also proposed a numerical method for calculating gas flows in the quasi-isobaric approximation with allowance for convective and other vortex flows generated in the reactor. The method proposed is well convergent and stable.

Because of the energy losses due to hydrogen dissociation, the gas temperature is limited to a level of 2500–2700 K. At high gas pressures, the main heat transport mechanism is diffusion of atomic hydrogen. At the discharge periphery, the main mechanism for energy transport is gas heat conduction.

Hence, the numerical model developed here makes it possible to predict the main parameters of microwave discharges in hydrogen over almost the entire range of the operating conditions in the CVD reactor. However, the working gas mixture in the reactor is hydrogen with an addition of carbon-containing gas (usually methane). In some cases, diamond films with specific properties are obtained by adding other gases (such as oxygen and nitrogen) to the working gas mixtures. Of course, in order to describe how a diamond film grows in a CVD reactor, it is necessary to know the detailed chemical composition of the gas mixtures and to clearly understand the reactions occurring in them. Discharges in hydrogen–methane mixtures were investigated, e.g., in [5, 6, 11, 15, 17]. Note, however, that it is atomic hydrogen that plays a key role in the growth of a diamond film [18]. On the other hand, our experiments show that, within a measurement accuracy of ±10%, adding methane (up to 5%) to the working gas does not change such parameters as the discharge volume, the gas temperature, and the degree of hydrogen dissociation (determined by the actinometric method). Consequently, the model described above, which is relatively simple and provides high-speed computations, can be applied to discharges not only in pure hydrogen but also in hydrogen-based working gas mixtures and thereby can be used to optimize the operating modes of CVD reactors. The main parameter that determines the growth rate of diamond films and their quality is the atomic hydrogen flux onto the substrate.

ACKNOWLEDGMENTS

We are grateful to the participants of the seminars of the Laboratory of Microwave Discharges at the Institute of Applied Physics of the Russian Academy of Sci-

ences for fruitful discussions of the results obtained. This study was supported in part by the Netherlands Organization for Scientific Research (NWO) (grant no. 047.016.019), the Ministry of Science and Education of the Russian Federation, and the US Civilian Research and Development Foundation for the Independent States of the Former Soviet Union under the Basic Research and Higher Education (BRHE) program (grant no. Y1-P-01-04).

REFERENCES

1. T. A. Grotjohn and J. Asmussen, in *Diamond Films Handbook*, Ed. by J. Asmussen and D. K. Reinhard (Marcel Dekker, New York, 2001), p. 211.
2. W. Tan and T. A. Grotjohn, Diamond Relat. Mater. **4**, 1145 (1995).
3. M. Fuener, C. Wild, and P. Koidl, Surf. Coat. Technol. **74–75**, 221 (1995).
4. K. Hassouni, T. A. Grotjohn, and A. Gicquel, J. Appl. Phys. **86**, 134 (1999).
5. S. V. Kotiuk, Y. A. Mankelevich, A. T. Rakhimov, and N. V. Suetin, Proc. Inst. Phys. Technol. **16**, 38 (2000).
6. K. Hassouni, X. Duten, A. Rousseau, and A. Gicquel, Plasma Sources Sci. Technol. **10**, 61 (2001).
7. A. L. Vikharev, A. M. Gorbachev, V. A. Koldanov, and D. B. Radishchev, Fiz. Plazmy **31**, 376 (2005) [Plasma Phys. Rep. **31**, 338 (2005)].
8. A. M. Gorbachev, V. A. Koldanov, and A. L. Vikharev, Diamond Relat. Mater. **10**, 342 (2001).
9. A. Taflove, *Advances in Computational Electrodynamics: The Finite-Difference Time-Domain Method* (Artech House, Boston, 1998).
10. J. Loureiro and C. M. Ferreira, J. Phys. D **22**, 1680 (1989).
11. Yu. A. Lebedev and I. L. Épshteĭn, Teplofiz. Vys. Temp. **36**, 534 (1998).
12. A. A. Samarskiĭ and Yu. P. Popov, *Differential Methods for Solving Gas-Dynamics Problems* (Nauka, Moscow, 1980) [in Russian].
13. L. D. Landau and E. M. Lifshitz, *Fluid Mechanics* (Nauka, Moscow, 1986; Pergamon, Oxford, 1987).
14. D. L. Baulch, C. J. Cobos, R. A. Cox, *et al.*, Combust. Flame **98**, 59 (1994).
15. Yu. A. Mankelevich, A. T. Rakhimov, and N. V. Suetin, Fiz. Plazmy **21**, 921 (1995) [Plasma Phys. Rep. **21**, 872 (1995)].
16. *Nonequilibrium Oscillatory Kinetics*, Ed. by M. Capitelli (Springer-Verlag, New York, 1986; Mir, Moscow, 1989).
17. R. A. Akhmedzhanov, A. L. Vikharev, A. M. Gorbachev, *et al.*, Diamond Relat. Mater. **11**, 579 (2002).
18. D. G. Goodwin, J. Appl. Phys. **74**, 6888 (1993); **74**, 6895 (1993).

Translated by O.E. Khadin

Plasma Physics Reports, Vol. 31, No. 11, 2005, pp. 978–983. Translated from Fizika Plazmy, Vol. 31, No. 11, 2005, pp. 1051–1056.

LOW-TEMPERATURE PLASMA

Instability of a Low-Pressure Hollow-Cathode Discharge in a Magnetic Field

E. M. Oks[1], A. Anders[2], I. G. Brown[2], I. A. Soloshenko[3], and A. I. Shchedrin[3]

[1] *Institute of High-Current Electronics, Siberian Division, Russian Academy of Sciences, Akademicheskiĭ pr. 4, Tomsk, 634055 Russia*

[2] *Lawrence Berkeley National Laboratory, Berkeley, CA 94720, USA*

[3] *Institute of Physics, National Academy of Sciences of Ukraine, pr. Nauki 144, Kiev, 03039 Ukraine*

Received December 1, 2004

Abstract—Mechanisms responsible for current oscillations at the ion branch of the probe characteristic are investigated experimentally and theoretically. A comparison between experiment and theory shows that the oscillations in a hollow-cathode discharge in a longitudinal magnetic field are most likely related to the onset of helical instability. *© 2005 Pleiades Publishing, Inc.*

1. INTRODUCTION

Glow discharges with a cold hollow cathode are a simple and convenient means for producing dense gaseous plasma at relatively low gas pressures [1]. The hollow-cathode effect, resulting in the efficient ionization of the residual gas, is related to the oscillatory motion of the primary electrons inside the cavity. Due to their high energy efficiency, hollow-cathode discharges have found wide use in ion sources [2], plasma electron sources [3], and plasma generators [4] utilized in fundamental and applied studies.

Applying a longitudinal magnetic field to the cathode cavity provides conditions for a more efficient ionization, which manifests itself in an increase in the plasma density and/or a decrease in the discharge voltage [5–9]. It was shown in [10], however, that applying a magnetic field not only increases the energy efficiency but can also lead to instabilities. Probe measurements demonstrated the presence of regular low-frequency current oscillations at the ion branch of the probe characteristics.

In this paper, we present results from theoretical and experimental studies of the mechanism responsible for this instability.

2. EXPERIMENTAL DEVICE AND MEASUREMENT TECHNIQUE

Experiments were carried out at the Lawrence Berkeley National Laboratory, United States. The key component of the experimental device (Fig. 1) was an aluminum hollow cathode (*1*) with a diameter of 6 cm and length of 17 cm. The diameter of the central aperture in the hollow cathode was 1 cm. A plane anode (*2*) was placed at a distance of about 1 cm from the cathode end. The magnetic field was produced by a 4-cm-long solenoid (*3*), which could easily be displaced along the cylindrical wall of the cavity. The magnetic field was nonuniform along the system axis. At a solenoid current of 30 A, the maximum field was 0.1 T. The calculated axial profile of the longitudinal component of the magnetic field was presented in our previous paper [10]. In some experiments, a collector electrode (*4*) was placed behind the anode in order to extract ions from the plasma. In combination with electrode *4*, this exper-

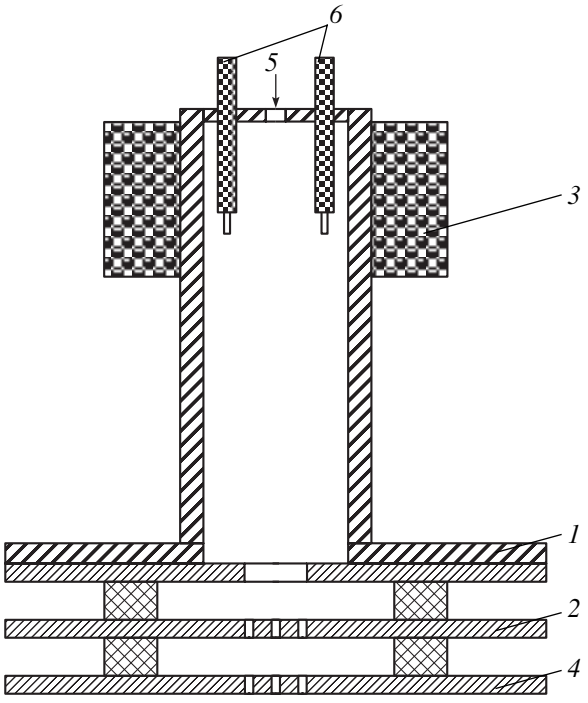

Fig. 1. Schematic of the experimental device: (*1*) hollow cathode, (*2*) anode, (*3*) solenoid, (*4*) accelerating electrode (collector), (*5*) gas-feed inlet, and (*6*) probes.

1063-780X/05/3111-0978$26.00 © 2005 Pleiades Publishing, Inc.

imental scheme was the simplest version of an ion source. It should be noted, however, that ion extraction did not affect the instability under study. An important element of the experimental setup was a Universal Voltronics power supply, providing a stabilized current from 50 mA to 1 A in a steady-state discharge mode.

The working gas (nitrogen, argon, or krypton) was fed into the cathode cavity through the upper end of the cathode (Fig. 1). Because of the limited flow capacity of the cathode aperture, the gas pressure inside the cavity was nearly one order of magnitude higher than that inside the vacuum chamber, pumped out by a cryogenic pump. The working-gas flow was stabilized by an electronic gas-feed system, which provided a constant gas pressure in the cavity in the course of experiment. The experiments were carried out at a gas pressure in the cavity of 0.7–2 Pa (5–15 mtorr).

The plasma parameters were measured by four identical cylindrical stainless-steel probes (*6*) positioned equidistantly along a 3-cm-diameter circumference at a distance of 3 cm from the upper end of the cavity (only two probes are shown in Fig. 1). The diameter of the collecting area of the probe was 1.2 mm, and its working length was 12 mm. Since the floating potential of the discharge plasma was higher than the cathode potential by nearly 300 V, it was sufficient to merely connect the probe to the cathode through a 50-Ω resistor in order to measure the ion saturation current of the probe. To measure the parameters of oscillations, we used a four-channel Tektronix TDS 3014 B oscilloscope and a standard computer procedure for processing measured signals.

3. EXPERIMENTAL RESULTS

Under our experimental conditions, the electron temperature and the plasma density were T_e = (2–4) eV and $n_e = (2–8) \times 10^{10}$ cm^{-3}, respectively [10]. In the absence of an external magnetic field (i.e., at a zero solenoid current), regular low-amplitude oscillations at a frequency of f = 50 kHz were observed in the probe ion current. The signals at this frequency were identical for all four probes, and the frequency remained unchanged when we varied the current and other discharge parameters. The cause of such a modulation of the probe ion current was the jitter of the stabilizing system of the discharge current, rather than plasma instability.

Applying a magnetic field above a certain critical level to the cathode cavity resulted in the appearance of an additional periodic probe signal, whose amplitude and frequency depended on the magnetic field, the discharge current, and the pressure and sort of the working gas. Typical probe signals are shown in Fig. 2. It is clearly seen that regular and well-reproducible oscillations are present in the signals from each of the four probes. The amplitude of these oscillations is four to six times larger than the oscillation amplitude in the absence of a magnetic field. Note that, the signal from each probe is delayed or advanced relative to the signals from the neighboring probes by nearly a quarter of the oscillation period. Such a phase shift indicates the onset of the m = 1 azimuthal mode of rotational plasma instability in the cathode cavity. A change in the direction of the magnetic field in the cavity (by changing the polarity of the solenoid current) leads to a change in the rotation direction of the plasma perturbation (Fig. 2b).

The threshold magnetic field required for the onset of instability increases with pressure and molecular mass of the working gas. The dependence of the oscillation frequency on the magnetic field, $f(B)$, is almost linear over a wide range of the magnetic field B (Fig. 3). As the gas pressure increases, the dependence $f(B)$ shifts toward higher values of B (Fig. 3).

At a fixed value of B, the oscillation frequency decreases with increasing pressure (Fig. 4). The use of a heavier working gas also leads to a decrease in f. For nitrogen, argon, and krypton at the same pressure, the frequencies of plasma density oscillations were equal to 22, 15, and 6 kHz, respectively. The heavier the gas, the higher the threshold magnetic field and the less pronounced the instability.

The discharge current also substantially affects the plasma instability. It can be seen from Fig. 5 that an increase in the discharge current I from 50 to 200 mA leads to a decrease in the oscillation frequency from 17 to 6 kHz. As the discharge current increases further, the dependence $f(I)$ tends to saturate. Note that a change in the oscillation frequency was always accompanied by a change in the oscillation amplitude: as the oscillation frequency increased, the oscillation amplitude usually decreased.

When the solenoid was displaced along the wall, the maximum of the plasma density followed the maximum of the magnetic field. This is confirmed by the experimentally observed change in the amplitude of the probe signal. The oscillation frequency in this case remained unchanged. When the solenoid was positioned far away from the probes, oscillations in the probe signals disappeared. When the solenoid was positioned near the lower end of the cavity (near the anode), similar oscillations appeared in the ion current extracted from the plasma. Although these oscillations were less regular than those in the probe signals, their frequency coincided with the oscillation frequency of the probe current.

4. THEORY

The above oscillations in the probe ion current may be attributed to the onset of helical instability [11, 12]. Helical waves in plasma are excited when the current flowing along the magnetic field **B** exceeds a certain critical level. When the plasma density is distributed uniformly across the magnetic field, surface helical waves are excited in a finite-width plasma column. In

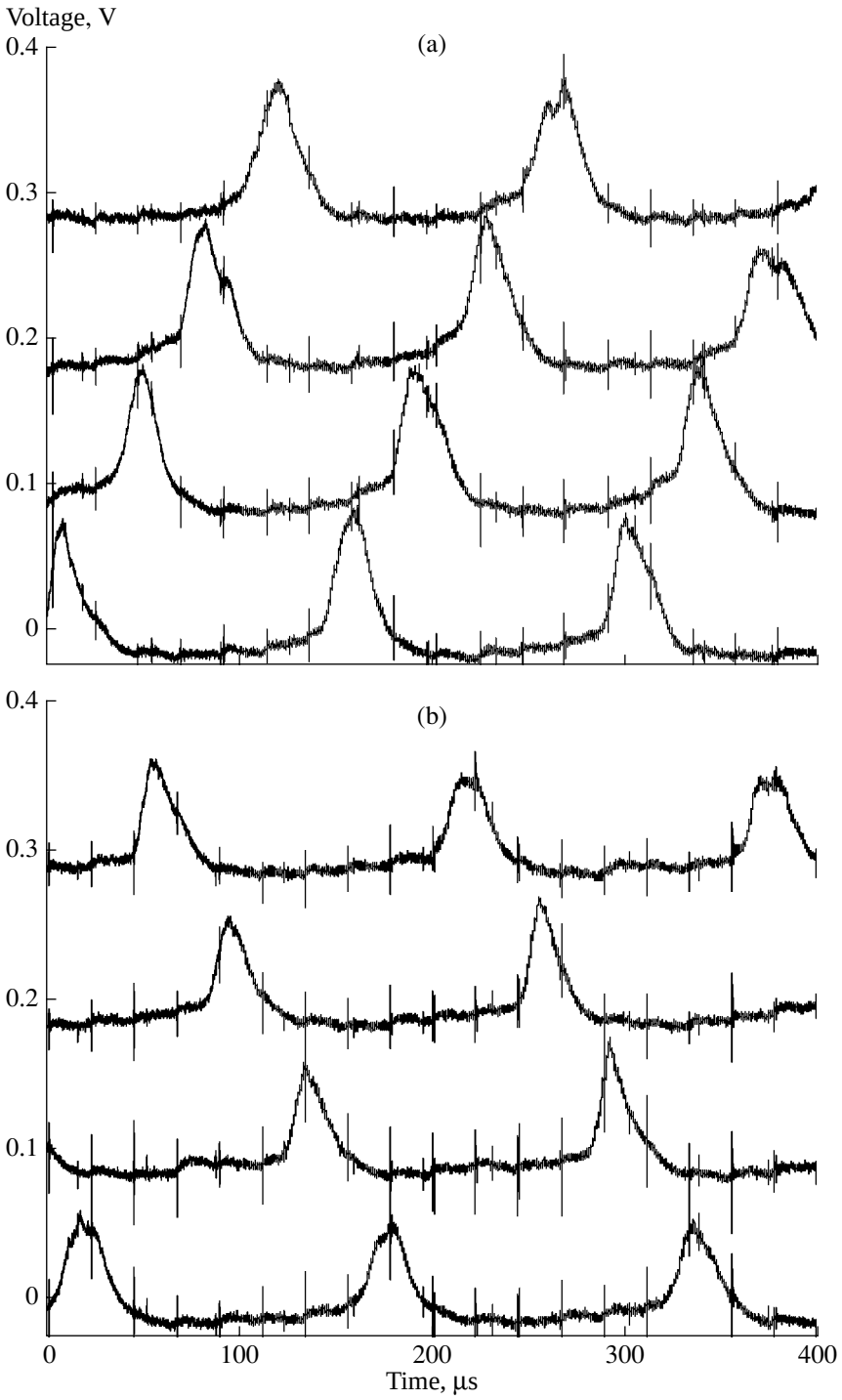

Fig. 2. Effect of the direction of the magnetic field on the probe ion current at a discharge current of $I = 200$ mA, gas (nitrogen) pressure of $p \approx 1.5$ Pa (11 mtorr), and maximum magnetic field of $B = 0.4$ mT. A 50-mV probe signal corresponds to an ion current of 1 mA (or a plasma density of $n \approx 10^{11}$ cm^{-3}). Plots (a) and (b) correspond to opposite directions of the magnetic field.

the case of a radially nonuniform plasma, internal helical waves are excited.

In a weak magnetic field, $(\mu_{e,i}B/c)^2 \ll 1$, where $\mu_{e,i}$ are the electron and ion mobilities, the criterion for the onset of helical instability has a simple physical meaning: the wave is excited if the velocity of the Hall drift in the transverse electric field of the wave, $\mathbf{E}'_\perp$ ($\mathbf{E}'_\perp \sim E$), and in the longitudinal magnetic field $\mathbf{B}$ exceeds the

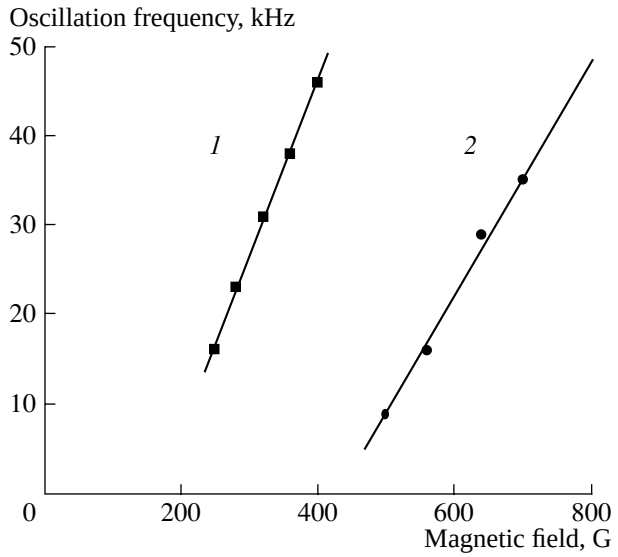

Fig. 3. Effect of the magnetic field on the oscillation frequency at I = 300 mA and gas (nitrogen) pressures of p = (*1*) 1.7 Pa (13 mtorr) and (*2*) 2.7 Pa (20 mtorr).

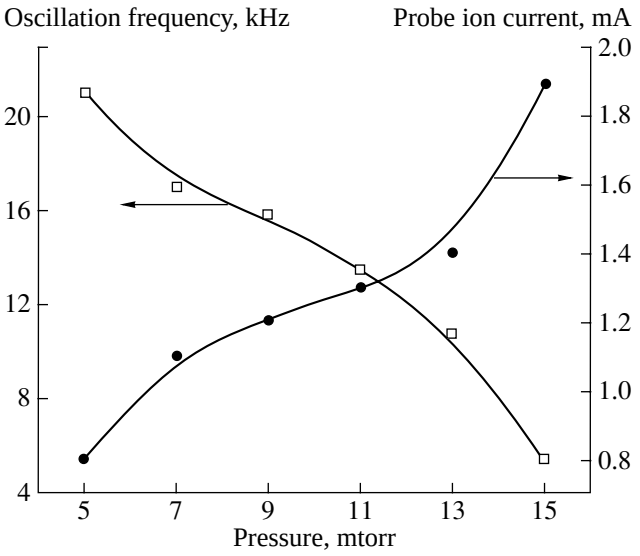

Fig. 4. Effect of the gas (nitrogen) pressure on the frequency and amplitude of oscillations at I = 300 mA and B = 0.4 mT.

velocity of ambipolar diffusion, which eliminates the perturbation [11, 12],

$$\frac{\mu_e \mu_i E B}{c} > \alpha \frac{D_a}{R}. \qquad (1)$$

Here, D_a is the coefficient of ambipolar diffusion; R is the chamber radius; and α is a numerical factor (of several units), which depends on the value of the plasma density gradient across the magnetic field. Criterion (1) is valid for both surface and internal helical waves.

In a strong magnetic field, such that $(\mu_e B/c)^2 \gg 1$ and $(\mu_i B/c)^2) > 1$ (as is the case under our experimental conditions), the dispersion relation describing the threshold characteristics of the internal helical instability is much more complicated [13, 14]. The dependence of the threshold electric field on the magnetic field in the positive column of a gas discharge was determined in [13] by numerically solving the dispersion relation (see Fig. 6). As will be shown below, the parameters of our experiment meet the criterion for the onset of helical instability.

The expression for the frequency f of helical oscillations in a positive gas-discharge column in a strong magnetic field at $\mu_e \gg \mu_i$ has a simple form [14],

$$2\pi f = \frac{1}{b_1 R}\sqrt{\frac{\mu_e}{\mu_i}}\frac{\mu_i E}{\sqrt{y}} - \frac{b_2}{R^2}\sqrt{\frac{\mu_i}{\mu_e}}\frac{\mu_i T_e}{\sqrt{y}}, \qquad (2)$$

where $b_1 = 0.413$, $b_2 = 0.295$, T_e is the electron temperature (in eV), and $y = \mu_e \mu_i B^2/c^2$.

In a hollow-cathode discharge (in contrast to the positive column), there are both the parallel (with respect to the magnetic field) and transverse components of the electric field ($E_\parallel$ and $E_\perp$, respectively), such that $E_\parallel \sim E_\perp \sim E$. In the presence of the transverse current component, the mechanism for the onset of helical instability remains the same, but the instability threshold is higher and, accordingly, the growth rate is lower [12]. Therefore, the amplitude of helical waves will be maximum in the region where $E_\parallel > E_\perp$. Under our experimental conditions, this region lies somewhere between the wall and the axis of the discharge chamber, because the amplitude of helical perturbations is zero

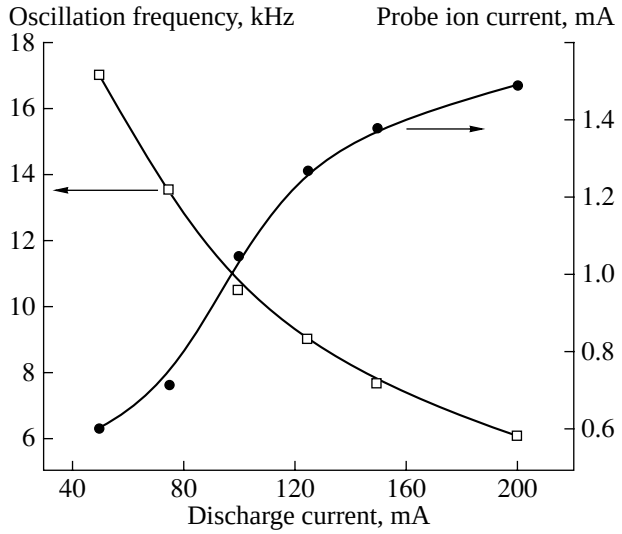

Fig. 5. Effect of the discharge current on the frequency and amplitude of oscillations at a gas (nitrogen) pressure of p = 1.5 Pa (11 mtorr), I = 300 mA, and B = 0.4 mT.

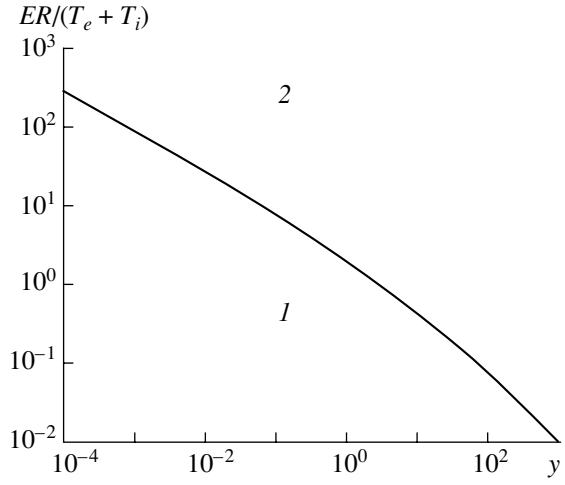

Fig. 6. Threshold electric field for the onset of helical instability as a function of the magnetic field ($y = \mu_e\mu_i B^2/c^2$) [13]: (*1*) stability domain and (*2*) instability domain.

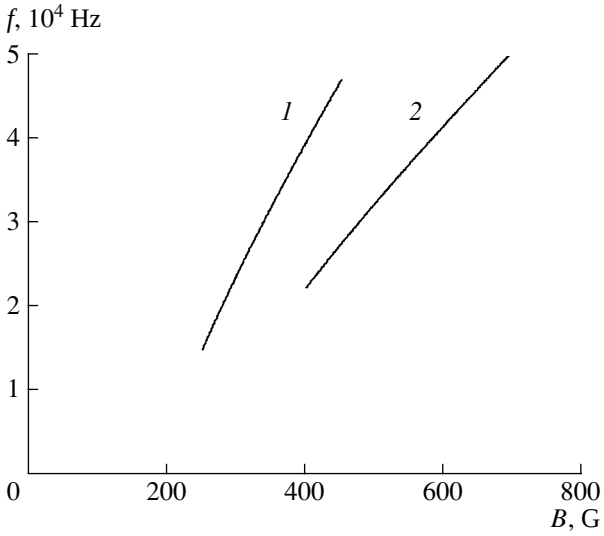

Fig. 7. Frequency of helical plasma oscillations as a function of the magnetic field at $T_e \approx 3$ eV, $\mu_i p \approx 0.5 \times 10^6$ cm^2 torr/(V s), $\mu_e/\mu_i \approx 10^2$, $n_e \approx 2 \times 10^{10}$ cm^{-3}, and gas pressures of p = (*1*) 1.7 and (*2*) 2.7 Pa.

on the axis [12]. In a strong magnetic field, the transverse component of the current is magnetized. Since $\mu_e \gg \mu_i$, the total current at the cathode is equal to

$$I \approx e\mu_i nS\frac{E}{\left(\frac{\mu_i B}{c}\right)^2}, \qquad (3)$$

where n is the plasma density and S is the cathode area.

From expression (3), we can estimate the average electric field in a discharge. For typical experimental parameters ($T_e \approx 3$ eV, $\mu_i p \approx 0.5 \times 10^6$ cm^2 torr/(V s), $\mu_e/\mu_i \approx 10^2$, p = 13 mtorr, $n_e \approx 2 \times 10^{10}$ cm^{-3}, and B = 200 G), the electric field is $E \sim 1$ V/cm. Accordingly, we have $ER/(T_e + T_i) \approx 1$ and $y \approx 10^2$. In this case, as can be seen from Fig. 6, the conditions for the onset of helical instability are achieved.

In view of expression (3), the frequency of helical oscillation (see formula (2)) as a function of the magnetic field and current has the form

$$2\pi f = \frac{1}{2enRS}\frac{1}{b_1}\sqrt{\frac{\mu_i}{\mu_e}}\sqrt{y} - \frac{b_2}{R^2}\sqrt{\frac{\mu_i}{\mu_e}}\frac{\mu_i T_e}{\sqrt{y}}. \qquad (4)$$

The first term on the right-hand side of Eq. (4) accounts for the ambipolar drift of a helical perturbation along the magnetic field. The second term accounts for the rotation of helical waves. Figure 7 shows the oscillation frequency of helical waves as a function of the magnetic field at a constant current for different pressures. At strong magnetic fields, the dependence of the frequency on the magnetic field becomes linear because the contribution of the rotational term in expression (4) decreases. As the pressure increases, the oscillation frequency decreases because of a decrease in the electron and ion mobilities.

It can be seen from Figs. 7 and 3 that the theoretical and experimental dependences of the oscillation frequency on the magnetic field at different pressures agree both qualitatively and quantitatively.

It follows from formula (4) that the use of a heavier gas should lead to a decrease in the oscillation frequency because of the lower ion mobility. This should also lead to an increase in the threshold magnetic field (Fig. 6).

As the discharge current increases (in a hollow-cathode discharge, the current is proportional to the electron density), the electron temperature increases monotonically and saturates at a level corresponding to the electronic excitation of molecules [10]. Therefore, the first term on the right-hand side of Eq. (4) is independent of the current, whereas the second term is proportional to the electron temperature. For this reason, as the current increases, the oscillation frequency should decrease monotonically and then saturate, which has also been confirmed experimentally.

To conclude, a comparison between experiment and theory shows that the oscillations in a hollow-cathode discharge in a longitudinal magnetic field are most likely related to the onset of helical instability.

ACKNOWLEDGMENTS

We are grateful to R. Macgill (Berkeley) for his assistance in carrying out our experiments. This work was supported in part by the US Department of Energy under the IPP Trust-2 USA–Russia research cooperation program (project nos. LBNL-T2-196 and 204), contract no. DE-AC03-76SF00098, and the US Civil-

ian Research and Development Foundation (grant no. 016-2 TO).

REFERENCES

1. B. Moskalev, *Hollow-Cathode Discharge* (Atomizdat, Moscow, 1968) [in Russian].
2. N. V. Gavrilov, G. A. Mesyats, G. V. Radkovskii, and V. V. Bersenev, Surf. Coat. Technol. **96**, 81 (1997).
3. D. M. Goebel and R. M. Watkins, Rev. Sci. Instrum. **71**, 388 (2000).
4. M. V. Shandrikov, A. V. Vizir, G. Y. Yushkov, and E. M. Oks, in *Emerging Applications of Vacuum-Arc-Produced Plasma, Ion, and Electron Beams*, Ed. by E. Oks and I. Brown (Kluwer, Amsterdam, 2002), p. 115.
5. V. M. Tkachenko and V. B. Tyutyunik, Zh. Tekh. Fiz. **42**, 49 (1972) [Sov. Phys. Tech. Phys. **17**, 34 (1972)].
6. V. N. Glazunov and A. S. Metel', Zh. Tekh. Fiz. **51**, 932 (1981) [Sov. Phys. Tech. Phys. **26**, 559 (1981)].
7. B. V. Pavlovic and J. S. Dobrosavljevic, Spectrochimica Acta B **47**, 297 (1992).
8. J.-J. Lai, Q.-M. Chen, and J.-L. Qiu, J. Phys. D **33**, 1785 (2000).
9. H. Baranková, L. Bárdos, and S. Berg, Surf. Coat. Technol. **94–95**, 578 (1997).
10. E. Oks, I. Brown, and A. Anders, Rev. Sci. Instrum. **75**, 1030 (2004).
11. A. V. Nedospasov, Usp. Fiz. Nauk **116**, 643 (1975) [Sov. Phys. Usp. **18**, 588 (1975)].
12. V. V. Vladimirov, Usp. Fiz. Nauk **115**, 73 (1975) [Sov. Phys. Usp. **18**, 37 (1975)].
13. R. R. Johnson and D. A. Jerde, Phys. Fluids **5**, 988 (1962).
14. V. V. Vladimirov, V. N. Gorshkov, and A. I. Shchedrin, Fiz. Plazmy **5**, 187 (1979) [Sov. J. Plasma Phys. **5**, 107 (1979)].

Translated by N.F. Larionova